ADA035600

Report AFRPL-TR-76-87

(12)

PROJECT DAME - TACTICAL INSTRUMENTED MISSILE SIMULATION TESTING

J. D. Burton
Rockwell International Corporation
Rocketdyne-McGregor
P. O. Box 548
McGregor, Texas

THIS DOCUMENT APPROVED
FOR
PUBLIC RELEASE
& UNLIMITED DISTRIBUTION

December 1976

Final Report

DDC
RECEIVED
FEB 14 1977
B

Air Force Rocket Propulsion Laboratory
Director of Science and Technology
Air Force Systems Command
Edwards AFB, California 93523

FOREWORD

This report was submitted by Rockwell International Corporation, Rocketdyne Division, P. O. Box 548, McGregor TX 76657, under Contract No. F04611-75-C-0069, Job Order No. 314812ME with the Air Force Rocket Propulsion Laboratory, Edwards, CA 93523.

This report has been reviewed by the Information Office/DOZ and is releasable to the National Technical Information Service (NTIS). At NTIS, it will be available to the general public, including foreign nations. This technical report is UNCLASSIFIED and suitable for public release.

MICHAEL E. BOND, 1LT, USAF
Project Engineer

LEE G. MEYER, Chief
Air-Launch Propulsion Section

FOR THE COMMANDER

CHARLES R. COOKE, Director
Solid Rocket Division

NOTICES

"When U. S. Government drawings, specifications, or other data are used for any purpose other than a definitely related Government procurement operation, the Government thereby incurs no responsibility nor any obligation whatsoever, and the fact that the Government may have formulated, furnished, or in any way supplied the said drawings, specifications or other data, is not to be regarded by implication or otherwise, or in any manner licensing the holder or any other person or corporation, or conveying any rights or permission to manufacture, use or sell any patented invention that may in any way be related thereto."

UNCLASSIFIED

SECURITY CLASSIFICATION OF THIS PAGE (When Data Entered)

REPORT DOCUMENTATION PAGE

READ INSTRUCTIONS BEFORE COMPLETING FORM

1. REPORT NUMBER: AFRPL-TR-76-87	2. GOVT ACCESSION NO.
3. RECIPIENT'S CATALOG NUMBER	
4. TITLE (and Subtitle): PROJECT DAME - TACTICAL INSTRUMENTED MISSILE SIMULATION TESTING	5. TYPE OF REPORT & PERIOD COVERED: Final Report. Jun 75 - Sep 76
6. PERFORMING ORG. REPORT NUMBER: R-4939	
7. AUTHOR(s): J. D. Burton	8. CONTRACT OR GRANT NUMBER(s): F04611-75-C-0069
9. PERFORMING ORGANIZATION NAME AND ADDRESS: Rockwell International Corporation, Rocketdyne Division, P. O. Box 548, McGregor TX 76657	10. PROGRAM ELEMENT, PROJECT, TASK AREA & WORK UNIT NUMBERS: JON 3148 12 ME
11. CONTROLLING OFFICE NAME AND ADDRESS: Air Force Rocket Propulsion Laboratory, Edwards AFB CA 93523	12. REPORT DATE: Dec 76
	13. NUMBER OF PAGES: 180
14. MONITORING AGENCY NAME & ADDRESS (if different from Controlling Office)	15. SECURITY CLASS. (of this report): Unclassified
	15a. DECLASSIFICATION/DOWNGRADING SCHEDULE

16. DISTRIBUTION STATEMENT (of this Report)

Approved for Public Release; Distribution Unlimited

17. DISTRIBUTION STATEMENT (of the abstract entered in Block 20, if different from Report)

18. SUPPLEMENTARY NOTES

19. KEY WORDS (Continue on reverse side if necessary and identify by block number)

*IN FLIGHT SIMULATION; THERMAL CYCLING; VIBRATION; MEASURING INSTRUMENTS; CALIBRATION; SOLID PROPELLANTS; CHARACTERISTICS; AGING

20. ABSTRACT (Continue on reverse side if necessary and identify by block number)

Report describes tests conducted and presents results obtained on a program in which results of a previous program (an instrumented modified 14-inch bomb dummy unit (BDU) flown on an F-111 aircraft) were applied, analytically, to an AIM-7E (Sparrow) motor. An inert Sparrow motor was instrumented with accelerometers, strain and stress gages, and thermocouples. It was then subjected to thermal, dynamic, and captive-flight simulation tests that cover the expected range of loadings to be encountered in captive flight on high-performance aircraft. Random vibration input control was based on BDU response during actual captive

DD FORM 1 JAN 73 1473 EDITION OF 1 NOV 65 IS OBSOLETE

UNCLASSIFIED

SECURITY CLASSIFICATION OF THIS PAGE (When Data Entered)

Block 20 Continued

flight, which compares favorably with MIL-STD-810C requirements at frequencies below 400 Hertz. An enhanced spectral input based on assumed response on aircraft such as an F-4 was also run. Both analysis and experiment indicate that stresses imposed on the motor from thermal changes are relatively low. Propellant characterization and aging data and gage calibration data are presented. Calibration data presented are sufficient to permit data reduction from actual captive-flight tests.

CONTENTS

Introduction and Summary 1
Propellant Formulation and Characterization 3
Uniaxial Tensile Properties 4
Strain Evaluation Cylinder Data 4
Peel Data 5
Biaxial Strip Data 5
Carton Propellant Aging Tests 6
Motor Design and Stress Analysis 7
Instrumentation and Bench Calibration 8
Clip Displacement Gages 8
Diaphragm Bond-Line Pressure Gages 8
Bond-Line Shear Gages 11
Gage Installation and In-Situ Calibration 13
Gage Installation 13
In-Situ Calibration of Bond-Line Gages 13
Rapid Heating Response 14
Motor Cast, Cure, and Cooldown 15
Final Instrumentation 17
Environmental Testing 19
Thermal Cycling 19
Sinusoidal Vibration 20
Captive-Flight Simulation 23
Conclusions 29

ACCESSION for
NTIS White Section
DDC Buff Section
UNANNOUNCED
JUSTIFICATION
BY
DISTRIBUTION/AVAILABILITY CODES
Dist. AVAIL. and/or SPECIAL
A

CONTENTS (Continued)

TABLES

1	TIM Propellant Formulation	3
2	Thermal Properties of Propellant RDS-011	5
3	Peel Strength, Propellant RDS-011	5
4	Summary of Normal Diaphragm Gage Bench Calibration	10
5	Shear Gage Bench Calibration Data Summary	12
6	Internal Accelerometer Calibration Data	17
7	Residual Stresses After Mandrel Removal	17
8	Sinusoidal Response of TIM to Transverse Vertical Vibration	21
9	Vibration Environment Comparison	24
10	Instrumentation Response, End of Loiter Simulation, Aeroheat Test 2	26
11	Random Vibration Response	27

FIGURES

1	Hybrid Uniaxial Tensile Test Specimen	31
2	Uniaxial Strain-Time History for Characterization	31
3	Master Uniaxial Relaxation Modulus, RDS-011	32
4	Smith Plot, RDS-011 Uniaxial Tensile Failure Data	33
5	Uniaxial Tensile Properties, RDS-011	34
6	RDS-011 Four-Inch SEC Data	35
7	Ninety-Degree Peel Test Specimen	36
8	Biaxial Strip Tensile Specimen	36
9	RDS-011 Biaxial Tensile Relaxation Modulus	37
10	RDS-011 Biaxial Constant Crosshead Rate Test Data	38
11	Effect of 77 F Aging on Uniaxial Strain Capability	39
12	Effect of 120 F Aging on Uniaxial Strain Capability	40
13	Effect of 145 F Aging on Uniaxial Strain Capability	41

FIGURES (Continued)

14	Effect of 77 F Aging on Modulus and Peel Strength	42
15	Effect of 120 F Aging on Modulus and Peel Strength	43
16	Effect of 145 F Aging on Modulus and Peel Strength	44
17	Tactical Instrumented Motor, SPARROW Mk 38 Mod 4 Configuration	45
18	Calculated Bond-Line Stresses, TIM Equilibrium Conditions	46
19	Calculated Change in Inner Bore Slot Width at -60 F	46
20	Mechanical Clip Displacement Gages	47
21	Bench Calibration for Clip Gage C-4	48
22	Bench Calibration for Clip Gage C-5	49
23	Clip Gage Calibration Prior to Installation	50
24	Normal Bond Stress Diaphragm Gage	51
25	Bench Calibration of Normal Gage N-6	52
26	Bench Calibration of Normal Gage N-7	53
27	Bench Calibration of Normal Gage N-8	54
28	Bench Calibration of Normal Gage N-9	55
29	Bench Calibration of Normal Gage N-13	56
30	Bench Calibration of Normal Gage N-15	57
31	Shear Stress Gage	57
32	Calibration for Shear Gage S-1 Sensitivity	58
33	Calibration for Shear Gage S-2 Sensitivity	59
34	Gage Locations on TIM Instrumented Lined Case	60
35	Instrumented SPARROW Case, Lower View	61
36	Instrumented SPARROW Case, Upper View	61
37	In-Situ No-Load Data, Gage N-6	62
38	Temperature Sensor Output, Gage N-6	63
39	In-Situ No-Load Data, Gage N-7	64
40	Temperature Sensor Output, Gage N-7	65
41	In-Situ No-Load Data, Gage N-8	66

FIGURES (Continued)

42	Temperature Sensor Output, Gage N-8	67
43	In-Situ No-Load Data, Gage N-9	68
44	Temperature Sensor Output, Gage N-9	69
45	In-Situ No-Load Data, Gage N-13	70
46	Temperature Sensor Output, Gage N-13	71
47	In-Situ No-Load Data, Gage N-15	72
48	Temperature Sensor Output, Gage N-15	73
49	In-Situ No-Load Data, Gage S-1	74
50	Temperature Sensor Output, Gage S-1	75
51	In-Situ No-Load Data, Gage S-2	76
52	Temperature Sensor Output, Gage S-2	77
53	Normal Gage Sensitivity, In-Situ Calibration	78
54	Case Temperature, Rapid Heating Test	79
55	No-Load Error, Gage S-1, Rapid Heating Test.	79
56	No-Load Error, Gage N-6, Rapid Heating Test.	80
57	No-Load Error, Gage N-7, Rapid Heating Test.	80
58	No-Load Error, Gage N-8, Rapid Heating Test.	81
59	No-Load Error, Gage N-9, Rapid Heating Test.	81
60	No-Load Error, Gage N-13, Rapid Heating Test	82
61	No-Load Error, Gage N-15, Rapid Heating Test	82
62	Average Motor Temperature During Cure	83
63	Normal Gage N-6 Cure Response	84
64	Normal Gage N-7 Cure Response	85
65	Normal Gage N-8 Cure Response	86
66	Normal Gage N-9 Cure Response	87
67	Normal Gage N-13 Cure Response	88
68	Normal Gage N-15 Cure Response	89
69	Shear Gage Cure Response	90
70	Average Motor Temperature, Postcure Cooldown	91
71	Forward End Normal Gage Response During Postcure Cooldown	92
72	Center Plane Normal Gage Response During Postcure Cooldown	93

FIGURES (Continued)

73	Aft End Normal Gage Response During Postcure Cooldown	94
74	Shear Gage Response During Postcure Cooldown	95
75	TIM Instrumentation Locations	96
76	Clip Gage C-4 Calibration	97
77	Clip Gage C-5 Calibration	97
78	Internal Pressure Gage Response Characterization Data	98
79	Forward End of TIM	99
80	Cable Connections on TIM	100
81	TIM Forward End Closure	100
82	Revised Temperature Response for Gage N-7	101
83	Revised No-Load Output for Gage N-7	101
84	Thermal Cycle Response, Gage N-6	102
85	Thermal Cycle Response, Gage N-7	103
86	Thermal Cycle Response, Gage N-8	104
87	Thermal Cycle Response, Gage N-9	105
88	Thermal Cycle Response, Gage N-13	106
89	Thermal Cycle Response, Gage N-15	107
90	Thermal Cycle Response, Gage S-1	108
91	Thermal Cycle Response, Gage S-2	109
92	Thermal Cycle Response, Clip Gage C-4	110
93	Thermal Cycle Response, Clip Gage C-5	110
94	Center Plane Normal Bond Stress	111
95	Bond-Line Thermal Shear Stress	112
96	Inner Bore Slot Width Thermal Response	113
97	TIM Dynamic Test Instrumentation	114
98	Ambient Sine Sweep Data, Averager Channel	115
99	Ambient Sine Sweep Data, Channel A-3	116
100	Ambient Sine Sweep Data, Channel A-4	117
101	Ambient Sine Sweep Data, Channel A-5	118

FIGURES (Continued)

102	Ambient Sine Sweep Data, Channel A-6	119
103	Ambient Sine Sweep Data, Channel A-7	120
104	Ambient Sine Sweep Data, Channel A-8	121
105	Ambient Sine Sweep Data, Channel N-6	122
106	Ambient Sine Sweep Data, Channel N-7	123
107	Ambient Sine Sweep Data, Channel N-8	124
108	Ambient Sine Sweep Data, Channel N-9	125
109	Ambient Sine Sweep Data, Channel N-13	126
110	Ambient Sine Sweep Data, Channel N-15	127
111	Ambient Sine Sweep Data, Channel S-1	128
112	Ambient Sine Sweep Data, Channel S-2	129
113	Ambient Sine Sweep Data, Channel C-4	130
114	Ambient Sine Sweep Data, Channel C-5	131
115	Nominal Vibration Control at Mk 38 Center of Gravity	132
116	A Target Control Temperature	133
117	B Target Control Temperature	133
118	SPARROW Inert Motor High-Performance Severe Flight Dynamic Spectrum Enhanced by Motor Response Data, Data Input Control, Motor Data.	134
119	Captive-Flight Test Setup with Shroud Open	135
120	Captive-Flight Test Setup with Shroud Closed	135
121	First Aeroheat Test	136
122	Second Aeroheat Test	137
123	Third Aeroheat Test	138
124	Fourth Aeroheat Test	139
125	Aeroheat Test 2, Thermal Response	140
126	Aeroheat Test 2, S-1 Thermal Response	140
127	Aeroheat Test 2, S-2 Thermal Response	141
128	Aeroheat Test 2, N-6 Thermal Response	141
129	Aeroheat Test 2, N-7 Thermal Response	142
130	Aeroheat Test 2, N-8 Thermal Response	142
131	Aeroheat Test 2, N-9 Thermal Response	143
132	Aeroheat Test 2, N-13 Thermal Response	143

FIGURES (Continued)

133	Aeroheat Test 2, N-5 Thermal Response	144
134	Aeroheat Test 2, C-4 Thermal Response	144
135	Aeroheat Test 2, C-5 Thermal Response	145
136	Aeroheat Test 3, Thermal Response	146
137	Aeroheat Test 3, N-6 Thermal Response	147
138	Aeroheat Test 3, N-7 Thermal Response	147
139	Aeroheat Test 3, N-8 Thermal Response	148
140	Aeroheat Test 3, N-9 Thermal Response	148
141	Aeroheat Test 3, N-13 Thermal Response	149
142	Aeroheat Test 3, N-15 Thermal Response	149
143	Aeroheat Test 3, S-1 Thermal Response	150
144	Aeroheat Test 3, S-2 Thermal Response	150
145	Aeroheat Test 3, C-4 Thermal Response	151
146	Aeroheat Test 3, C-5 Thermal Response	151
147	Random Vibration, Averaged Channel	152
148	Random Vibration, Channel A-3	153
149	Random Vibration, Channel A-4	154
150	Random Vibration Aeroheat, Channel A-5	155
151	Random Vibration, Aeroheat, Channel A-7	156
152	Random Vibration Aeroheat, Channel A-8	157
153	Random Vibration, Aeroheat, Channel N-6	158
154	Random Vibration, Aeroheat, Channel N-7	159
155	Random Vibration, Aeroheat, Channel N-9	160
156	Random Vibration, Aeroheat, Channel N-13	161
157	Random Vibration, Aeroheat, Channel N-15	162
158	Random Vibration Aeroheat, Channel C-3	163
159	Random Vibration, Aeroheat, Channel C-5	164

INTRODUCTION AND SUMMARY

The Air Force has been intensely involved in measuring the captive flight environment of tactical air-launched missiles under a continuing AFRPL project, Determination of Aircraft Missile Environment (DAME). Much of the work has been conducted on an instrumented modified 14-inch Bomb Dummy Unit (BDU) flown on an F-111 aircraft.[1] While that effort was directed primarily toward obtaining rocket motor response, data were also collected for the forward section and launch lug components. The result of that effort was a ground test environmental envelope that represents motor captive-flight environment.

As a logical extension of that effort, the results of the BDU program were applied, analytically, to an AIM-7E (SPARROW) motor. This report describes that effort. An inert SPARROW motor was instrumented with accelerometers, strain and stress gages, and thermocouples. The motor was then subjected to thermal, dynamic, and captive-flight simulation tests as evolved from results of the BDU program.

The program is discussed in chronological sequence of the efforts involved. An inert propellant was formulated based on the LPC-667 inert propellant used in the BDU. Using propellant characterization data and finite-element computer codes, the response of the motor to various thermal environments was analyzed. Stress sensors for bond-line radial stress measurement and clip gages for determining inner bore displacements were fabricated and installed. The bond-line gages were installed in the lined case, and an extensive in-situ calibration of these gages was conducted. The motor was then cast and cured, and the mandrel was removed. Following installation of the remaining gages, the motor was

---

[1] Burton, J. D.: Project DAME - Flight and Simulation Testing of a Modified Bomb Dummy Unit, Final Report, AFRPL-TR-76-60, Rockwell International Corporation, Rocketdyne Division, McGregor, Texas, October 1976.

sealed and subjected to thermal, dynamic, and captive-flight simulation tests. Instrumentation outputs were analyzed, and the observed responses were compared to the initial predictions. Measured thermal stresses were lower than predicted. Dynamic response was about as expected although the predictive techniques for this type load is minimally accurate.

The instrumented inert motor, along with a set of drawings locating the gages and their associated wiring diagrams, were delivered to the AFRPL for use as a test vehicle in captive-flight testing.

PROPELLANT FORMULATION AND CHARACTERIZATION

For the purposes for which the Tactical Instrumented Motor (TIM) is intended, it is required that an inert propellant be used. The propellant used in the BDU was an inert HTPB formulation made by Lockheed Propulsion Company of Redlands, California, in the late 1960s. Based on experience with the BDU, it was decided to utilize this or a similar formulation for the TIM. Because of the toxicity of toluene di-isocyanate (TDI) used in the LPC-667 propellant, isophorone di-isocyanate (IPDI) was used in the TIM propellant, RDS-011. The propellant formulation is shown in Table 1.

TABLE 1. TIM PROPELLANT FORMULATION

Ingredients	Wt %
R-45M Polymer	13.83
IPDI Curative	1.02
AO-2246 Antioxidant	0.01
Isodecyl Pelargonate	2.99
HX-752	0.15
Aluminum, Type II	47.00
Ground Ammonium Sulfate	35.00
Total	100.00

The propellant is cured by exposure to 145 degrees (F) for 12 days. Mechanical properties characterization including aging data were fairly comprehensive for an inert propellant. These data are discussed below.

UNIAXIAL TENSILE PROPERTIES

Uniaxial tensile data were obtained on hybrid Class A tab-ended dog-bones, Figure 1. The tests were conducted over the range -65 to 165 F using the strain-time history shown in Figure 2. Relaxation modulus data are plotted in Figure 3. A Smith plot of the uniaxial tensile failure characteristics is presented in Figure 4. Constant strain rate initial tangent modulus and failure data are plotted in Figure 5. Time-temperature superposition was determined empirically by shifting the relaxation modulus data laterally to obtain the continuous curve of Figure 3. The tensile failure data represent the maximum stress on the specimen (not necessarily maximum force) as determined by correcting the cross-sectional area of the specimen for the applied strain assuming a Poisson's ratio of about 0.5. The failure strain is the strain at maximum true stress and is very nearly equal to the rupture strain. Note, from Figure 5, that this propellant has an excellent strain capability that is quite flat over a wide range of rates.

STRAIN EVALUATION CYLINDER DATA

Four 4-inch-diameter strain evaluation cylinders (SECs) with web fractions ranging from 64 to 75% were fabricated and temperature cycled between -65 and 135 F. No failures occurred in any of the cylinders. Measured bore strain vs temperature for these tests are plotted in Figure 6. The measured strain at -65 F is low because of the method of measurement, which requires removing the SEC from the temperature cycling chamber. At this extreme condition, due to rapid warm-up, the measurement is always low. A least squares curve fit of these data (corrected for the 13-inch length of the cylinder) was used to calculate a plane strain equivalent. From this, a linear coefficient of thermal expansion and an effective Poisson's ratio as well as a mean strain-free temperature were computed. The best fit was obtained from these data. The values are shown in Table 2.

TABLE 2. THERMAL PROPERTIES OF PROPELLANT RDS-011

Linear Coefficient of Thermal Expansion, $(\text{deg F})^{-1}$	5×10^{-5}
Poisson's Ratio	0.495
Mean Strain Free Temperature, deg F	154

PEEL DATA

The 90^{0} peel test is a semi-quantitative measure of the propellant/liner bond strength. The specimen used is illustrated in Figure 7. The force required to initiate peel when the liner is pulled at a constant crosshead rate of 0.2 in./min is recorded and divided by the width of the specimen to produce a peel measurement in pounds per linear inch, pli. Values obtained are shown in Table 3.

TABLE 3. PEEL STRENGTH, PROPELLANT RDS-011

Test Temperature, deg F	90^{0} Peel Measurement, pli
170	0.43
77	1.03
-47	11.2

BIAXIAL STRIP DATA

A limited tensile spectrum was run using a biaxial strip specimen as shown in Figure 8. Since no replicates were used, the data scatter appears quite large; but, in fact, it indicates the usual scatter obtained on propellant tensile tests. The relaxation modulus, shifted using the a_T determined from the uniaxial spectrum, is shown in Figure 9. Tensile failure data are shown in Figure 10. Comparison of these biaxial data with the uniaxial tensile data revealed a moderate increase

in relaxation modulus and slight increases in constant crosshead rate modulus and rupture strain.

CARTON PROPELLANT AGING TESTS

To obtain an indication of the manner in which this propellant would change with motor age after casting, a limited laboratory aging study was conducted with propellant cast, cured, and stored in sealed, lined cartons. Twelve cartons were aged, four at each of three temperatures, 77, 120, and 145 F. The cartons were sampled after 1, 3, 6, and 15 weeks storage at the respective temperatures; and uniaxial and 90° peel bond specimens were tested. Three of the four characteristics tested showed significant change with age. Uniaxial strain capability, plotted in Figures 11 through 13, decreased. The greatest change occurred, of course, at 145 F. The indicated rate of decrease at the 15-week aging point was about 0.073 in./in./decade of time measured in weeks. The capability at 15 weeks exposure to 145 deg F is about 0.495 in./in.; so one could expect a strain capability after 3 years of at least 0.42 in./in. and after 30 years of 0.35 in./in. Similar changes were noted in the uniaxial relaxation modulus (increasing with time at elevated temperature storage) and 90° peel bond data (also increasing with time at elevated storage) as shown in Figures 14 through 16. Only tensile strength data showed no significant change during the 15-week aging study. From the initial value of 124 psi, the range of data for all tests fell between 112 and 129 psi.

MOTOR DESIGN AND STRESS ANALYSIS

The TIM is of the Sparrow Mk 38 Mod 4 configuration. The grain, shown in Figure 17, is a five-point-star configuration with a slight taper to permit mandrel removal from the forward end. Using the configuration and the propellant characterization data, a stress analysis was conducted to determine structural soundness and estimate motor response to various environmental conditions. A quasi-viscoelastic solution, based on substituting a time-temperature equivalent relaxation modulus yields the bond-line normal stress and longitudinal shear stress plotted in Figure 18. The normal bond stress decreases from the level in the motor center-plane to about 40% of that value at about 4 inches from the ends of the motor. A maximum inner bore strain of 6.6% was calculated for the -60 F soak condition. The separation (slot width) of star points at about 4 inches from the ends of the motor was calculated to be 0.088 inch and about 0.22 inch near the center-plane at a radius of 1.7 inches, Figure 19. A simple dynamic analysis yields a bond stress of about 0.1 psi/g for vibration transverse to the centerline of the motor.

Inasmuch as the minimum strain capability is about 0.41 in./in. and the cold tensile strength is about 160 psi, the maximum strain of 0.066 in./in. and bond stress of 7.5 psi do not significantly challenge the structural integrity of the grain.

INSTRUMENTATION AND BENCH CALIBRATION

Propellant response is monitored, in the motor, by stress sensors and clip-gage displacement sensors described below. The installation procedure and gage locations are described in the following section.

CLIP DISPLACEMENT GAGES

The clip-type displacement gage is simply a mechanical spring that bends under a displacement loading. The spring is instrumented with semi-conductor strain gages, Figure 20, to measure bending induced by displacement. The output is generally linear with displacement but also varies somewhat with temperature. No-strain outputs and response to displacement for the two gages, C-4 and -5, installed in the TIM are plotted in Figures 21 and 22. These data were obtained in bench calibration. The apparent non-linearity is actually due to uncertainty in the displacement measurement as a subsequent 80 F bench calibration just prior to installation, Figure 23, revealed.

DIAPHRAGM BOND-LINE PRESSURE GAGES

The advent of the bond-line stress gage 10 years ago opened an entirely new approach to solid rocket motor loads definition. Although these instruments have been in use for a decade, some problems remain. The basic diaphragm gage is illustrated in Figure 24. The principle of operation is: The thin instrumented membrane (diaphragm) that faces the propellant grain deflects under pressure in a bending mode, the strain gage(s) bonded to the membrane respond to the bending, and gage response is monitored in a bridge circuit as shown in Figure 24. Because the semi-conductor strain gages are temperature sensitive, a compensating resistance is included in the circuit to assist in minimizing the change in the active gage output due solely to temperature. By including a

second bridge circuit, this compensating gage can be monitored to indicate temperature.

One of the biggest problems associated with diaphragm normal stress gages is the interaction between the grain and the gage. On the one hand, the presence of the gage upsets the local stress field in the motor. To offset this effect, the gage is embedded in a hemisphere of propellant, Figure 24, the radius of the hemisphere being about two times the gage diameter. This embedded gage/propellant block is then calibrated as the measuring instrument. Because of the relatively large size of this instrumented block, its use is limited to grain web fractions larger than the block itself. In the case of TIM, this dimensional conflict is marginal, i.e., the minimum instrumented web is only about 0.25-inch greater than the thickness of the gage block.

The second facet of the grain/gage interaction problem is the effect of the grain properties on the gage. The actual bending pattern of the diaphragm is influenced by the stiffness of the adjacent material. Since the propellant stiffness (modulus) is time and temperature dependent and susceptible to change with age, these variables affect gage response. This feature requires a comprehensive calibration of the embedded gage over the range of temperatures and loads. Results of such a calibration for the six normal bond stress gages for the TIM are plotted in Figures 25 through 30, and a summary of the no-load output, E_0; sensitivity, m; and gage temperature output, E_T, is presented in Table 4. For a gage output, E_r, at any temperature, T, stress is calculated from:

$$\sigma_r = \frac{E_r(T) - E_0(T)}{-m} \quad \text{psi}$$

The apparent non-linearity in gage output vs pressure is due partially to uncertainty in the control variable (pressure), especially at temperatures above zero and partially to the viscoelastic nature of the propellant embedding material. The hysteresis observed at the colder temperatures is

TABLE 4. SUMMARY OF NORMAL DIAPHRAGM GAGE BENCH CALIBRATION

	Temperature, deg F										
	155	150	70	68	65	20	13	-30	-35	-46	-60
N-6											
No-load Output, E_o, mv	--	2.6	--	--	4.3	2.1	--	-3.1	--	--	-34.5
Pressure Sensitivity, m, mv/psi	--	0.95	--	--	1.03	1.06	--	0.97	--	--	0.46
Temperature Output, E_T, mv	--	146	--	--	19	-52	--	-112	--	--	-145
N-7											
No-load Output, E_o, mv	7.0	--	--	3.8	--	-0.2	--	--	-9.4	--	-28.8
Pressure Sensitivity, m, mv/psi	1.01	--	--	1.03	--	1.02	--	--	0.92	--	0.61
Temperature Output, E_T, mv	234	--	--	23	--	-88	--	--	-191	--	-229
N-8											
No-load Output, E_o, mv	-4.8	--	--	4.6	--	-1.9	--	--	-18.1	--	-30.4
Pressure Sensitivity, m, mv/psi	0.57	--	--	0.55	--	0.50	--	--	0.41	--	0.15
Temperature Output, E_T, mv	125	--	--	-11	--	-72	--	--	-125	--	-126
N-9											
No-load Output, E_o, mv	0.44	--	--	5.5	--	1.6	--	--	-4.6	--	-22.0
Pressure Sensitivity, m, mv/psi	1.16	--	--	1.20	--	1.15	--	--	0.96	--	0.55
Temperature Output, E_T, mv	132	--	--	-28	--	-117	--	--	-197	--	-221
N-13											
No-load Output, E_o, mv	-6.2	--	2.5	--	--	--	4.3	--	--	-7.6	-9.7
Pressure Sensitivity, m, mv/psi	0.89	--	0.97	--	--	--	1.00	--	--	0.97	0.86
Temperature Output, E_T, mv	222	--	36	--	--	--	-79	--	--	-185	-206
N-15											
No-load Output, E_o, mv	7.9	--	5.0	--	--	--	3.6	--	--	-6.3	-8.5
Pressure Sensitivity, m, mv	0.46	--	0.55	--	--	--	0.53	--	--	0.51	0.51
Temperature Output, E_T, mv	203	--	6	--	--	--	-114	--	--	-228	-251

further evidence of the viscoelastic nature of the propellant and of its effect on gage output. At times on the order of 30 minutes and at uniform temperatures, this effect is minimal. Under rapid rates of temperature change, such as aeroheating, the effect is probably much greater than the stress change to be detected.

BOND-LINE SHEAR GAGES

Bond-line shear stress is monitored by a device fabricated from a block of propellant that contains two high-elongation strain gages as shown in Figure 31. When properly oriented this gage measures longitudinal stress at the propellant/liner interface. Because of the viscoelastic effect of the propellant from which the gage is fabricated, the gage must be calibrated with respect to time and temperature. Gage outputs are monitored in a bridge circuit in the same manner as the gages described previously. The gages are oriented and thermally compensated in such a manner as to minimize gage sensitivity to radial stresses and temperatures. As in the case of the normal gages, however, a second bridge circuit using fixed resistors and one of the semi-conductor strain gages is provided to sense temperature at the gage.

The shear gages, S-1 and -2, were calibrated in a double-lap shear test fixture. Responses were obtained by applying a fixed load and monitoring gage output as a function of time and temperature. The data were then shifted vertically and horizontally in much the same manner that propellant property data are shifted to obtain a single master response curve. These data are shown in Figures 32 and 33 for the two shear gages. Table 5 summarizes the no-load output and temperature response. The data, although superimposed with a time-temperature equivalence function, are obtained for equilibrium temperature conditions. It is not readily shown that gage outputs for a condition of rapid thermal change could be interpreted with any significant degree of accuracy.

TABLE 5. SHEAR GAGE BENCH CALIBRATION DATA SUMMARY

Temperature, deg F	S-1		S-2	
	No-load Output, E_o, mv	Temperature Output, E_T, mv	No-load Output, E_o, mv	Temperature Output, E_T, mv
150	-3.9	95	2.9	103
110	-2.2	31	1.0	41
78	0.2	-6	-0.1	5
20	2.7	-71	-3.5	-58
-20	4.6	-115	-4.1	-99
-57	14.9	-154	-3.1	-130
-70	13.8	-161	-3.5	-142

Checks of gage linearity, i.e., constant sensitivity with load-level change, indicate that gage variation is within the scatter of data. In bench calibration tests, Gage S-2 proved virtually insensitive to normal stress; while Gage S-1 showed a sensitivity to normal stress of about 0.15 mv/psi at 80 F.

Following bench calibration, the gages were prepared for installation in the motor. This preparation included trimming the propellant plugs, cutting wires to the proper length, and some final checks. Installation of the gages and in-situ calibration are described in the following section.

GAGE INSTALLATION AND IN-SITU CALIBRATION

GAGE INSTALLATION

The gages that measure bond-line response were, of course, installed before the propellant was cast. A toluene-rich adhesive was used to bond the six normal stress and two shear stress gages to the liner. Each "gage" consisted of a gage, a bridge completion circuit, and a thermocouple, all embedded in a propellant plug as described in the preceding section. The locations of the installed gages are shown in Figure 34; photographs taken after the installation are presented in Figures 35 and 36. The motor was then sealed and subjected to pressurization and thermal cycling to provide an in-situ calibration of the normal stress gages and no-load calibration of the shear gages as discussed below.

IN-SITU CALIBRATION OF BOND-LINE GAGES

The sealed motor case was exposed to equilibrium and slow rate-of-change temperature cycling over the range of -65 to 175 F. Pressurization from -10 to 30 psig was used to obtain normal gage sensitivity data. No-load and temperature sensor outputs for each of the eight gages are plotted in Figures 37 through 52. Normal gage sensitivities are summarized in Figure 53.

It is immediately apparent that no-load data for most of these gages are radically different from those measured in bench calibration. Temperature sensor data are slightly different, and sensitivity data are virtually identical. The reason for the difference in no-load output is not apparent. The most probable causes are:

1. In the motor the gages use a common power supply (5 volt) and a common ground. They are, therefore, connected in parallel as opposed to the single gage used in bench calibration.

2. The bridge completion units were installed in the propellant plug after bench calibration (which is used to verify compensation circuitry). Mechanical loads induced on the fixed resistors could have altered output.

Although these changes are not explained, it should be noted that they are not uncommon, based on similar experiences. In-situ no-load and calibration data are the required baseline for evaluating gage response in the cast motor.

RAPID HEATING RESPONSE

In an attempt to evaluate the uncertainty that would result from evaluating gage response data under conditions of rapid thermal change such as aeroheating, the instrumented case was vented to the atmosphere to maintain a pressure-free state inside the case. The case was moved from a -60 F conditioning cell to an adjoining cell that had been pre-conditioned to 160 F. Gage outputs were recorded at frequent intervals. The evaluation was performed by calculating the difference in gage output from the no-load output at the indicated temperature. The comparison was made using the temperature measured by the embedded thermocouple (near the gage/liner interface) and again using gage temperature sensor indications. The second comparison yielded the most favorable results and is discussed here. Data are plotted in Figures 54 through 61.

All gages exhibit a significant response to the transient thermal condition. The error is generally indicative of tension on the diaphragm gages and ranges from 1 to 8 psi. Lower errors are associated with gages that are subjected to the lowest rate of temperature rise due to the method of holding the case during this test. The rate of rise of case temperature was about half that expected in an aeroheat simulation. Therefore, somewhat larger errors could be expected in actual flight conditions. The response seen here is typical of this type gage and is due to the interaction of the diaphragm and propellant plug during the transient thermal condition.

MOTOR CAST, CURE, AND COOLDOWN

Following the in-situ calibration, the motor was cast with RDS-011 propellant. Internal instrumentation was disconnected before the casting operation was begun and reconnected immediately following cast to provide gage response during propellant cure. The instrumented case was pre-conditioned to about 145 F before the propellant was cast and the propellant was mixed at an elevated temperature so that when the gages were reconnected, case wall temperature was about 115 F. Gage monitoring at the rate of once per hour was continuous throughout the 288-hour cure period. The cure oven was to have been controlled to 145 F during this period, but the temperature was elevated after data from thermocouples attached to the embedded gages (Figure 62) indicated the temperature of the motor was about 6 deg F below the desired 145 F. Near the end of the cure cycle, a technician monitoring the cure oven reduced the control temperature so that for the last 3 days of cure, the average motor temperature was again low by 2 to 3 deg F.

Normal gage outputs are shown in Figures 63 through 68; shear gage outputs are plotted in Figure 69. These data are most interesting. For the first 40 hours of cure, although some significant temperature changes occur, the gage responses are moderately small, which indicates propellant was flowing through the forward end overcast ring bleed holes and allowing the amount of propellant in the case to fluctuate with temperature. At about 40 hours, however, the gages begin to respond in the extreme to small changes in temperature. This indicates solidification of the propellant at the forward end, thereby precluding hydrostatic stress relief through propellant flow. Compressive stresses on the order of 30 to 40 psi were developed as the average grain temperature rose to 145 to 146 F. Temperature fluctuation caused primarily by entries to the cure oven (for other reasons than TIM processing) caused sizeable stress oscillations. From about 120 to 140 hours, average temperature steadily

declined over an ~ 2.5 deg F range resulting in significant drops in the compressive load. At about 214 hours, the temperature of the cure oven was lowered almost 5 deg F, resulting in development of slight tension loads at the gages. Gages N-6 and S-1 indicate release of the tensile load, which indicates partial release between the propellant grain and the mandrel.

At the end of cure, the motor was moved into an 85 deg F room to cool down for mandrel removal. Thermal and stress gage histories for this 14-hour period are plotted in Figures 70 through 74. Gage response reveals a little about what occurs during cooldown. When compared with readings taken before the grain was cast, gages at the forward plane, N-6, N-7, and S-1, indicate that during the first 1 to 3 hours of cool-down the grain pulls away from the overcast ring and partially releases from the mandrel, i.e., the load on Gage N-6 drops but that on Gage N-7 remains in tension. The same comparison for gages at the center plane, N-8, N-9, and N-13, indicates mandrel release on the 0 degree side (N-8), slight residual tension on N-13, and significant tension on N-9 at 180 degrees. Finally, at the aft plane, Gages N-15 and S-2, a slight shear builds for the first hour then rapidly releases while the grain slowly pulls away from the mandrel on the side (0 degree) of Gage N-15.

From these cure and cool-down data, it was expected that a nonuniform residual stress state would exist in the motor following mandrel removal. Further, the data indicated a significant release between the grain and mandrel. This was confirmed when the mandrel was removed with a lifting force of < 500 pounds. A lifting force of > 1000 pounds had been required to remove the mandrel on an earlier dry-run test. The mandrel used for the final cast had been polished and freshly coated with Teflon.

Visual and X-ray inspection of the motor following mandrel removal revealed no defects. The motor was returned to the test area for installation of inner bore instrumentation.

FINAL INSTRUMENTATION

Following mandrel removal, the motor bore was instrumented with an assortment of thermocouples, clip strain gages, accelerometers, and an internal pressure gage as indicated in Figure 75. Calibration data for the two clip gages and the internal pressure gage are shown in Figures 76 through 78. Calibration data for the accelerometers are listed in Table 6. Photographs showing the forward end of the motor, Figures 79 through 81, show the instrumentation cables exiting through the forward closure.

TABLE 6. INTERNAL ACCELEROMETER CALIBRATION DATA

	Accelerometer/Location	
	BU60/Forward End	BU61/Aft End
Charge Sensitivity at 100 Hz, pC/g	16.8	18.5
Voltage Sensitivity with 300 pF Capacitance, mv/g	14.2	15.6
Maximum Error, 20 to 2000 Hz, %	2	2

Gage readings taken with the motor at 77 F following mandrel removal and 2 days relaxation are tabulated along with residual stress in Table 7.

TABLE 7. RESIDUAL STRESSES AFTER MANDREL REMOVAL

	Gage							
	N-6	N-7	N-8	N-9	N-13	N-15	S-1	S-2
Response (E_R), mv	36.9	4.5	10.6	19.4	-0.9	3.6	-12.4	-2.5
No-load (E_o), mv	27.3	7.6	6.3	16.7	11.1	6.7	-8.4	-0.3
Sensitivity Factor, mv/psi	1.04	1.05	0.55	1.23	0.96	0.52	4.4	3.3
Stress (σ), psi	-4.2	3.0	-7.8	-2.2	12.5	6.0	-0.9	-0.7

Residual shear stresses are small but are as expected for 77 F, showing load toward the center plane of the motor. Those gages that indicated early mandrel release, i.e., N-6 and N-8, show significant residual compression. Those indicating partial or slow release, N-7, N-13, and N-15, show significant tension. Gage N-9, which showed little release during cooldown, has a small residual compression at ambient.

With final closing of the instrumented motor, environmental testing was begun.

ENVIRONMENTAL TESTING

Environmental testing of the TIM covered three areas: (1) thermal cycling, (2) sinusoidal vibration, and (3) captive-flight simulation. These tests were conducted to characterize motor response and, in the case of captive-flight simulation, to demonstrate the application of a test determined from actual flight conditions to which the Bomb Dummy Unit (BDU) was subjected, as reported in AFRPL-TR-76-60.

Before thermal cycling was begun, a shift in gage output of normal stress gages N-7 and -8 was noted. No satisfactory explanation for these changes could be found though the unique construction of these two gages (dummy compensating gage mounted on the gage support ring) suggests a cause related to the attachment of the dummy gage to the diaphragm wall. The shift occurred for both stress and temperature outputs. The dummy gage is suspect because temperature output involves only that gage. A calculation of resistance change based on the shift in temperature output can be applied to the no-load calibration data to adjust these data to the new response. Since Gage N-8 performed poorly in subsequent testing, as described later, only data from Gage N-7 was corrected in this manner. New no-load and temperature response curves are shown in Figures 82 and 83. All subsequent calculations of thermal response are based on the in-situ calibration data except that for Gage N-7, which uses the data shown here.

THERMAL CYCLING

The TIM was thermally cycled between 160 and -60 F in approximately 40 deg F steps of at least 1-day duration. Two complete cycles were conducted, but data from the first cycle were discounted when moisture condensation on an external connector was discovered. The connector was sealed to prevent condensation on the conductors before the second test cycle was run.

Gage outputs during the second cycle are plotted in Figures 84 through 93. It is apparent that the outputs are smooth functions of temperature, indicative of good gage response. Analysis of the data to obtain stresses and displacements based on the calibrations described previously yielded the results shown in Figures 94 through 96. Normal stresses, Figure 94, are somewhat different from that expected. Stress measured by Gage N-15 at the aft end of the motor is virtually zero. Stress at the forward plane, measured by Gages N-6 (at 180^0) and N-7 (at 0^0) has an average of 2.7 psi, which is obtained by adding tensile stresses recorded on N-7 and compressive stresses recorded on N-6. Average stress at the center plane is somewhat higher. Data from Gage N-8 has been neglected since it had shown significant drift and noise. Shear stresses are essentially as expected as are the inner bore displacements measured between the star slots (compare with Figures 18 and 19). The apparent error in bond-line normal stress is primarily attributable to the relative size of the instrumented propellant plug and the grain web fraction. Because of gage/grain interaction, it is necessary to calibrate the gage embedded in a propellant plug. Because of the size of the plug, we have, in effect, calibrated out a significant portion of the induced stress. This is exemplified by the no-load "error" observed in the rapid heating test during in-situ calibration. The only alternatives would be to use much smaller gages with shorter service lives or reduce the size of the embedded plug and rely on analysis to obtain the proper stress. The latter, if it were acceptable, would, however, imply that satisfactory stress analysis methods are available, in which case the gage would not be required in the first place.

SINUSOIDAL VIBRATION

Following the thermal cycling tests, the motor was subjected to sinusoidal vibration in the transverse vertical axis. The tests were conducted at a 3 g input level over the range of 10 to 2000 Hertz and at temperatures of -20, 85, and 165 F. Dynamic responses of the internal

accelerometers and stress/strain gages along with the externally mounted case accelerometers were recorded for each sine sweep. The accelerometers were located as shown in Figure 97. Ambient (85 F) sine sweep data are plotted in Figures 98 through 114. From these data and data at -20 and 165 F, key response frequencies and their respective amplitude ratios were determined (see Table 8).

TABLE 8. SINUSOIDAL RESPONSE OF TIM TO TRANSVERSE VERTICAL VIBRATION

Frequency, Hz	235	325	500--800	1570	1770
Amplitude Ratio	3	2	8	4	3

These responses are primarily as recorded at the external case accelerometers at the forward and aft ends of the motor. These results, in addition to characterizing the ground vibration response of the TIM, provide the basis for the captive/flight simulation tests described below.

The response of Gage N-8 was very noisy and erratic. This and the other difficulties (output shifts) with this gage make its reliability so low that the gage may be considered non-functional. Shear gage data, while significant, indicate a very low level of dynamic shear stress; therefore, the shear gages were not monitored during captive-flight simulation testing.

Page 22 is blank

CAPTIVE-FLIGHT SIMULATION

Ground simulation of the captive-flight environment is a goal for motor qualification testing. An approach to the design of such a test is discussed in the BDU Final Report (AFRPL-TR-76-60). The fundamental response curve, from that report, is shown in Figure 115 for the vertical direction.

A comparison between this fundamental input control and that specified in MIL-STD-810C is of interest.

The Sparrow is treated in the category of External Stores Carried on Airplanes in accordance with Part 514.2, Procedure IIB of MIL-STD-810C. From Table 514.2IV of that document, we obtain the governing equations:

$$\text{Cut-off frequency for high end, } f_1 = 10^5 \left(\frac{t}{R^2}\right) \text{ Hz} \qquad (1)$$

where

t - case thickness, in.
R - motor radius, in.

$$\text{Low frequency amplitude, } W_1 = (5)\ (10^{-3})\left(\frac{N}{3T}\right)^{1/4} \text{ g}^2/\text{Hz} \qquad (2)$$

where

N - maximum number of expected service missions
T - test time per axis, hr (for functional tests N = 3, T = 1)

$$\text{High-frequency amplitude, } W_2 = (5)(10^{-5})\left(\frac{q}{\rho}\right)^2\left(\frac{N}{3T}\right)^{1/4} g^2/\text{Hz} \qquad (3)$$

where

q - maximum flight dynamic pressure, lb/sq ft

ρ - average store weight density, lb/cu ft

q is taken to be 1200 lb/sq ft for the endurance test and 1800 lb/sq ft for the functional test. Special adjustments require multiplying the result from Eq. 3 by 4 when testing the motor section.

Translating these requirements into quantitative form, we obtain the comparison of Table 9 below.

TABLE 9. VIBRATION ENVIRONMENT COMPARISON[a]

MK 38 SPARROW ρ = 86 lb/cu ft N = 200 R = 4 in. t = 0.074 in. T = 100				
	Functional		Endurance	
	MIL-STD-810C	DAME	MIL-STD-810C	DAME
W_1	0.005 g^2/Hz	0.004 g^2/Hz	0.006 g^2/Hz	0.0064 g^2/Hz
W_2	0.010 g^2/Hz	0.0006 g^2/Hz	0.007 g^2/Hz	0.0010 g^2/Hz[b]
f_1	462 Hz	410 Hz[b]	462 Hz	410 Hz[b]

[a] In both cases, the DAME observation and the MIL-STD-810C requires enhancement of the random curve according to observed resonances for the unit. Testing under MIL-STD-810C is at constant temperature; DAME includes aeroheat response.

[b] In the BDI data, a second cut-off occurs at about 800 Hertz. From 800 to 2000 Hertz, the PSD level rises from W_2 to approximately equal to W_1.

The essence of the comparison is that for frequencies below 400 Hertz, little change is observed between the two environments. For frequencies above 400 Hertz, however, the MIL-STD-810C requires a significantly higher input. In terms of effect on a case-bonded solid propellant motor, the difference is not critical. For components sensitive to high frequency, the differences could become important.

Aerodynamic temperature profiles selected for testing are shown in Figures 116 and 117. Figure 116 simulates a mission in which the aircraft, starting from a nominal ground condition of 80 F, takes off, climbs to ~ 35,000 feet, and loiters at low speed. Following low-speed loiter, a dash to Mach 2 is assumed. The second profile, Figure 117, is based on a low-level flight, dash, then low-speed flight at high altitude.

Dynamic simulation is determined from the basic profile recorded during BDU testing on an F-111. Two levels of testing, basic and 10 x basic, were used. The actual control profile is shown in Figure 118 where alterations to account for the response of this motor to vibrations are indicated. The vibration control for these tests is the average vibration level at the forward and aft external case accelerometers.

Photographs of the motor set up for captive flight simulation testing are shown in Figures 119 and 120. The case temperature, averaged from four thermocouples at 90^{0} intervals around the aft gage plane, is plotted with the target temperature for the four tests in Figures 121 through 124. Inlet air was directed onto the motor aft end to protect the instrumentation. Control difficulties on the first test, Figure 121, resulted in a higher rate of heating than had been planned. Temperature profiles on the remaining three tests were closely matched.

Although thermal stress response is highly unreliable due to the demonstrated no-load error during the time the thermal gradient is high, data from the second test using long loiter followed by aeroheat are plotted in Figures 125 through 135. The 60-minute loiter simulation results in stress/strain changes as indicated in Table 10. With the exception of data from Gages N-6 and -8, which indicate a shift in no-load data, (-3.2 and 10.8 psi for N-6 and -8, respectively), the results agree quite well considering the transient nature of the test. The normal gages do not show a sudden jump when aeroheat is started. This is attributed to the thickness of liner in this motor, which would tend to absorb load (and heat) from the case.

TABLE 10. INSTRUMENTATION RESPONSE, END OF LOITER SIMULATION, AEROHEAT TEST 2

	Change in Response
Forward	
N-7	2.6 psi
S-1	-3.6 psi
C-5	0.027 in.
Center	
N-9	2.4 psi
N-13	-0.5 psi
Aft	
N-15	2.6 psi
S-2	-1.8 psi
C-4	0.024 in.

Aeroheat Tests 3 and 4 represent the Terrain Following Radar (TFR)-dash-loiter sequence. Gage responses for Test 3 are plotted in Figures 136 through 146. The response range indicates a lower level of stress at the bond line as a result of this type profile.

Random vibration, imposed during these aeroheat cycles, completed the captive-flight simulation. Representative responses of the gages during vibration are shown in Figure 147 through 159. Almost all gage responses are at frequencies below 800 Hertz. Data from the four tests are summarized in Table 11. In the case of input level of 10 x basic levels, the rms responses increase, as expected, by a factor of ~3. Dynamic bond-line normal stresses reach rms levels of ~2 psi.

TABLE 11. RANDOM VIBRATION RESPONSE

Gage	RMS Response Over 10 to 2000 Hertz			
	Test A-1	Test A-2	Test B-1	Test B-2
Average (Control)	2.86	7.48	2.29	7.49
A-3, g	2.31	9.11	2.26	8.44
A-4, g	6.05	15.12	5.18	14.58
A-5, g	2.44	8.85	2.56	8.44
A-7, g	2.98	11.63	3.17	10.83
A-8, g	4.61	14.06	4.55	13.40
N-6, mv	0.23	0.71	0.30	0.69
N-7, mv	0.71	2.18	0.69	1.76
N-9, mv	0.63	1.57	0.58	1.83
N-13, mv	0.57	1.93	0.64	1.98
N-15, mv	0.37	1.10	0.38	1.01
C-5, mv	0.95	3.02	0.87	2.62
C-4, mv	0.64	2.77	0.77	2.81

Page 28 is blank

CONCLUSIONS

The TIM was subjected to a variety of environmental tests that cover the expected range of loadings to be encountered in captive flight on modern high-performance aircraft such as the F-111. The random vibration input control was based on BDU response from captive flight on an F-111. This response compares favorably with MIL-STD-810C requirements at frequencies below about 400 Hertz. An enhanced spectral input based on assumed response on aircraft such as an F-4 or F-15 was also run on the TIM. Both analysis and experiment indicate that the stresses imposed on the motor from thermal changes are relatively low (< 10 psi). Dynamic stresses (< 5 psi) are measurable but are also quite low.

The TIM represents a well characterized and structurally sound test vehicle that should be available for captive flight loads definition for many years. The propellant is thoroughly characterized, and aging data indicate that the rate of change of mechanical properties should be minimal over the next decade.

The shear and clip gages performed reliably and repeatably over several thermal cycles. The bond-line normal stress gages showed some tendency to shift in no-load output; but because of the manner in which they are wired, this shift may be monitored and, if required, corrected in the future. Only one gage, N-8, was found to drift somewhat erratically and to be noisy under dynamic load.

For the motor to be flown, it would have to be mated to a missile with provision to accommodate the modified forward closure through which the instrumentation wires are fed. Data presented in this report define the range of responses so that a recording system could easily be set up. Calibration data presented are sufficient to permit data reduction from actual captive-flight tests. Regular pressurization and equilibrium temperature conditioning tests are recommended to verify the condition of the normal stress gages.

Page 30 is blank

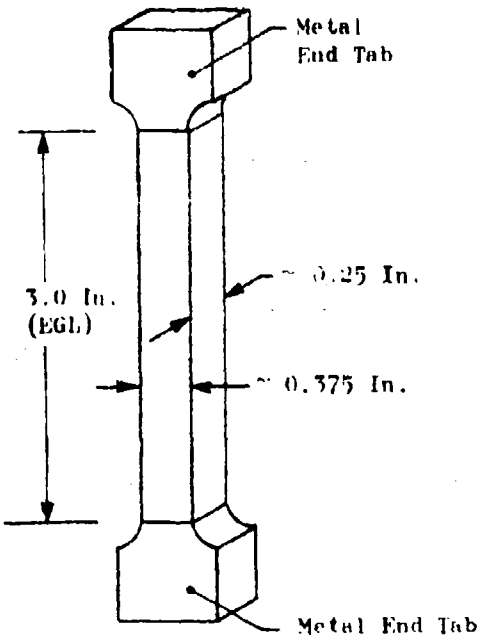

Figure 1. Hybrid Uniaxial Tensile Test Specimen

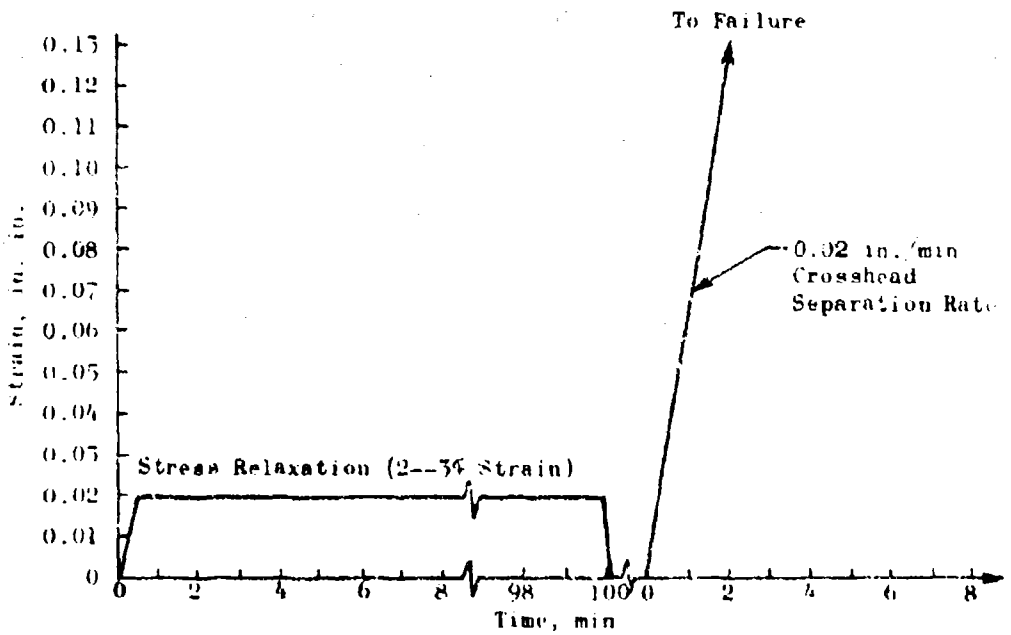

Figure 2. Uniaxial Strain-Time History for Characterization

Figure 7. Master Uniaxial Relaxation Modulus, RDS-011

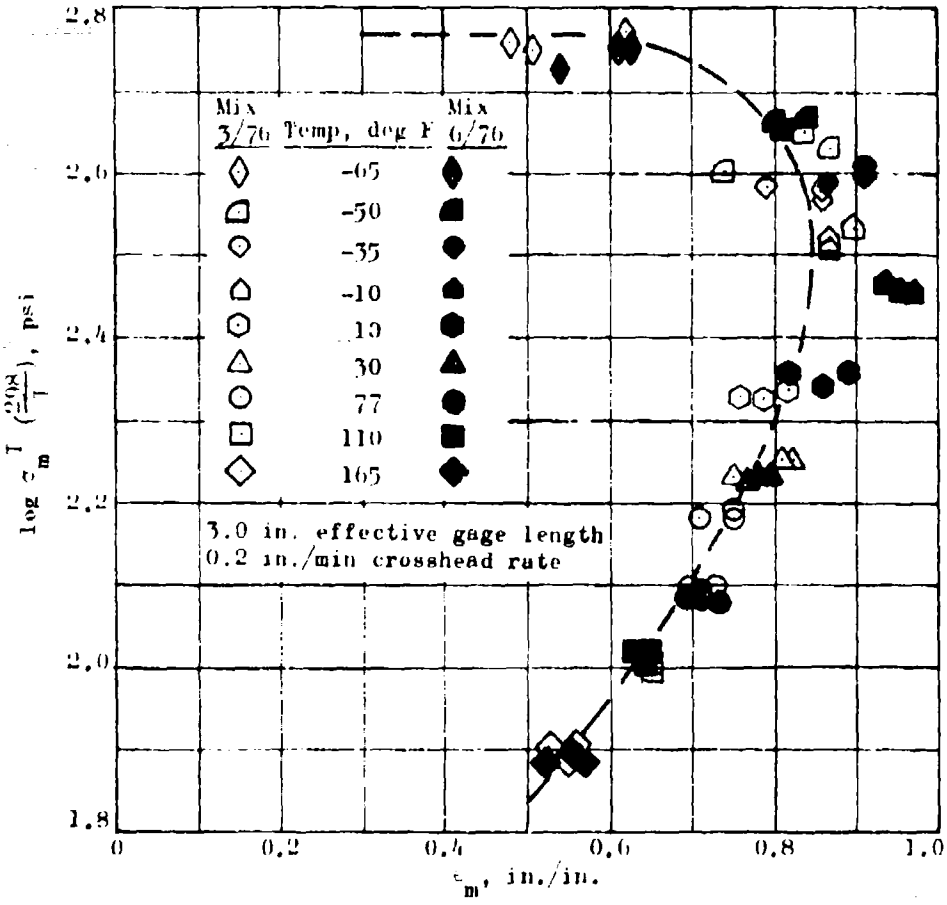

Figure 4. Smith Plot, RDS-011 Uniaxial Tensile Failure Data

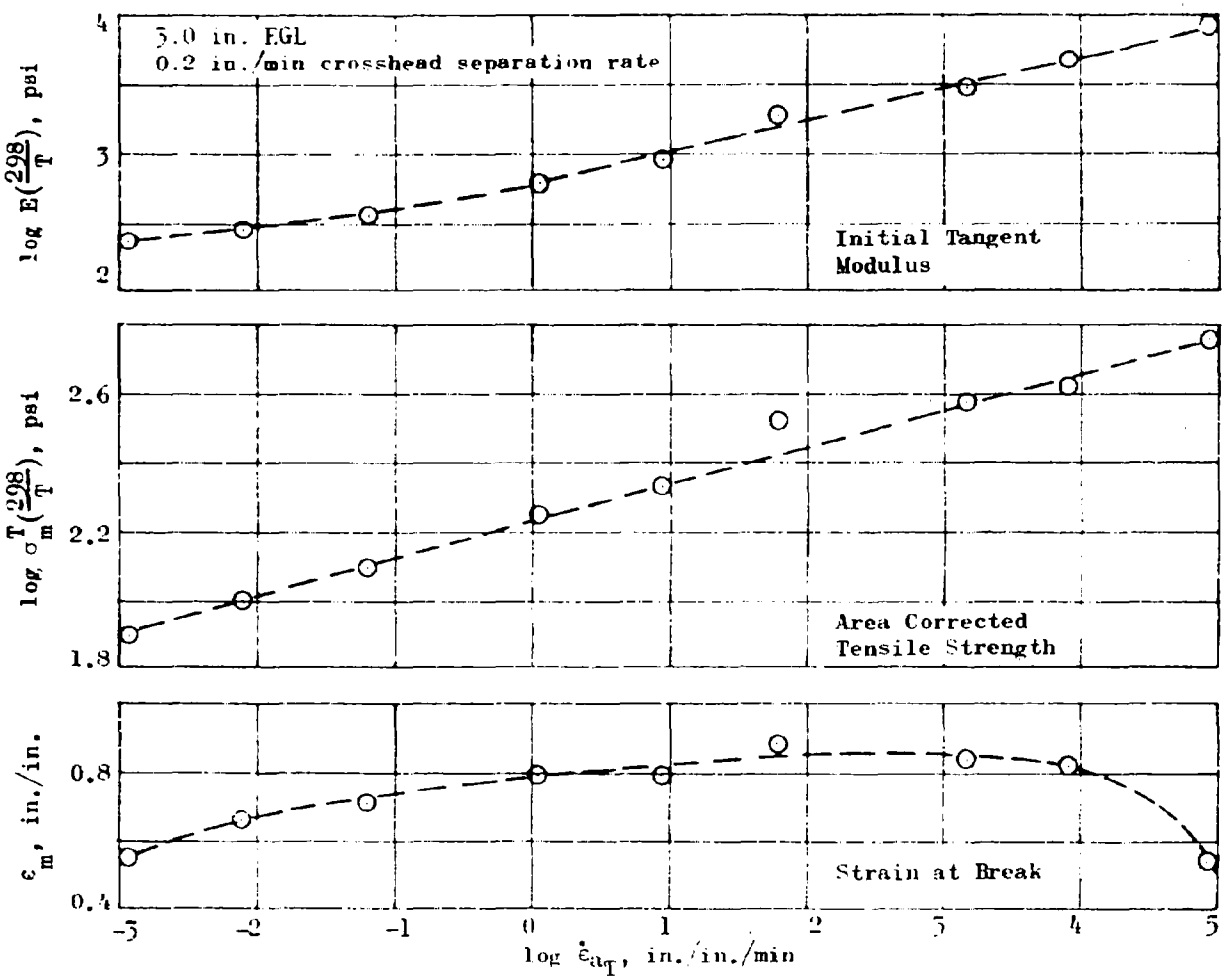

Figure 5. Uniaxial Tensile Properties, RDS-011

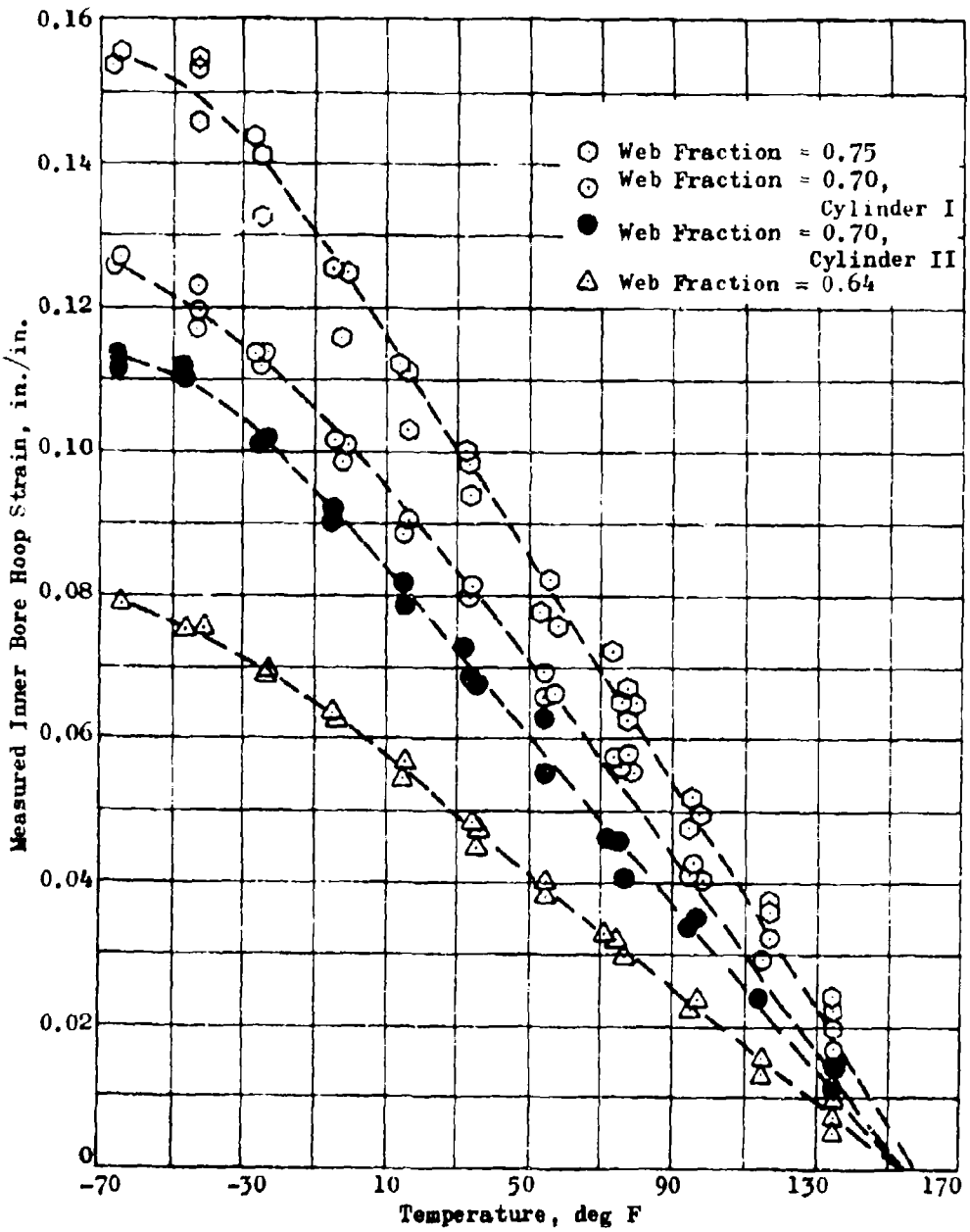

Figure 6. RDS-011 Four-Inch SEC Data

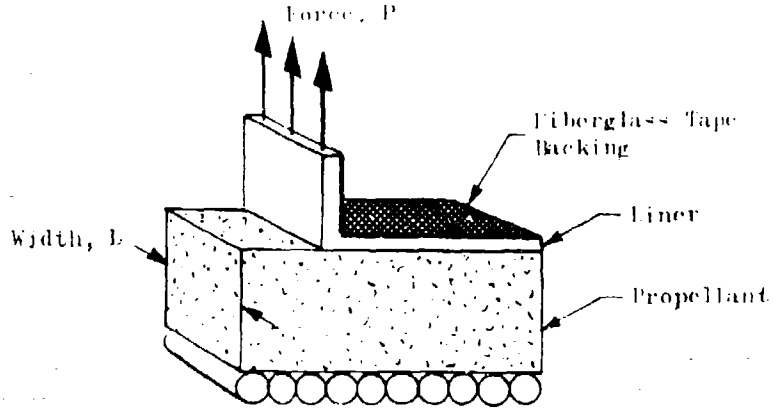

Figure 7. Ninety-Degree Peel Test Specimen

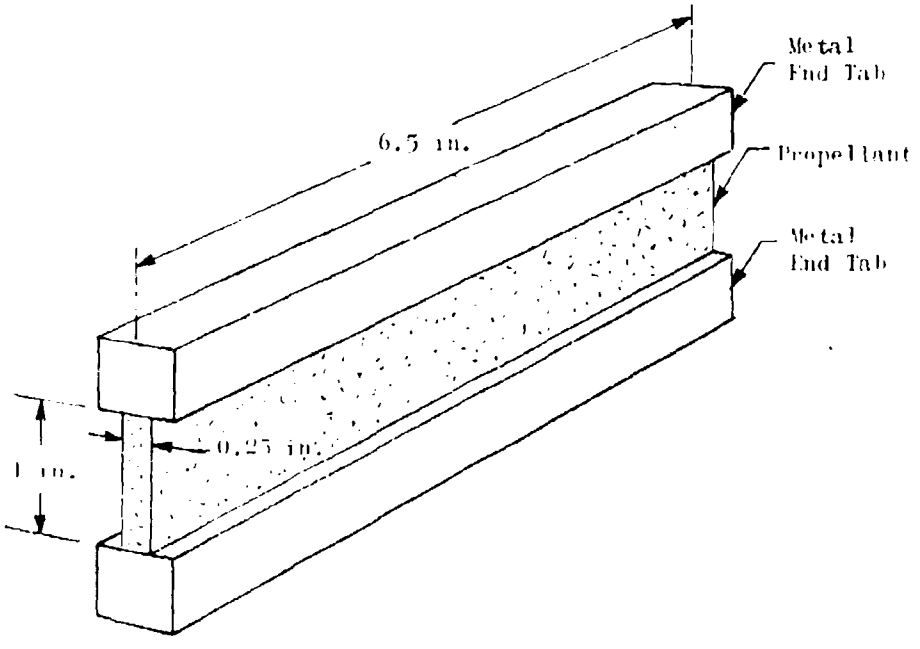

Figure 8. Biaxial Strip Tensile Specimen

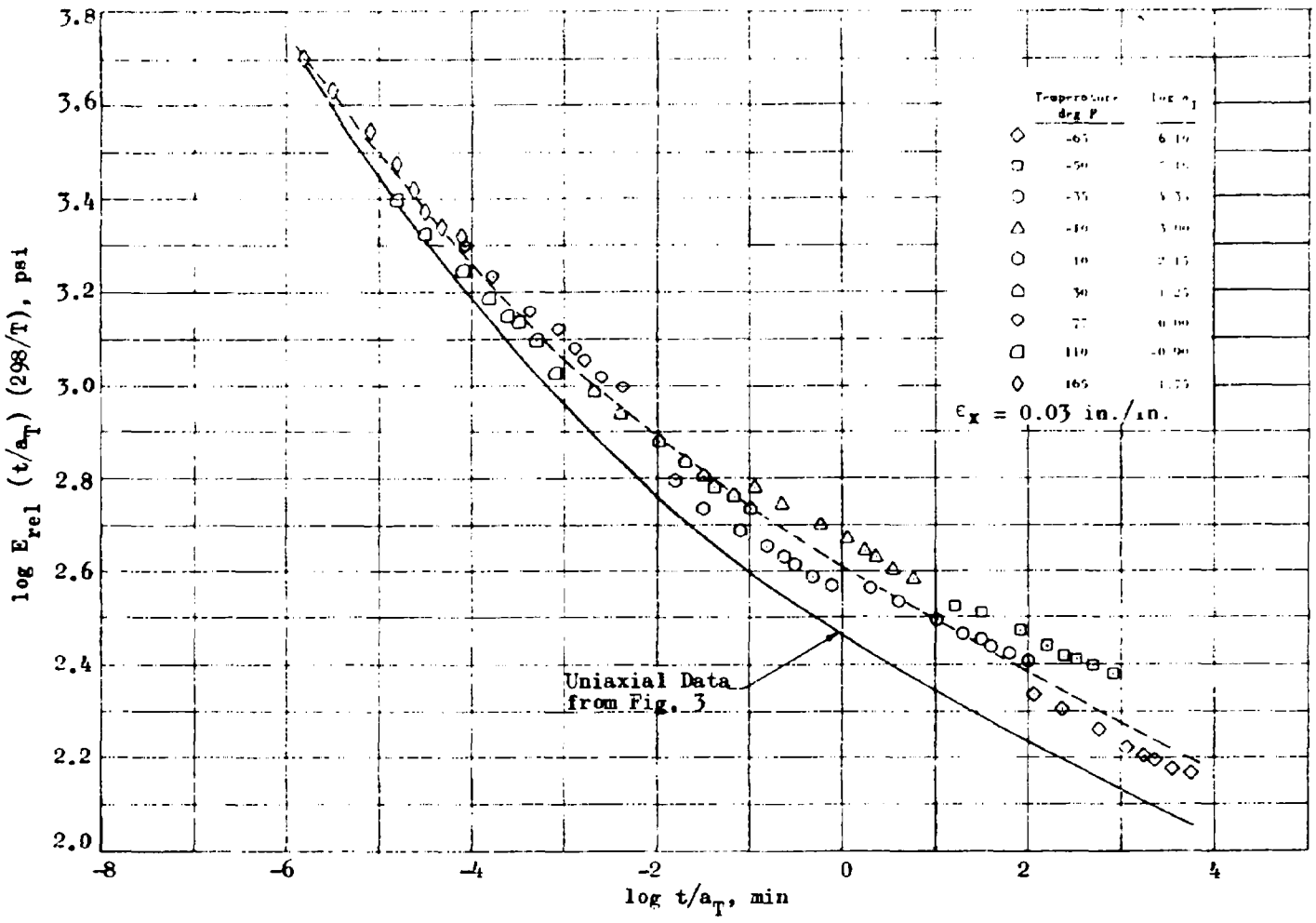

Figure 9. RDS-011 Biaxial Tensile Relaxation Modulus

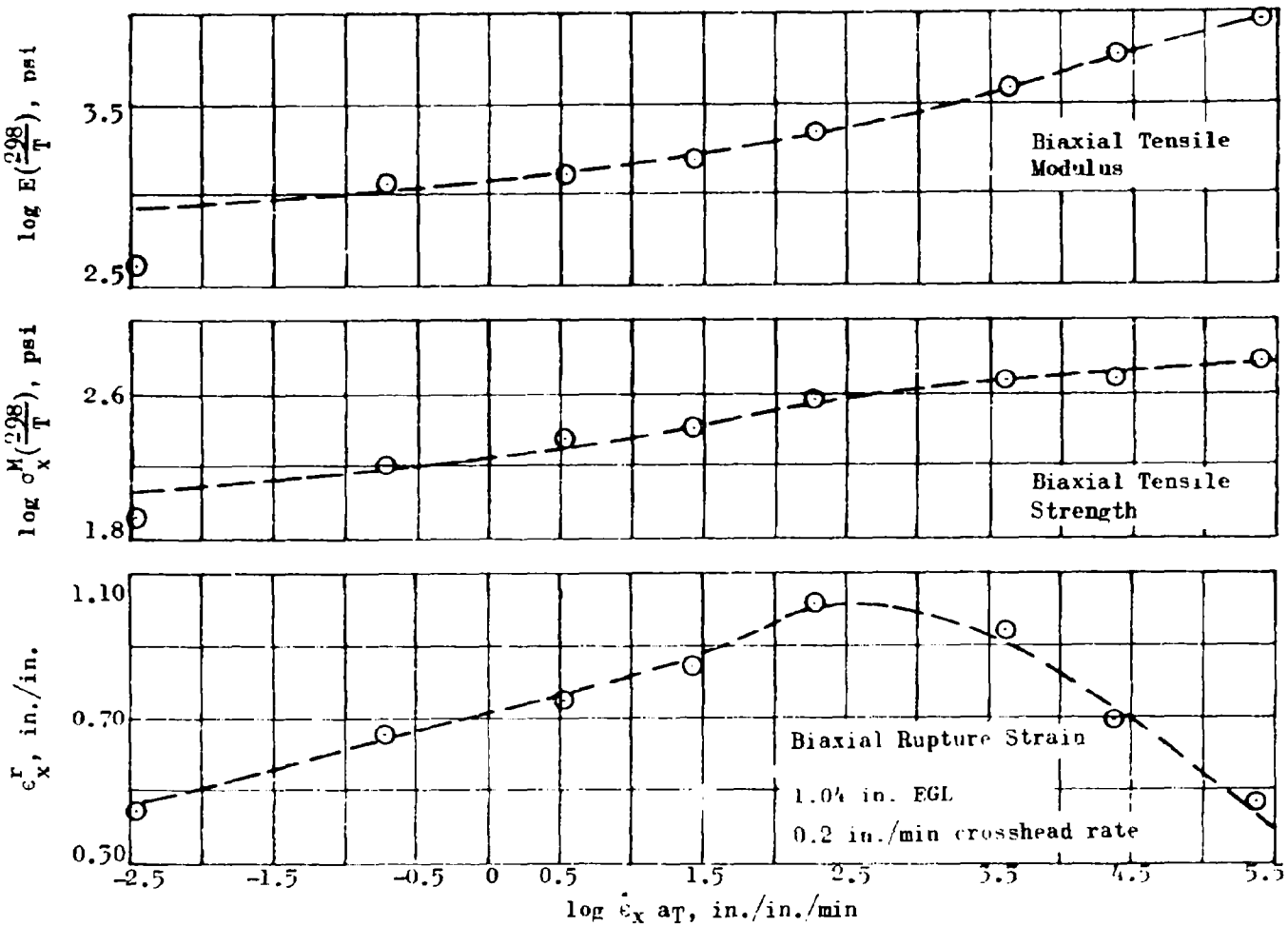

Figure 10. RDS-011 Biaxial Constant Crosshead Rate Test Data

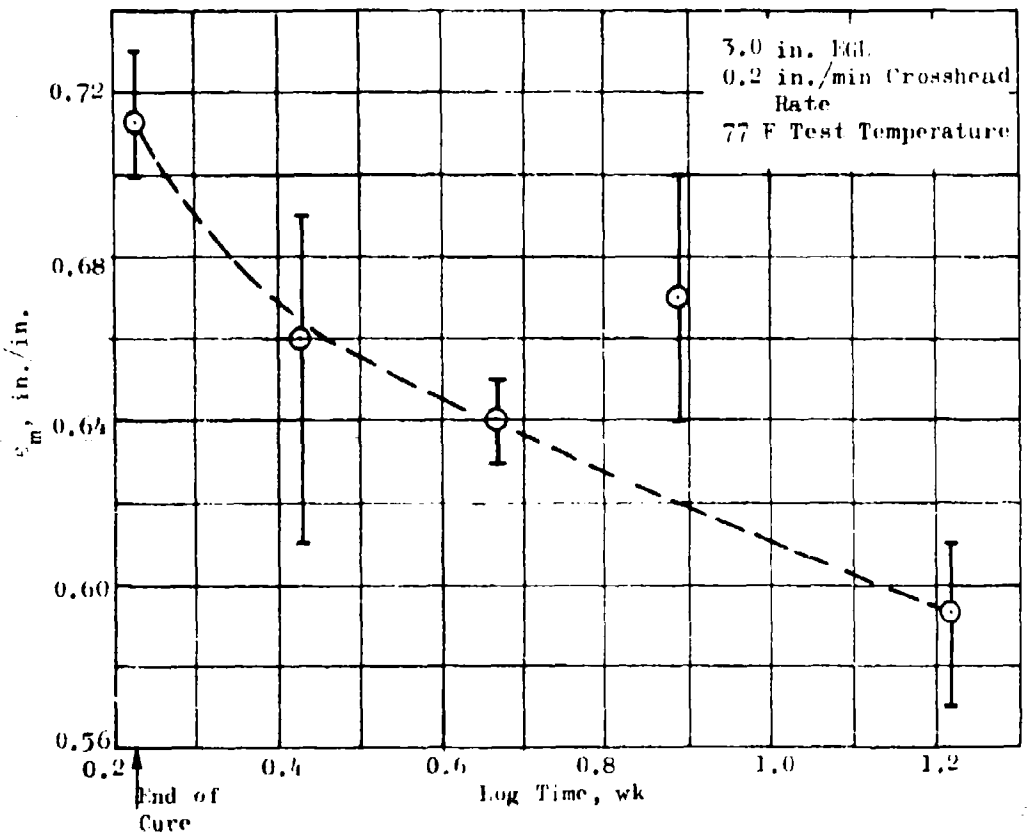

Figure 11. Effect of 77 F Aging on Uniaxial Strain Capability

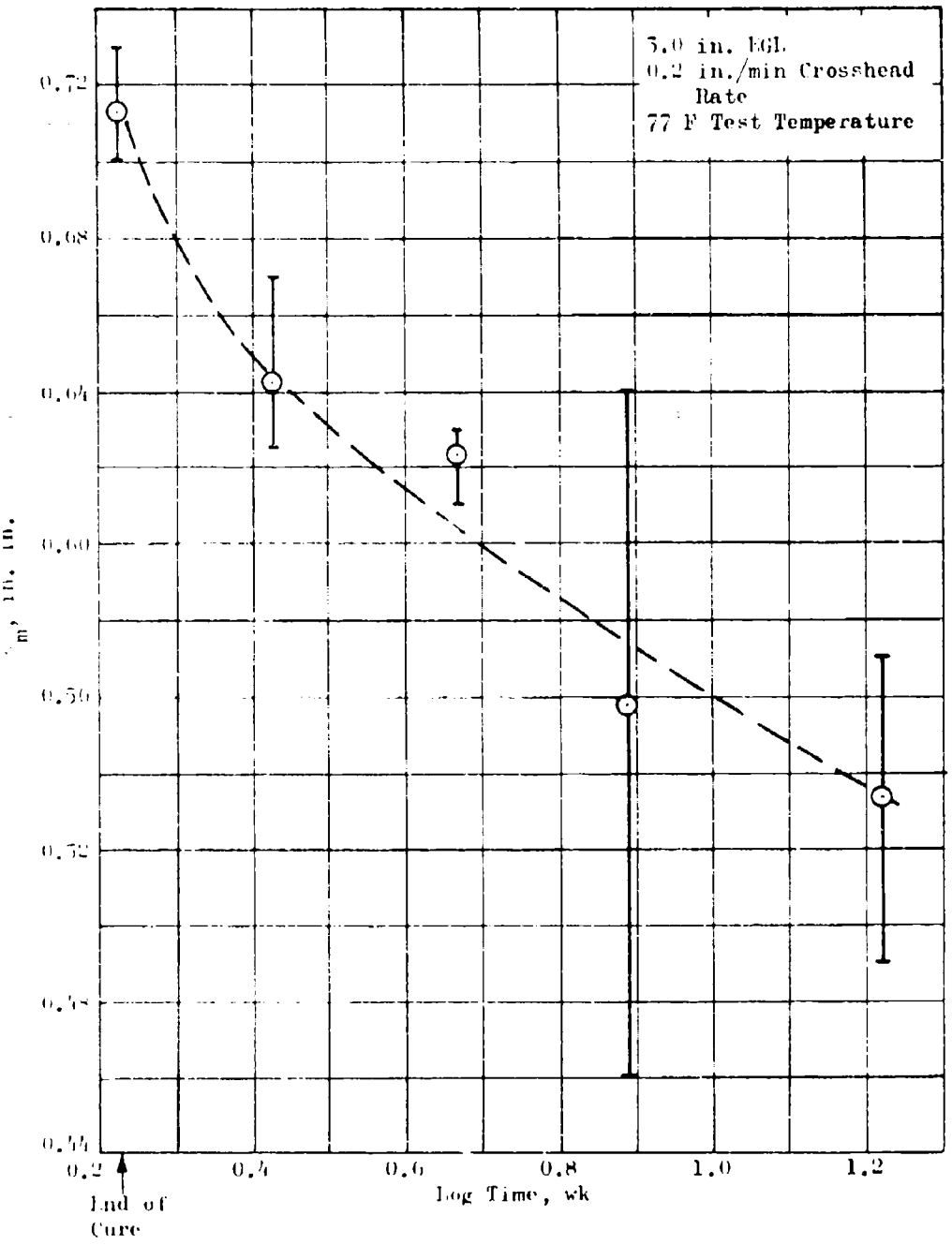

Figure 12. Effect of 120 F Aging on Uniaxial Strain Capability

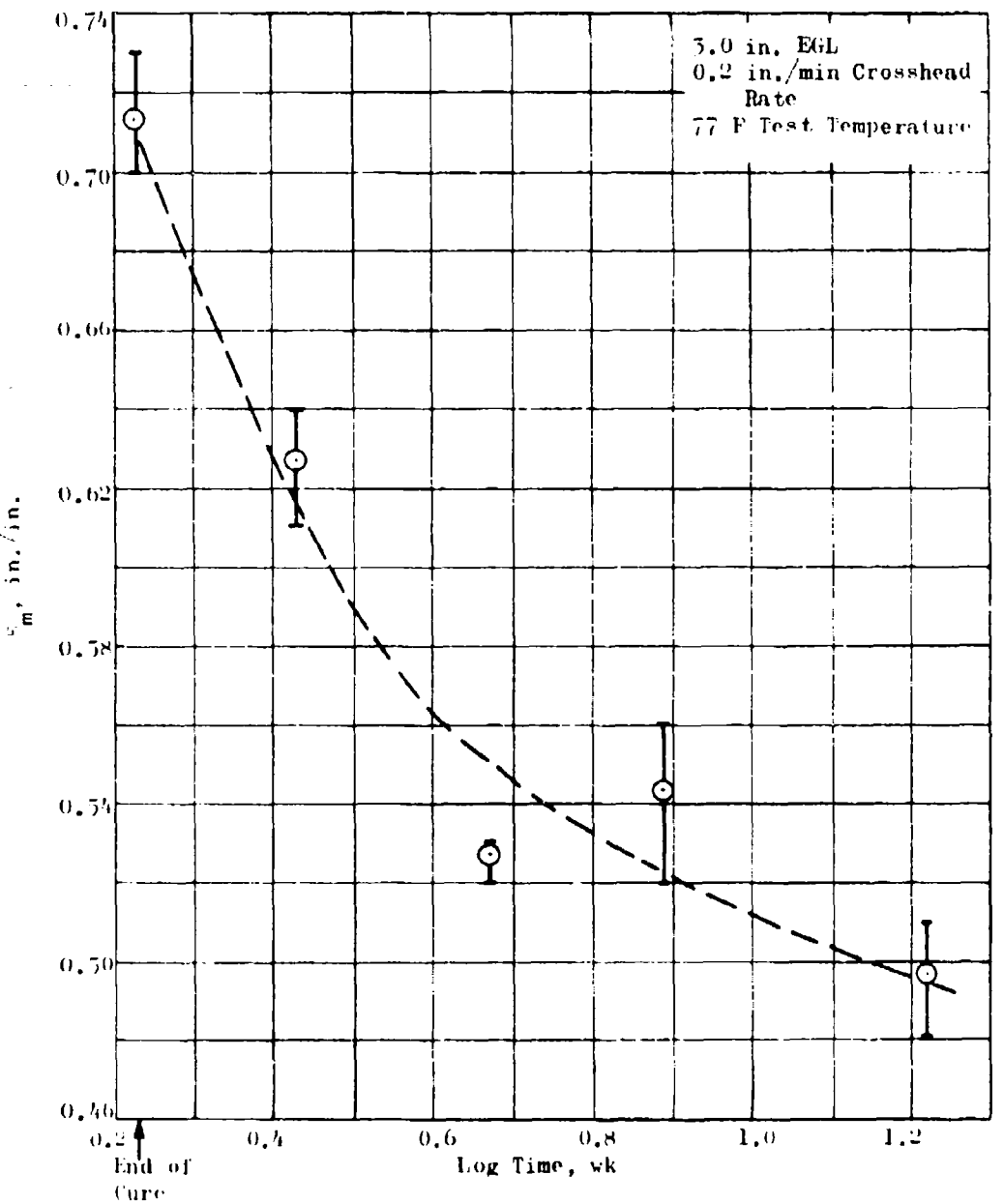

Figure 13. Effect of 145 F Aging on Uniaxial Strain Capability

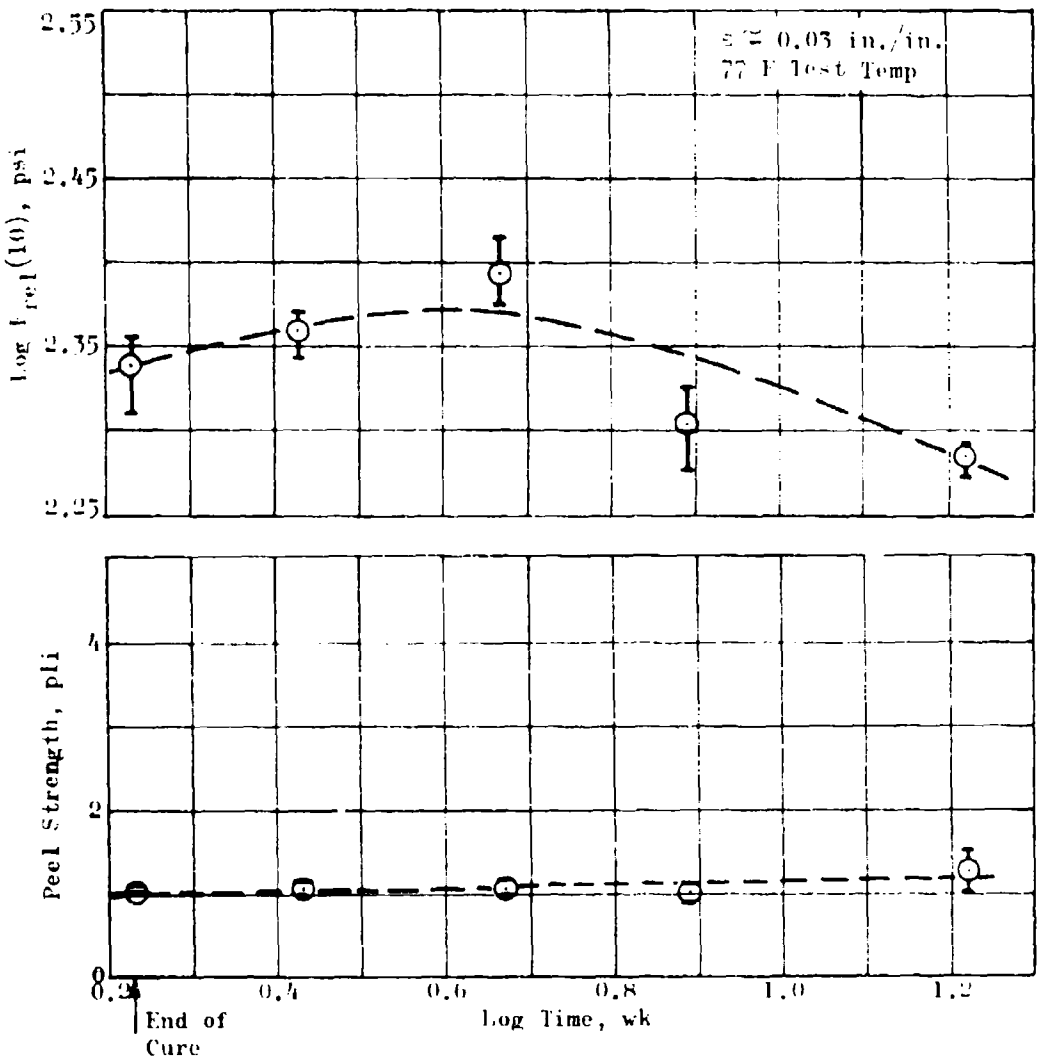

Figure 14. Effect of 77 F Aging on Modulus and Peel Strength

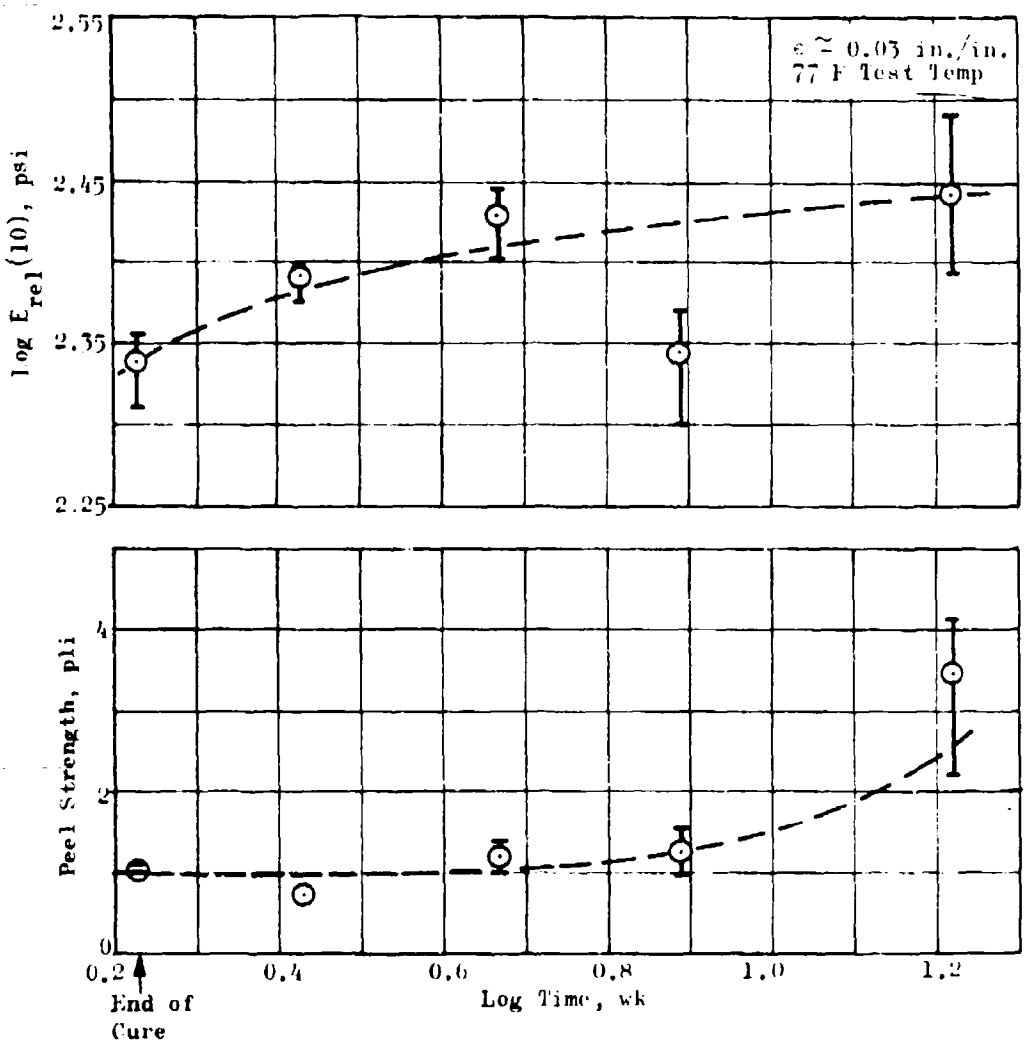

Figure 15. Effect of 120 F Aging on Modulus and Peel Strength

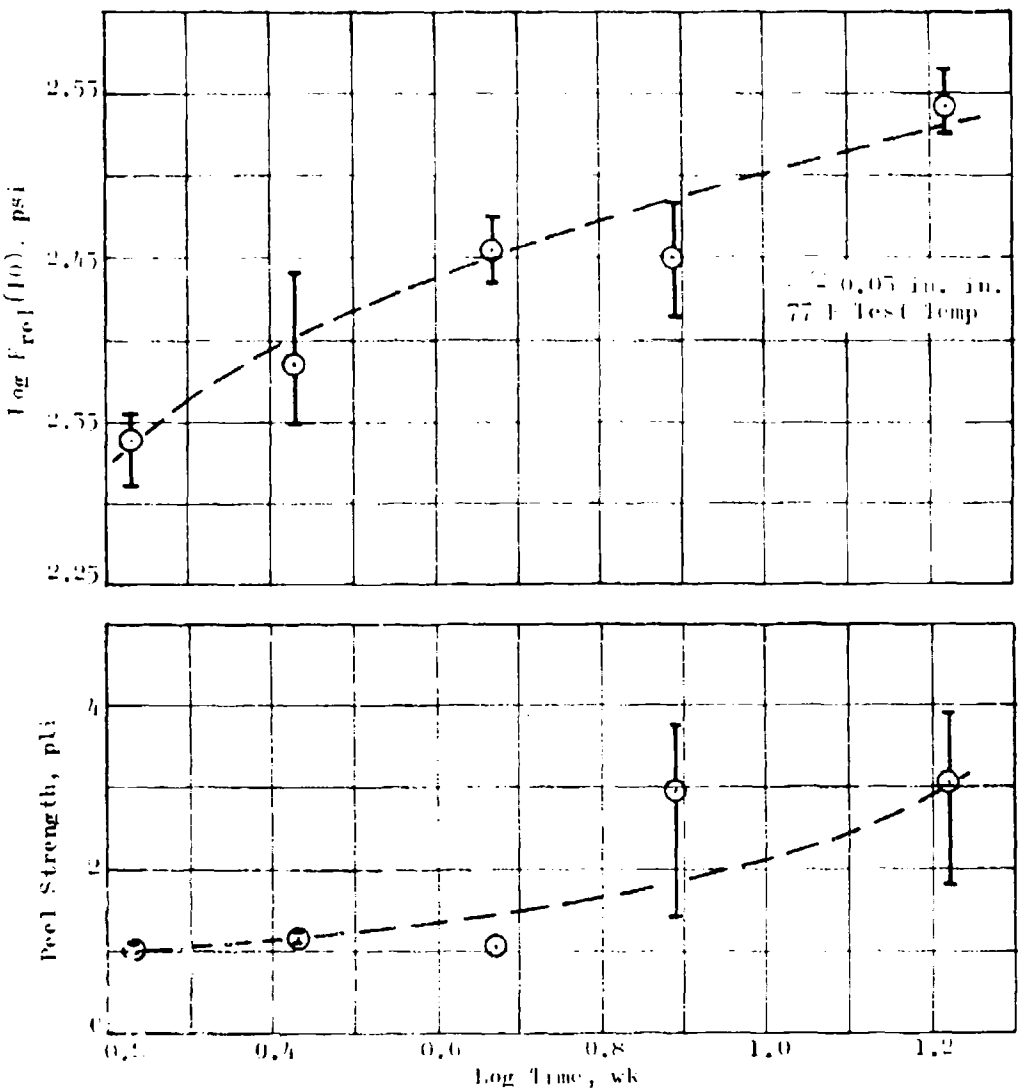

Figure 36. Effect of 145 F Aging on Modulus and Peel Strength

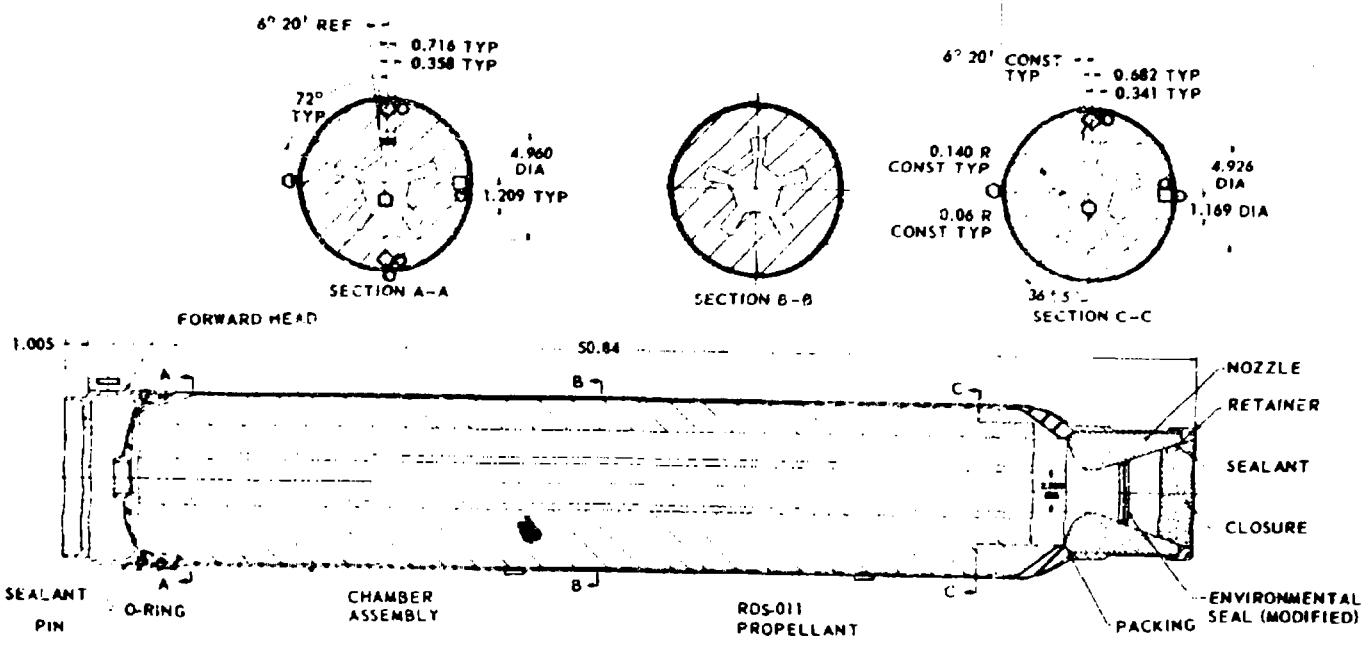

Figure 17. Tactical Instrumented Motor, Sparrow Mk 38 Mod 4 Configuration

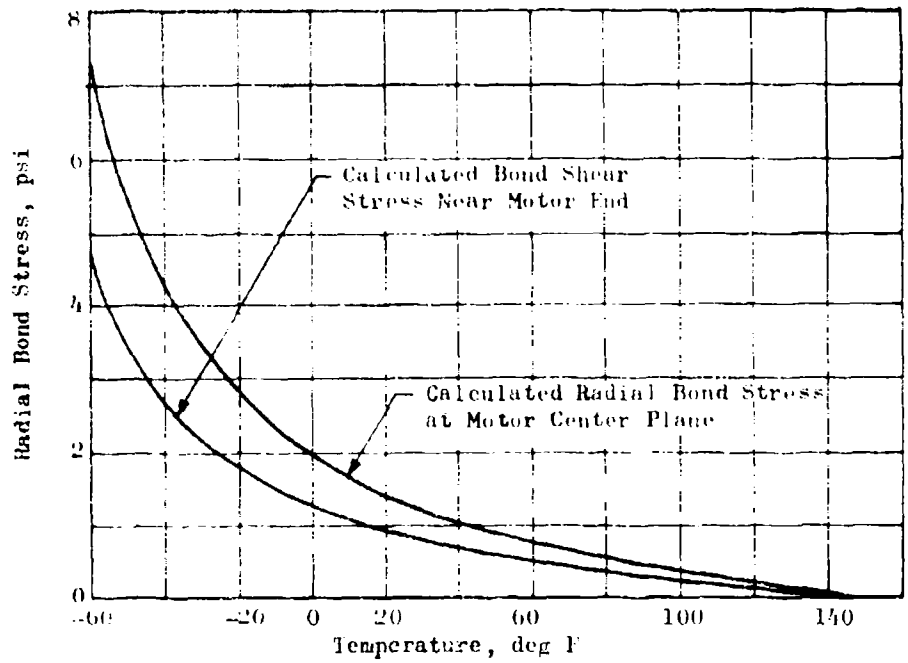

Figure 18. Calculated Bond-Line Stresses, TIM Equilibrium Conditions

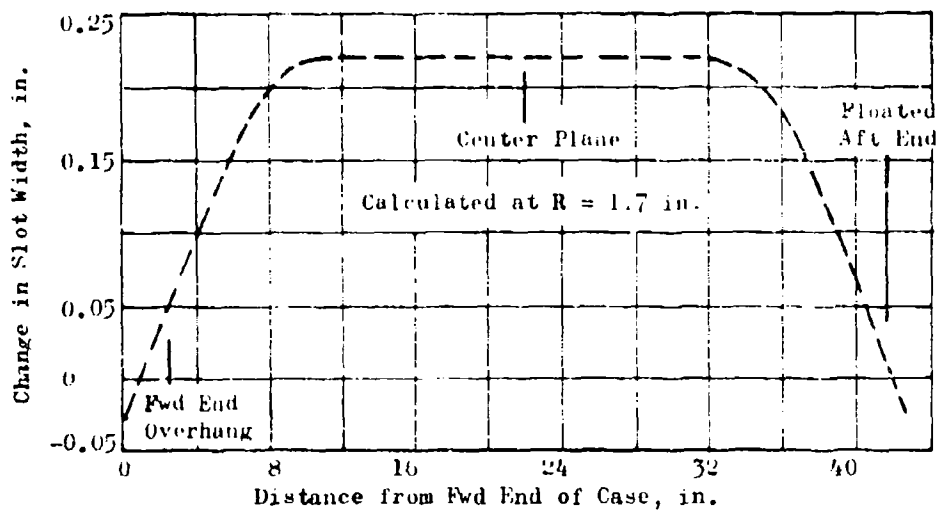

Figure 19. Calculated Change in Inner Bore Slot Width at -60 F

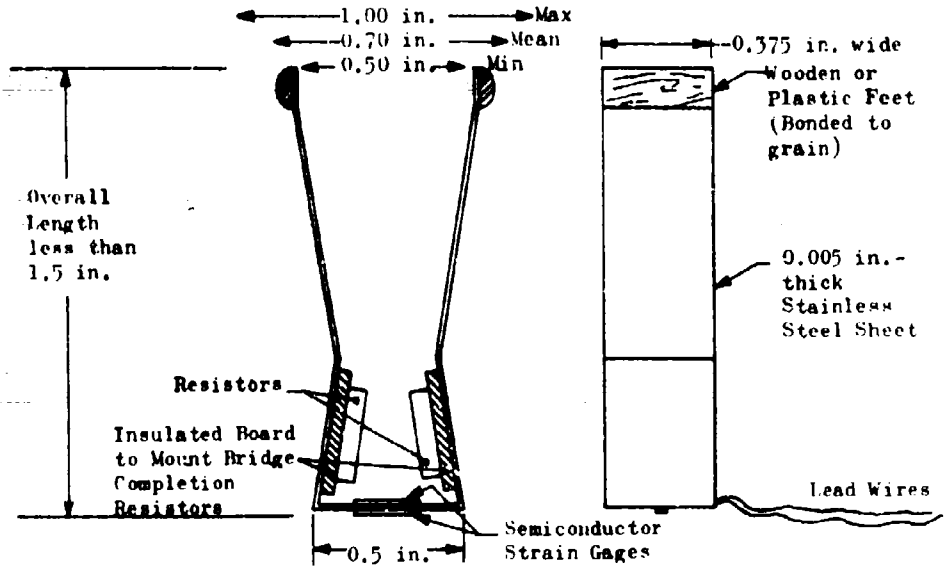

Clip Gage C-5 for TIM

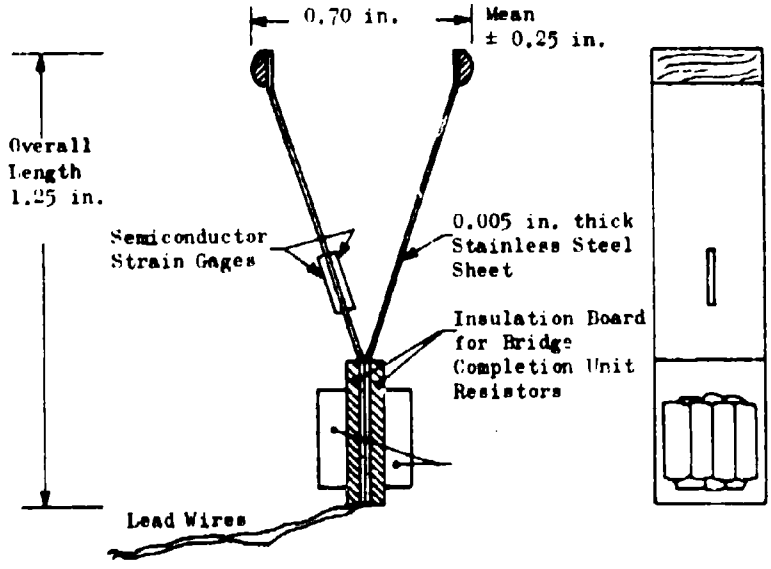

Clip Gage C-4 for TIM

Figure 20. Mechanical Clip Displacement Gages

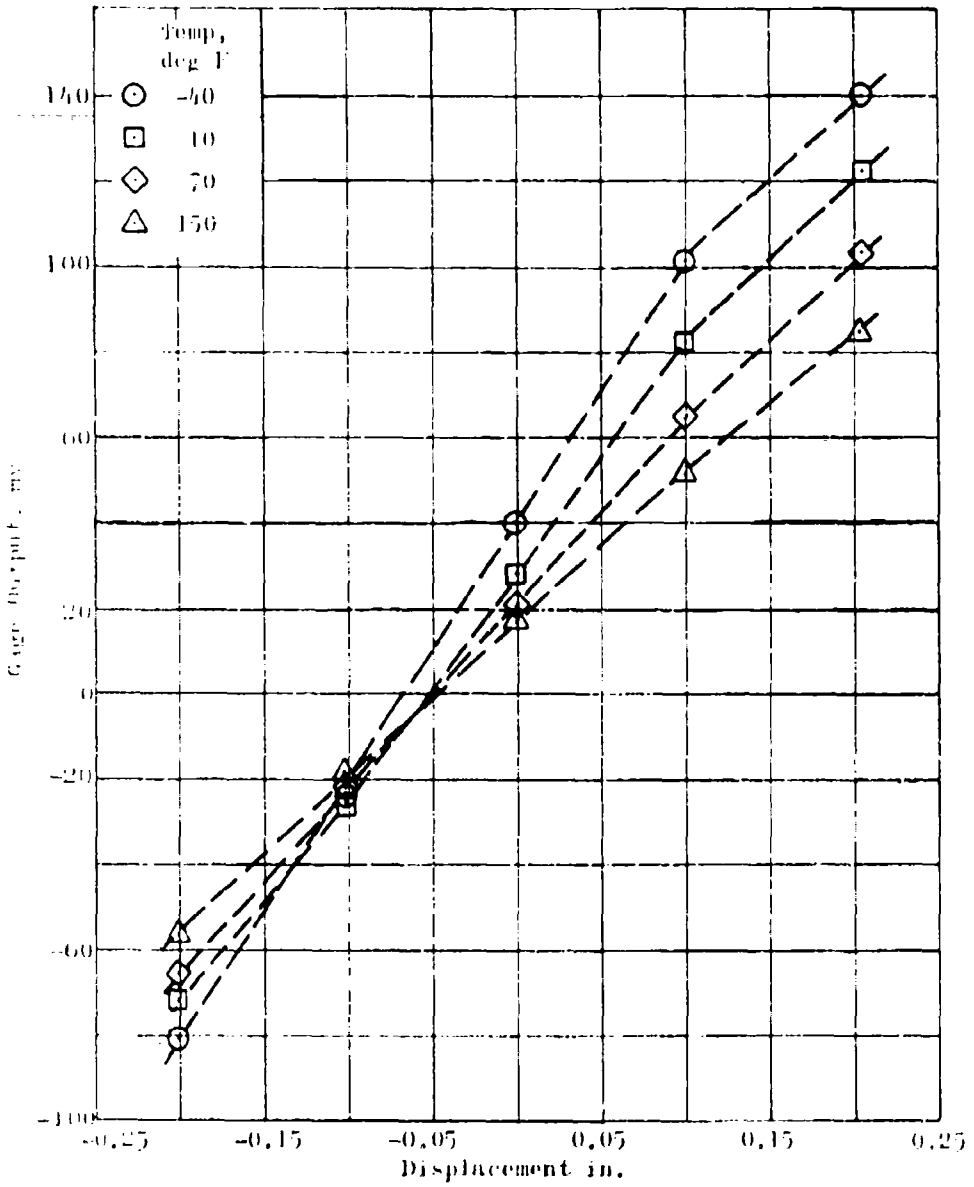

Figure 21. Bench Calibration for Clip Gage C-4

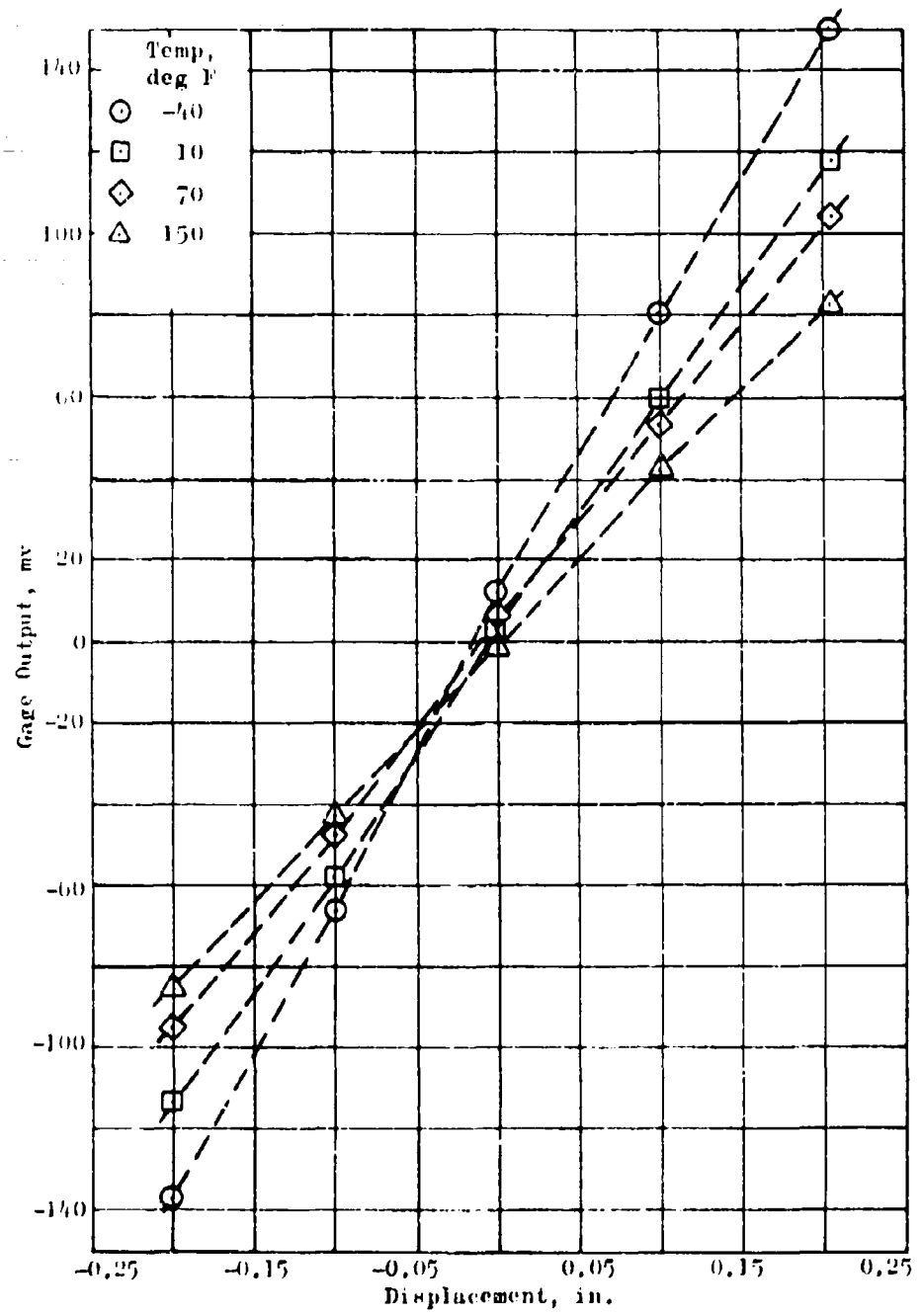

Figure 22. Bench Calibration for Clip Gage C-5

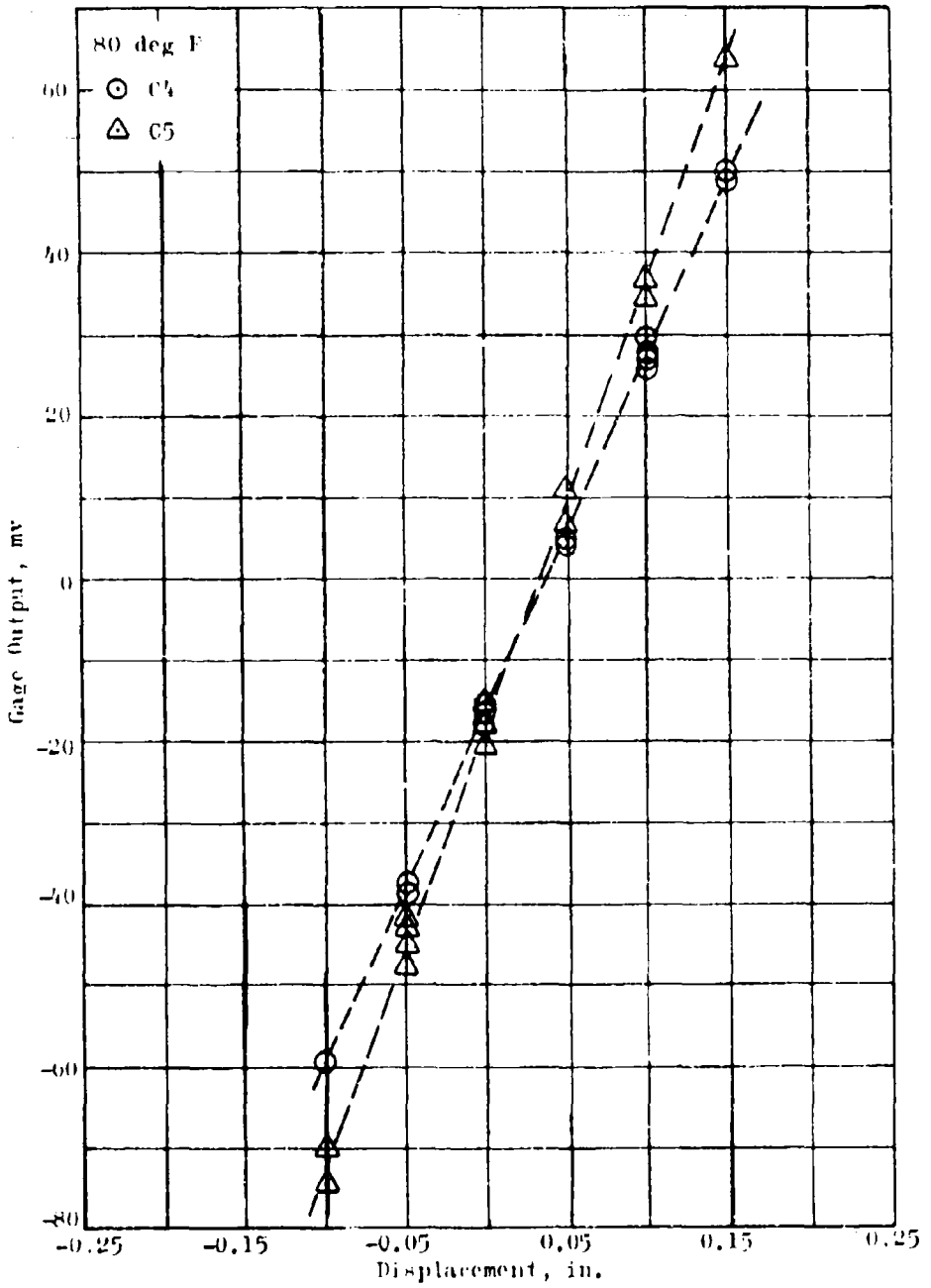

Figure 23. Clip Gage Calibration Prior to Installation

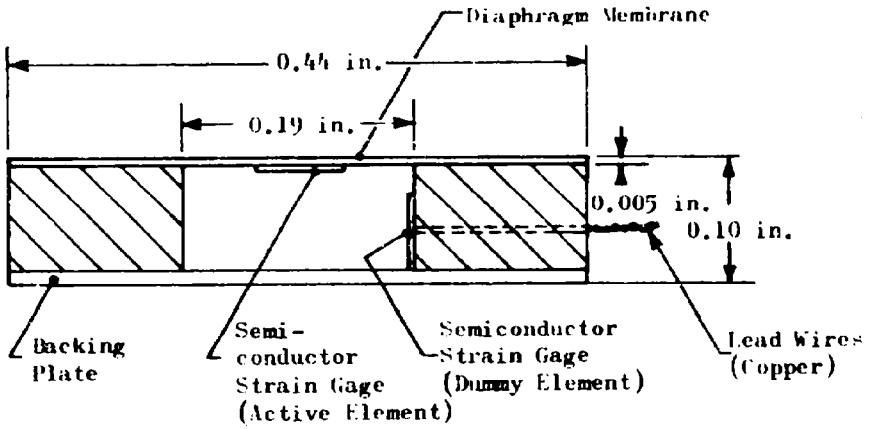

a. Normal Stress Diaphragm Gage

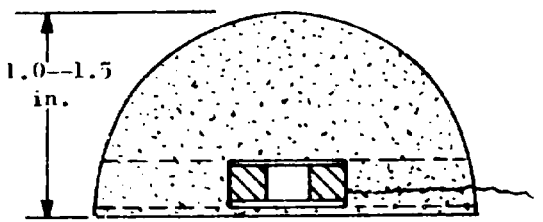

b. Gage Embedded in Propellant Plug

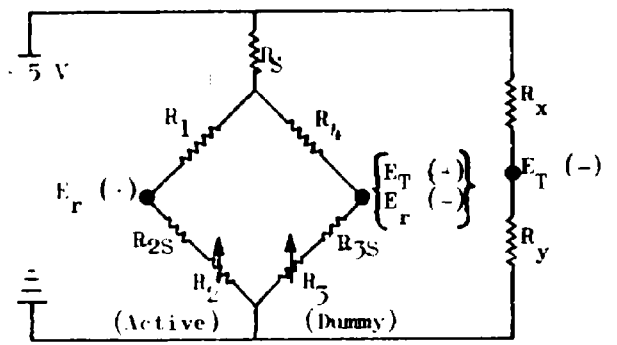

c. Bridge Circuitry for Normal Stress Gage

$E_r(T) \quad E_r(-) - E_r(-)$

$E_T(T) \quad E_r(-) - E_T(-)$

Figure 24. Normal Bond Stress Diaphragm Gage

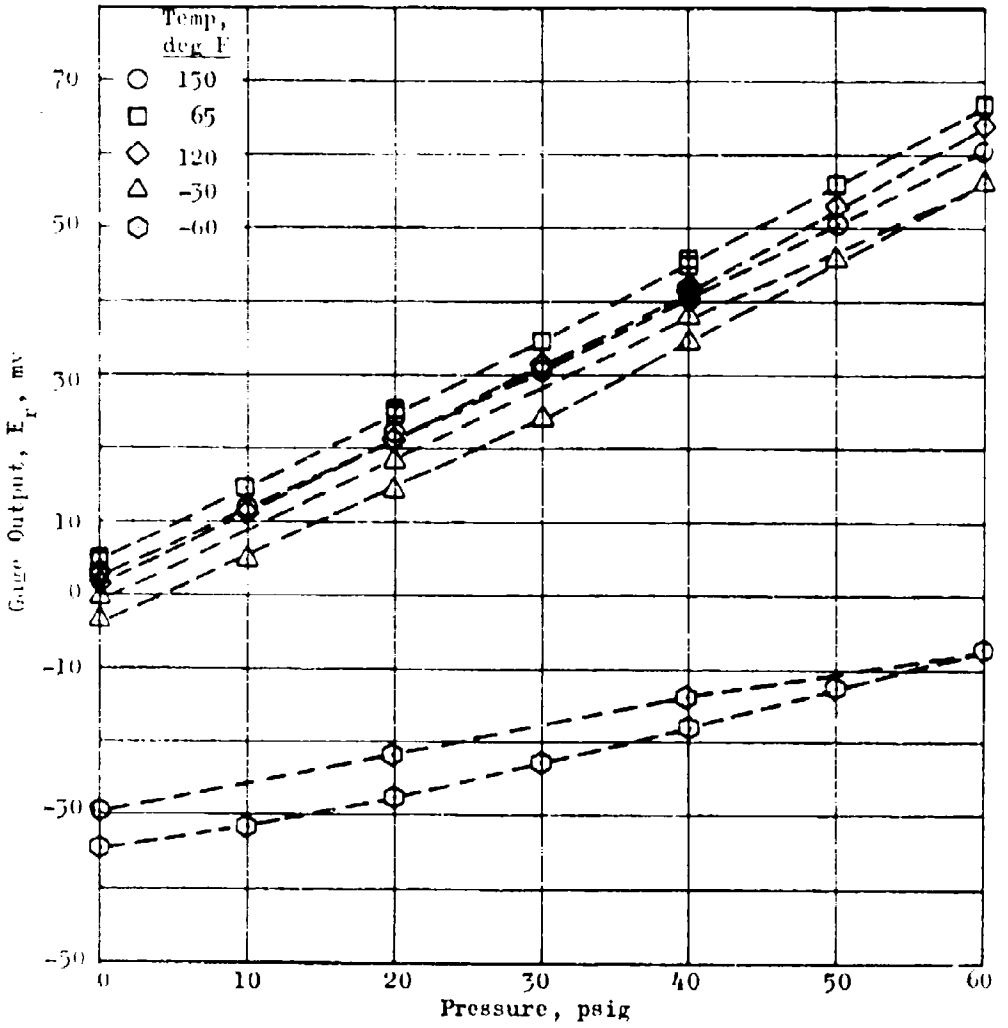

Figure 25. Bench Calibration of Normal Gage N-6

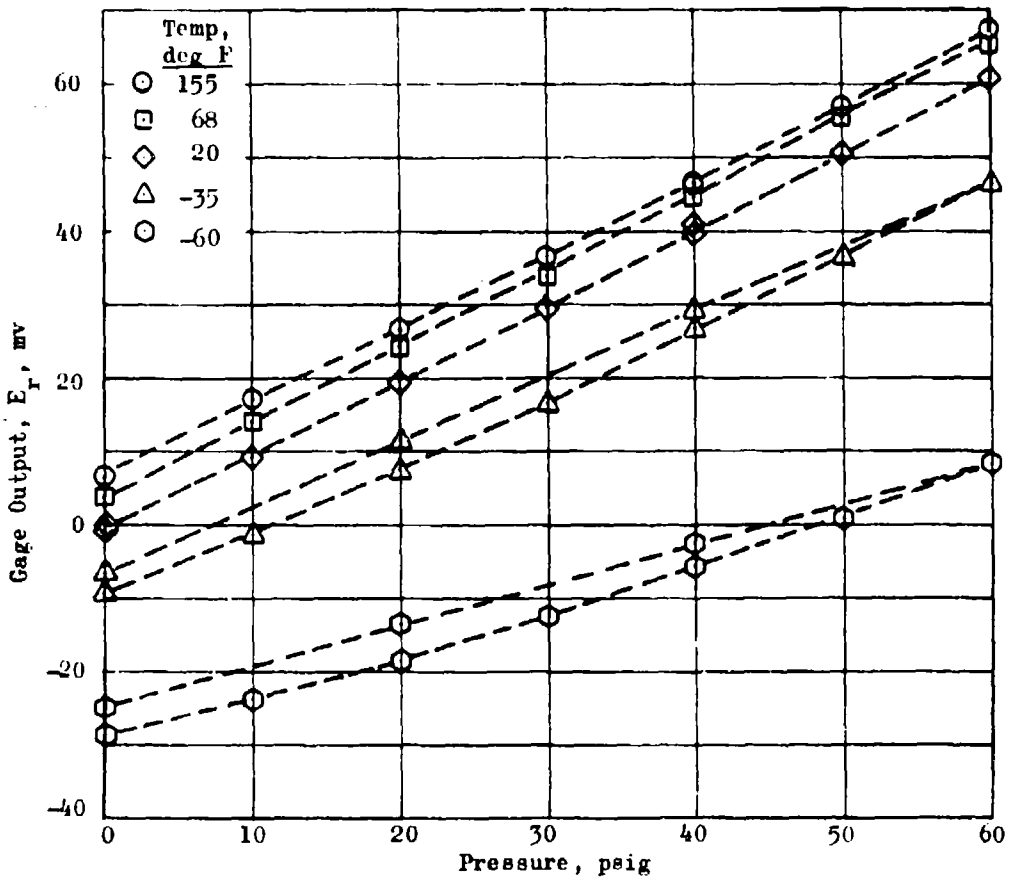

Figure 26. Bench Calibration of Normal Gage N-7

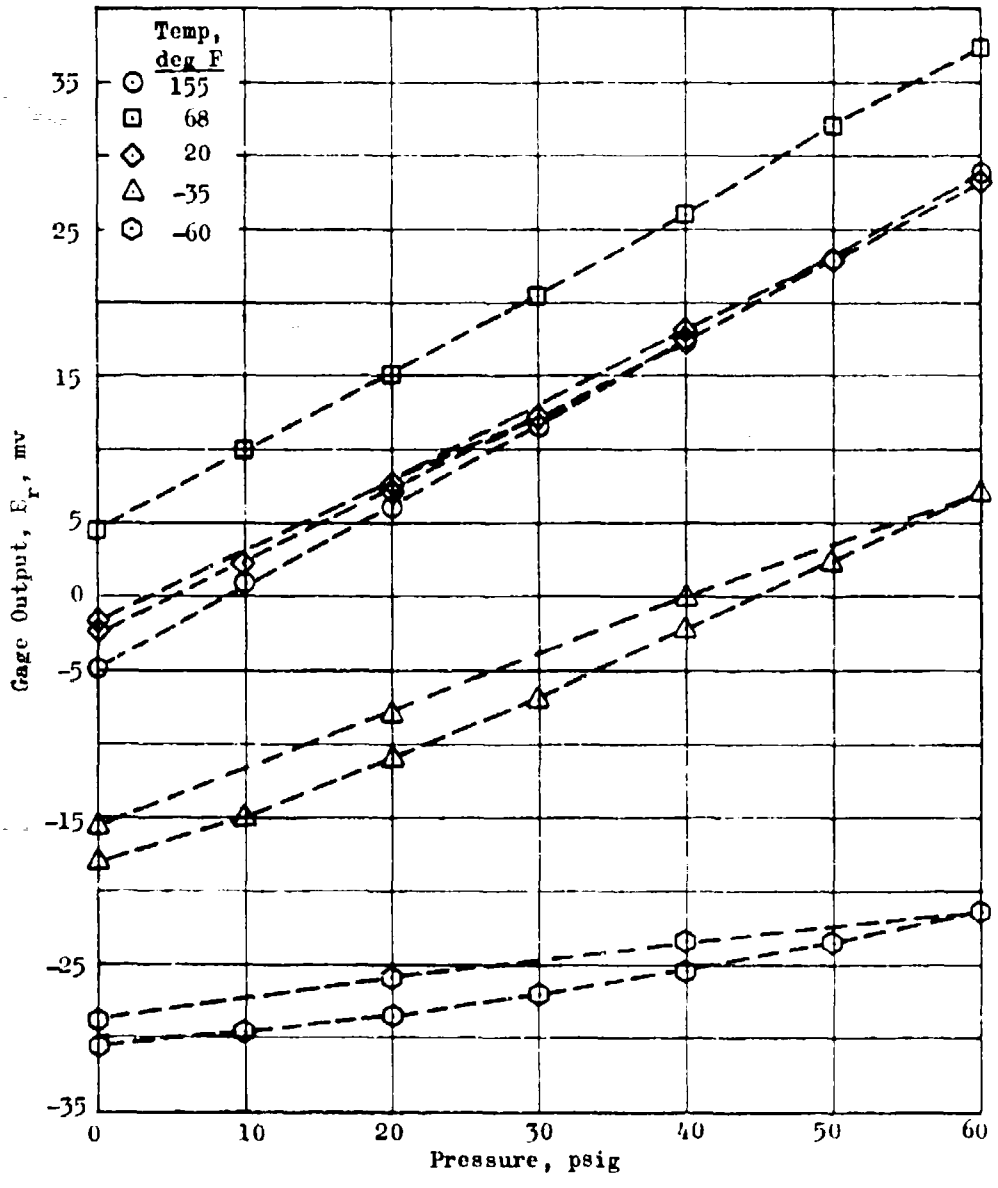

Figure 27. Bench Calibration of Normal Gage N-8

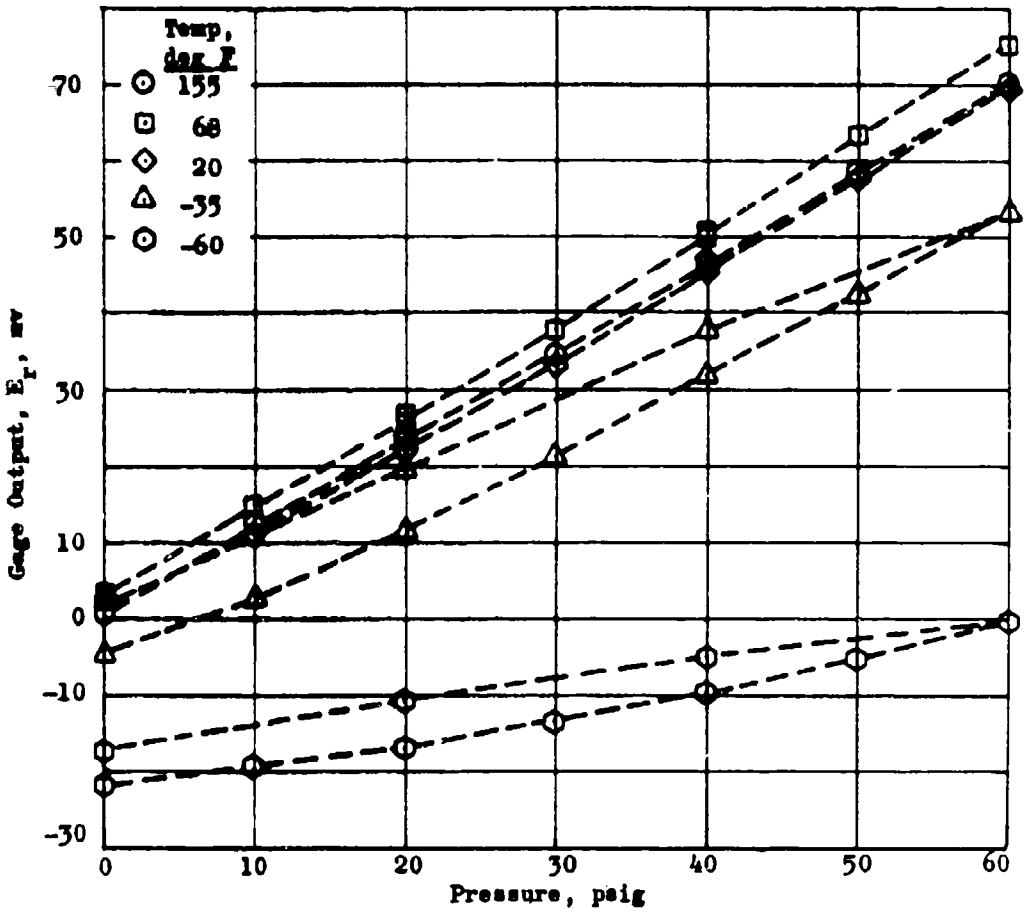

Figure 28. Bench Calibration of Normal Gage N-9

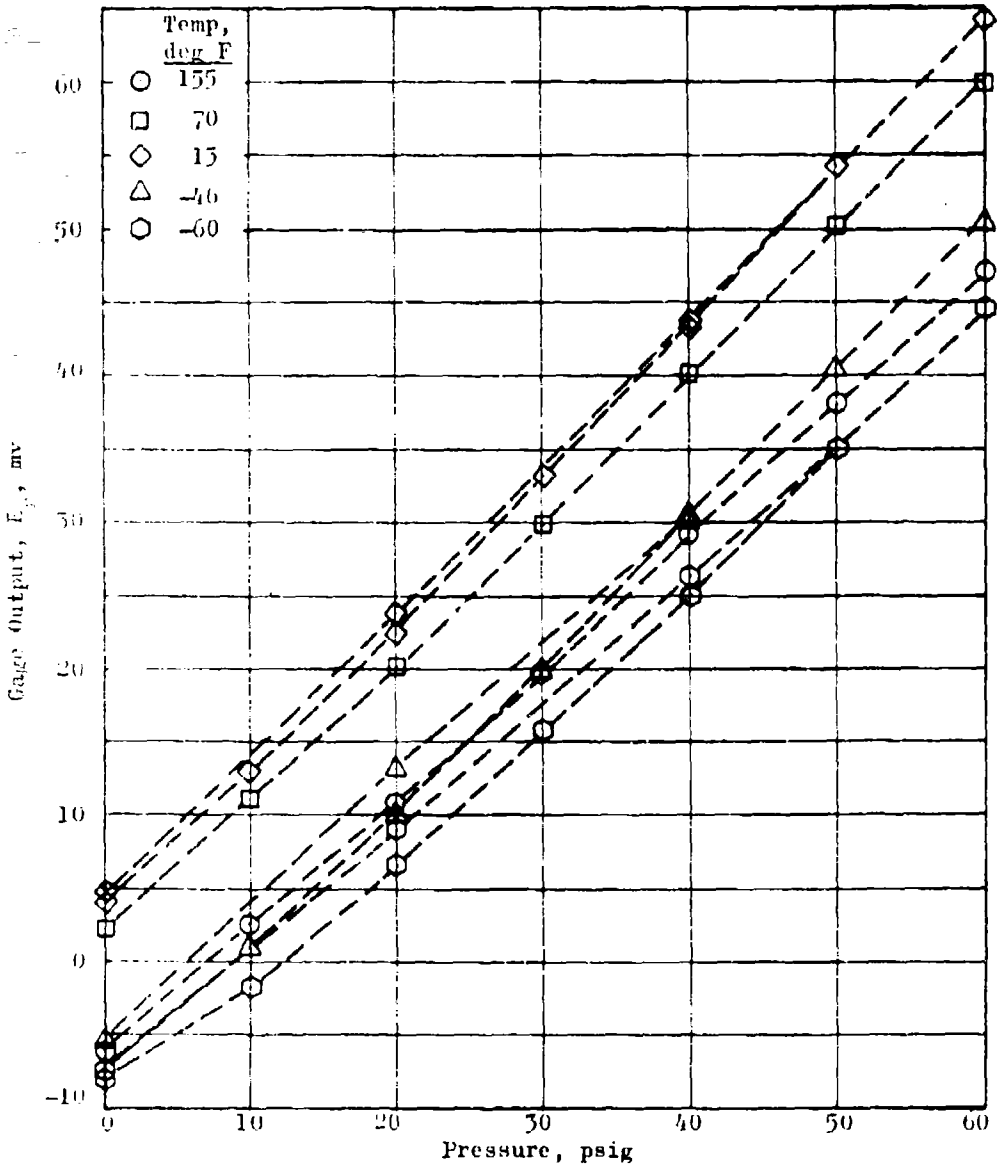

Figure 29. Bench Calibration of Normal Gage N-13

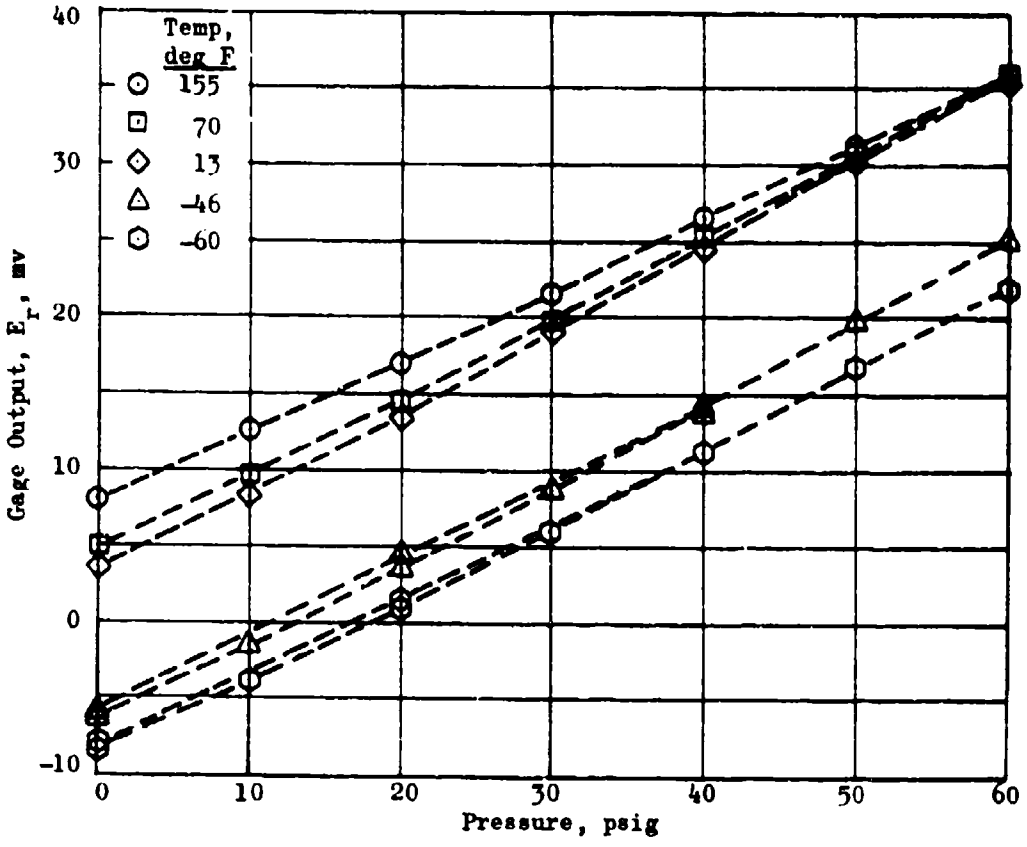

Figure 30. Bench Calibration of Normal Gage N-15

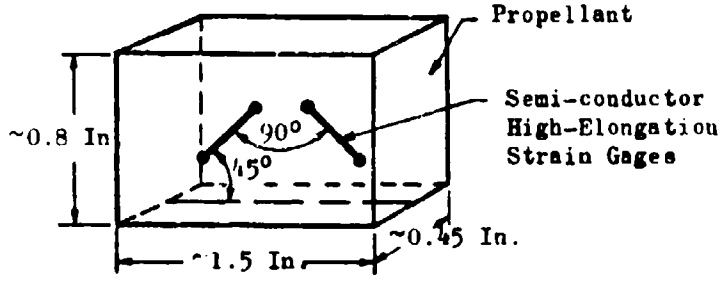

Figure 31. Shear Stress Gage

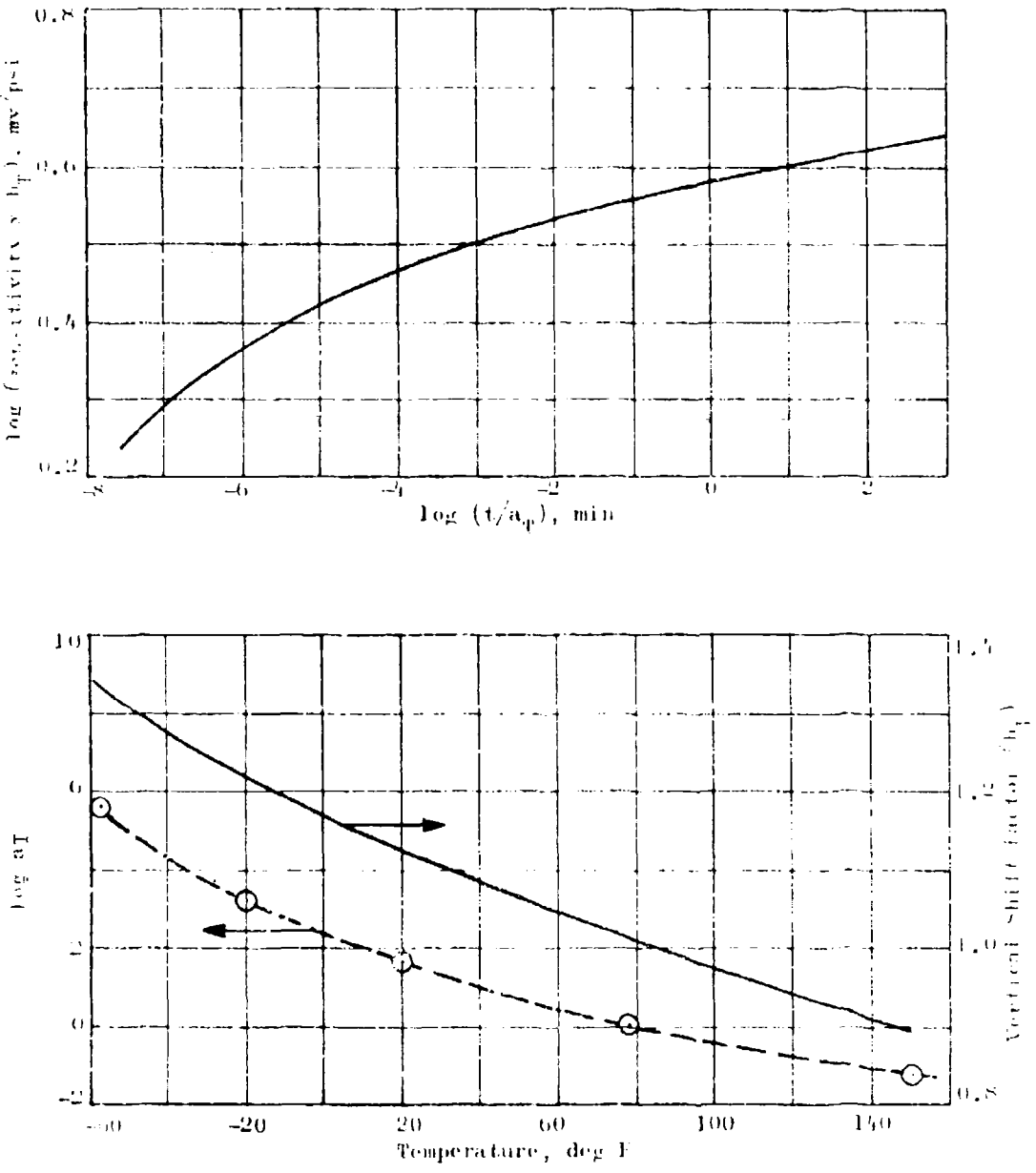

Figure 32. Calibration for Shear Gage S-1 Sensitivity

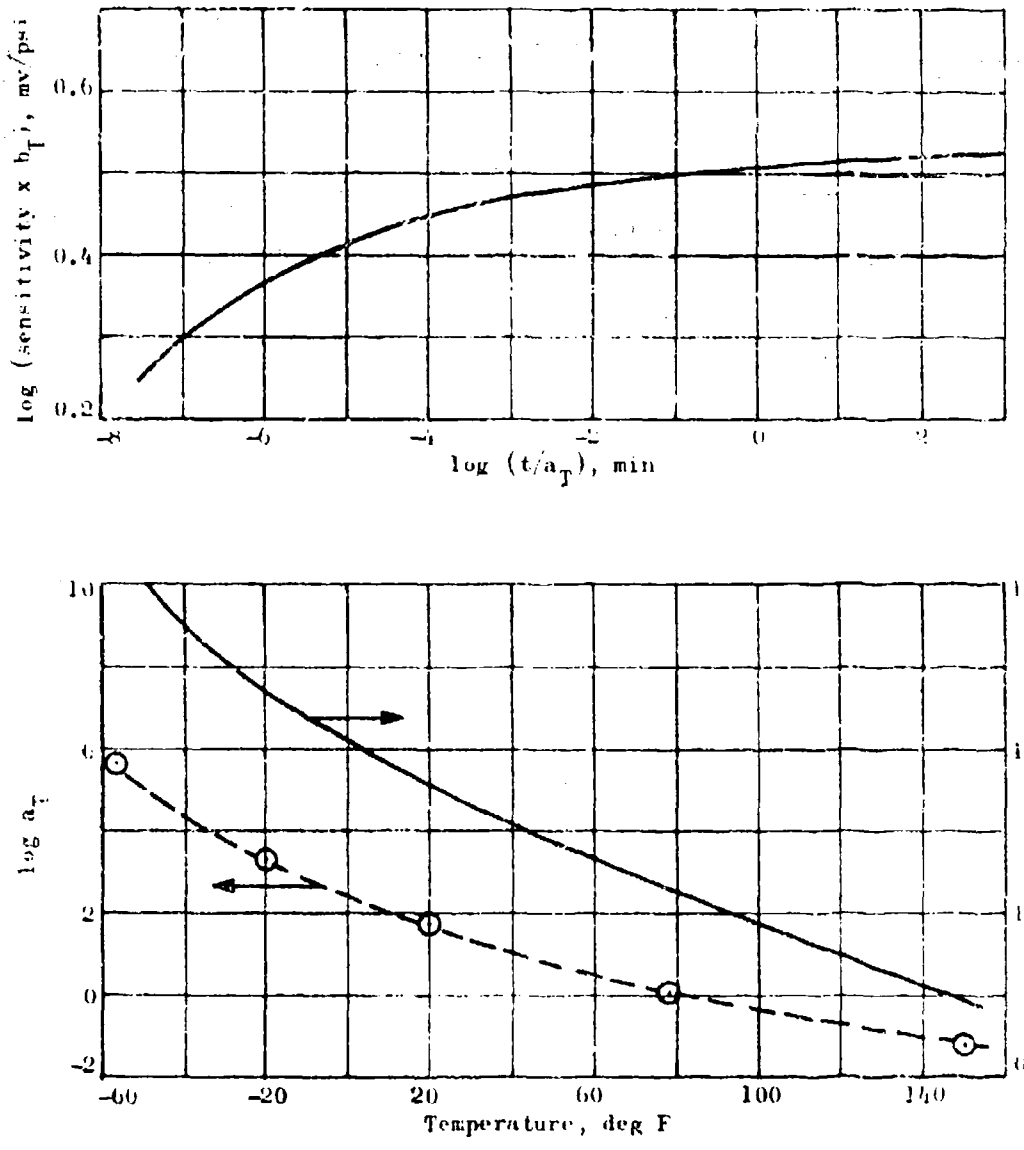

Figure 33. Calibration for Shear Gage S-2 Sensitivity

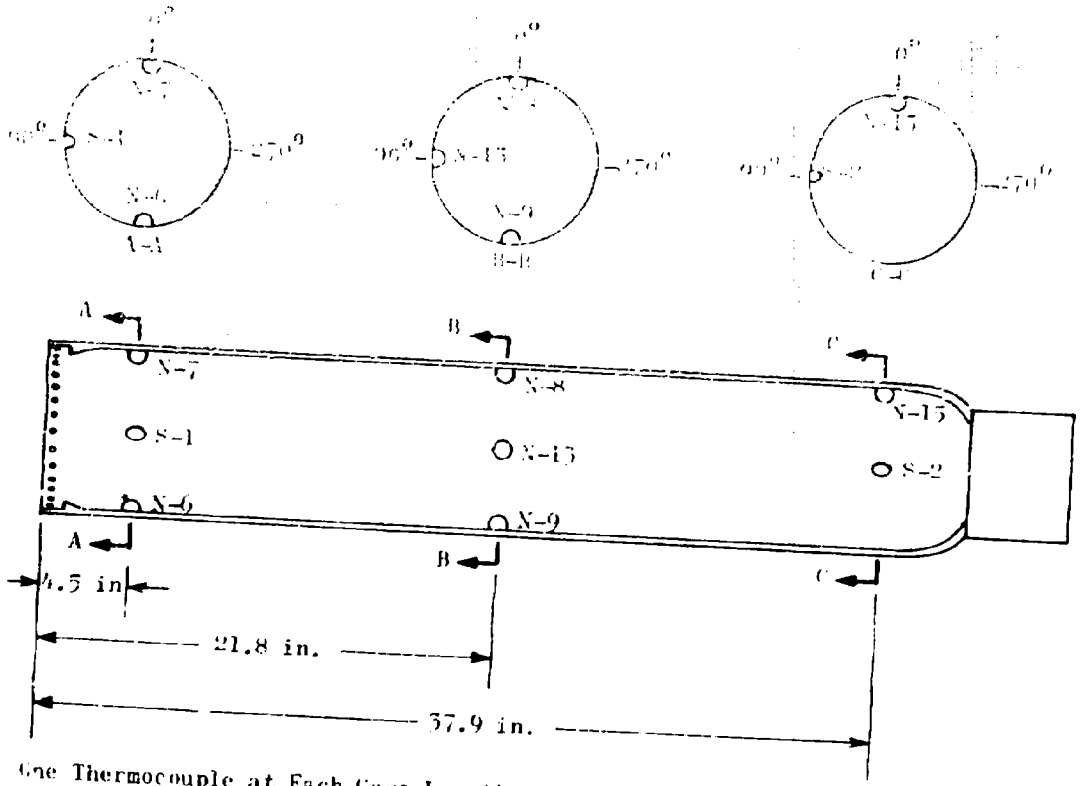

Figure 34. Gage Locations on TIM Instrumented Lined Case

76-163

Figure 35. Instrumented SPARROW Case, Lower View

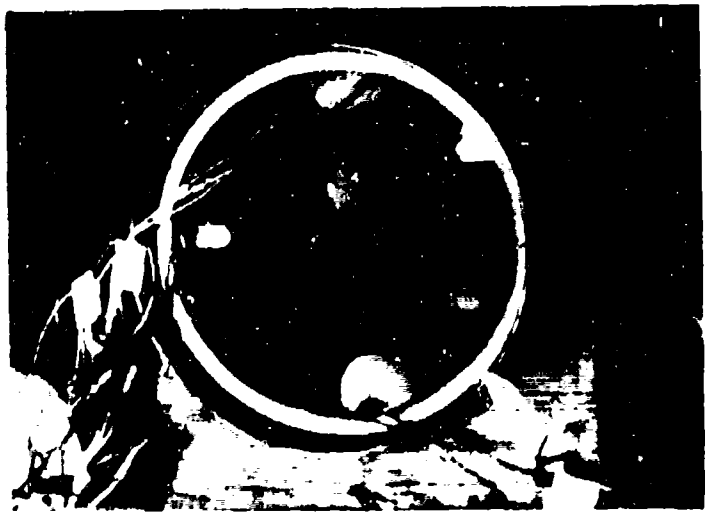

76-162

Figure 36. Instrumented SPARROW Case, Upper View

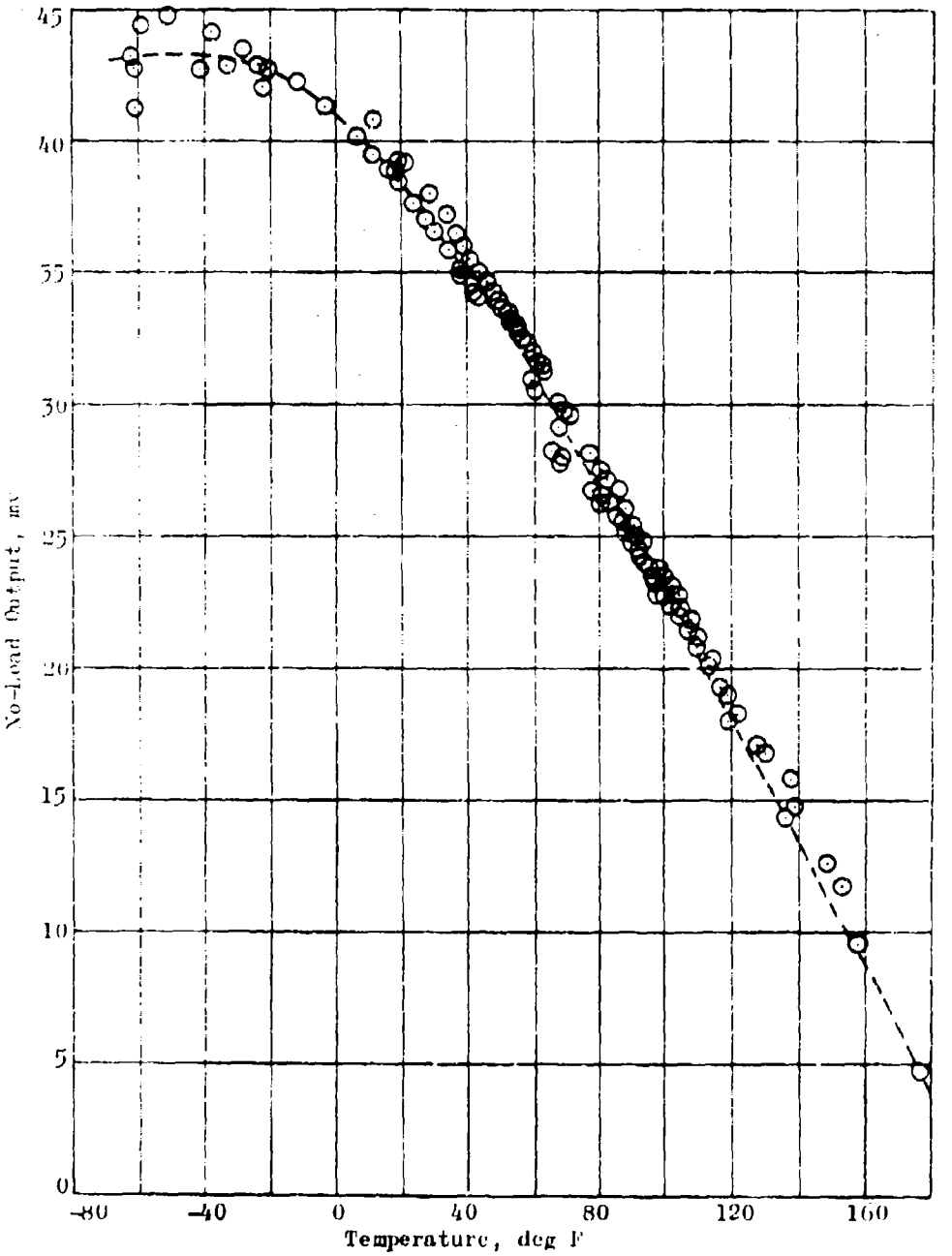

Figure 37. In-Situ No-Load Data, Gage N-6

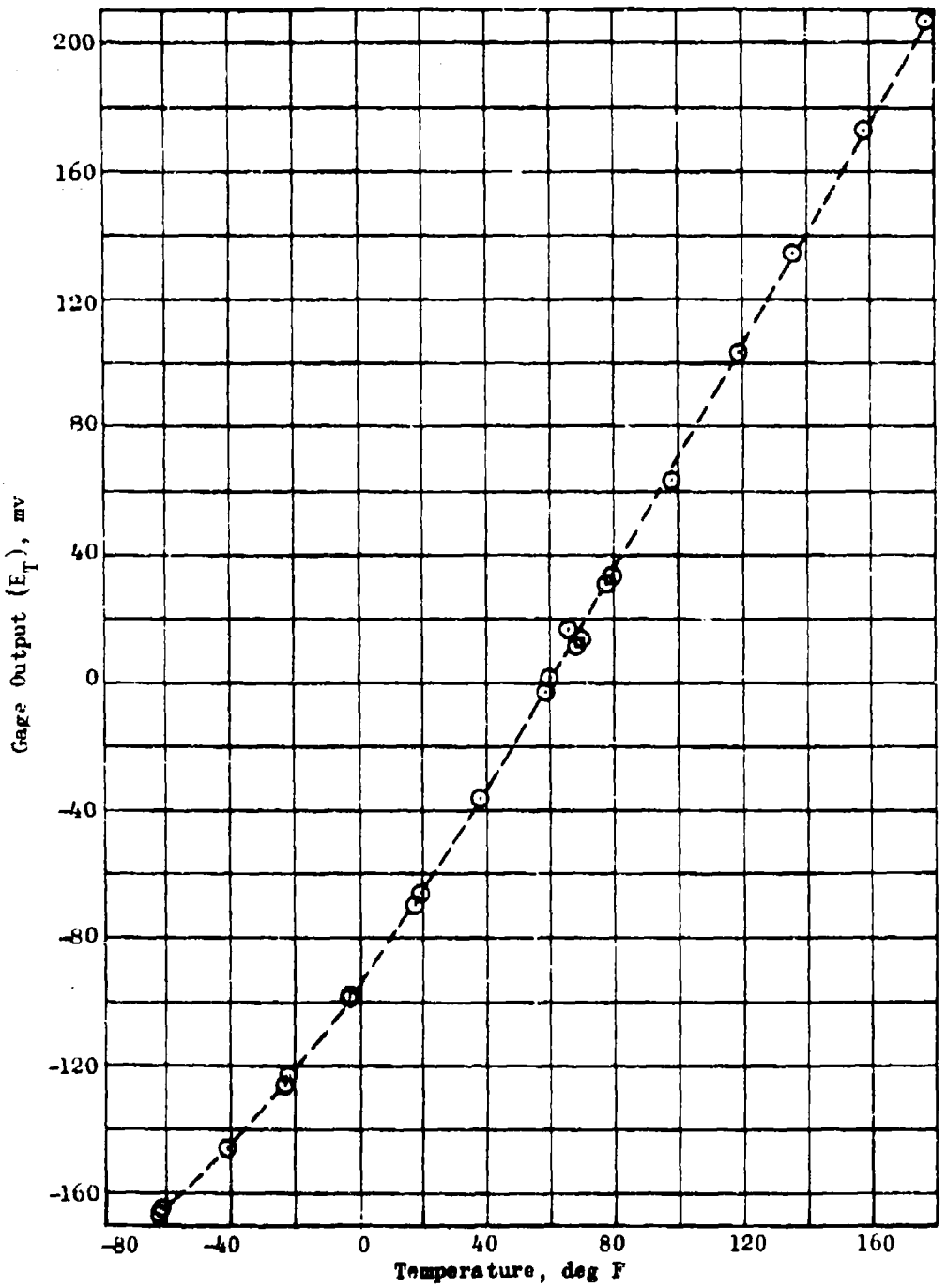

Figure 38. Temperature Sensor Output, Gage N-6

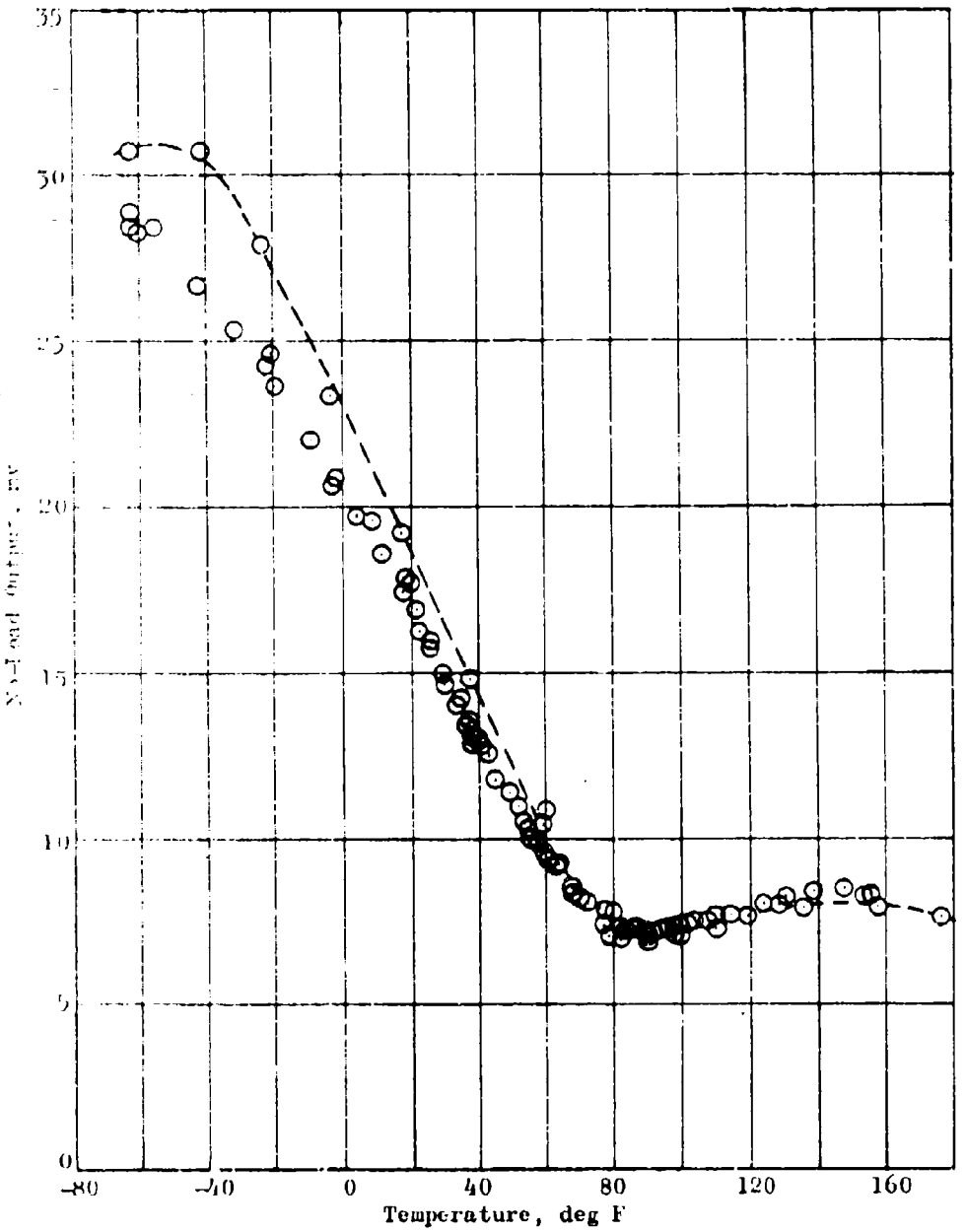

Figure 39. In-Situ No-Load Data, Gage N-7

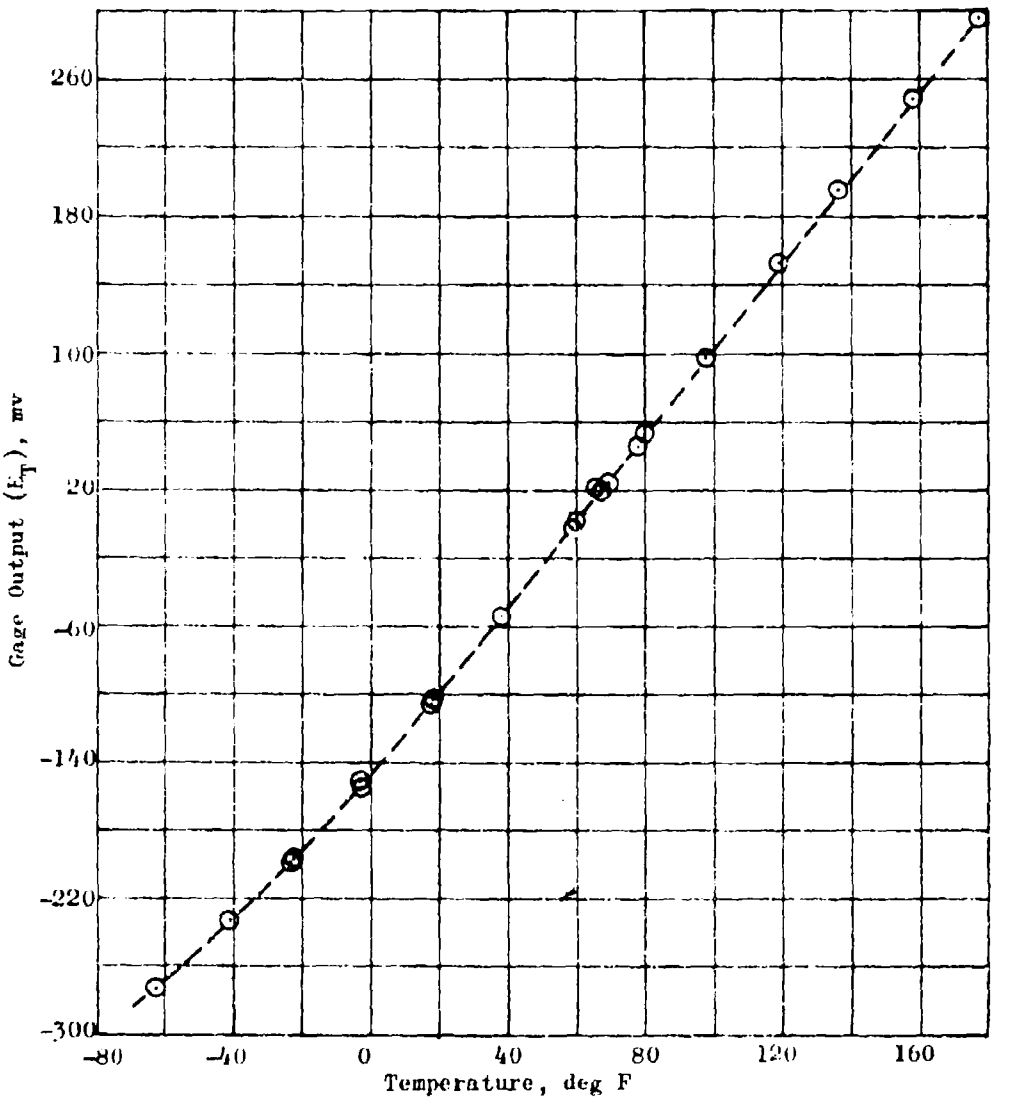

Figure 40. Temperature Sensor Output, Gage N-7

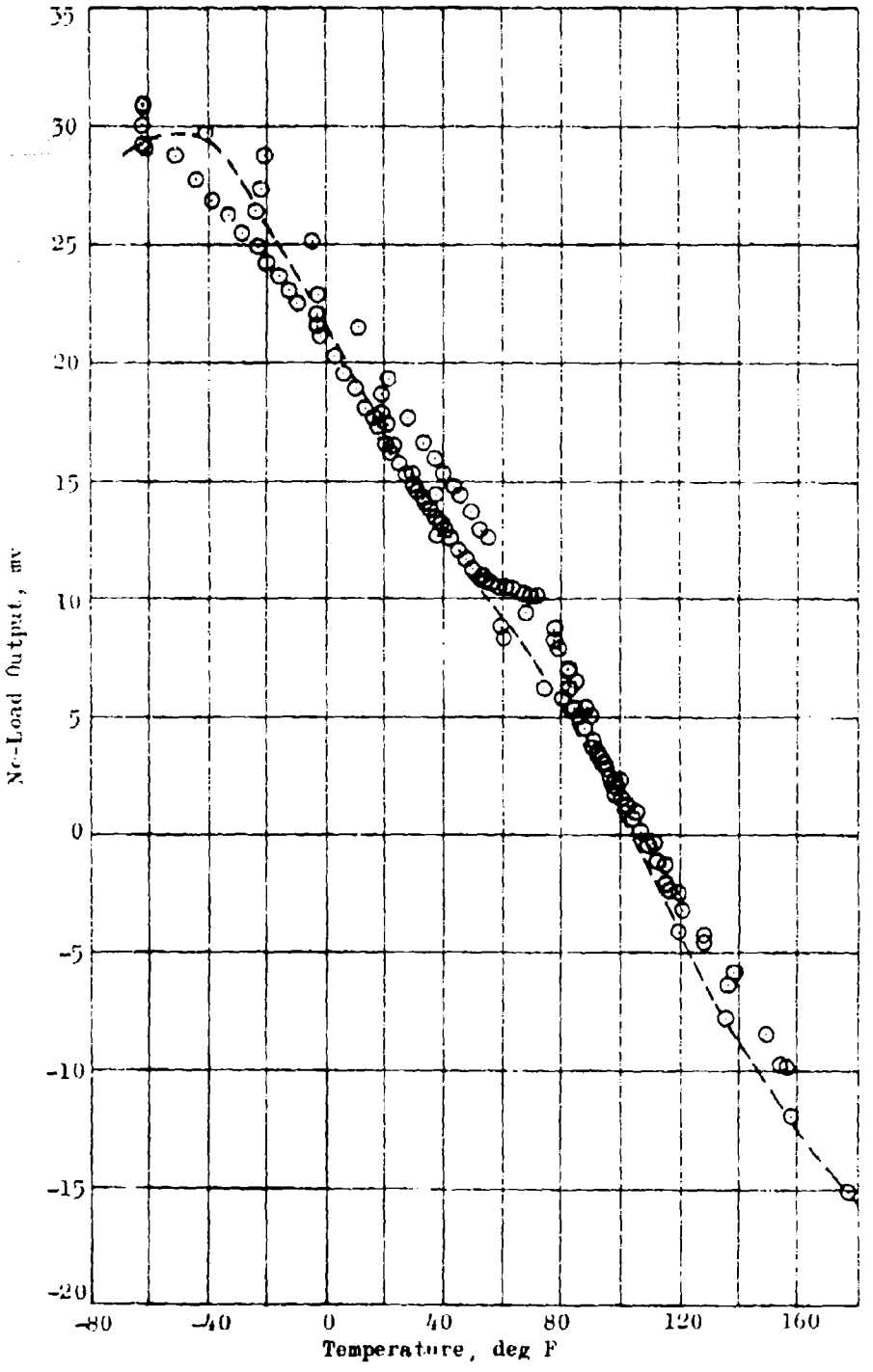

Figure 41. In-Situ No-Load Data, Gage N-8

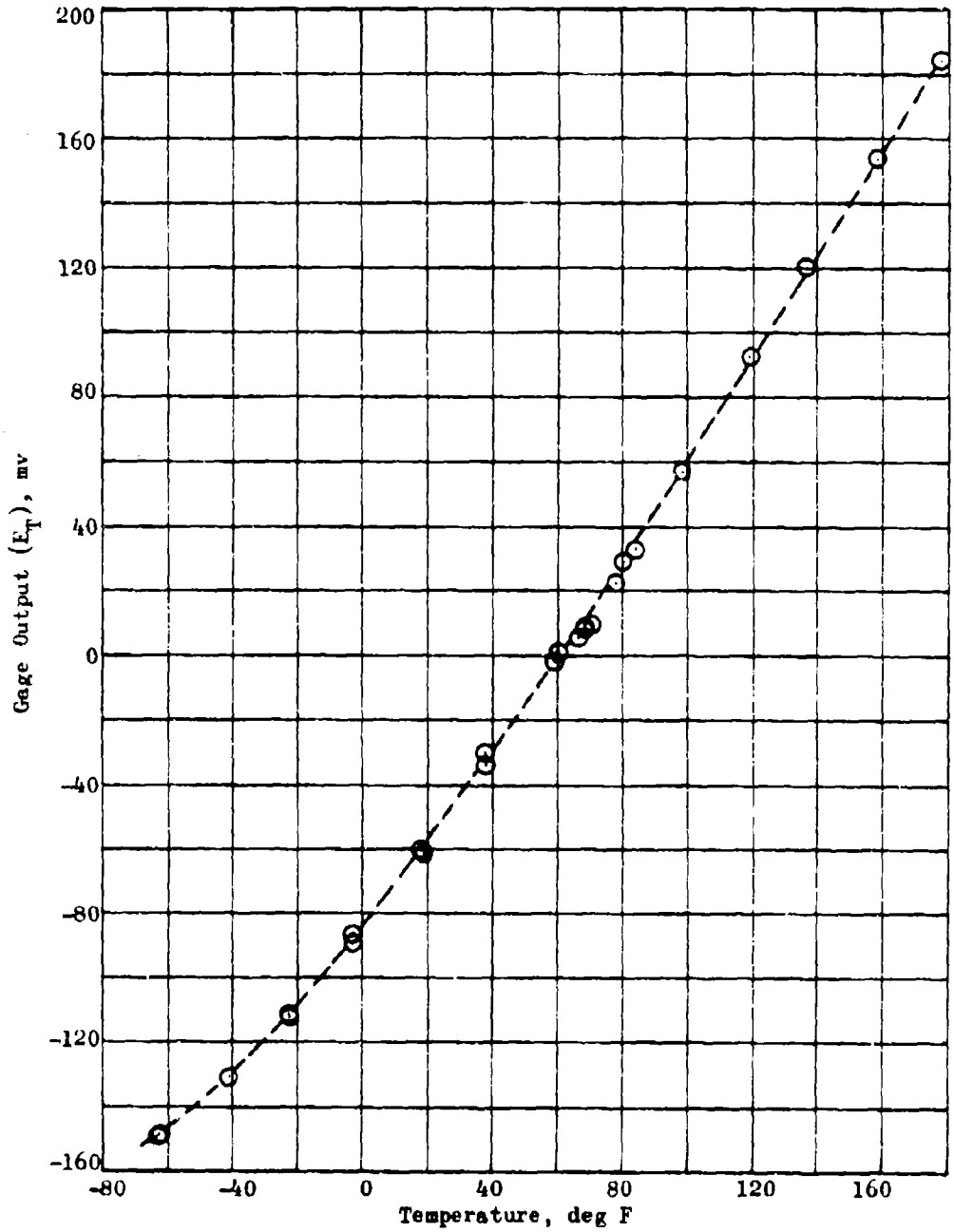

Figure 42. Temperature Sensor Output, Gage N-8

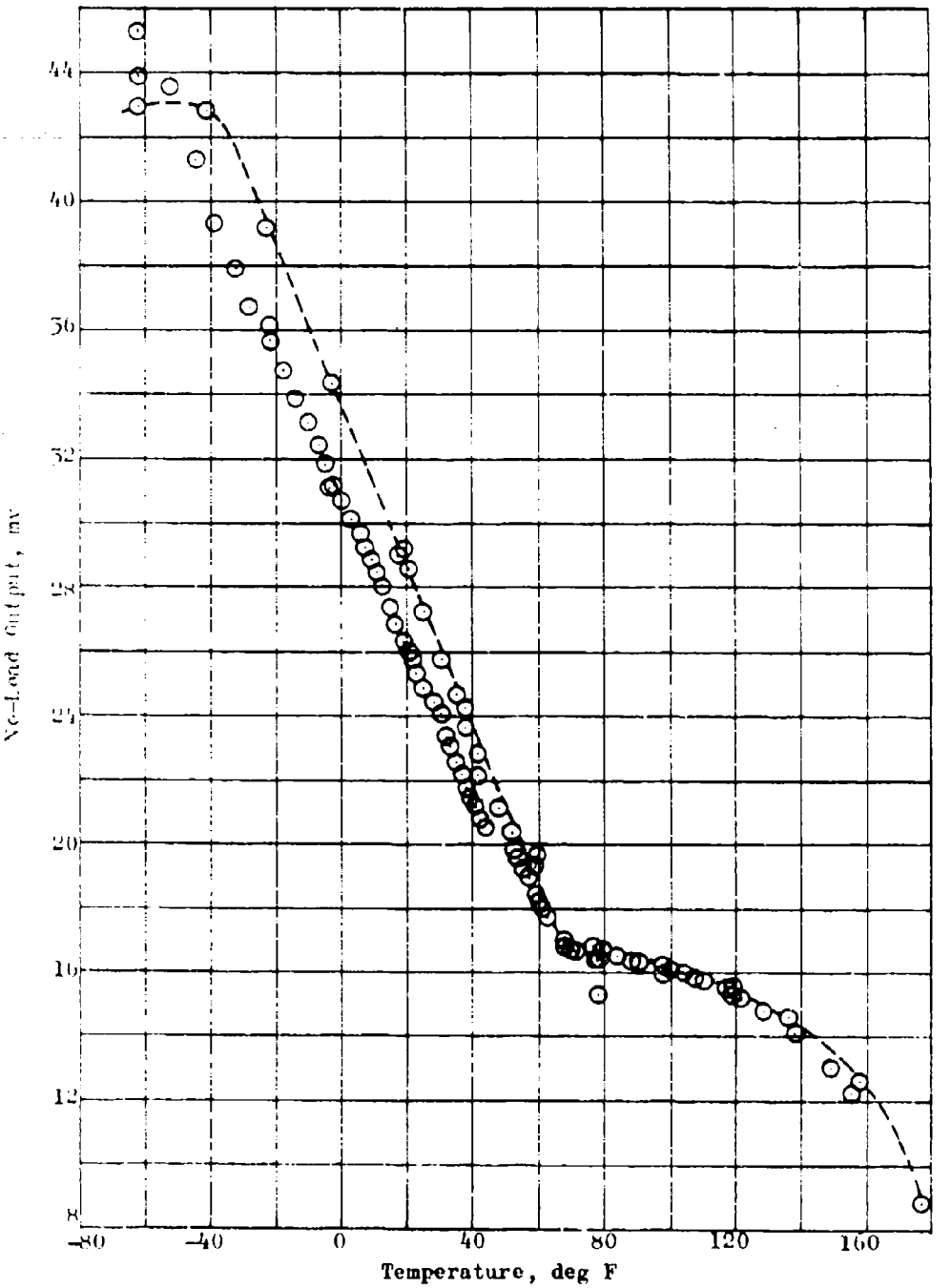

Figure 43. In-Situ No-Load Data, Gage N-9

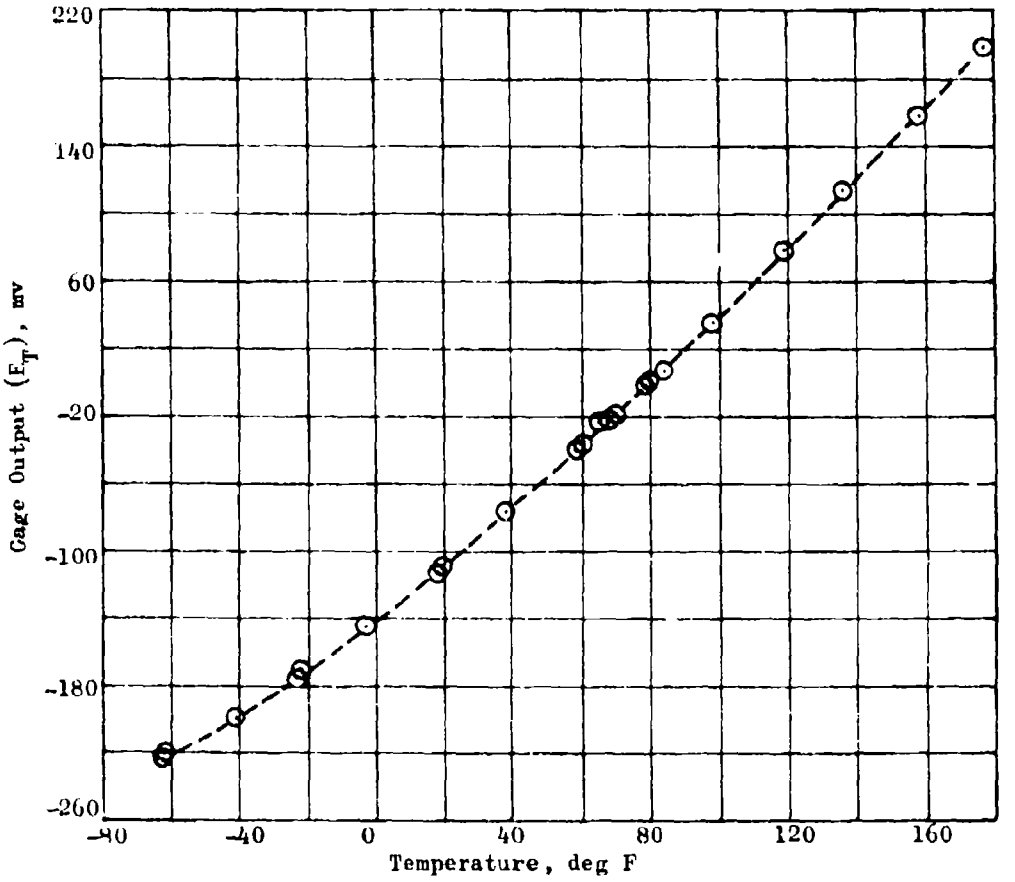

Figure 44. Temperature Sensor Output, Gage N-9

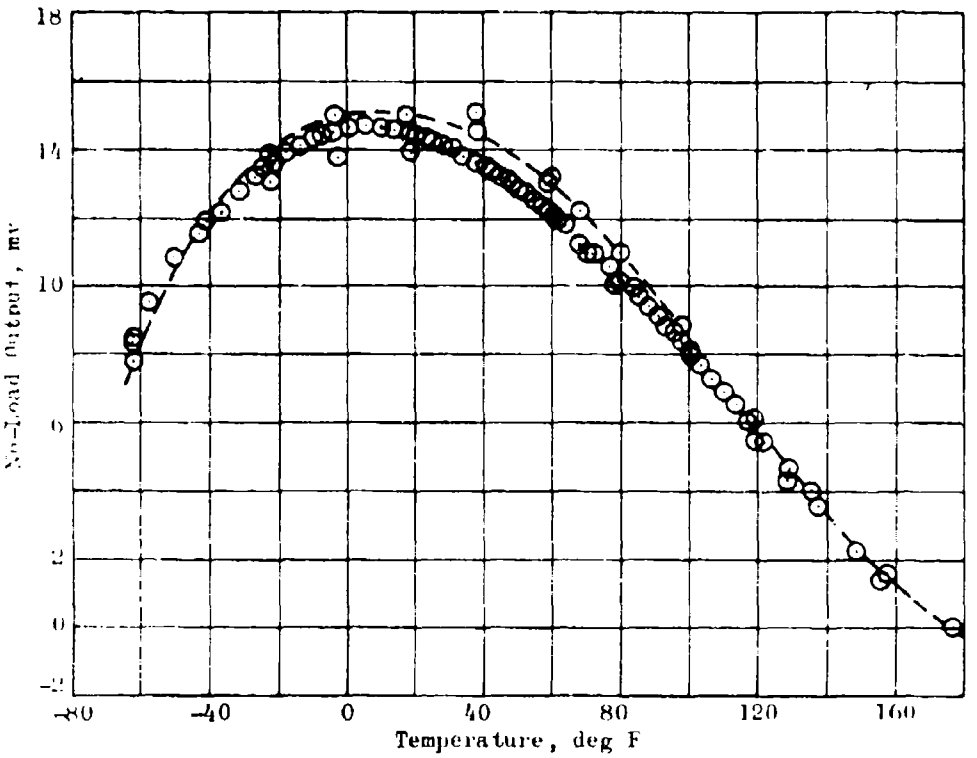

Figure 45. In-Situ No-Load Data, Gage N-13

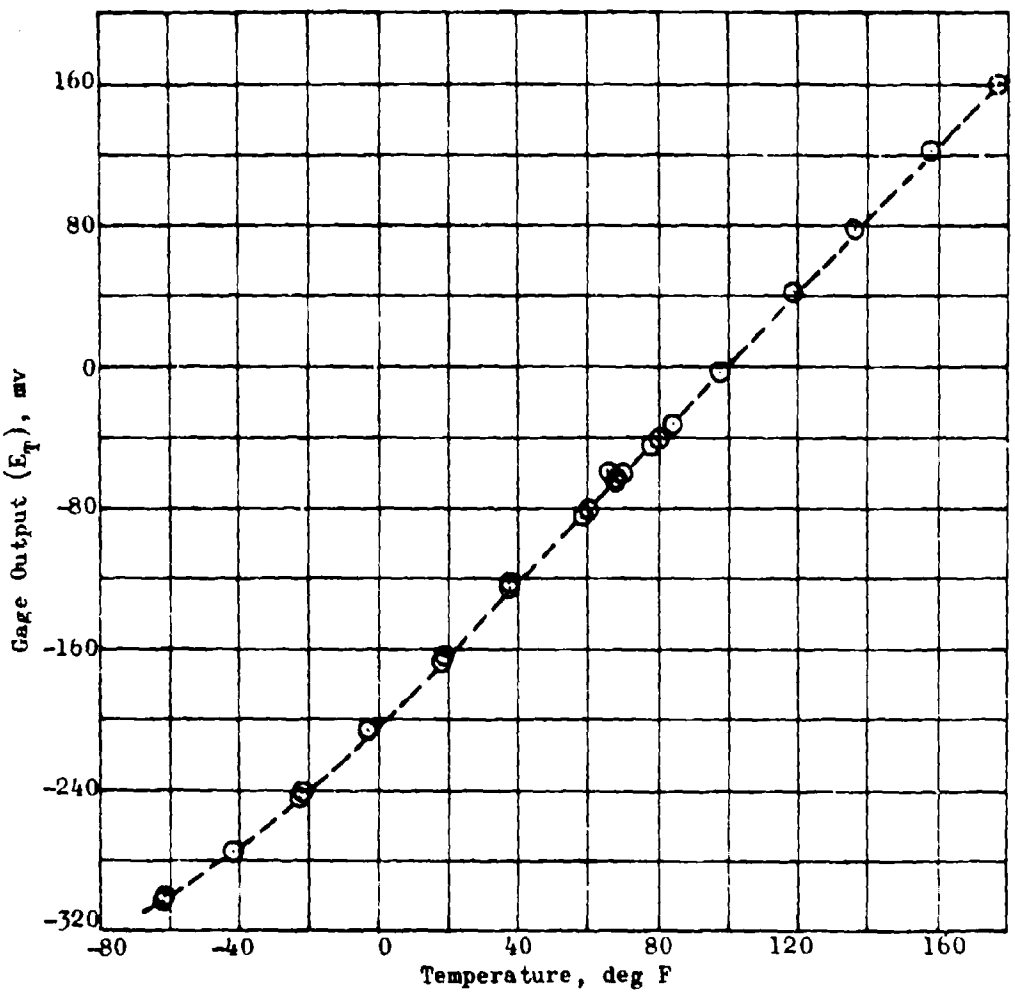

Figure 46. Temperature Sensor Output, Gage N-13

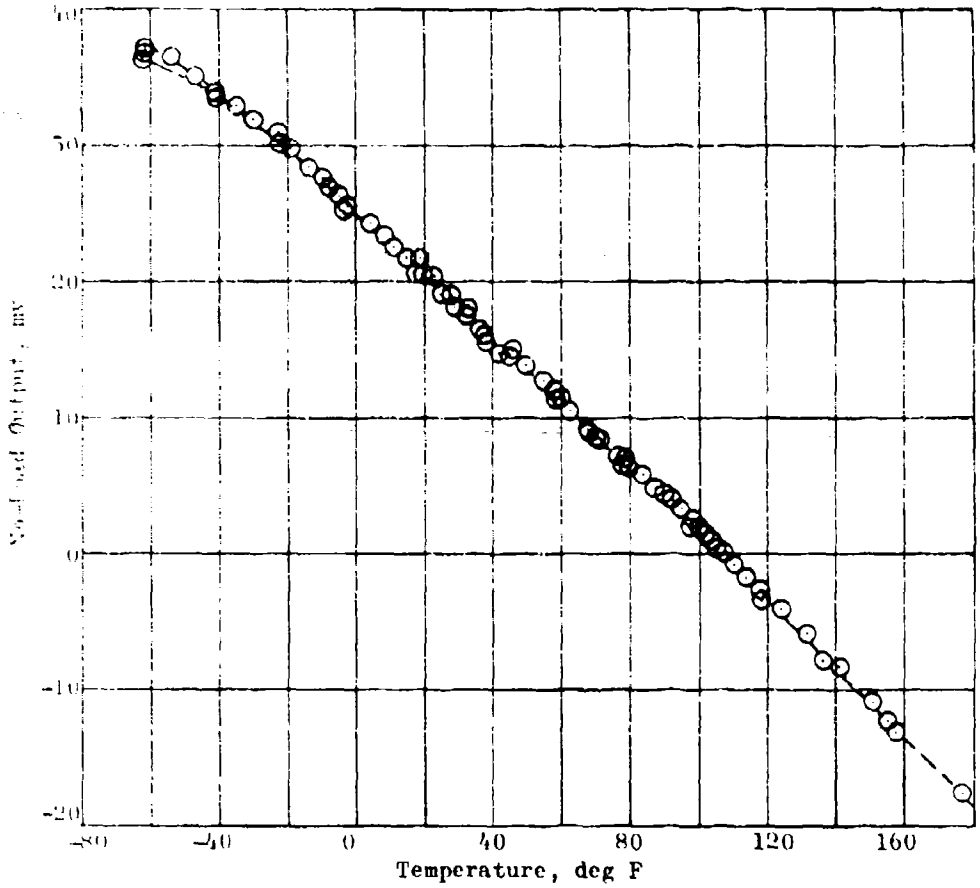

Figure 47. In-Situ No-Load Data, Gage N-15

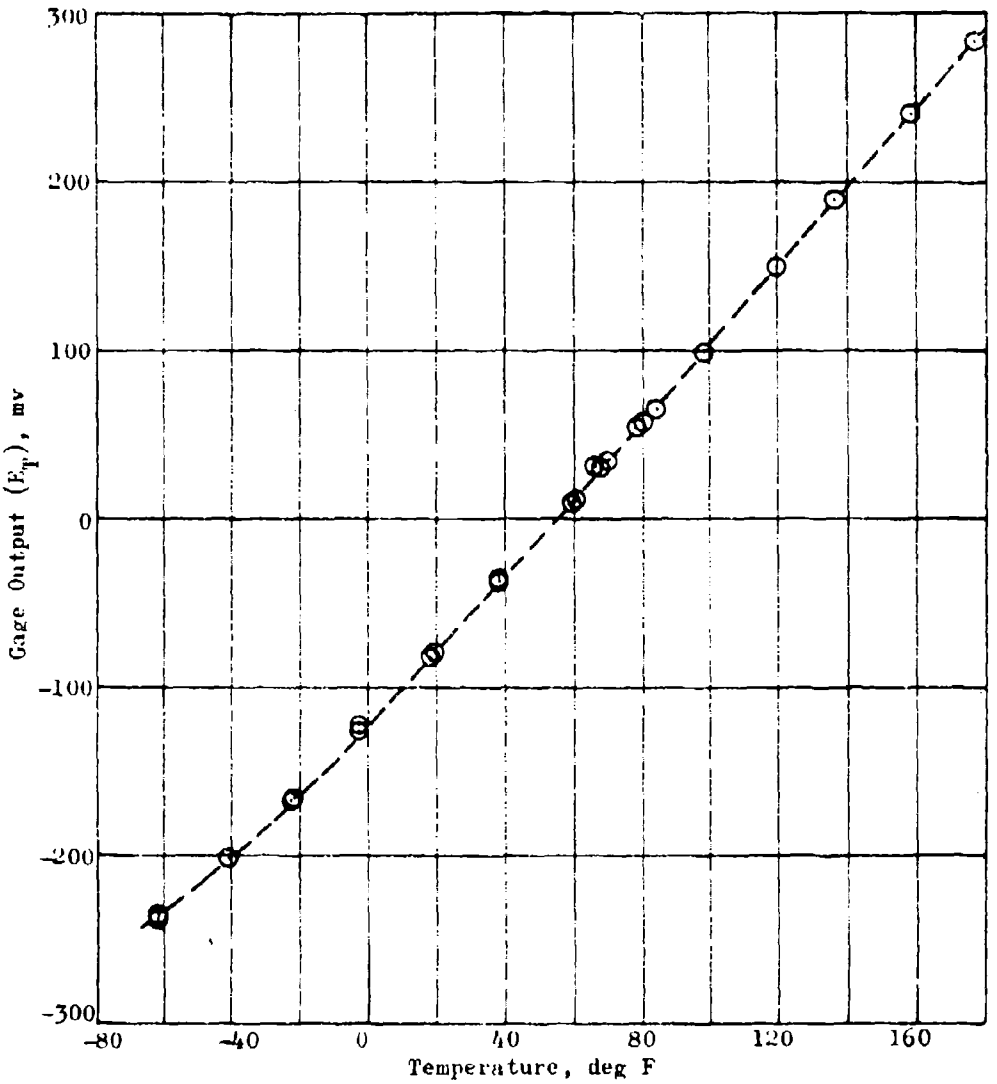

Figure 48. Temperature Sensor Output, Gage N-15

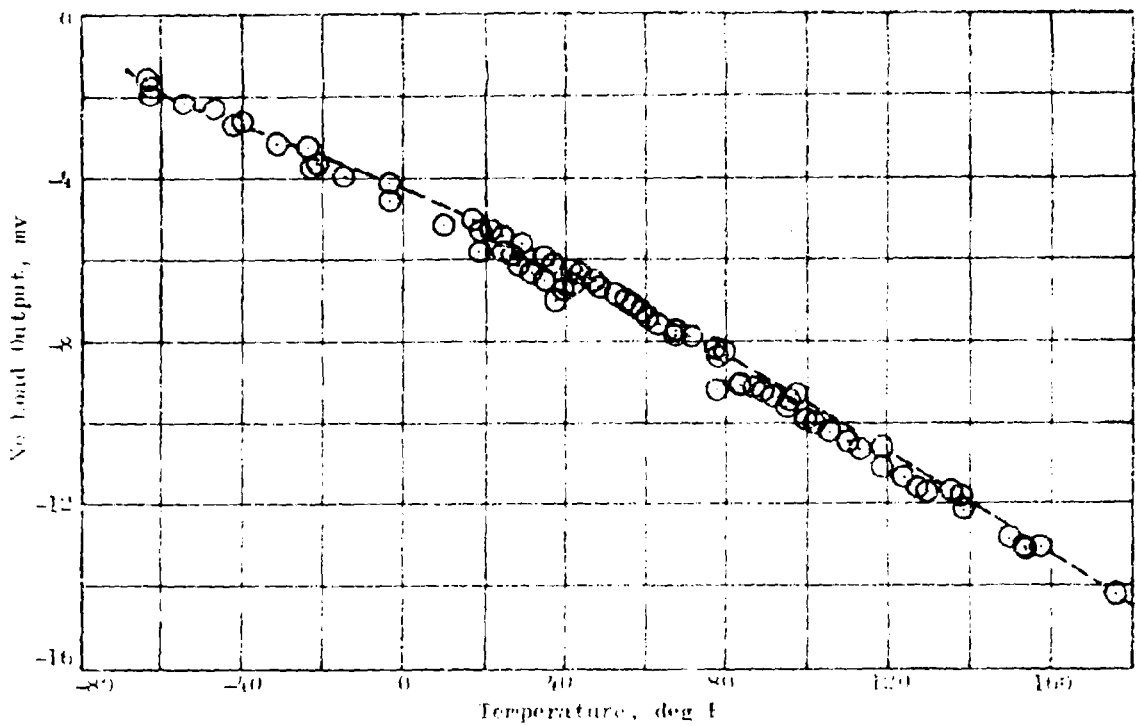

Figure 49. In-Situ No-Load Data, Gage S-1

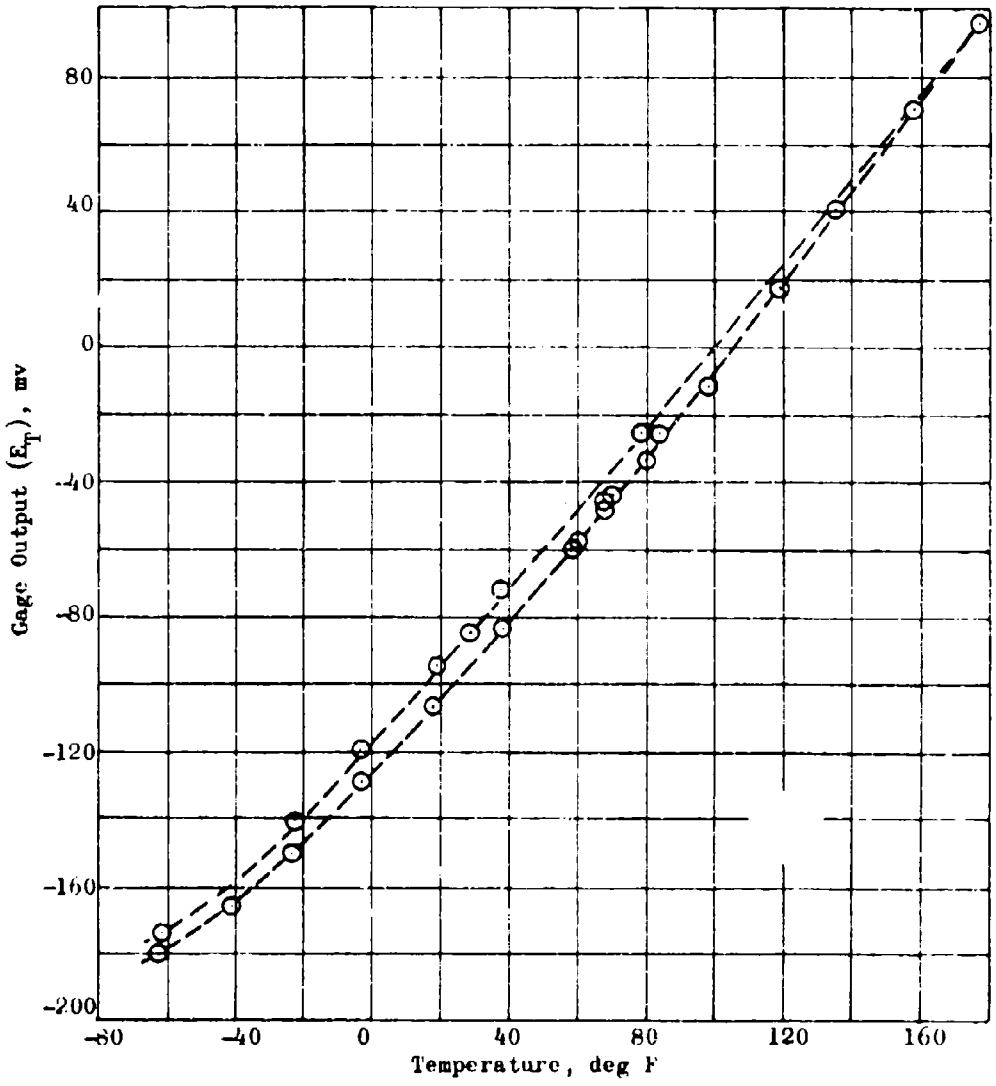

Figure 50. Temperature Sensor Output, Gage S-1

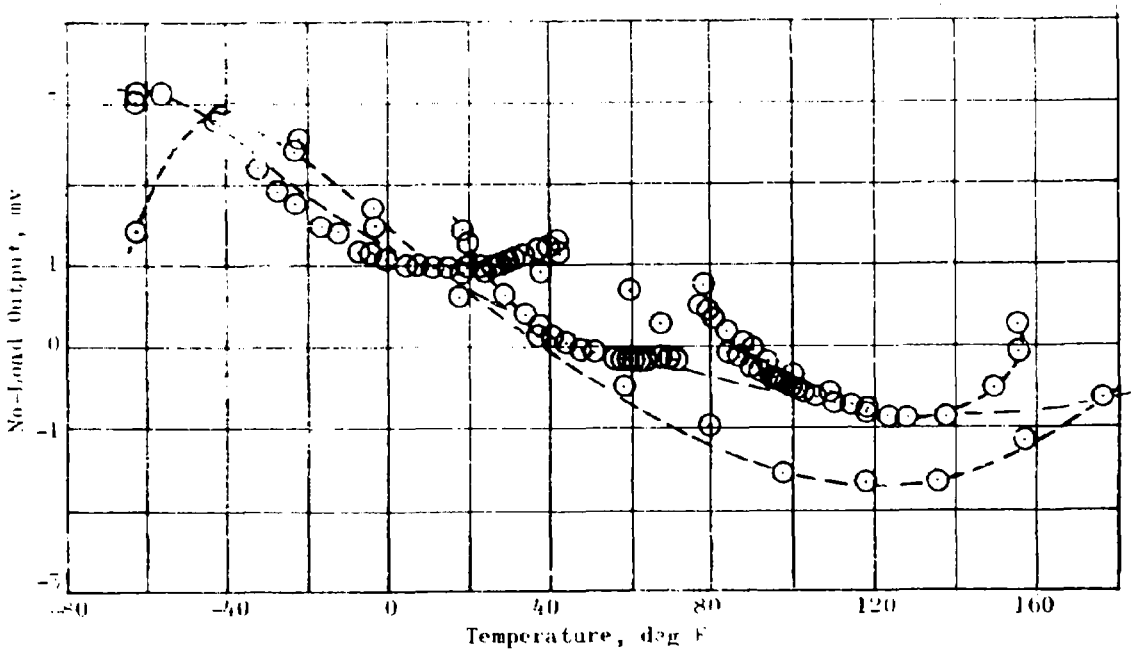

Figure 51. In-Situ No-Load Data, ·e S-2

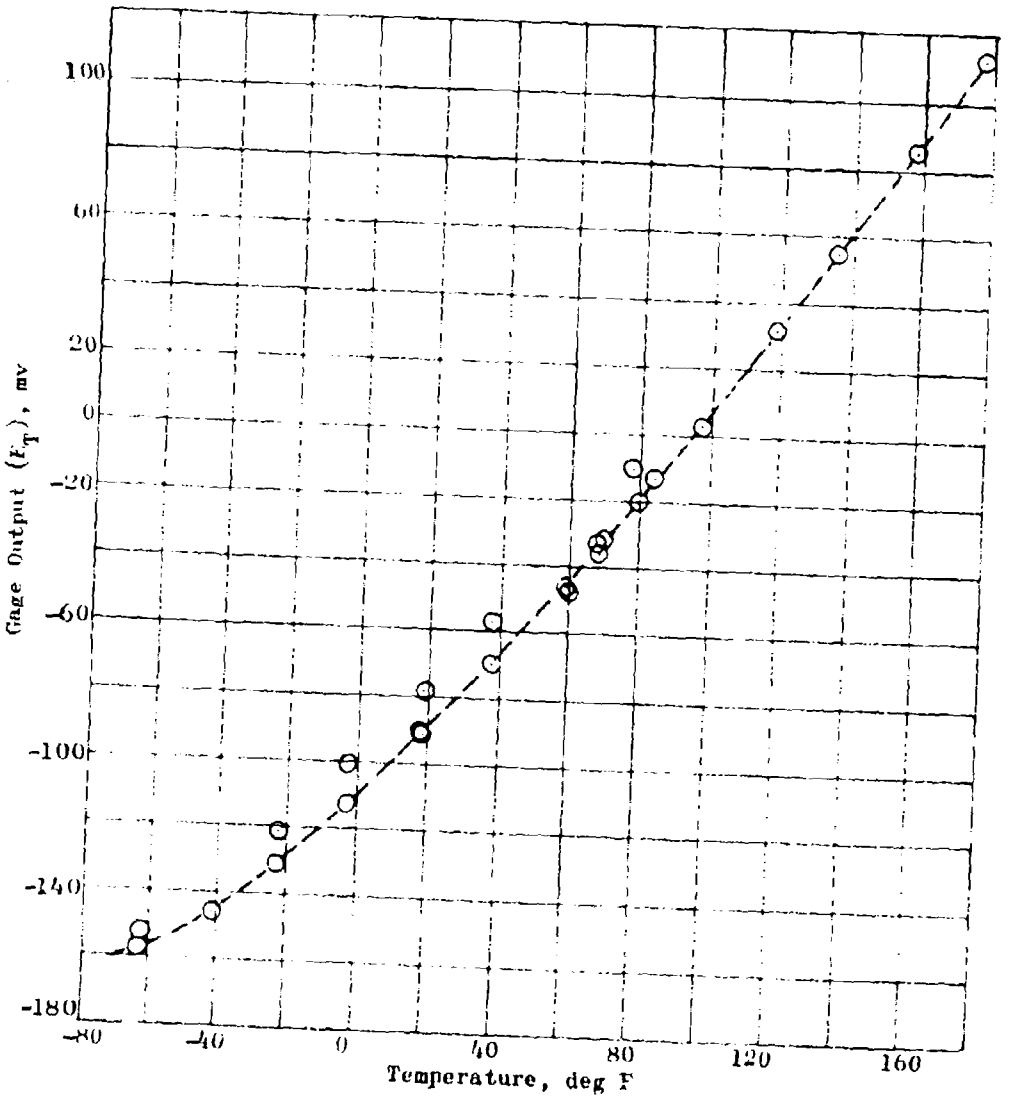

Figure 52. Temperature Sensor Output, Gage S-2

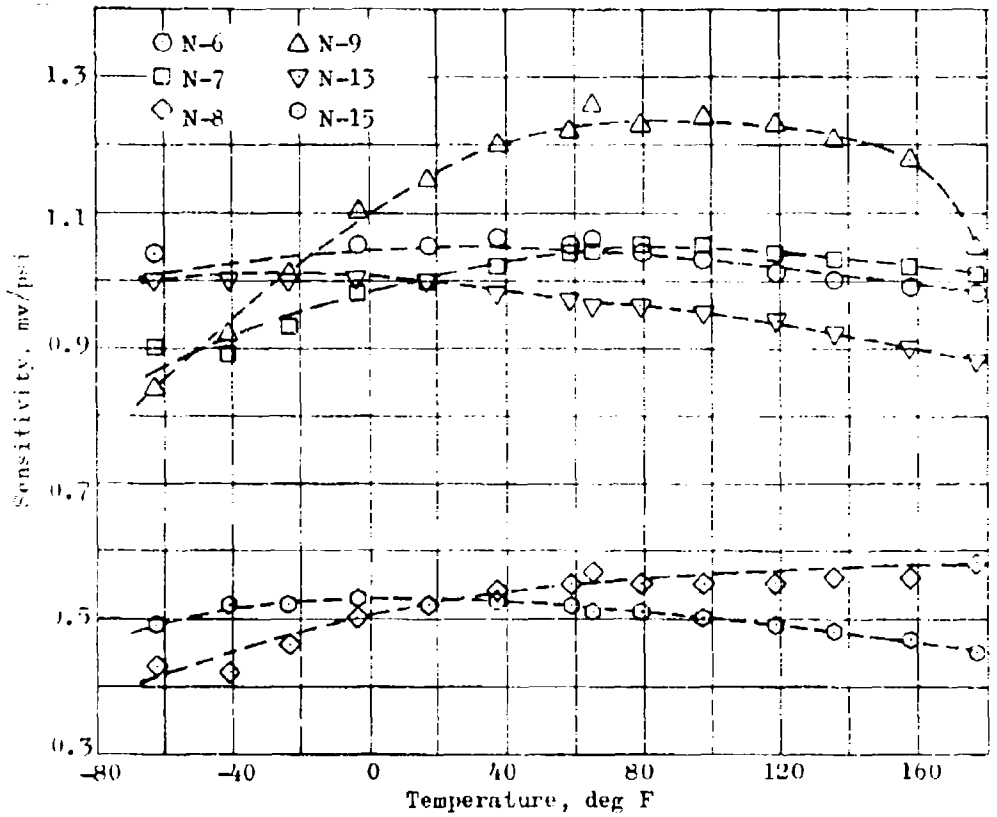

Figure 53. Normal Gage Sensitivity, In-Situ Calibration

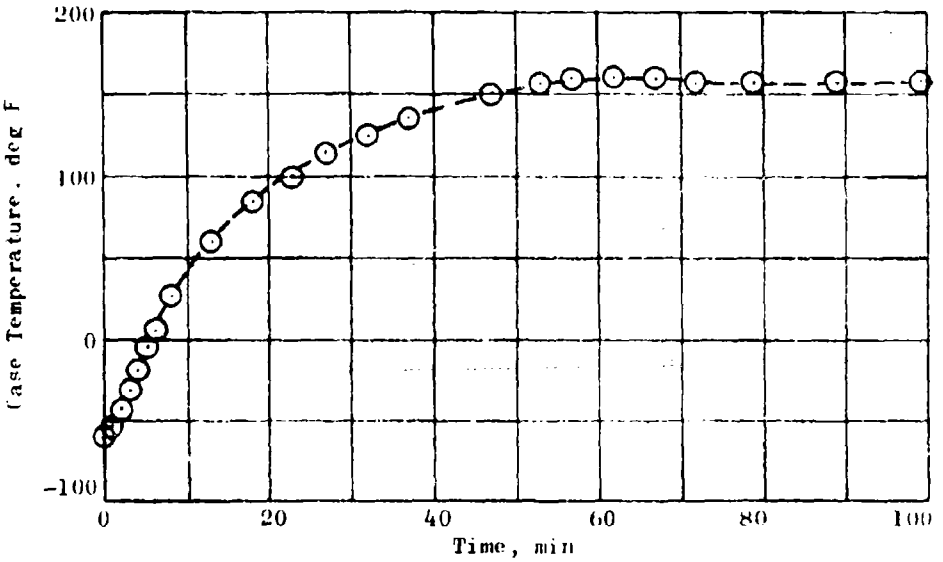

Figure 54. Case Temperature, Rapid Heating Test

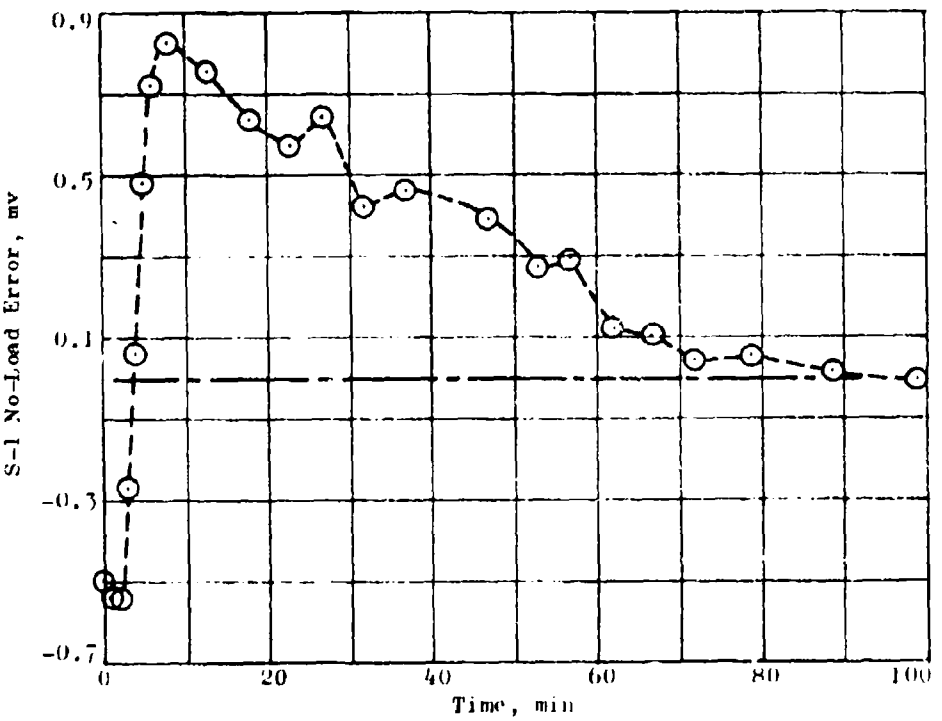

Figure 55. No-Load Error, Gage S-1, Rapid Heating Test

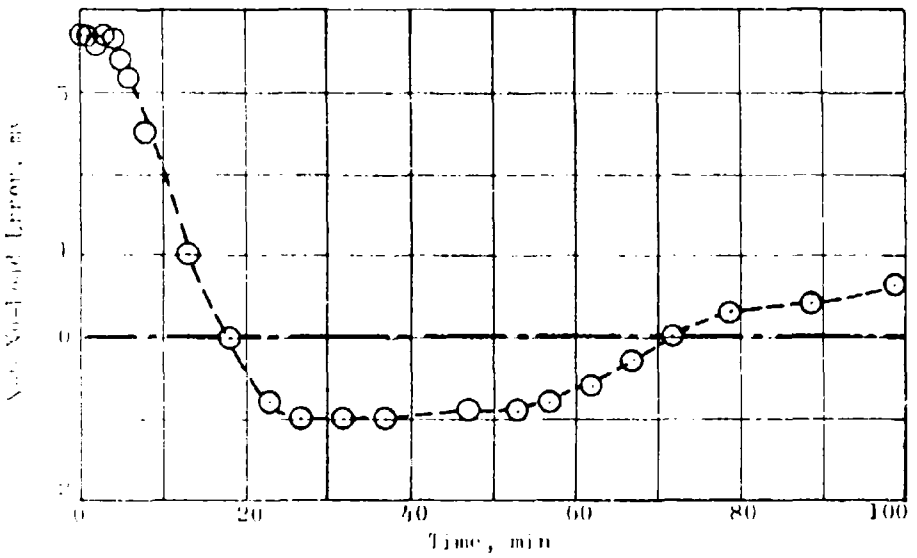

Figure 56. No-Load Error, Gage N-6, Rapid Heating Test

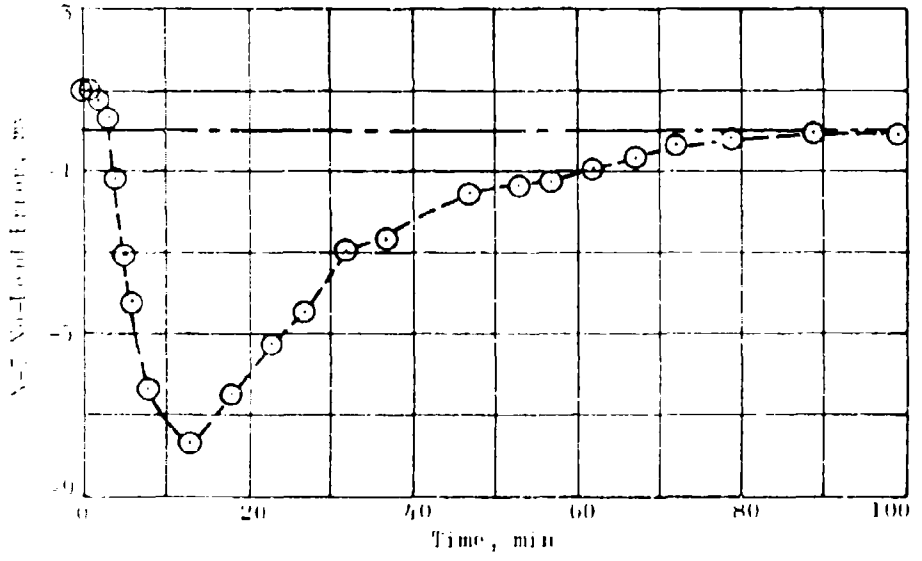

Figure 57. No-Load Error, Gage N-7, Rapid Heating Test

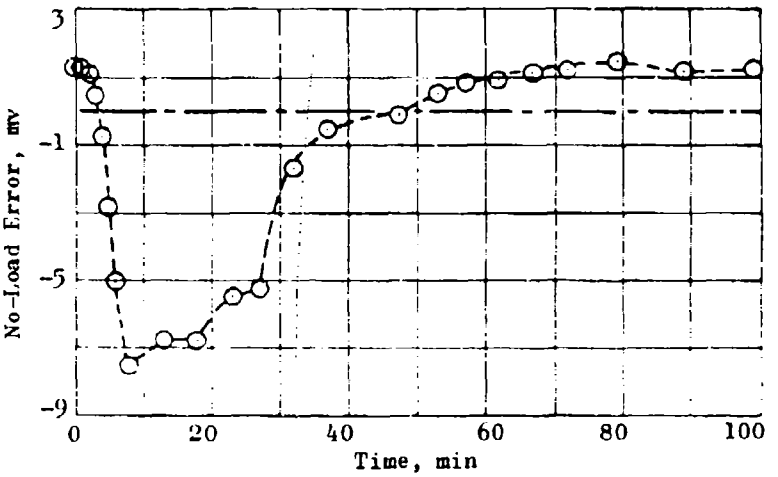

Figure 58. No-Load Error, Gage N-8, Rapid Heating Test

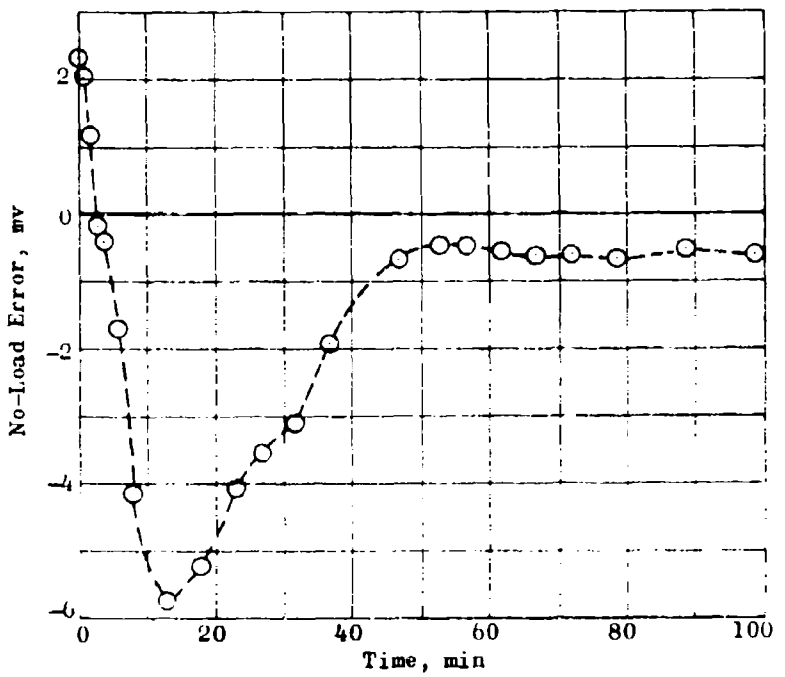

Figure 59. No-Load Error, Gage N-9, Rapid Heating Test

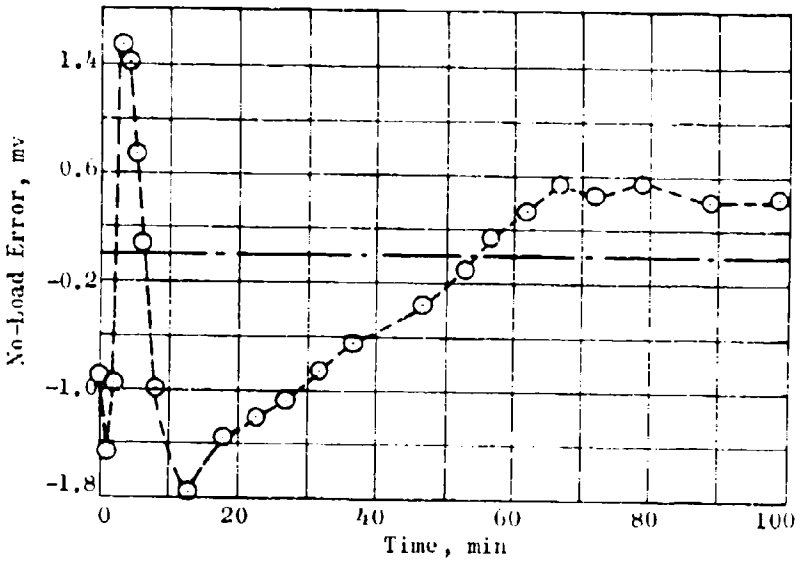

Figure 60. No-Load Error, Gage N-13, Rapid Heating Test

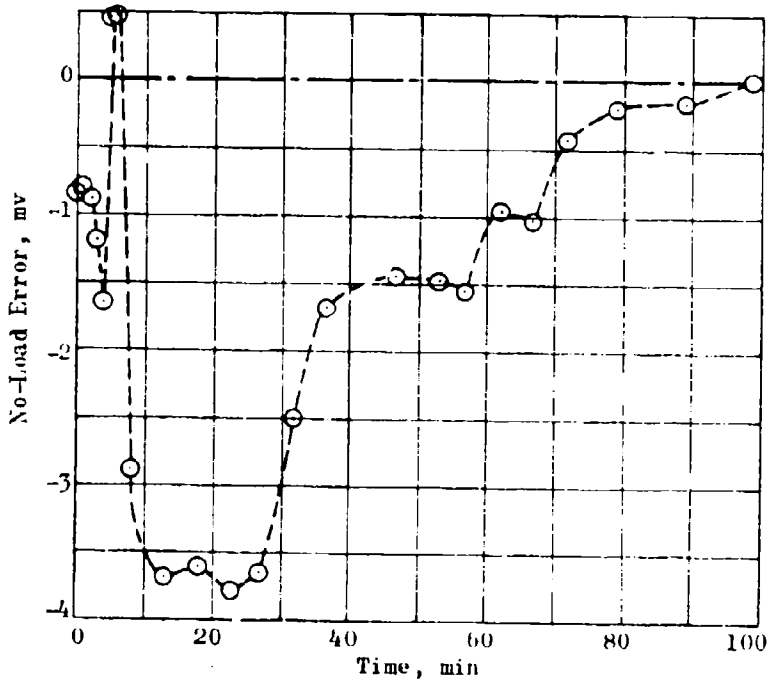

Figure 61. No-Load Error, Gage N-15, Rapid Heating Test

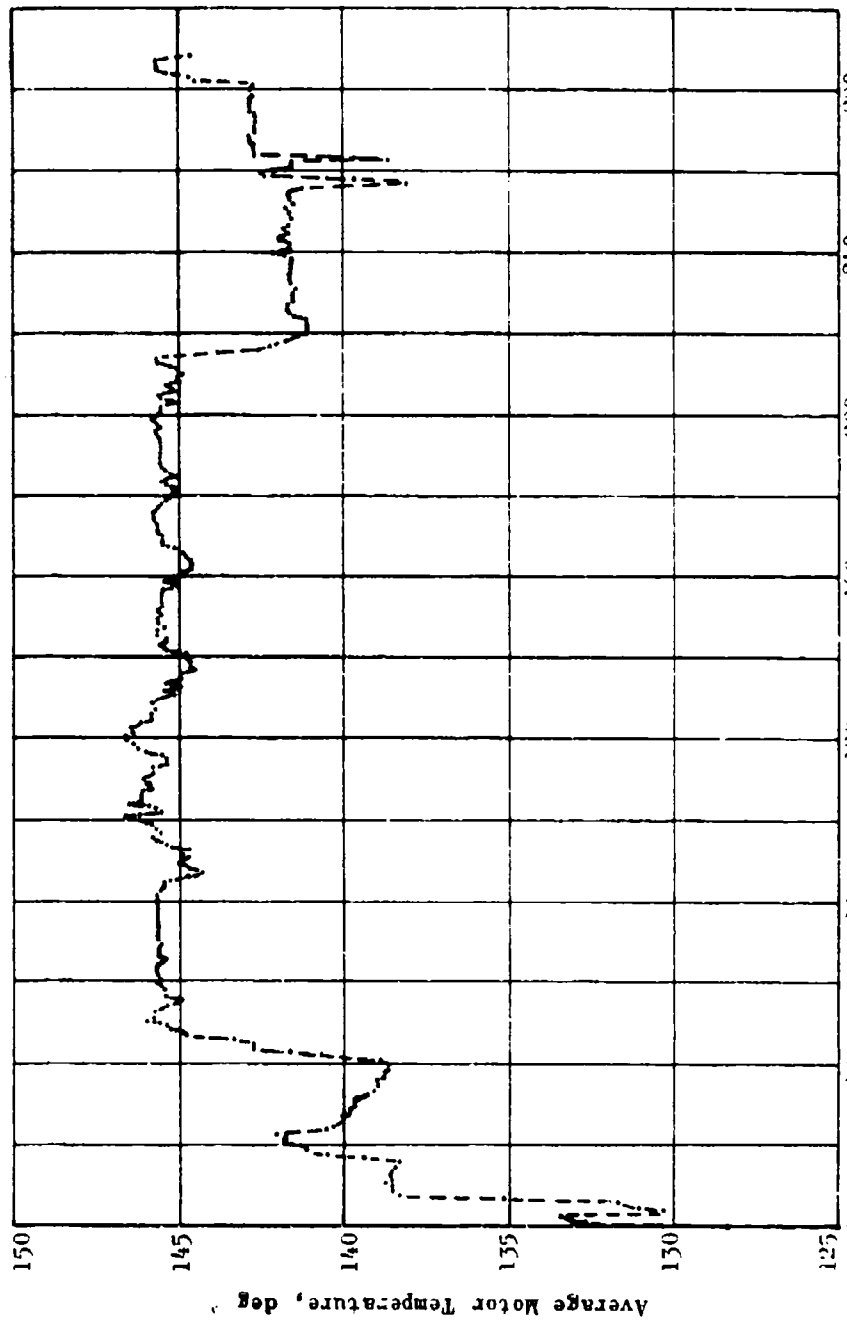

Figure 62. Average Motor Temperature During Cure

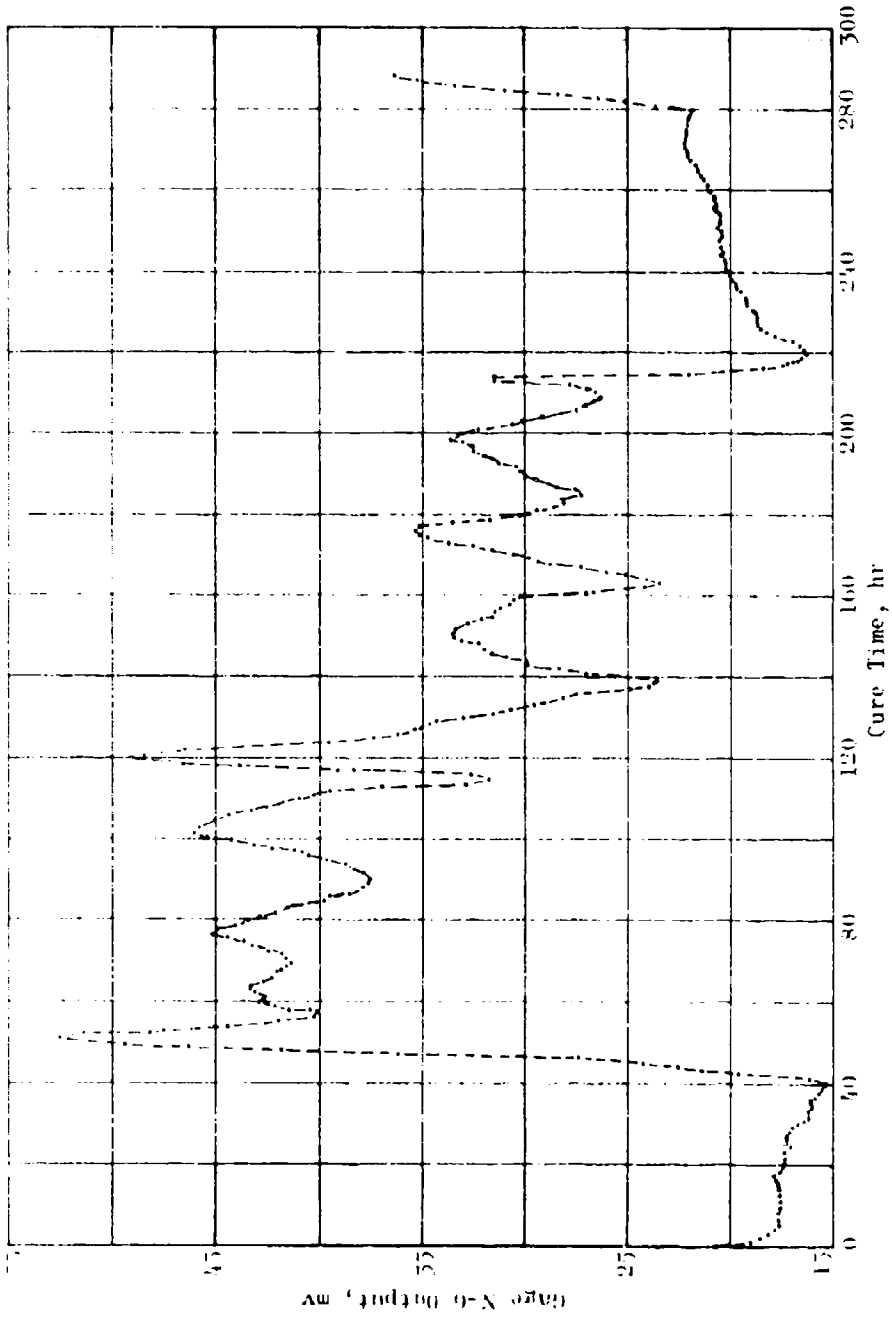

Figure 65. Normal Gage X-6 Cure Response

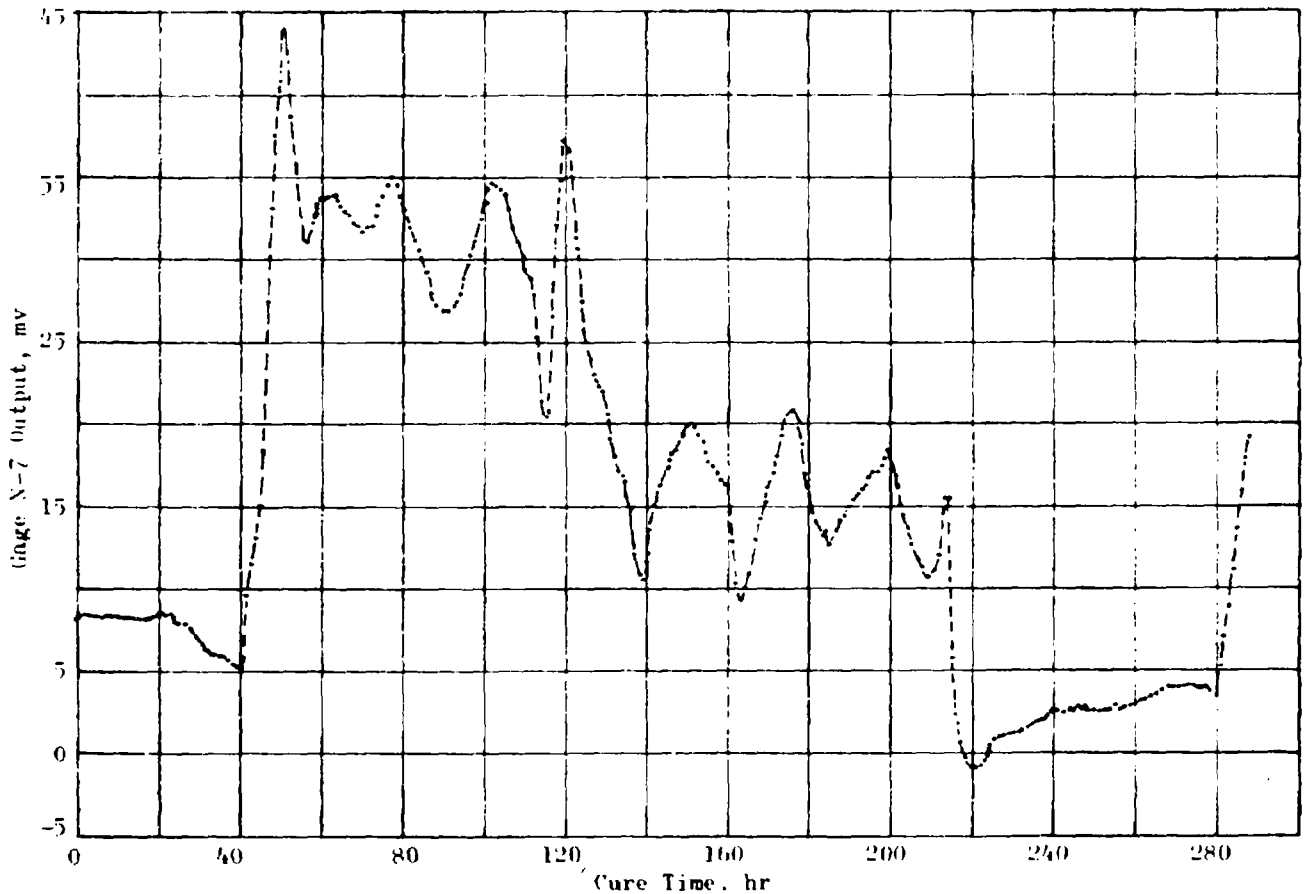

Figure 64. Normal Gage N-7 Cure Response

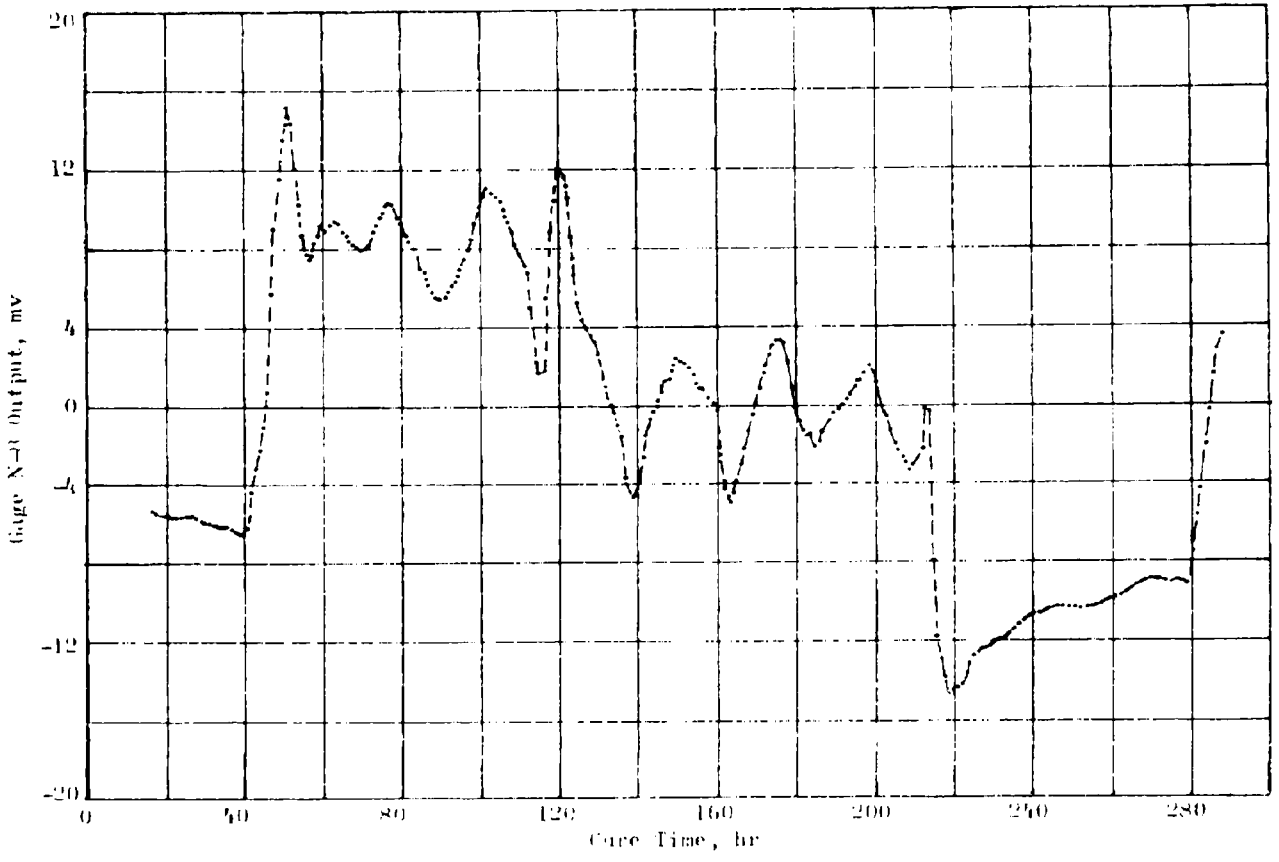

Figure 65. Normal Gage X-8 Cure Response

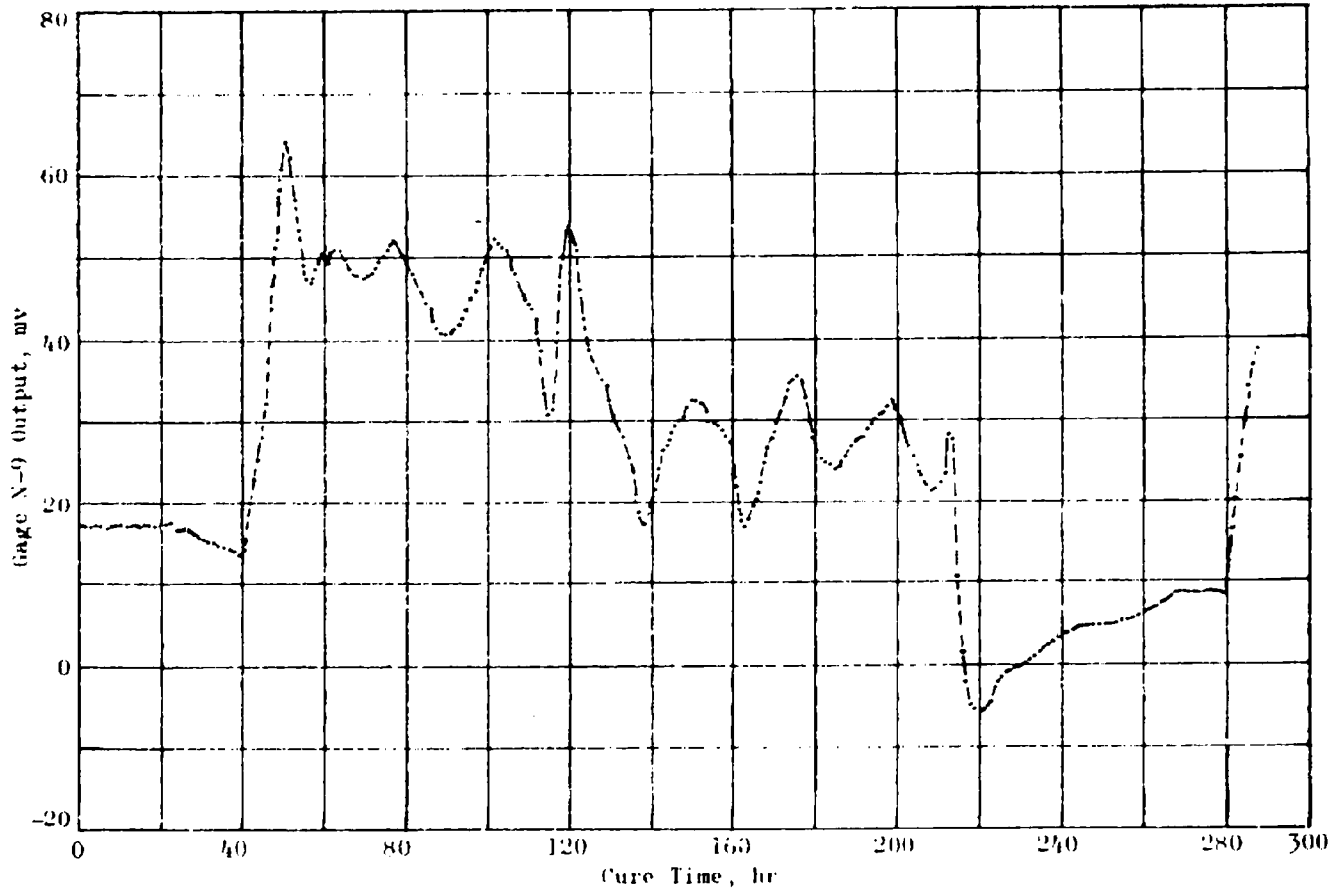

Figure 66. Normal Gage N-9 Cure Response

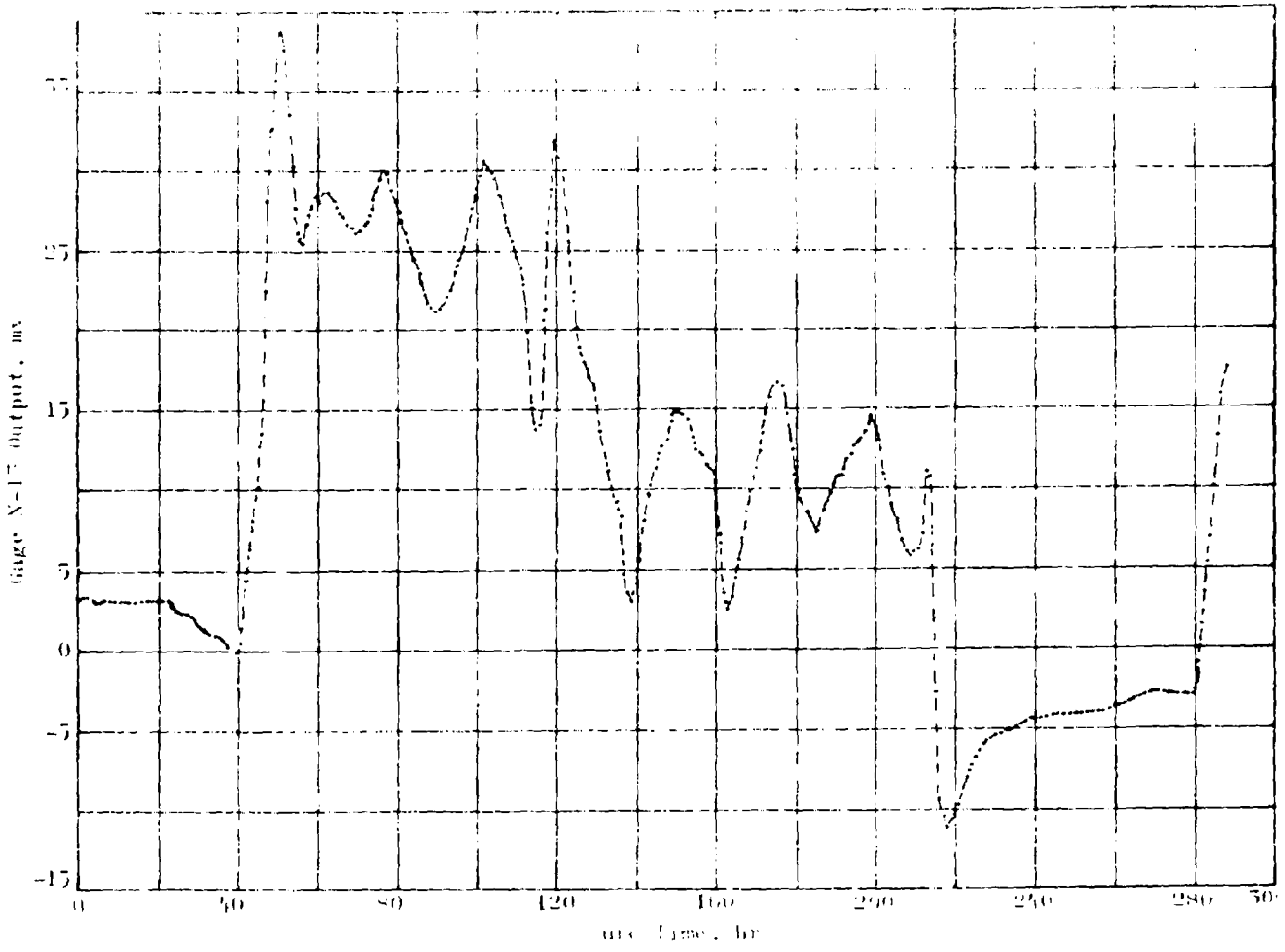

Figure 67. Normal Gage X-17 Core Response

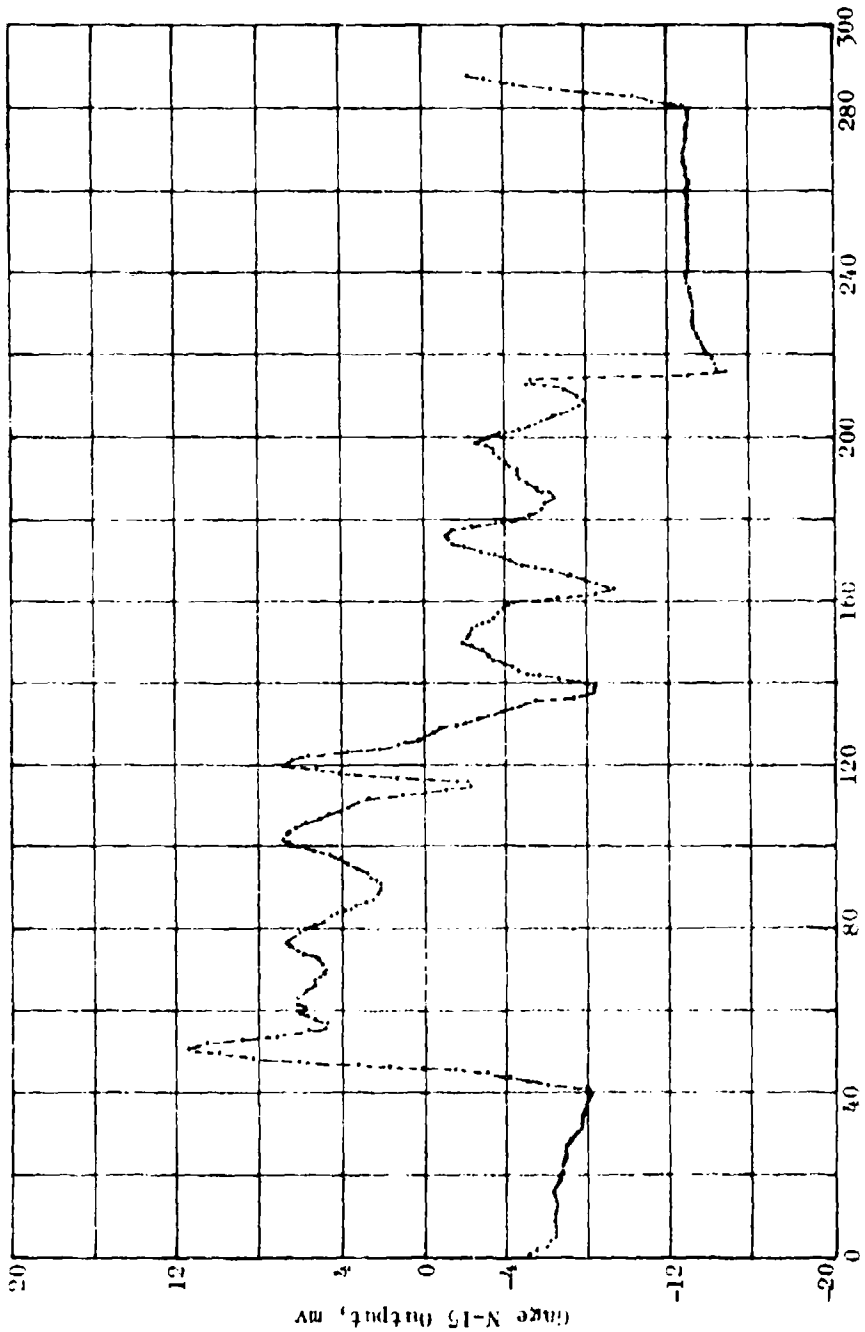

Figure 68. Normal Gage N-15 Cure Response

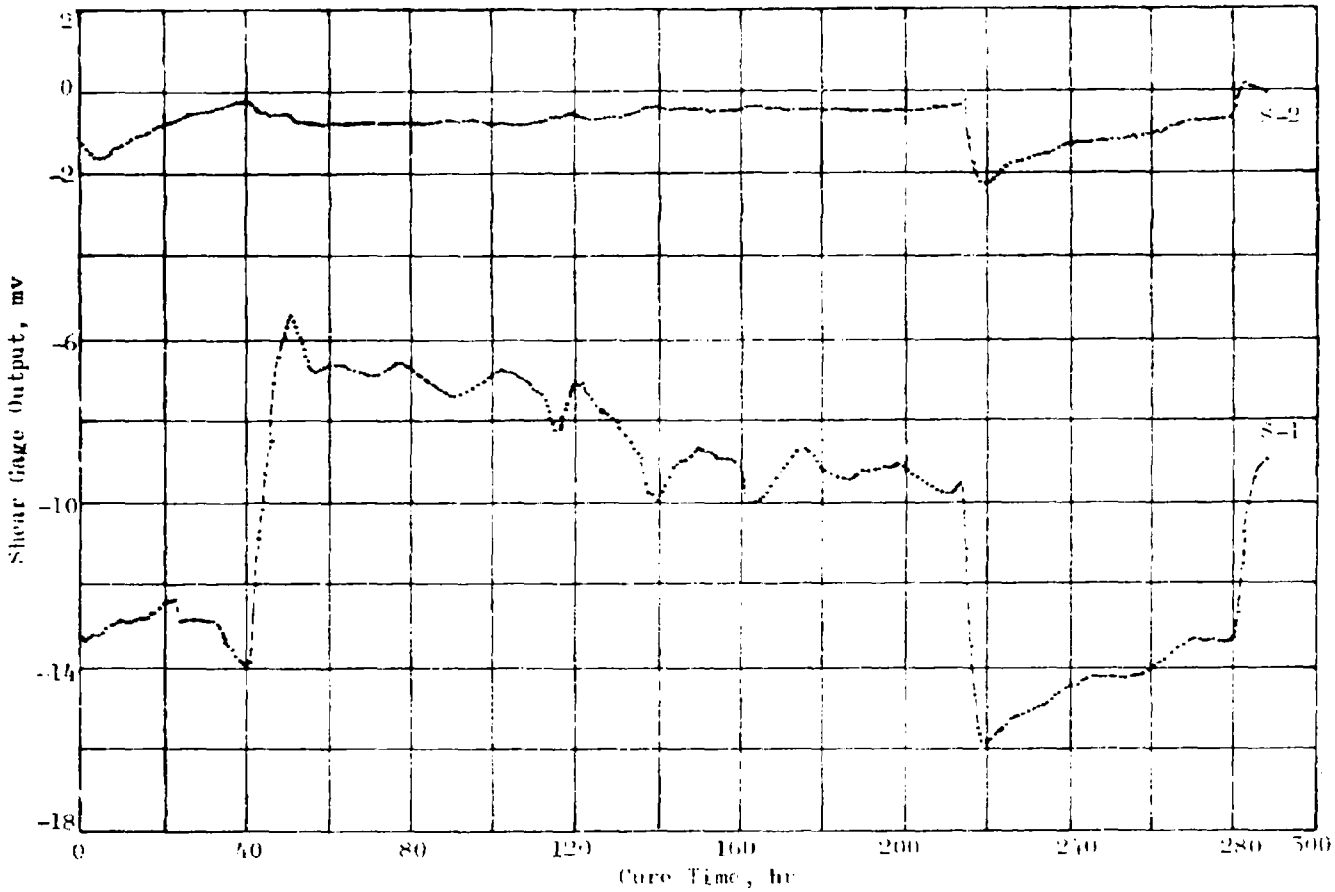

Figure 69. Shear Gage Cure Response

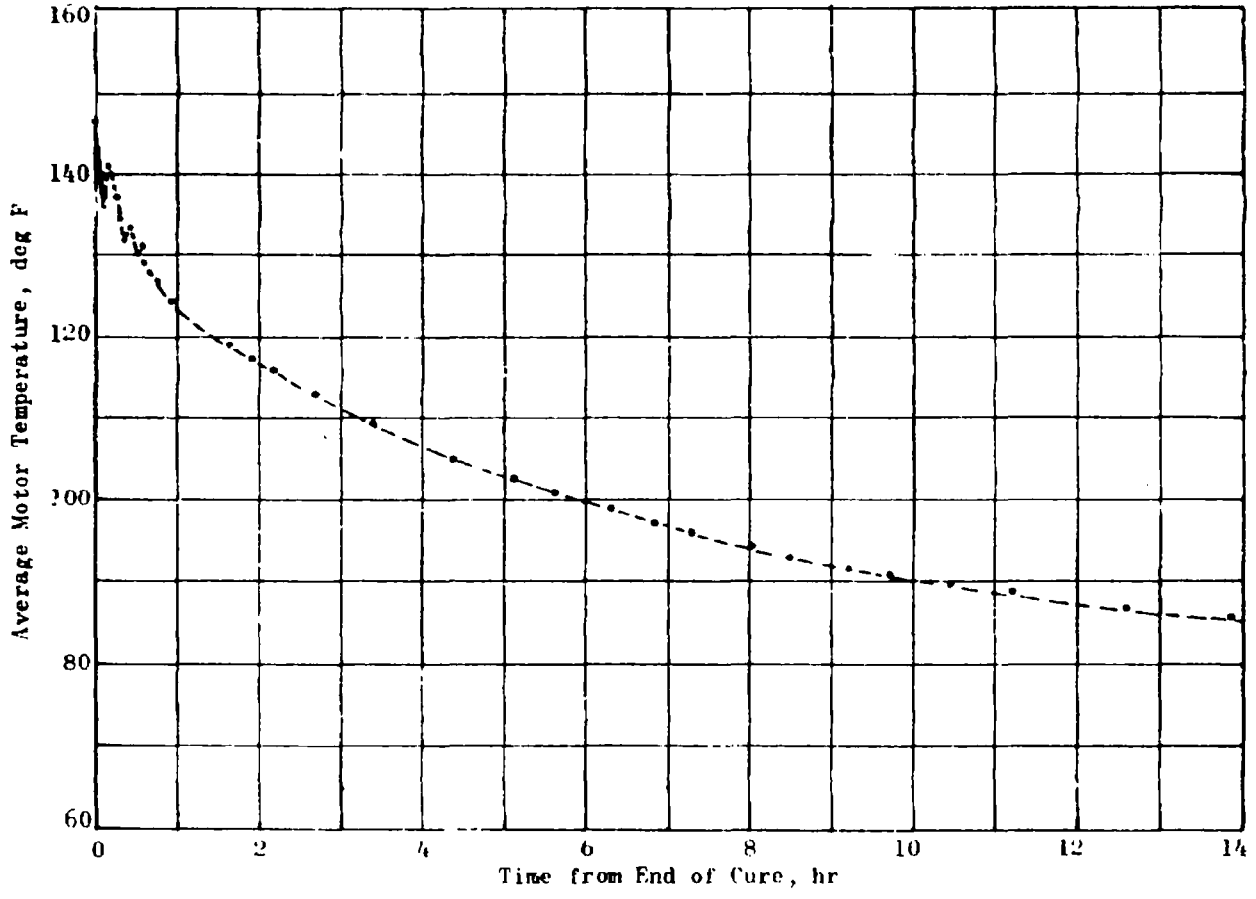

Figure 70. Average Motor Temperature, Postcure Cooldown

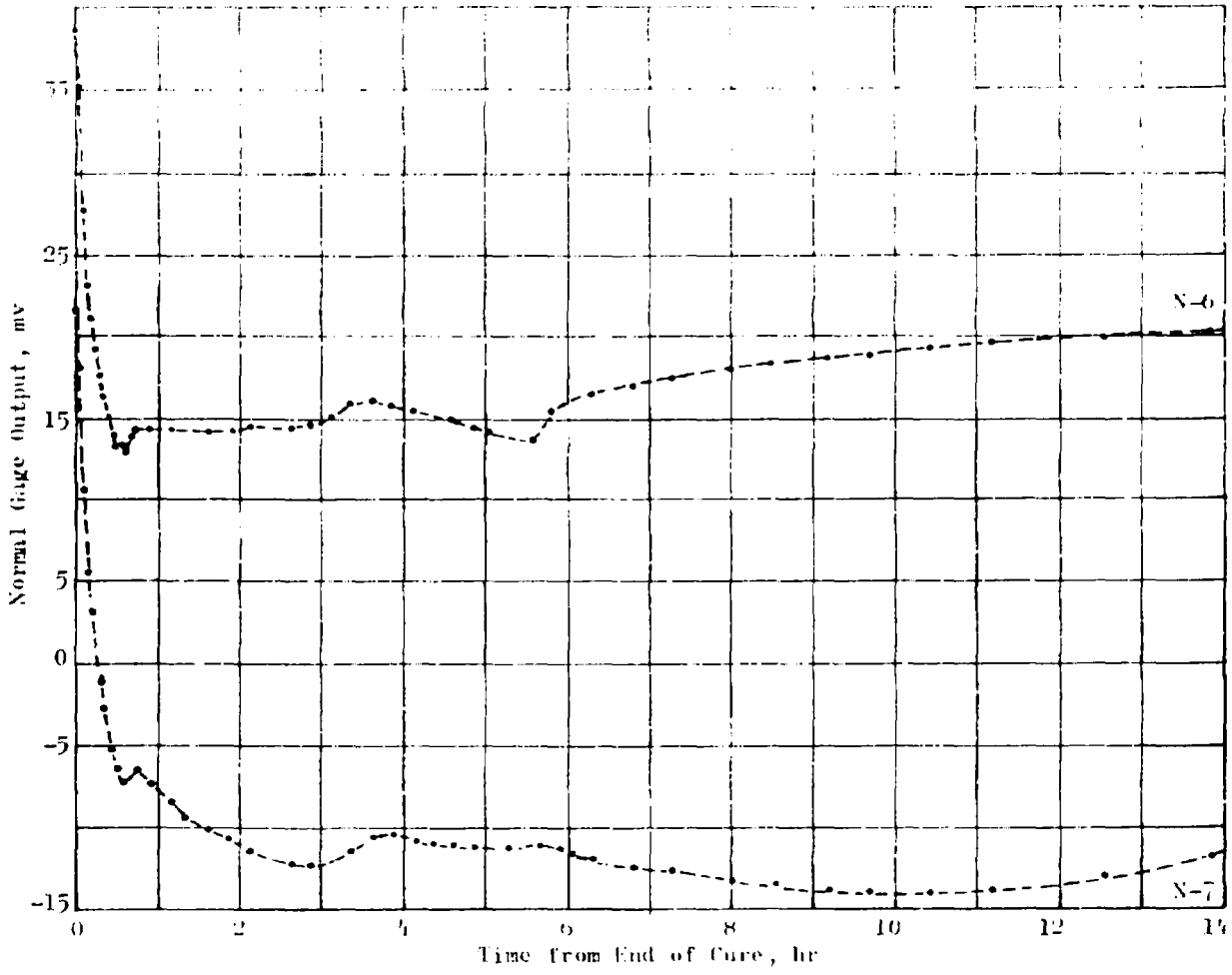

Figure 71. Forward End Normal Gage Response During Postcure Cooldown

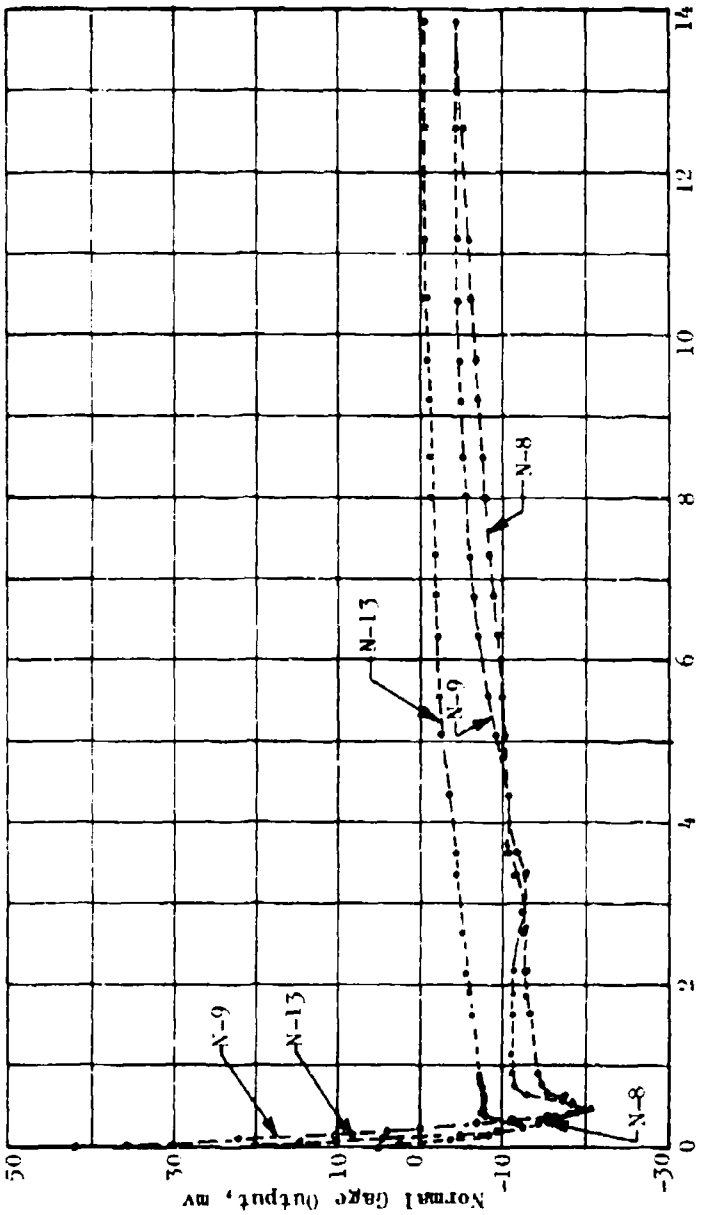

Figure 72. Center Plane Normal Gage Response During Postcure Cooldown

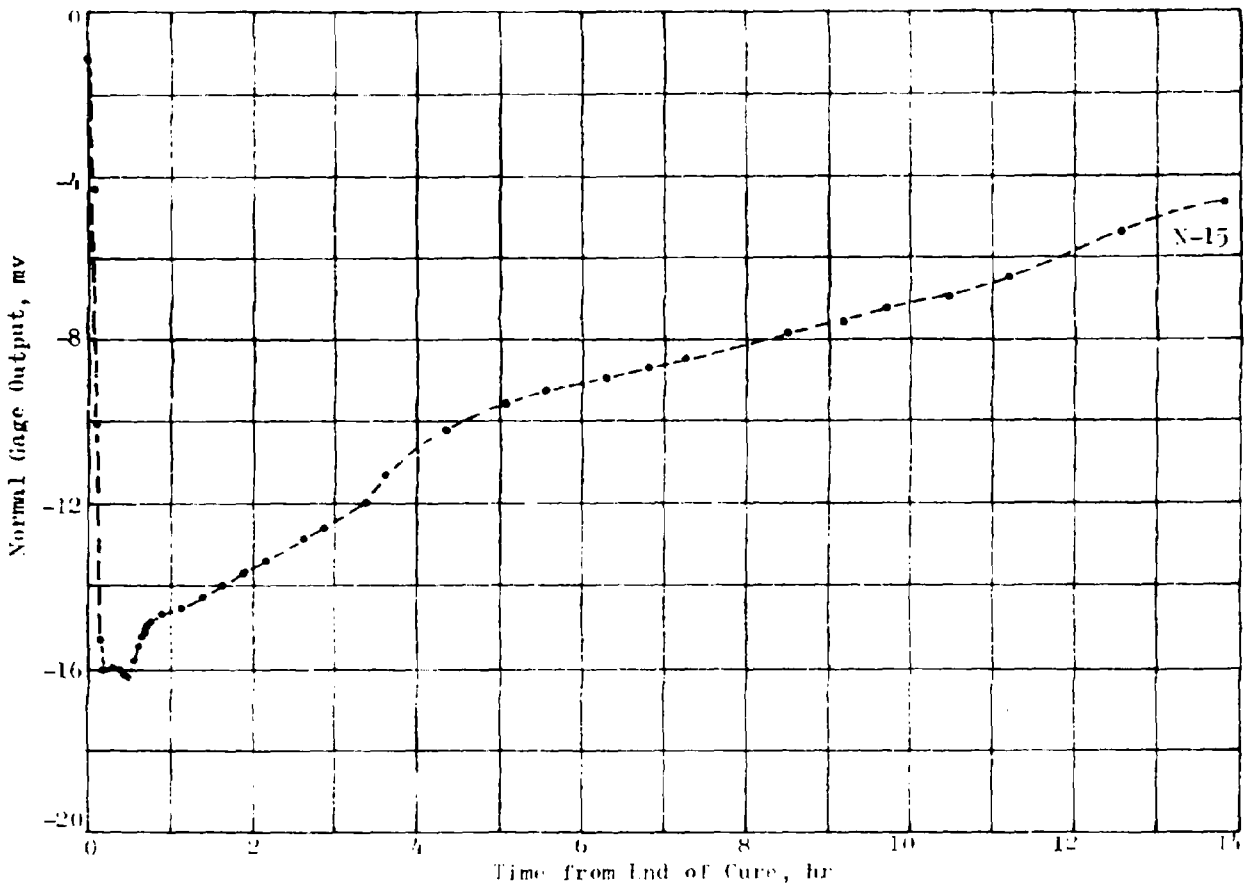

Figure 73. Aft End Normal Gage Response During Postcure Cooldown

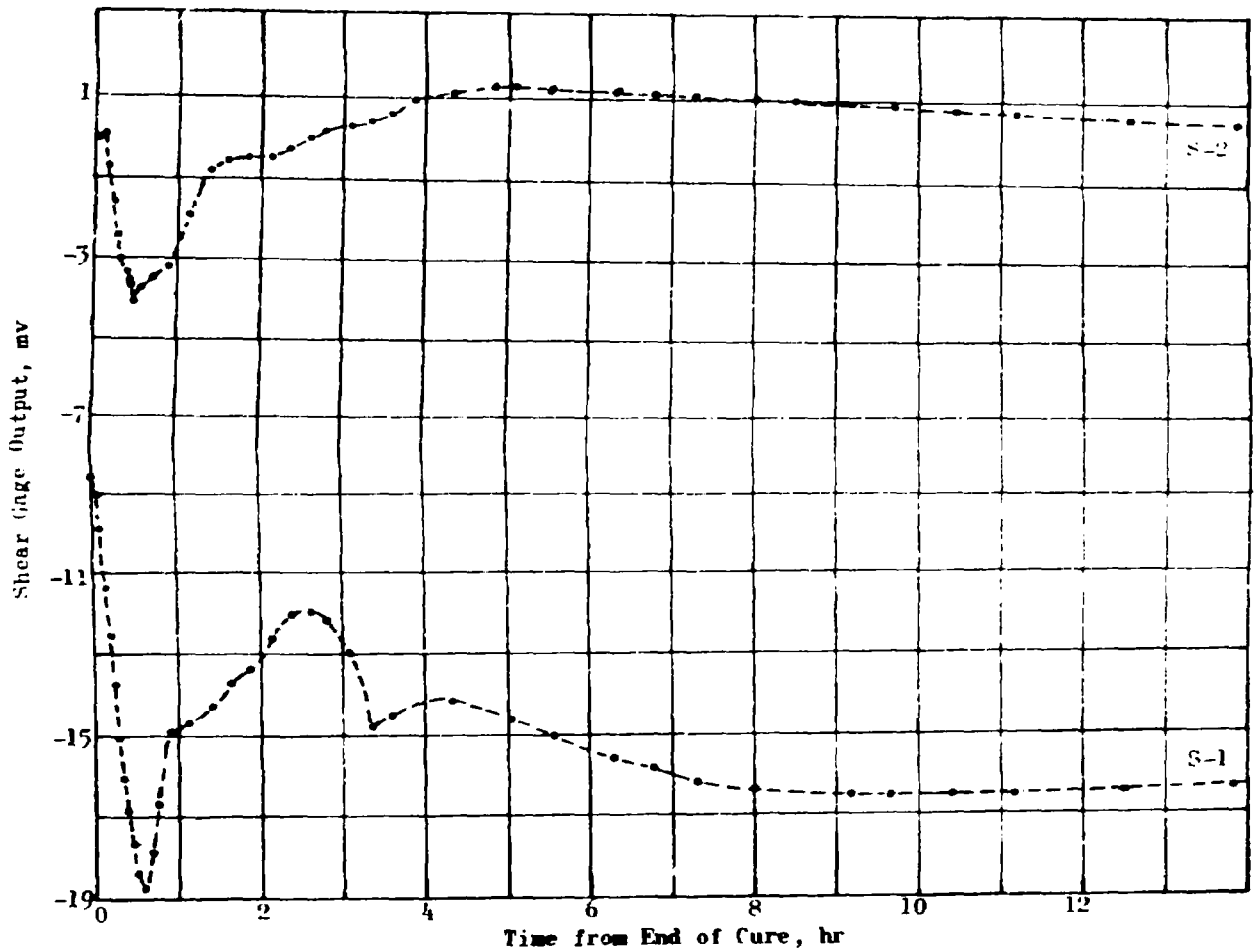

Figure 74. Shear Gage Response During Postcure Cooldown

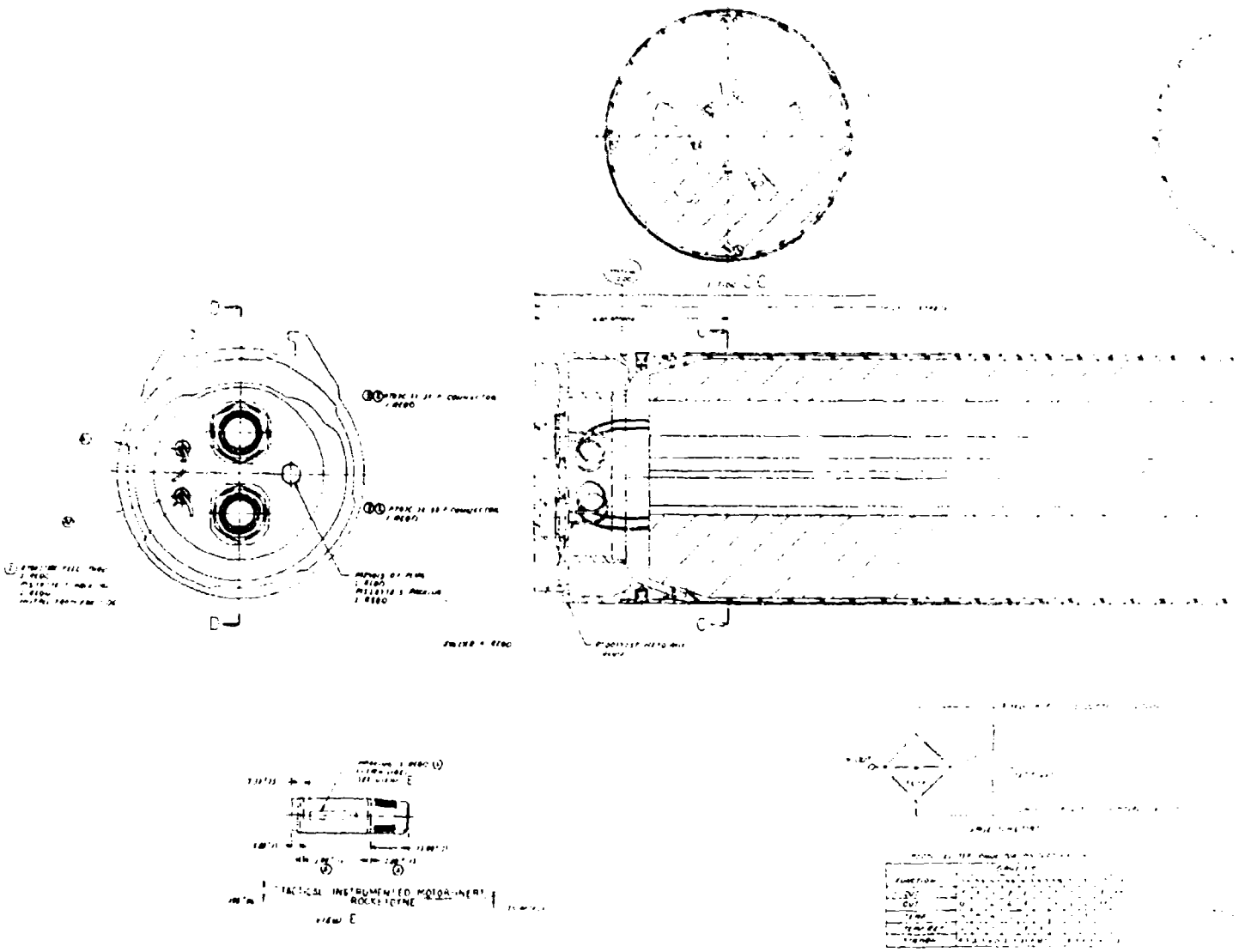

Figure 75. TIM Instrumentation Locations

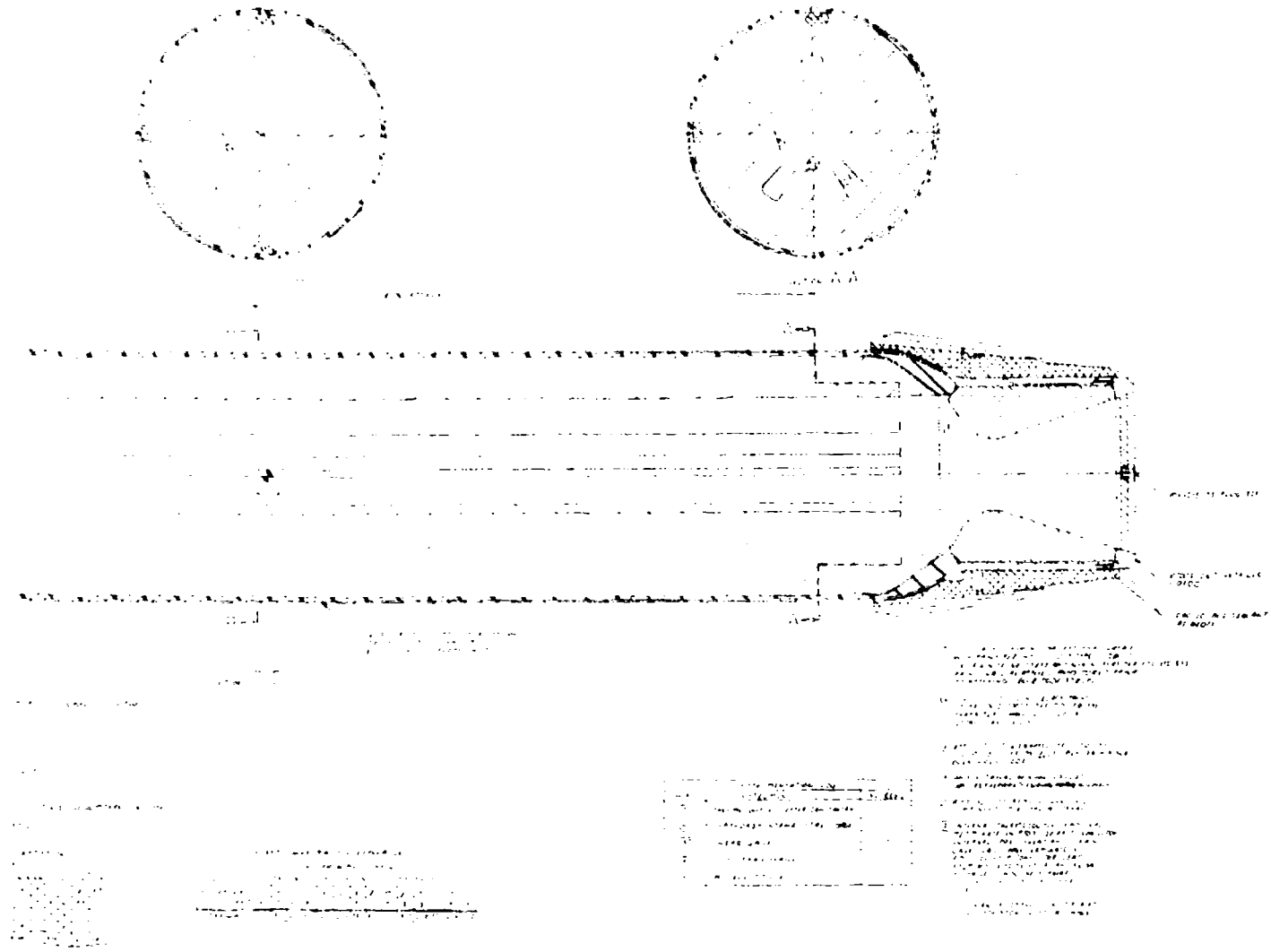

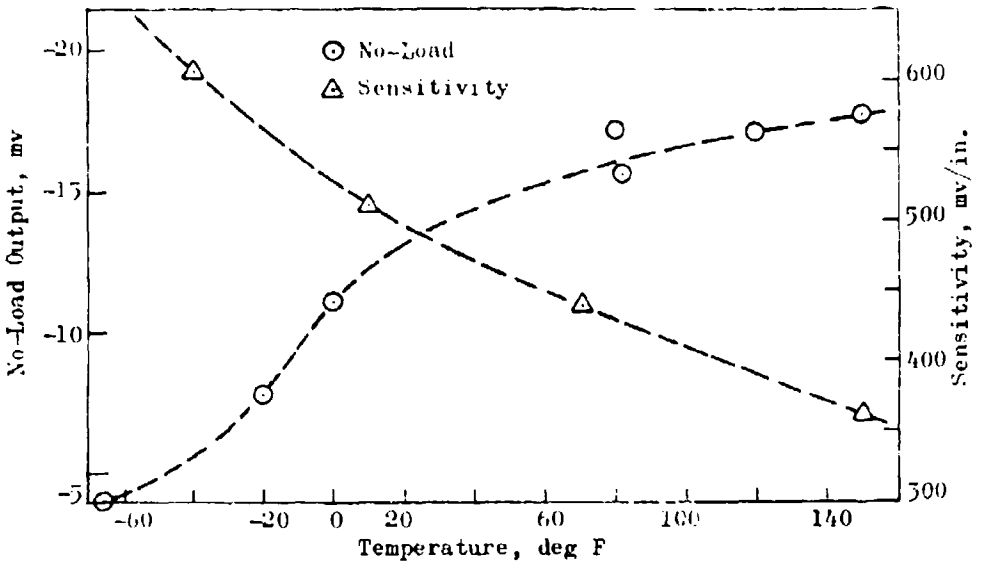

Figure 76. Clip Gage C-4 Calibration

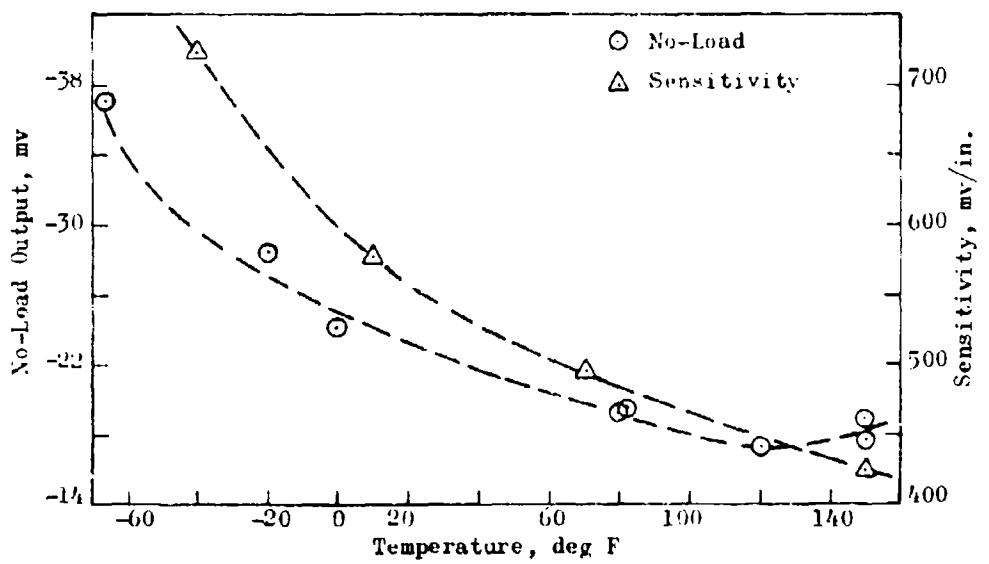

Figure 77. Clip Gage C-5 Calibration

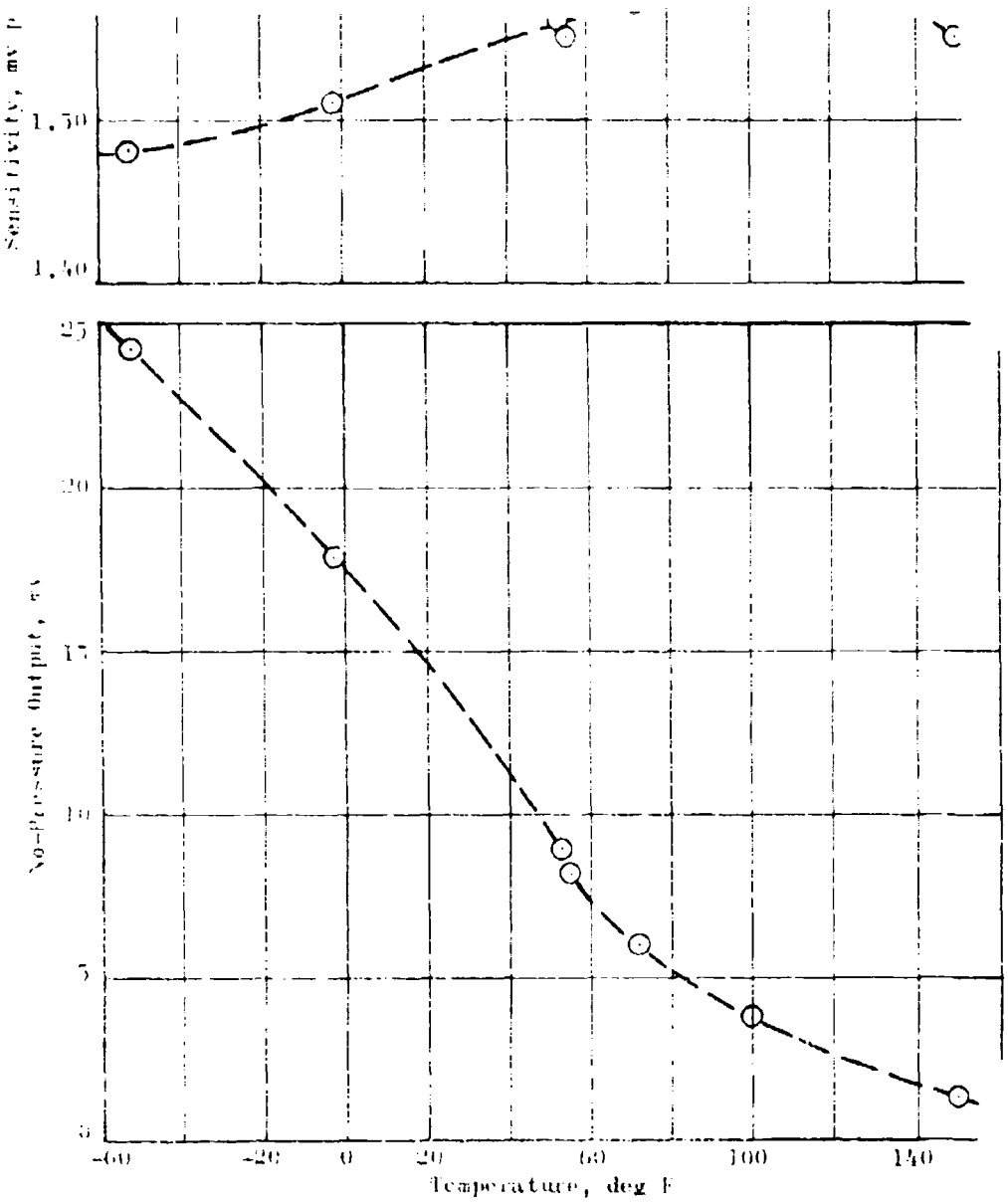

Figure 78. Internal Pressure Gage Response Characterization Data

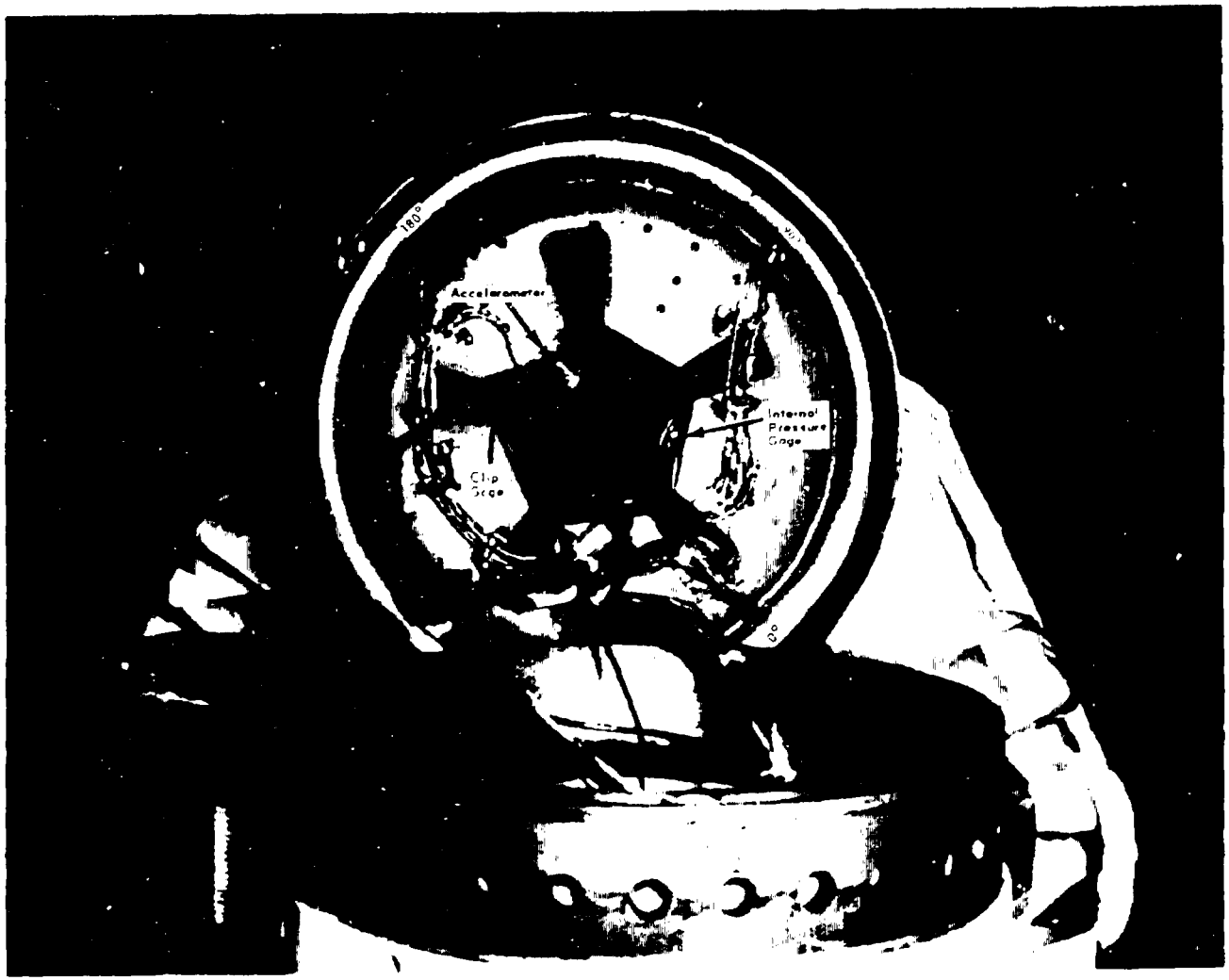
180°
Accelerometer
Internal
Pressure
Gage
Clip
Gage
90°

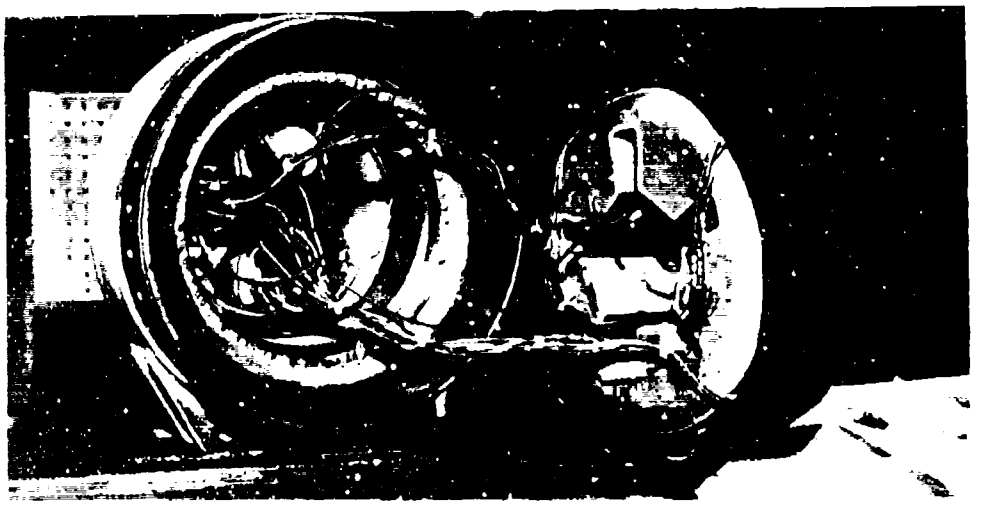

76-217

Figure 80. Cable Connections on TIM

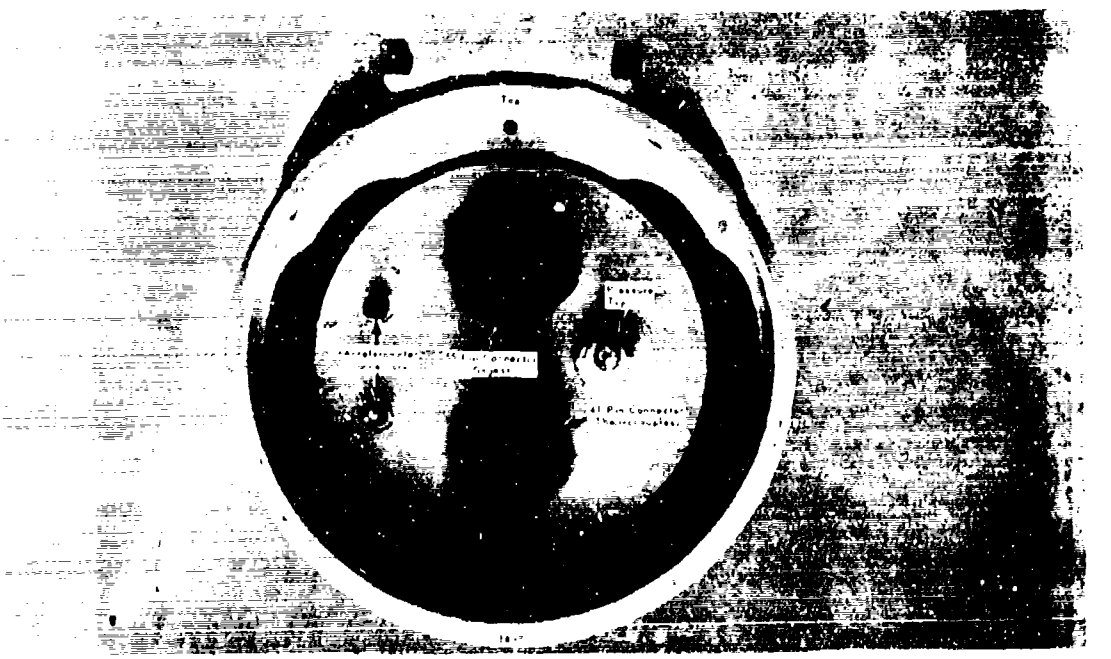

76-214

Figure 81. TIM Forward End Closure

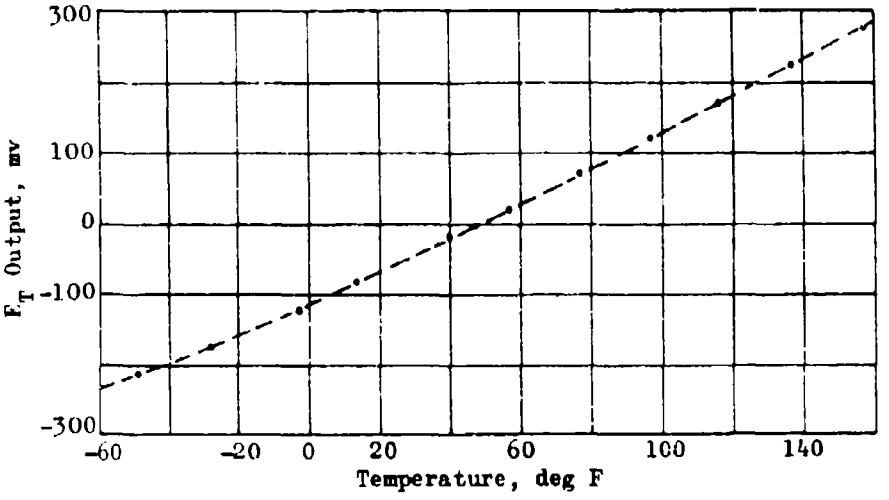

Figure 82. Revised Temperature Response for Gage N-7

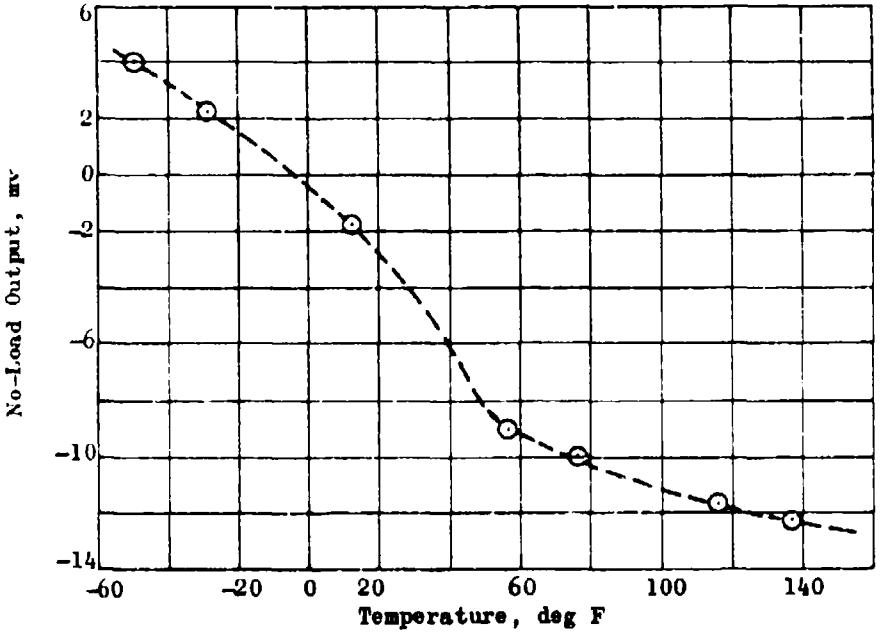

Figure 83. Revised No-Load Output for Gage N-7

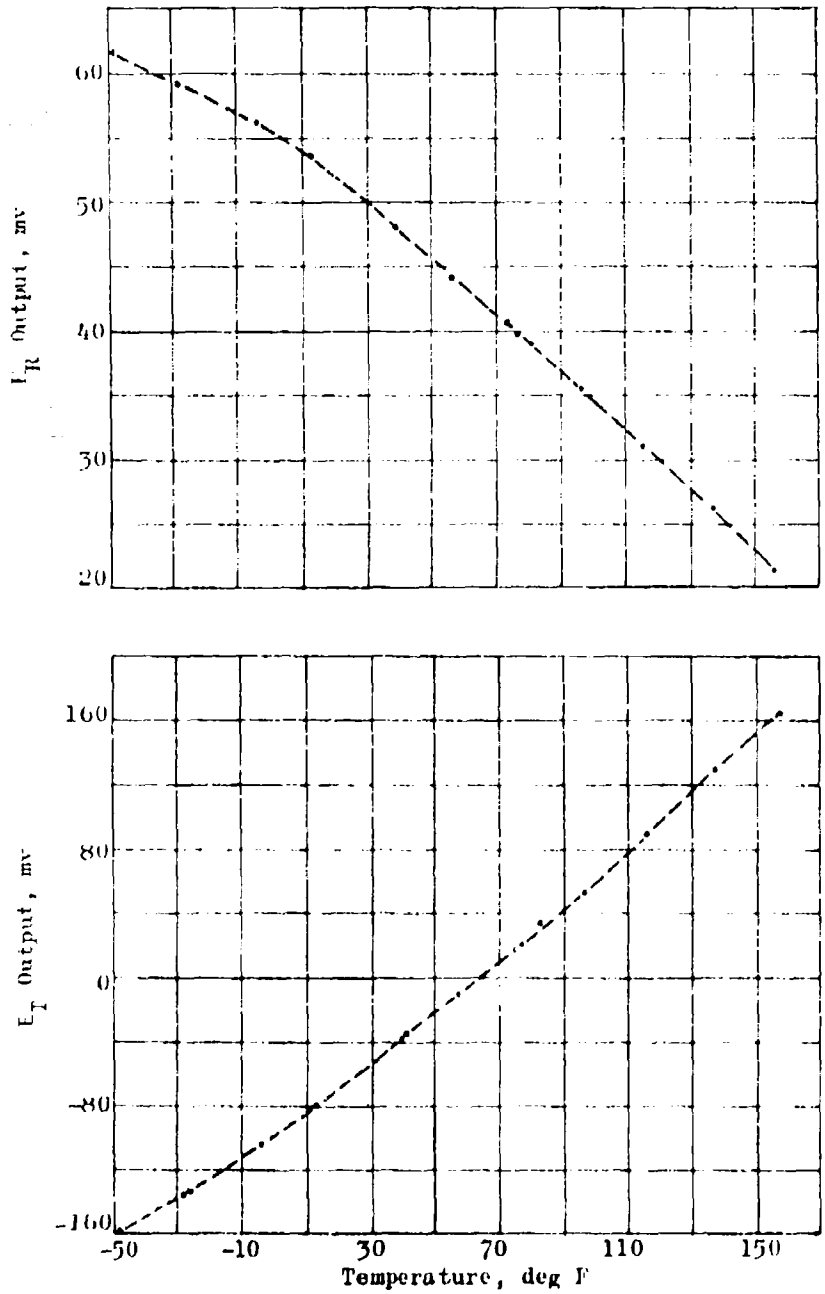

Figure 84. Thermal Cycle Response, Gage N-6

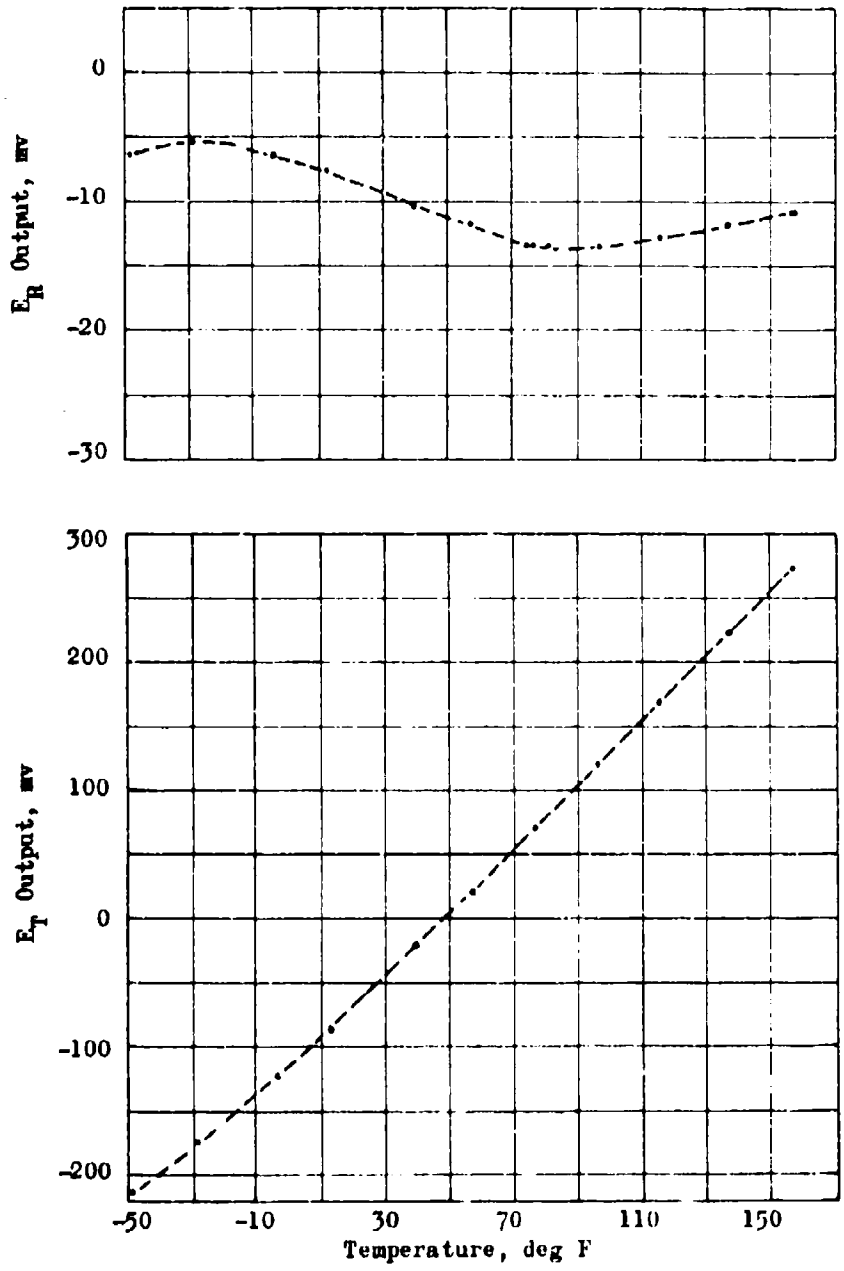

Figure 85. Thermal Cycle Response, Gage N-7

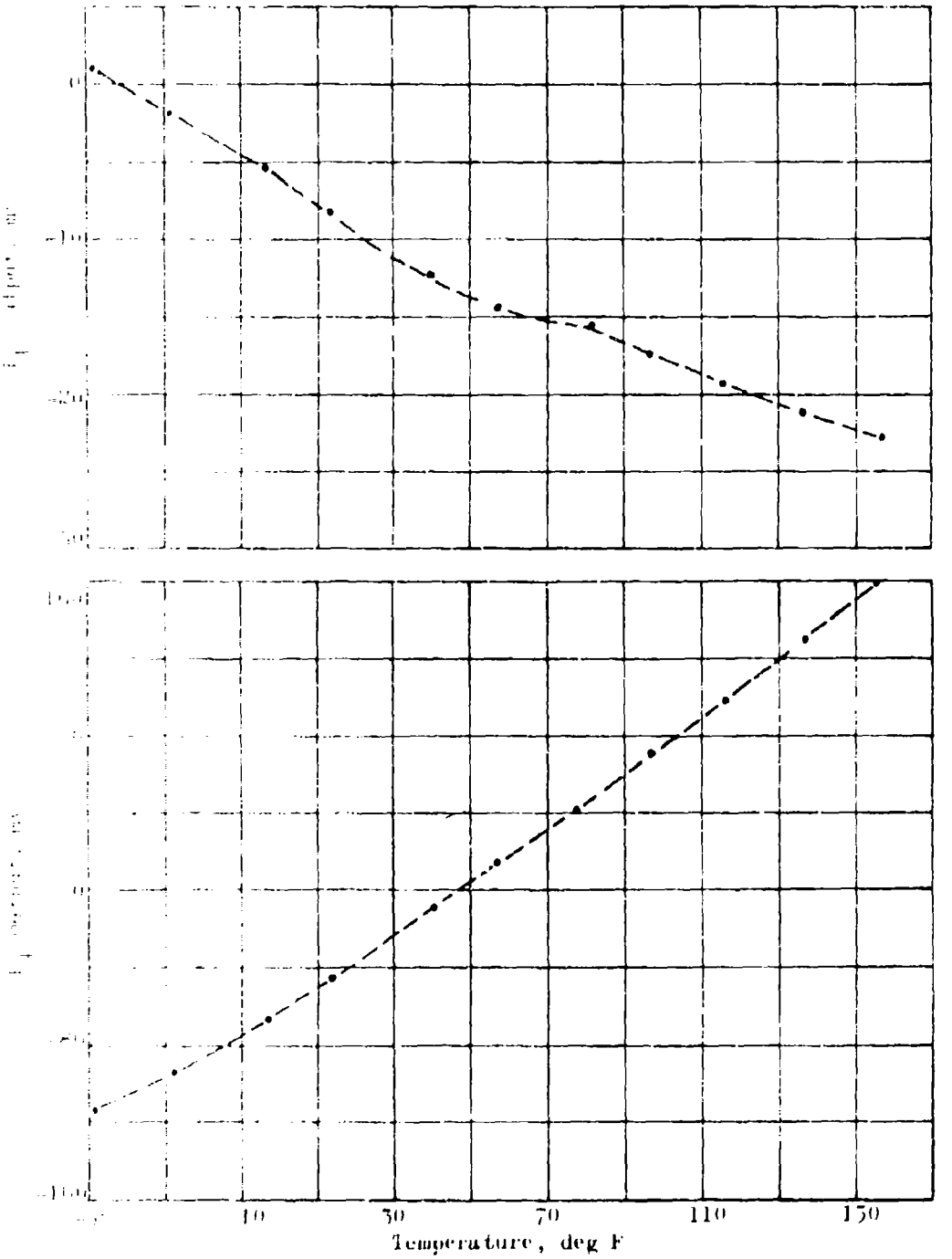

Figure 86. Thermal Cycle Response, Gage N-8

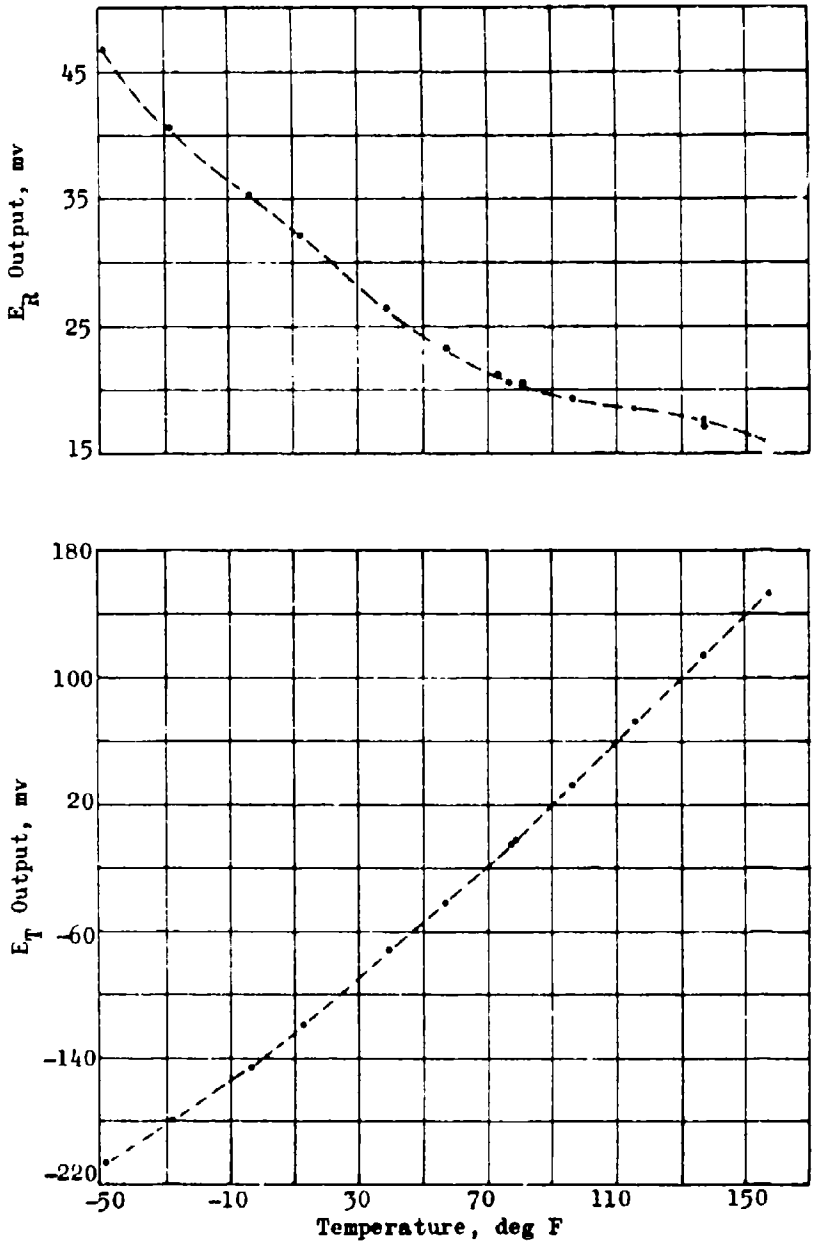

Figure 87. Thermal Cycle Response, Gage N-9

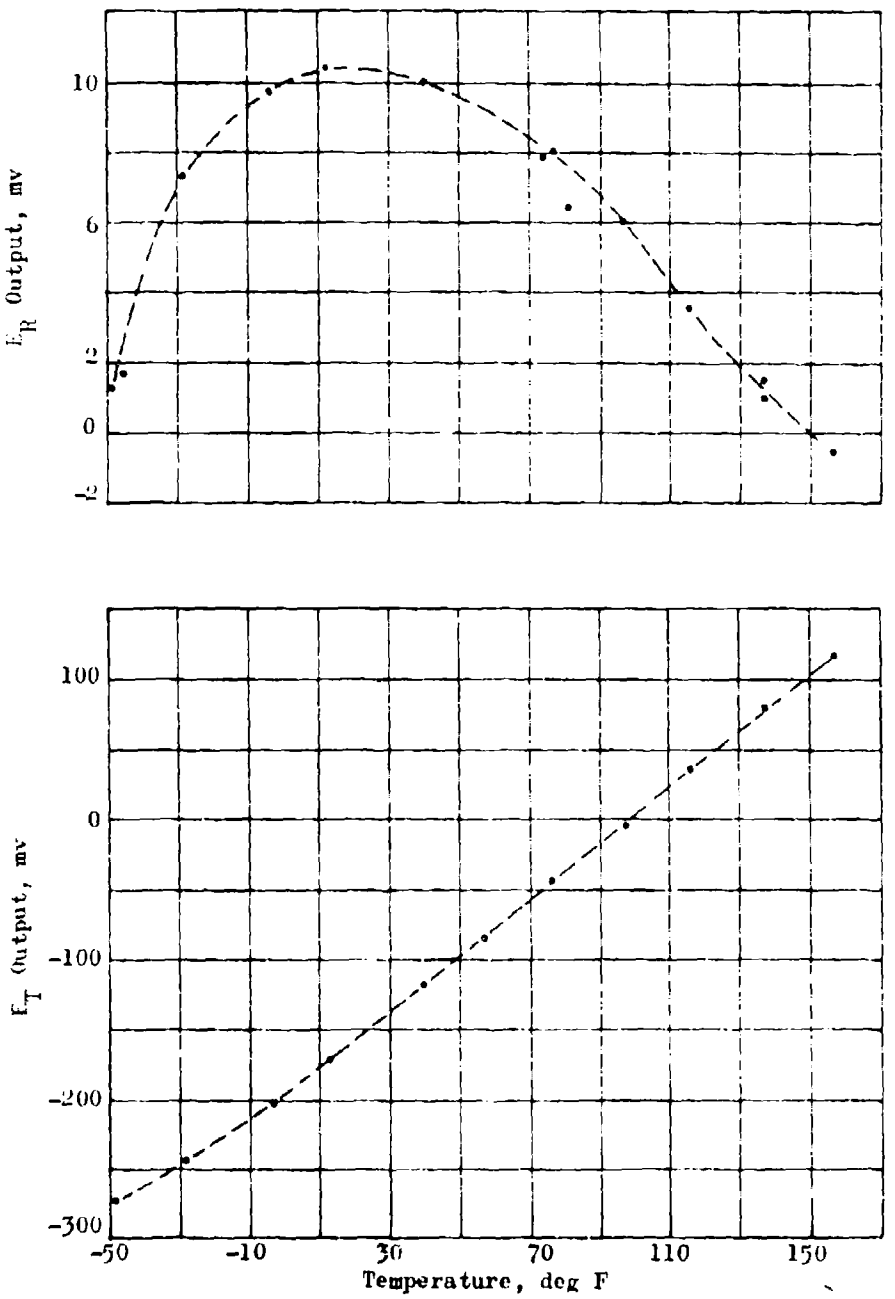

Figure 88. Thermal Cycle Response, Gage N-13

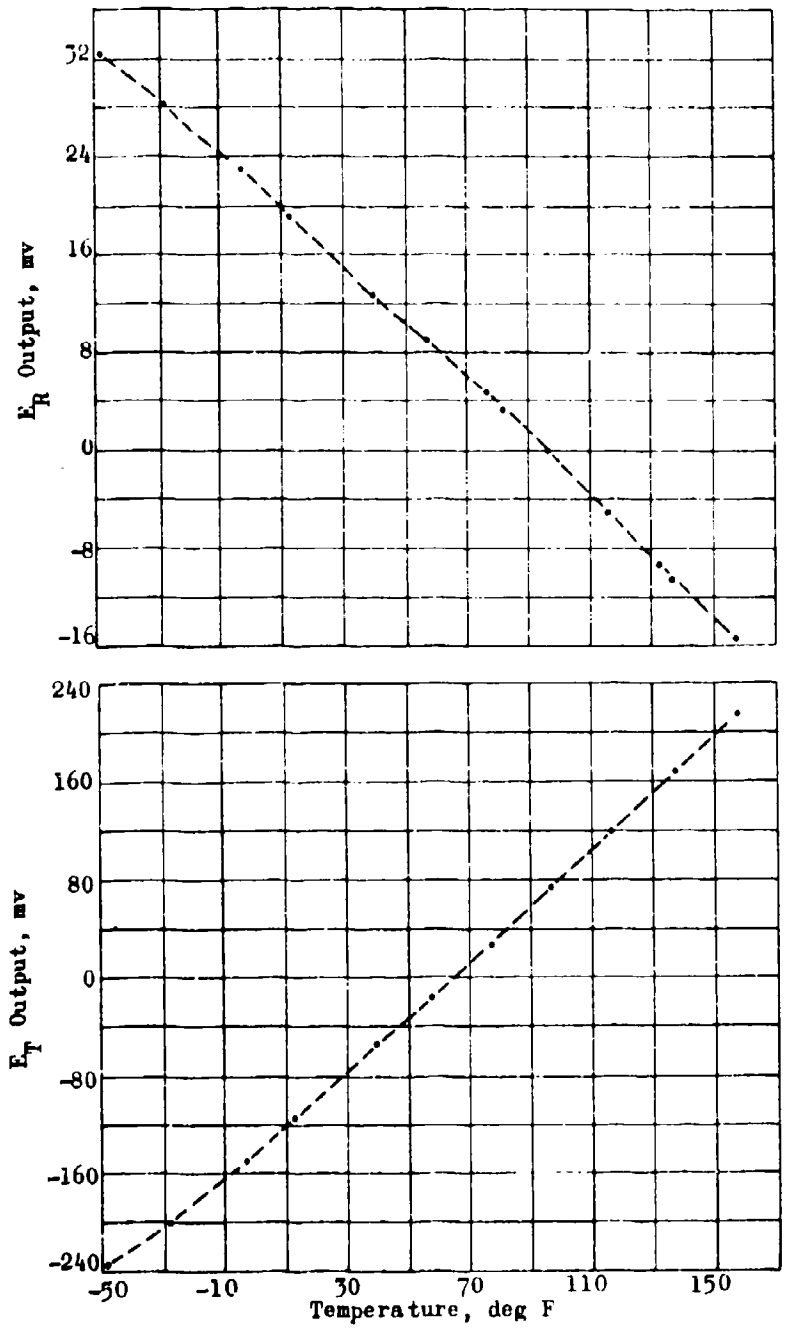

Figure 89. Thermal Cycle Response, Gage N-15

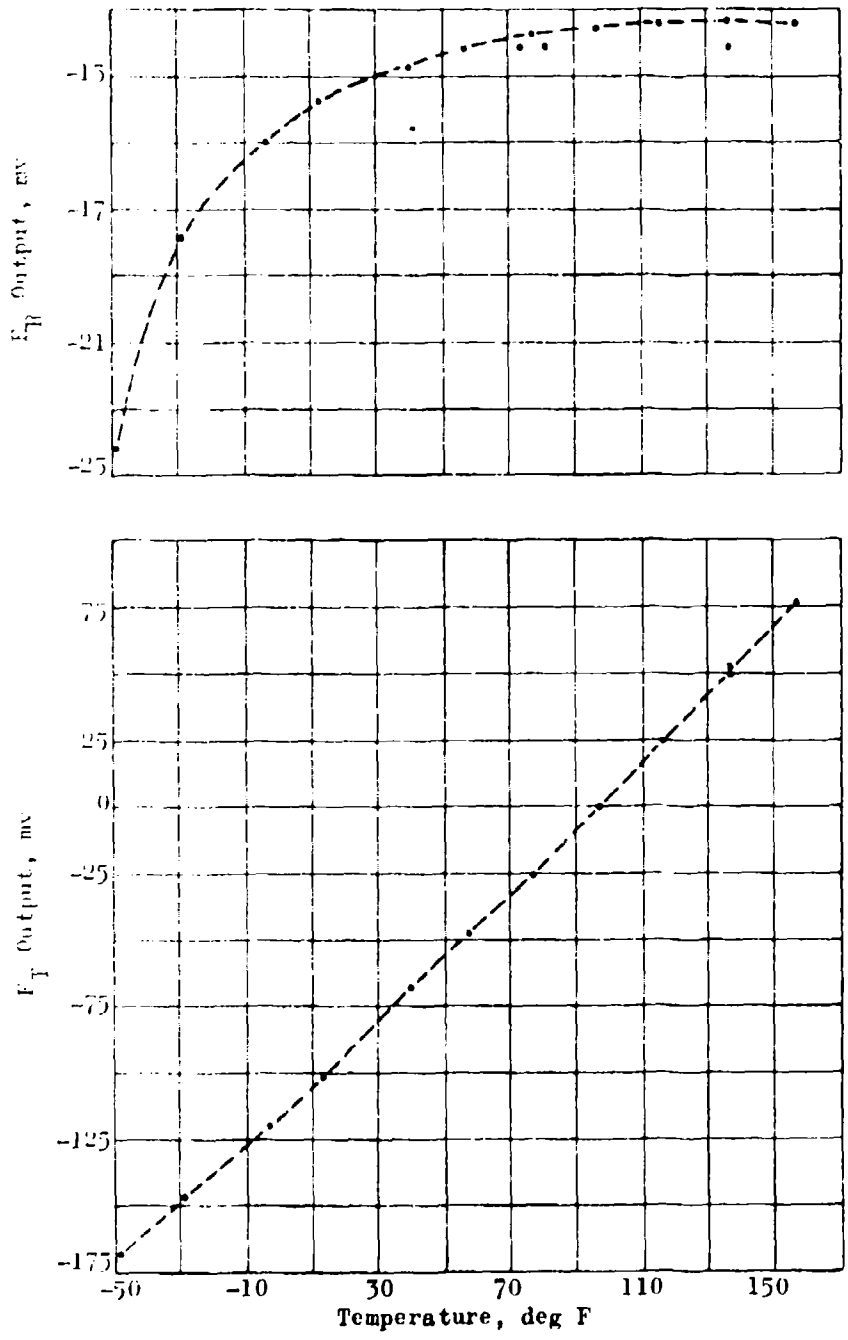

Figure 90. Thermal Cycle Response, Gage S-1

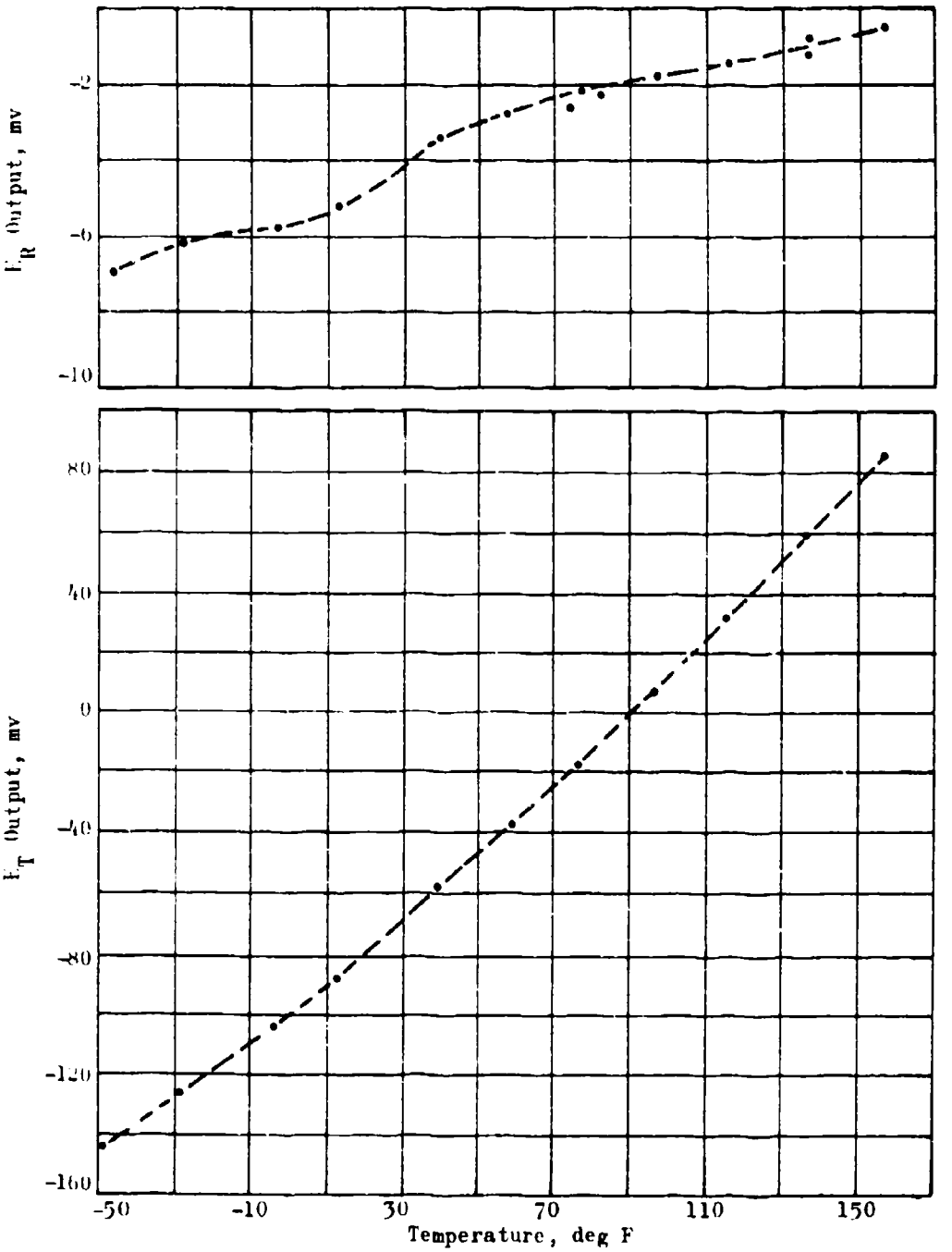

Figure 91. Thermal Cycle Response, Gage S-2

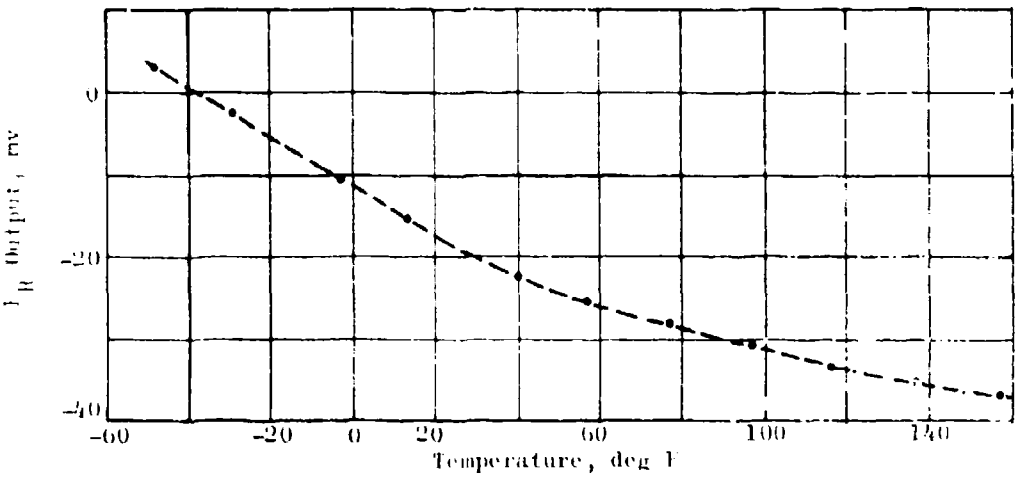

Figure 92. Thermal Cycle Response, Clip Gage C-4

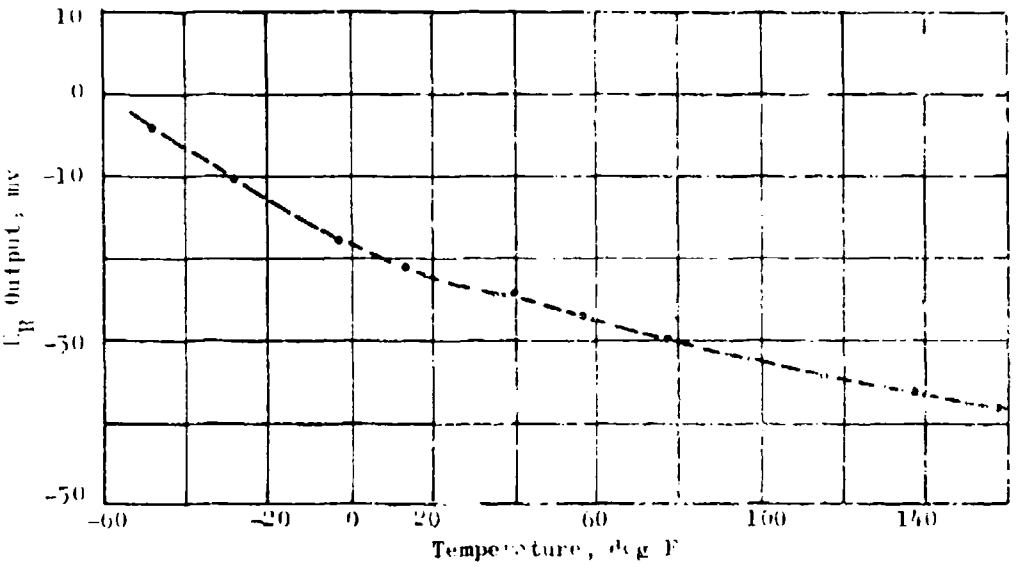

Figure 93. Thermal Cycle Response, Clip Gage C-5

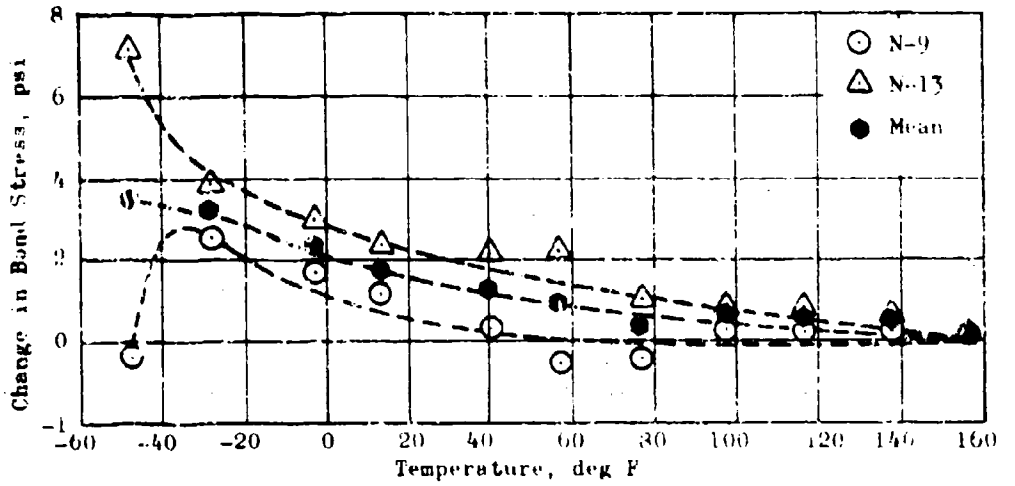

Figure 94. Center Plane Normal Bond Stress

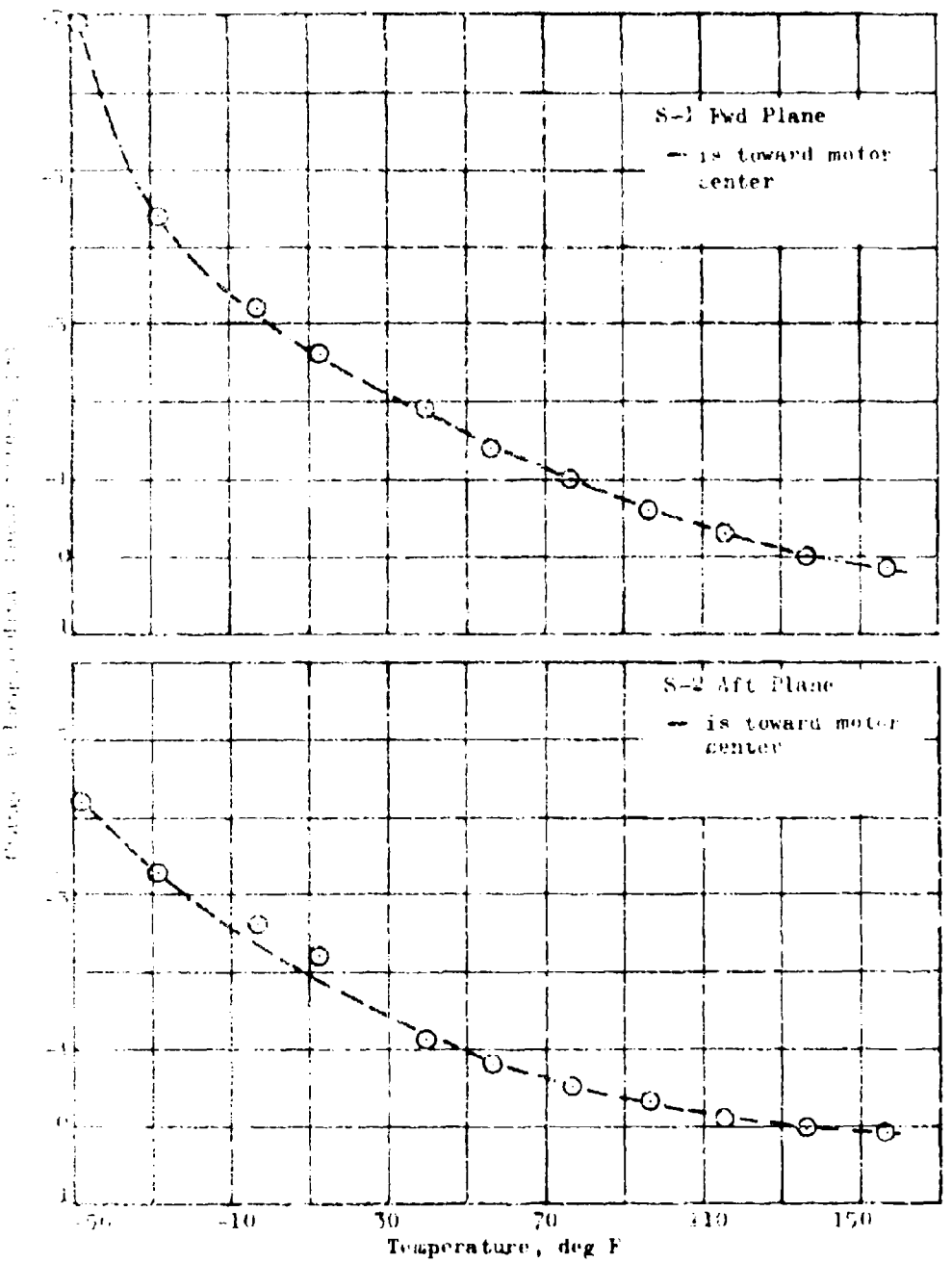

Figure 95. Bond-Line Thermal Shear Stress

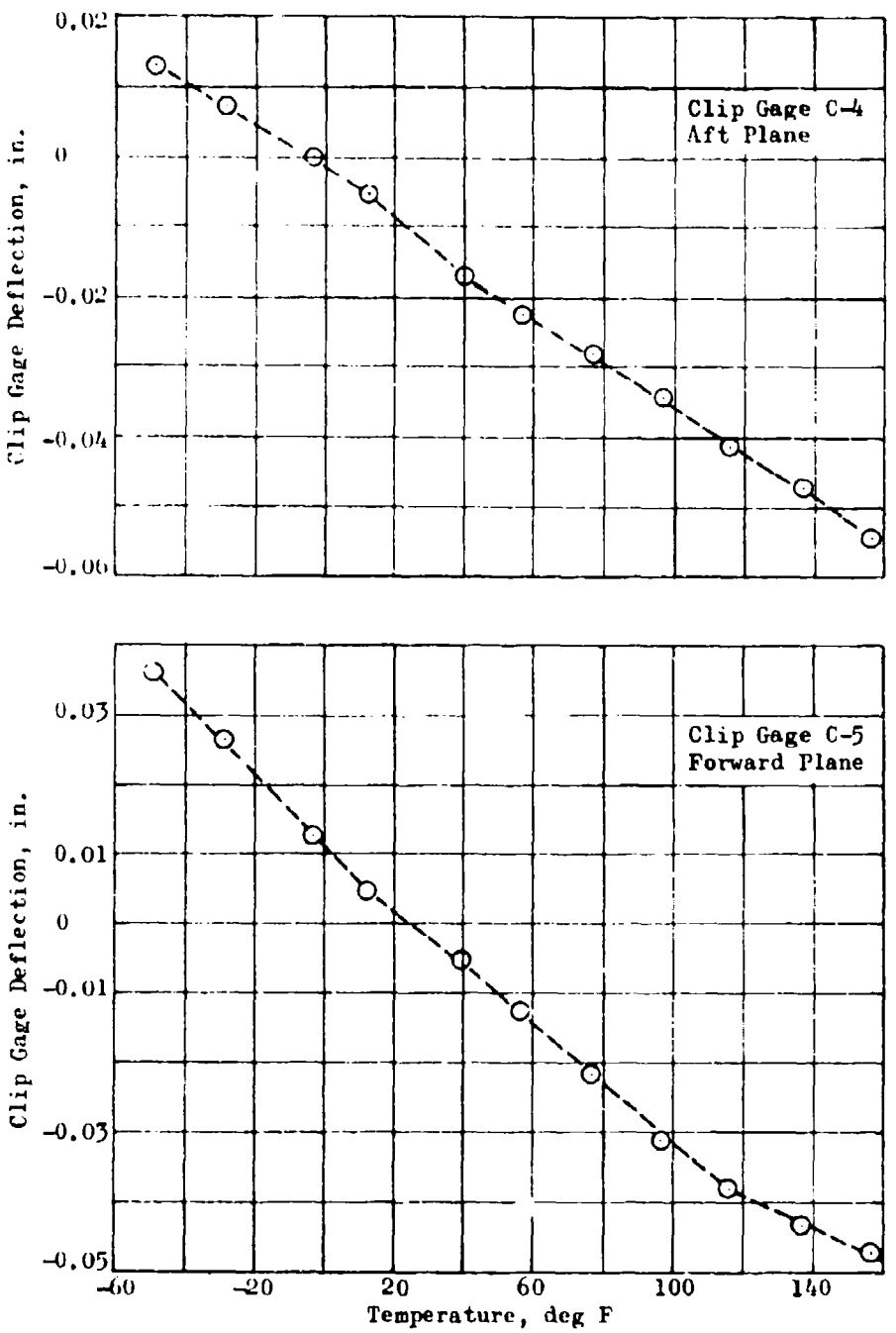

Figure 96. Inner Bore Slot Width Thermal Response

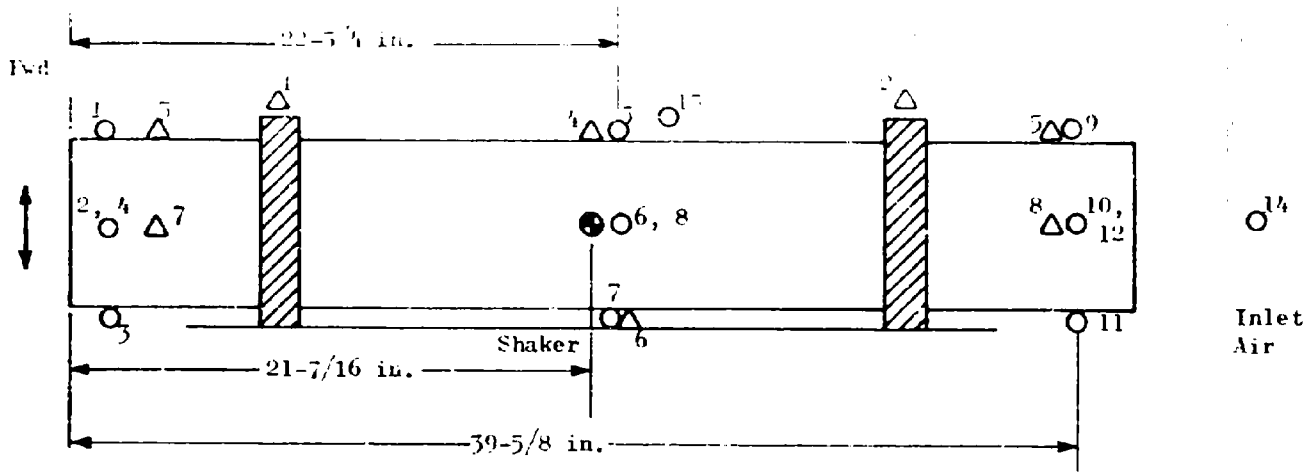

△ Accelerometers (8)
- Shaker (1)
- Control (2), avg of input at attach bands
- Internal (2), as installed
- External (3), adjacent to internal accelerometers and in line at cg

○ Thermocouples (14)
- Inlet Air (1)
- Chamber air near cg (1)
- 90° around motor at 1--2 inches from fwd and aft end and at cg (12)
- Use avg of 4 at aft end for control target in aeroheat

Other Internal Gages: DC - 11 stress/strain gages
9 thermal gage outputs
13 thermocouples

AC - 10 stress/strain gages

Figure 97. TIM Dynamic Test Instrumentation

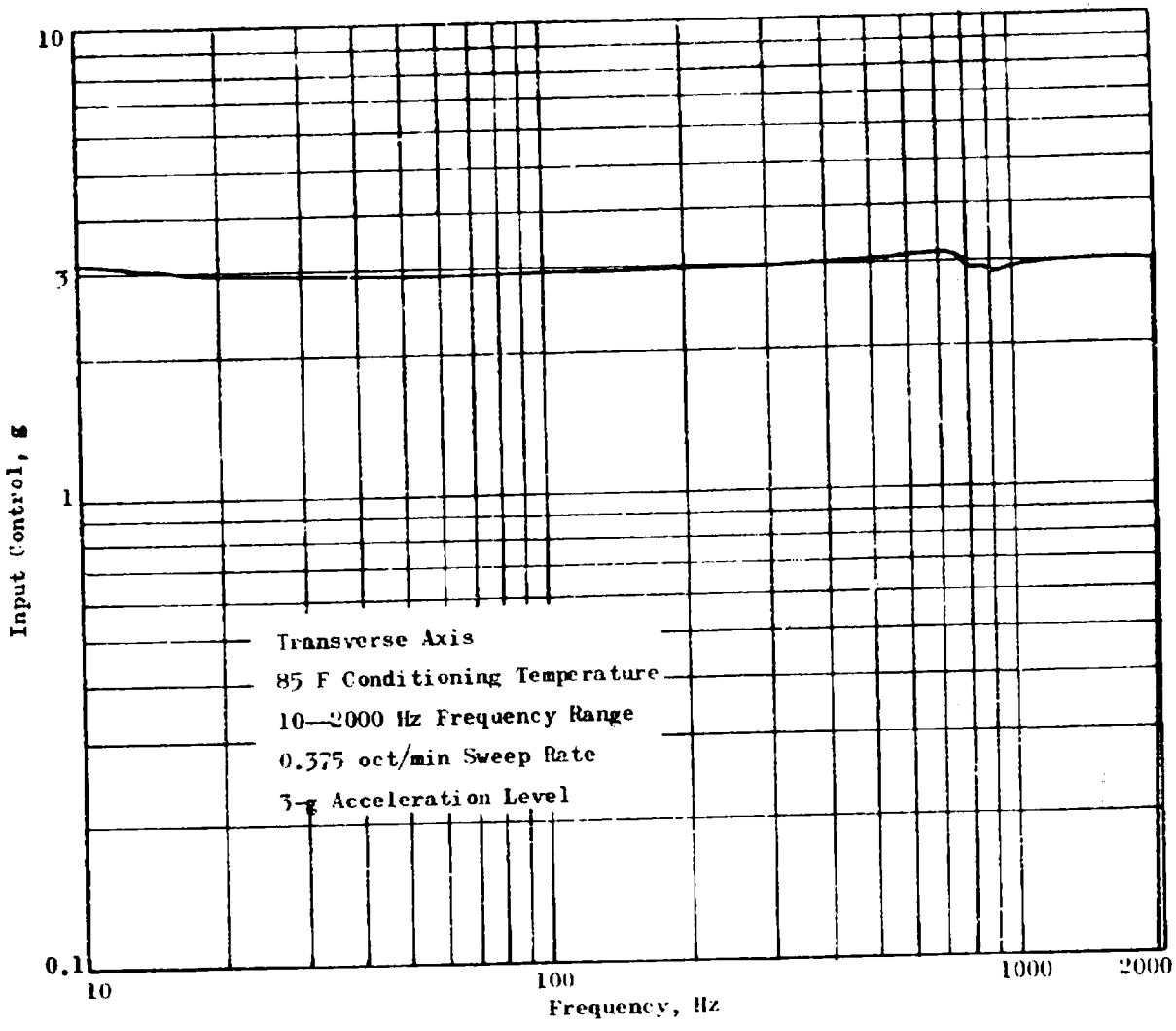

Figure 98. Ambient Sine Sweep Data, Averager Channel

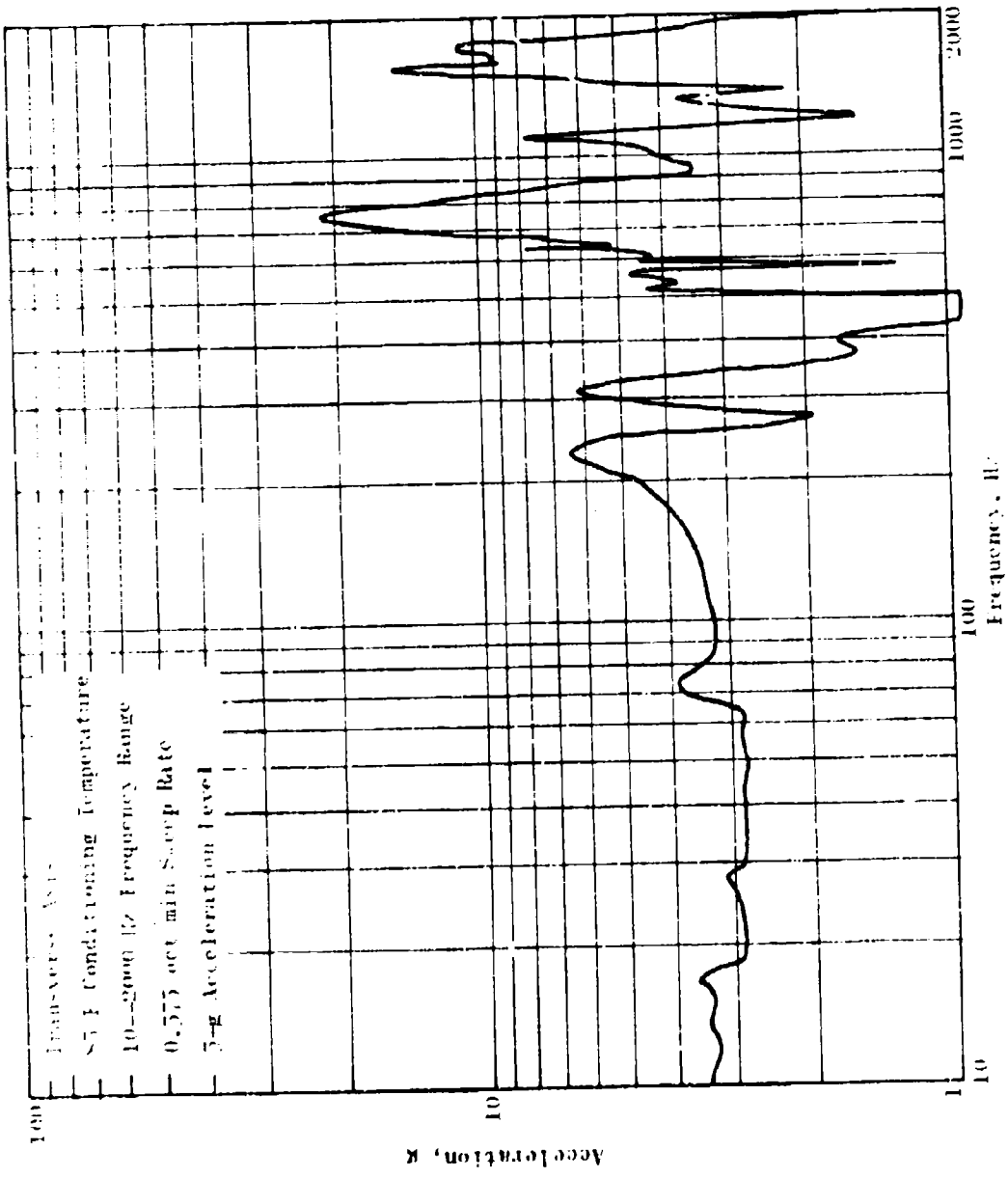

Figure 90. Ambient Sine Sweep Data, Channel A-7

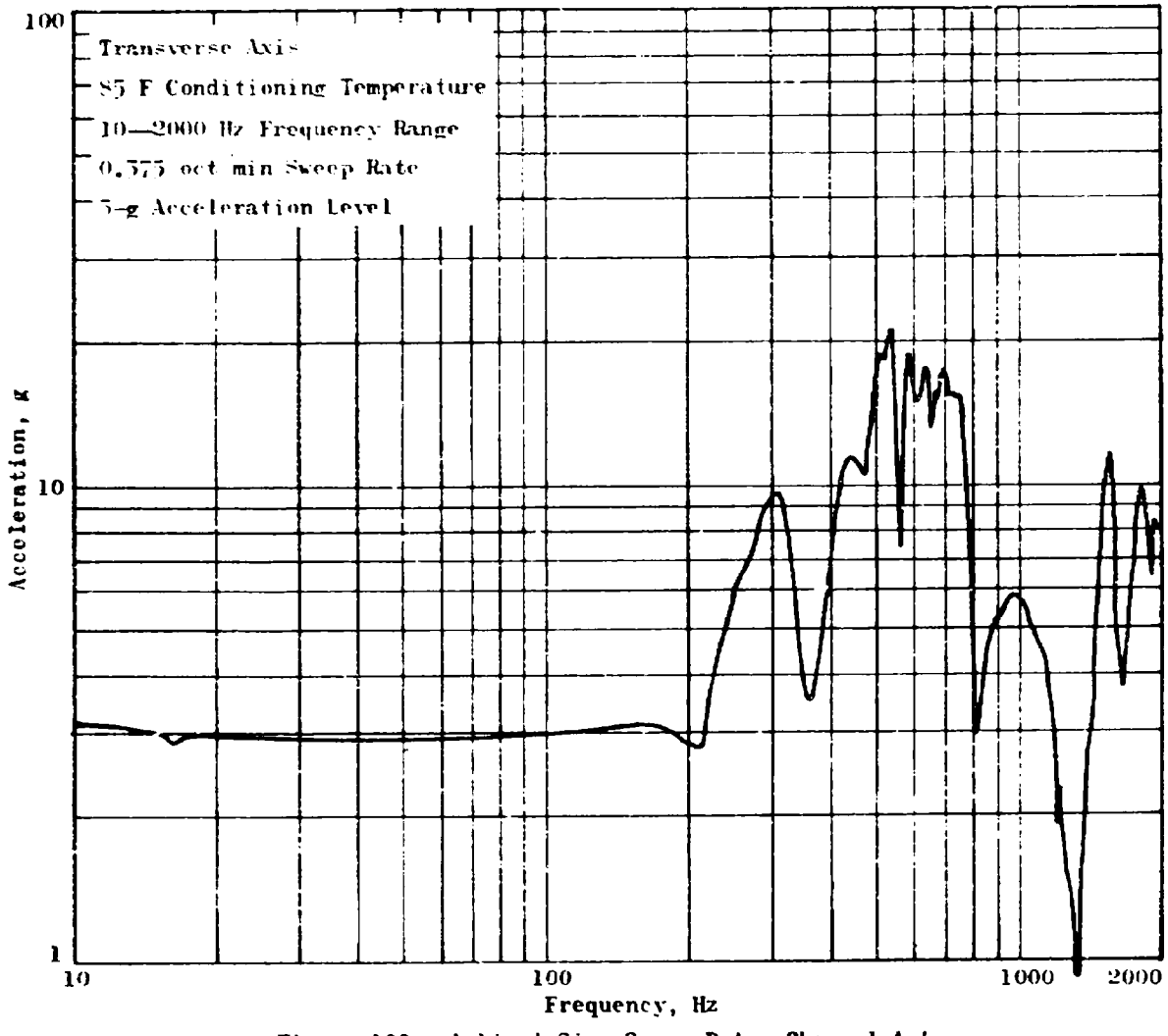

Figure 100. Ambient Sine Sweep Data, Channel A-4

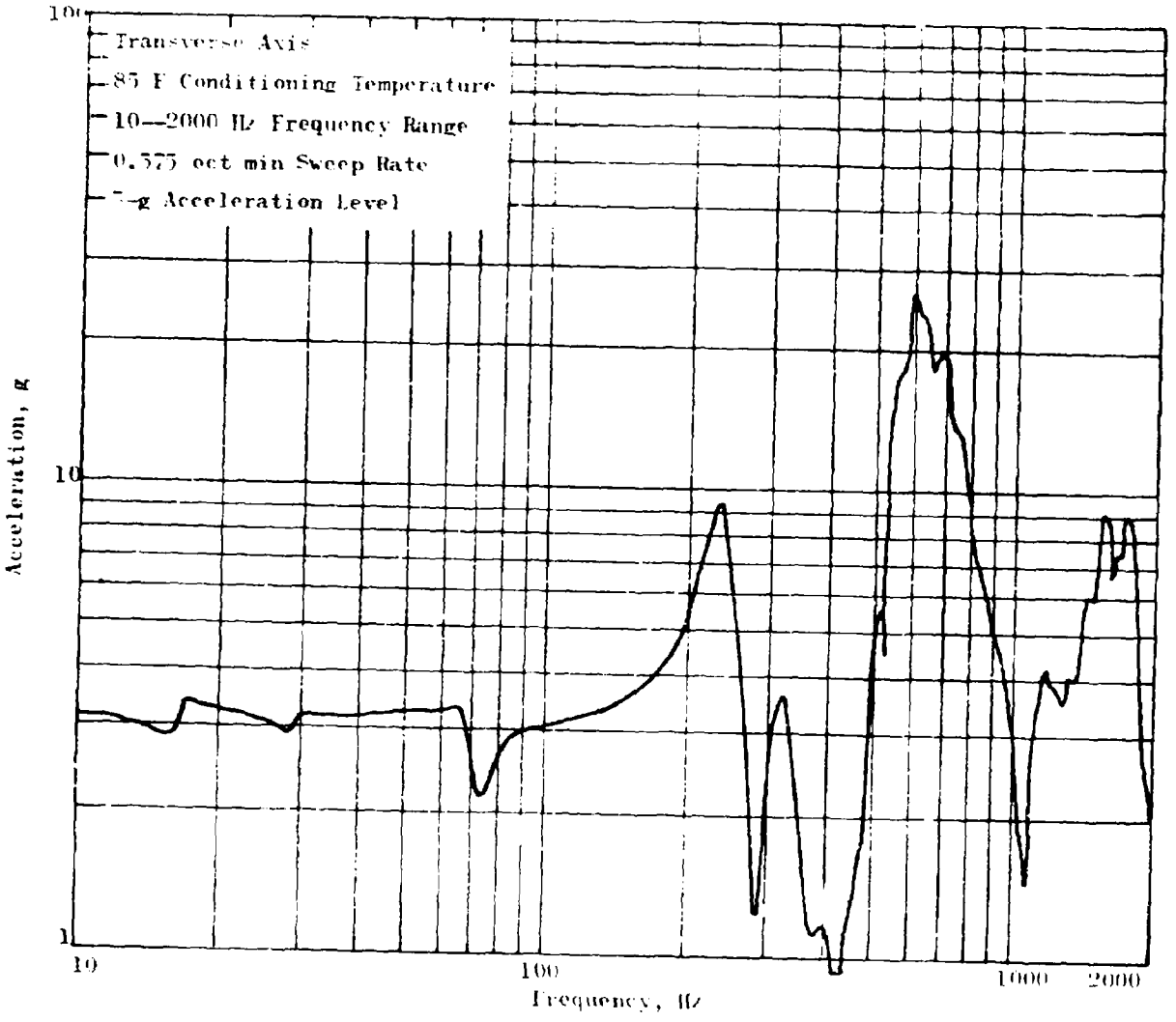

Figure 101. Ambient Sine Sweep Data, Channel A-5

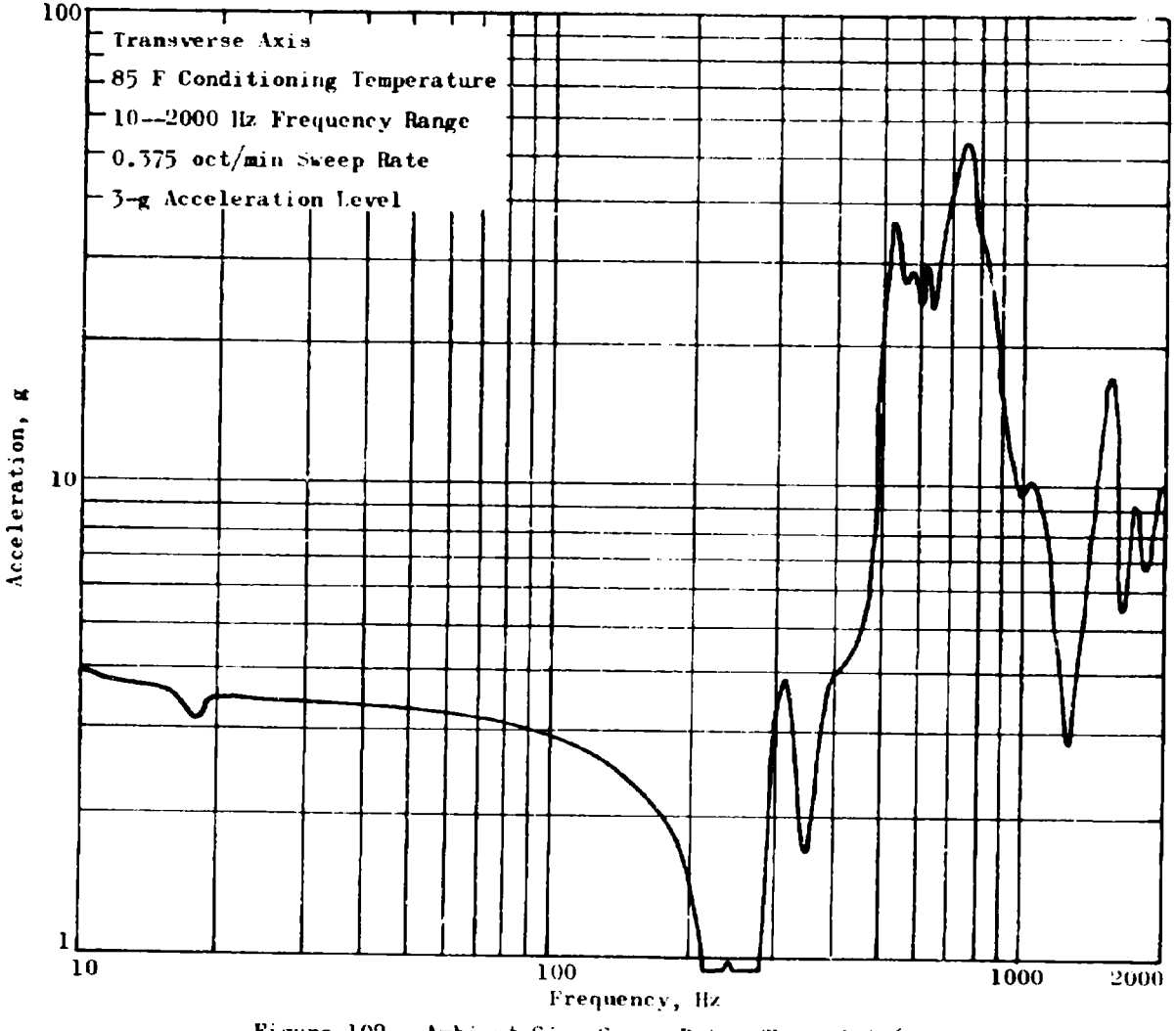

Figure 102. Ambient Sine Sweep Data, Channel A-6

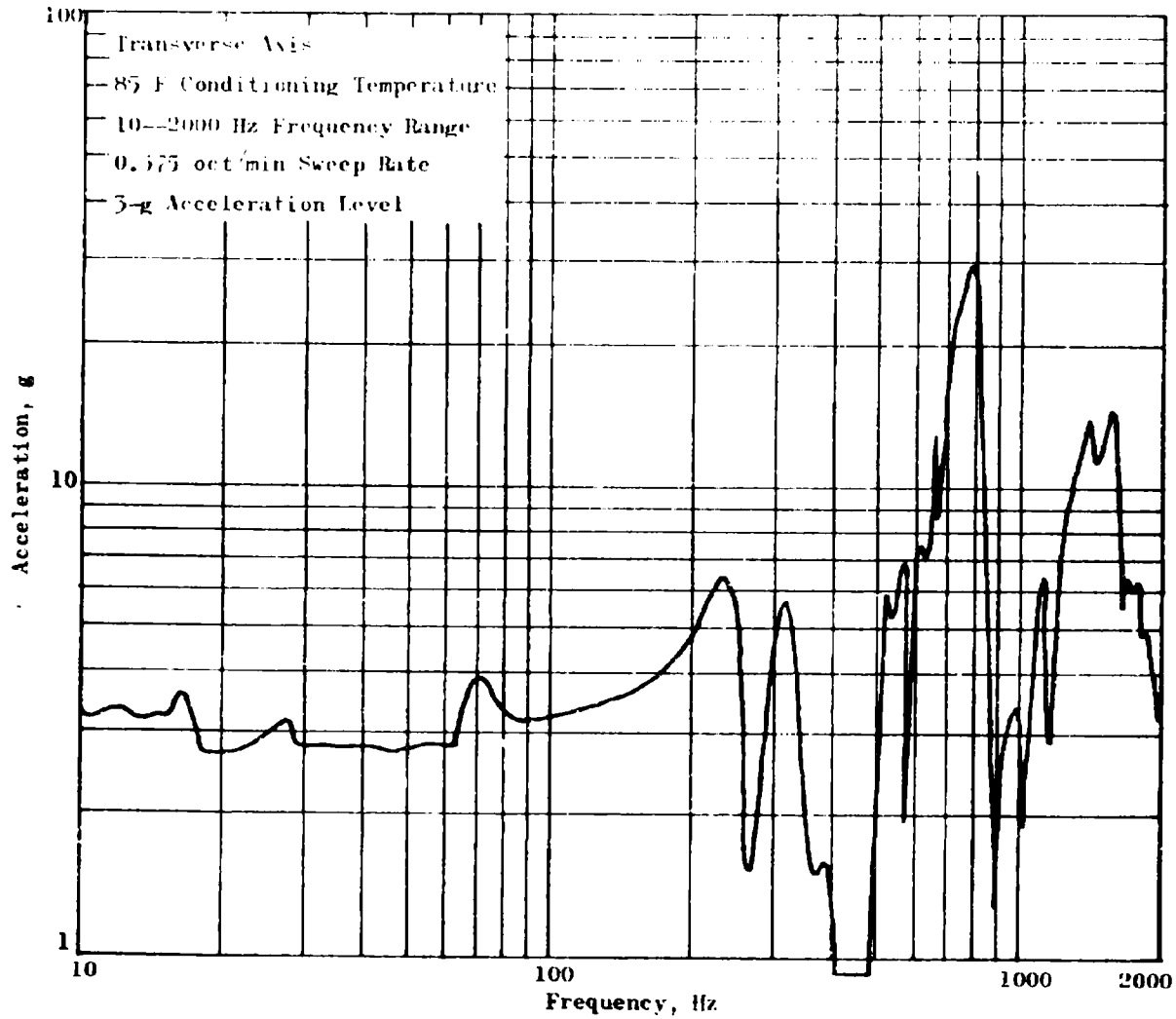

Figure 103. Ambient Sine Sweep Data, Channel A-7

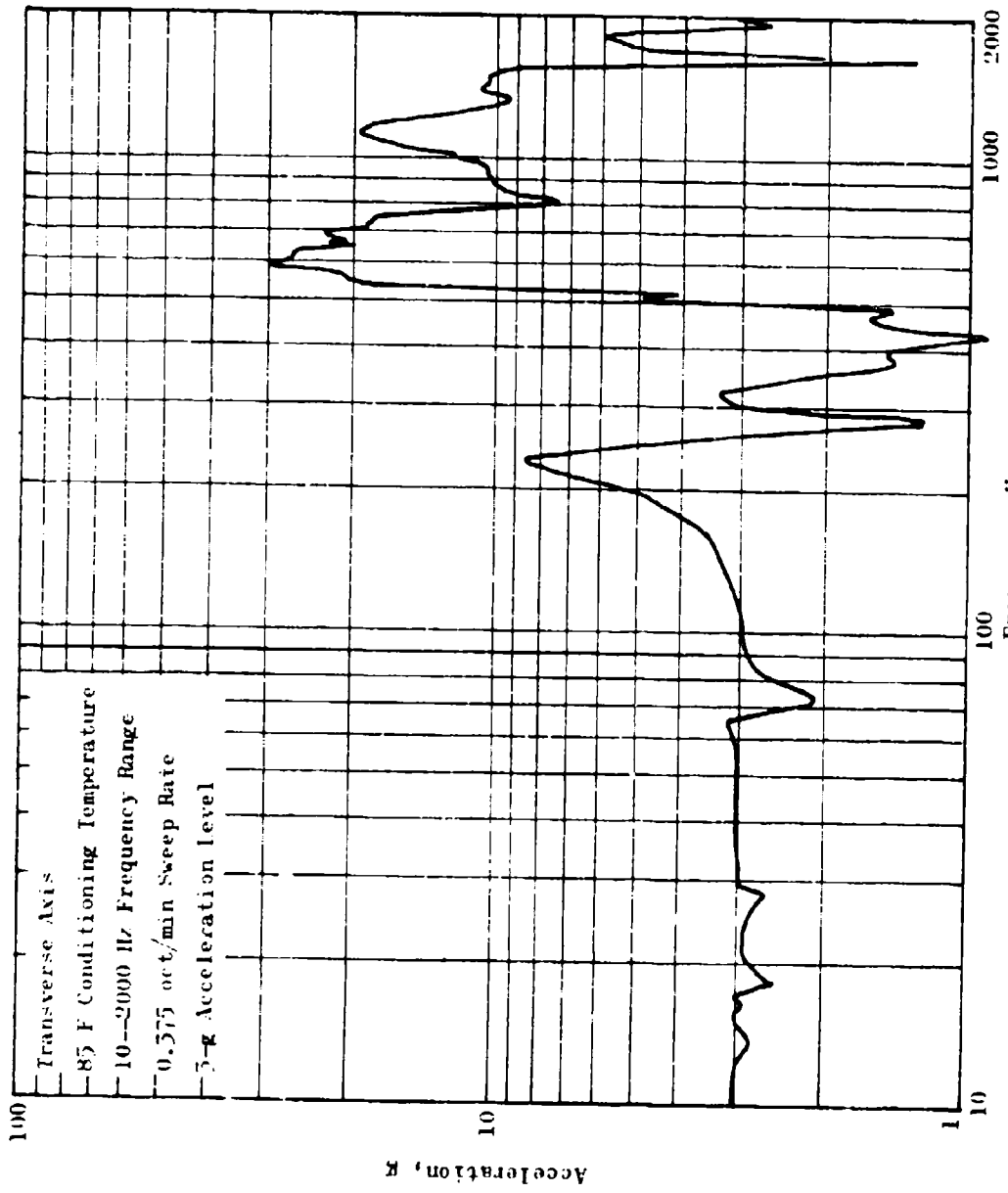

Figure 104. Ambient Sine Sweep Data, Channel A-8

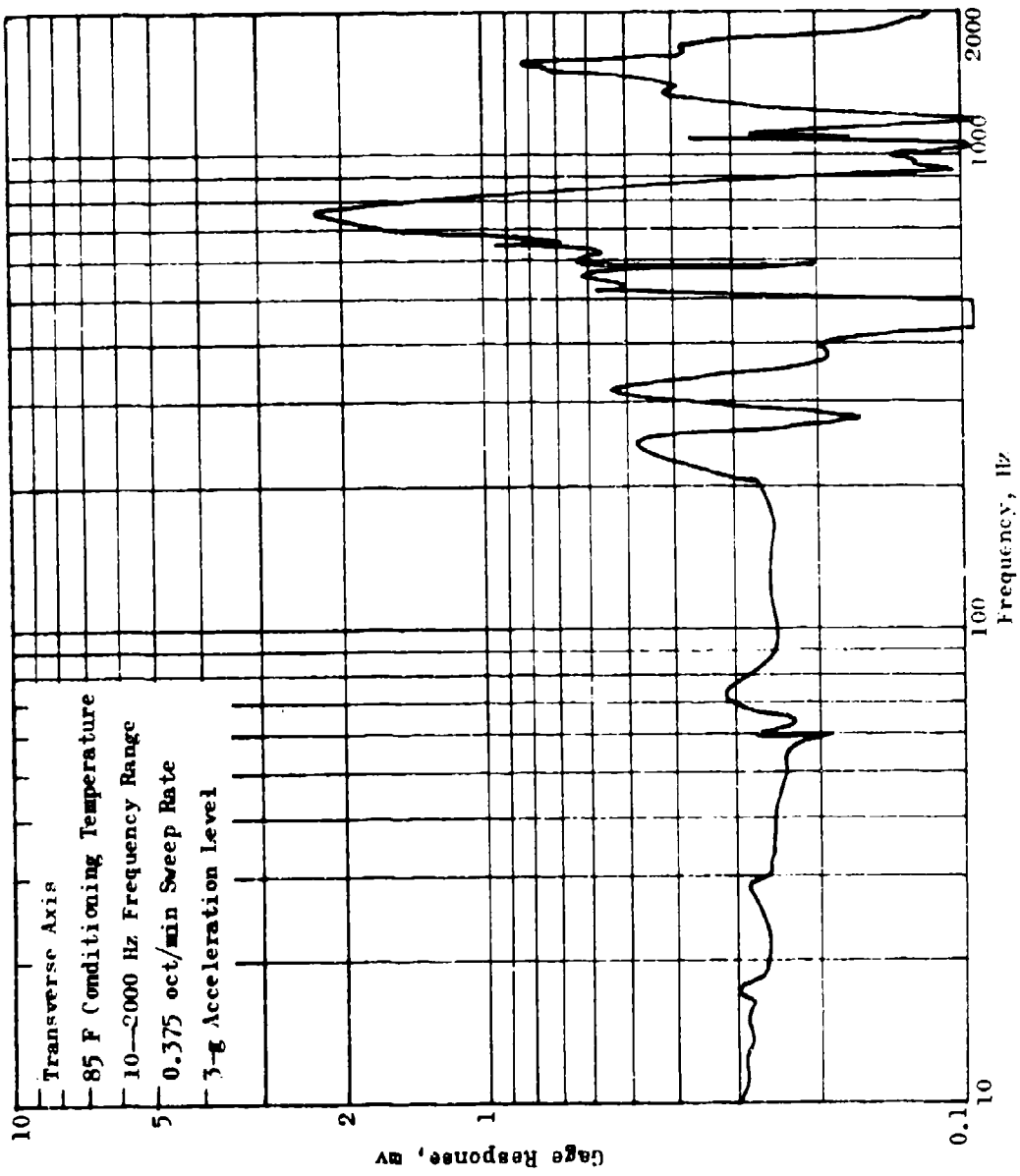

Figure 105. Ambient Sine Sweep Data, Channel X-6

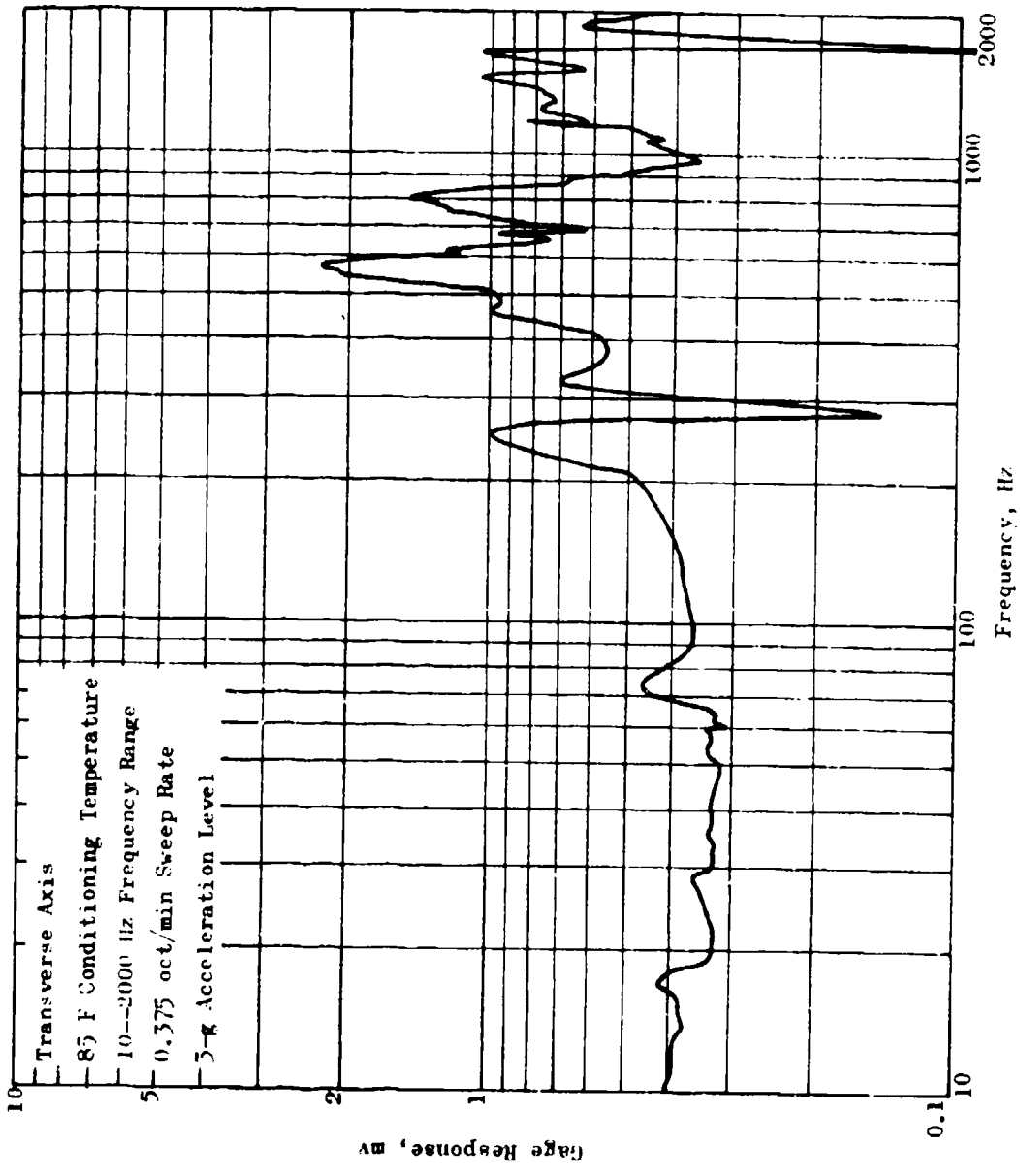

Figure 106. Ambient Sine Sweep Data, Channel N-7

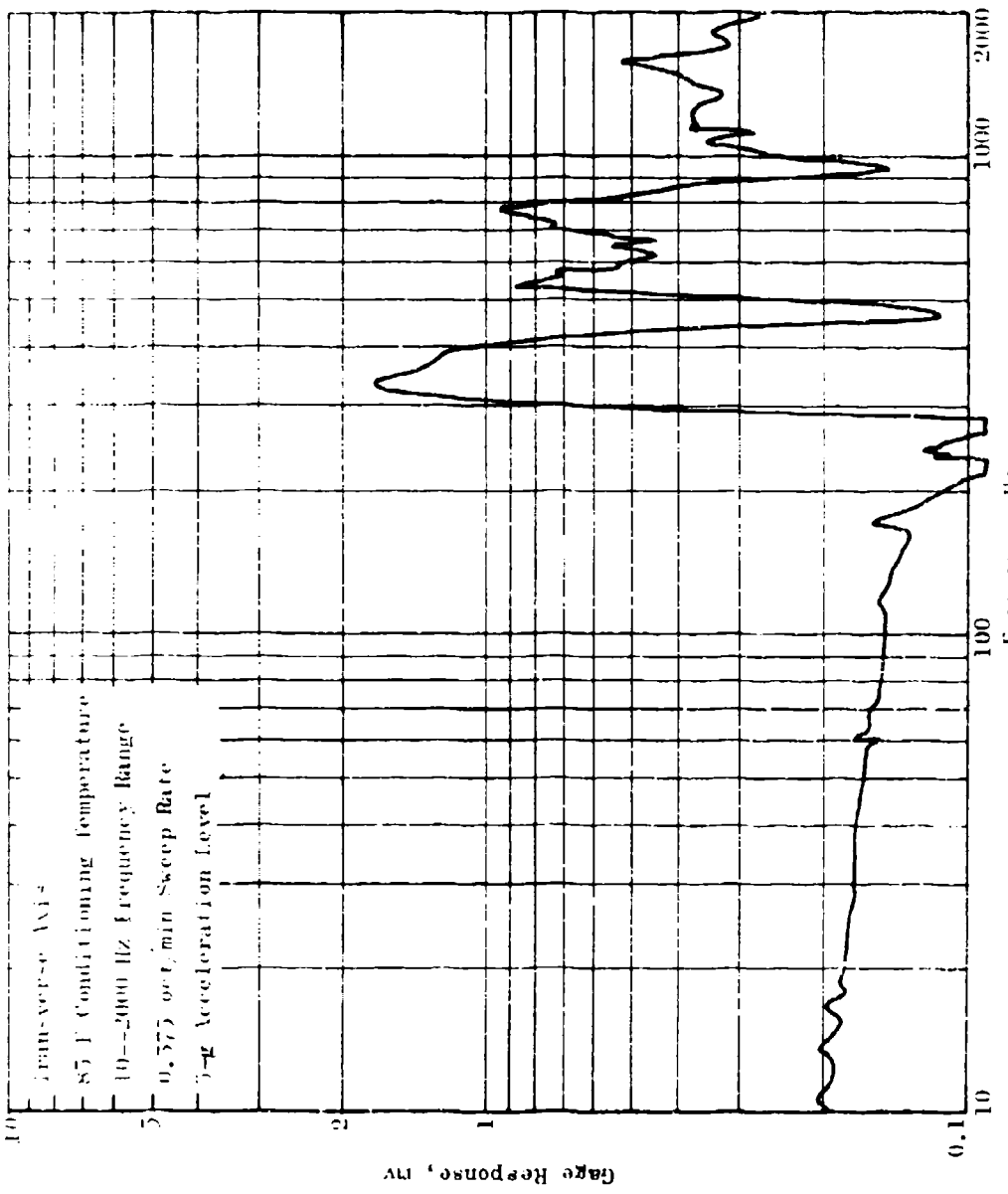

Figure 107. Ambient Sine Sweep Data, Channel X-8

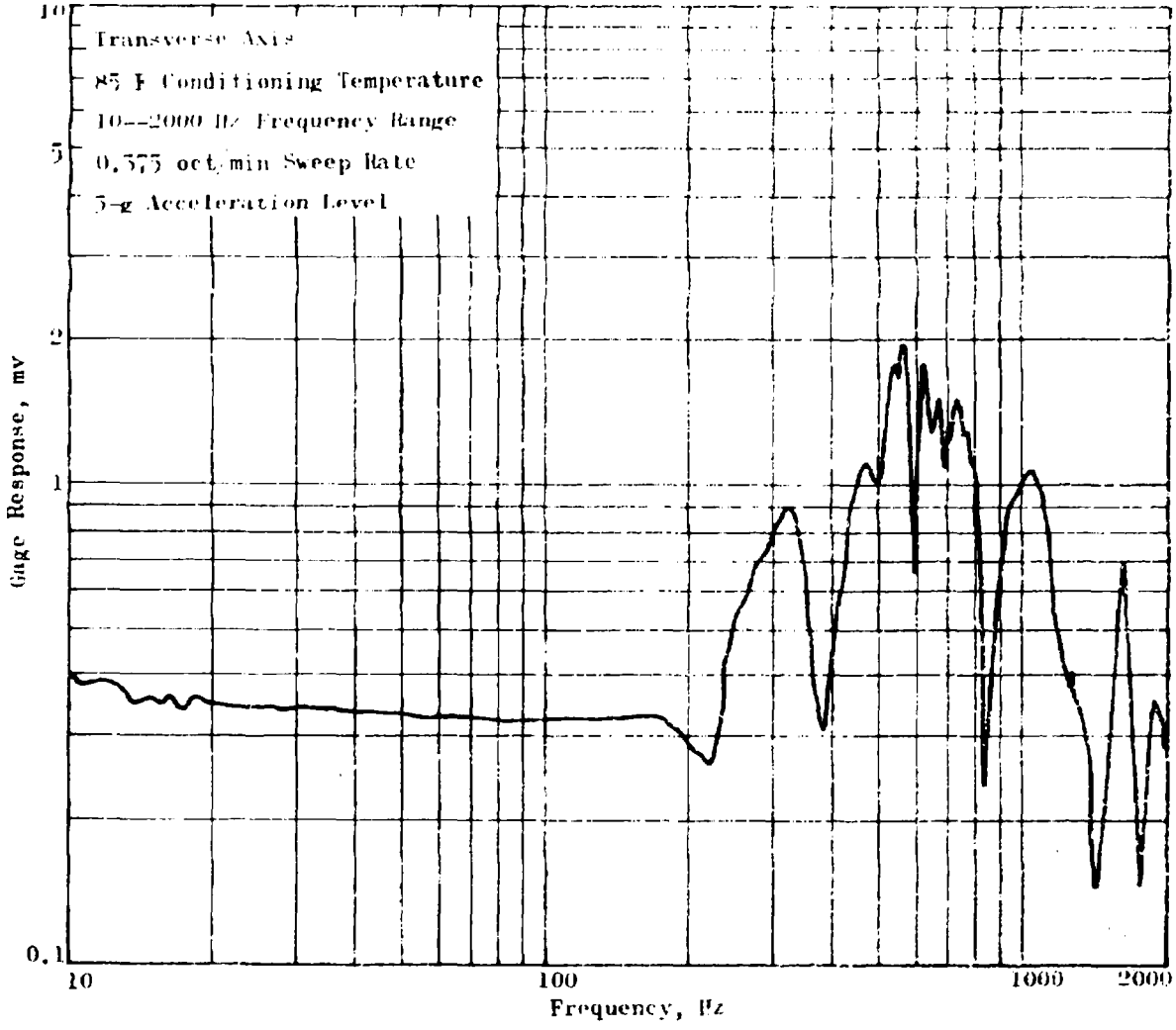

Figure 108. Ambient Sine Sweep Data, Channel N-9

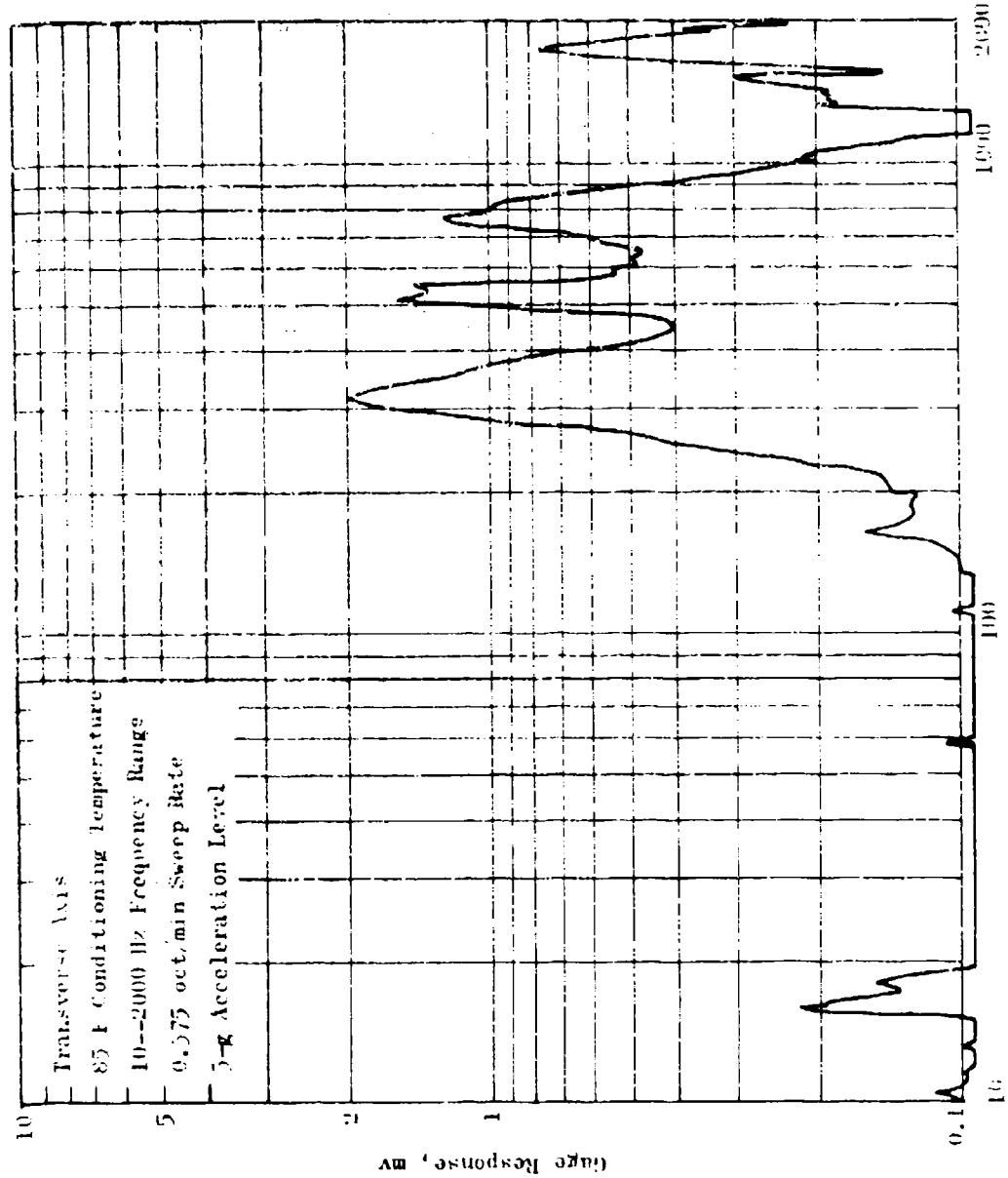

Figure 109. Ambient Sine Sweep Data, Channel X-15

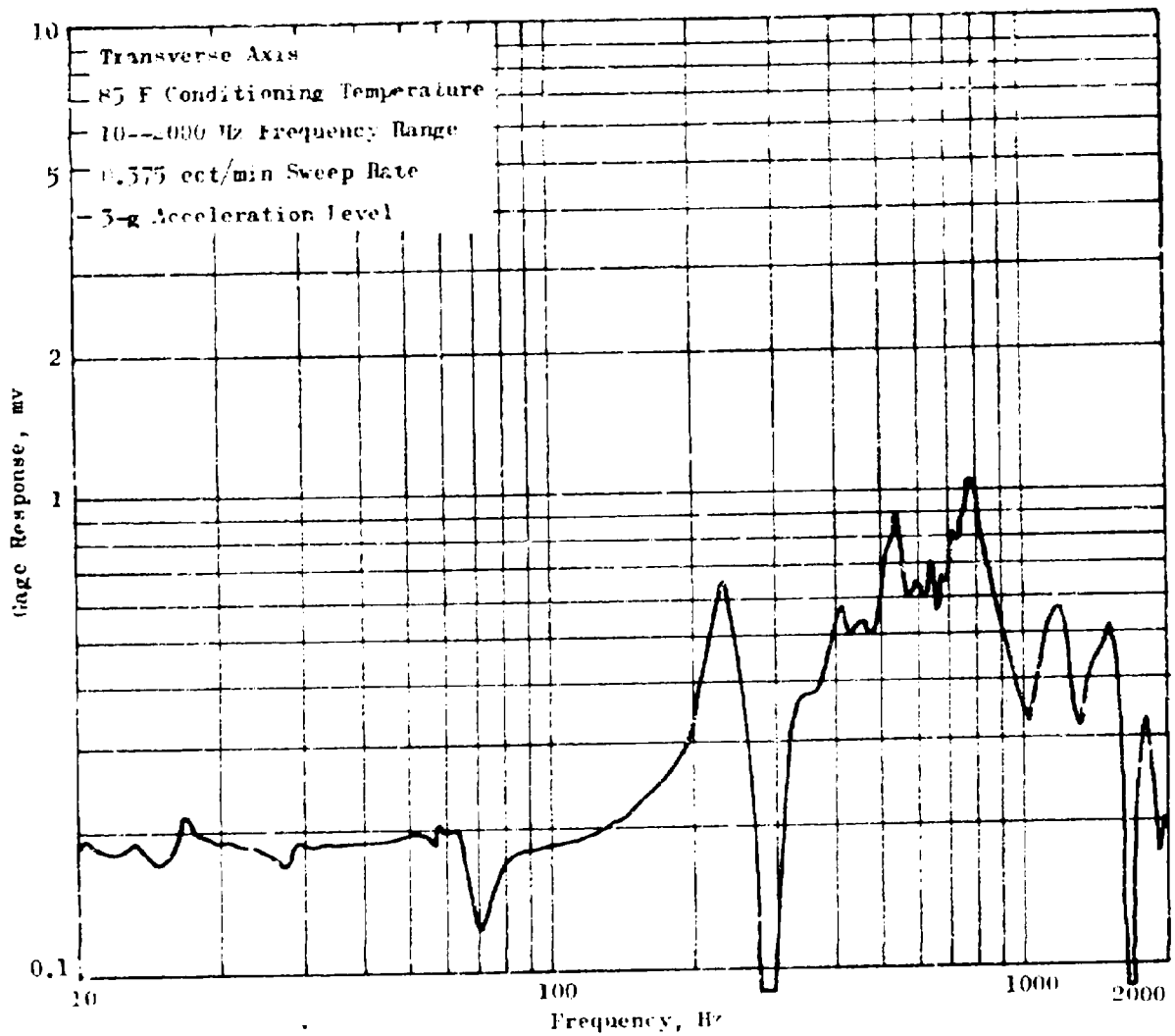

Figure 110. Ambient Sine Sweep Data, Channel N-15

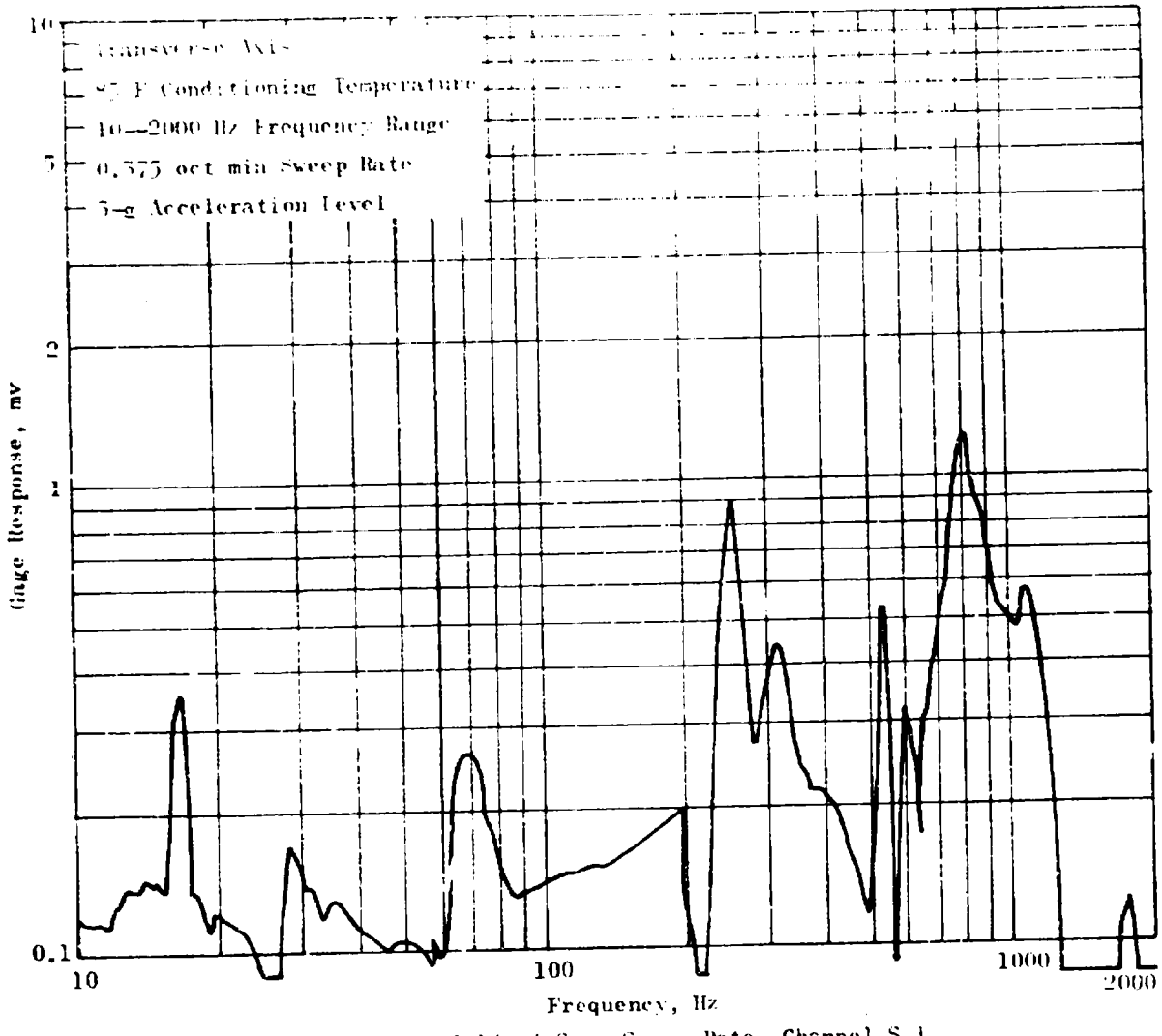

Figure 111. Ambient Sine Sweep Data, Channel S-1

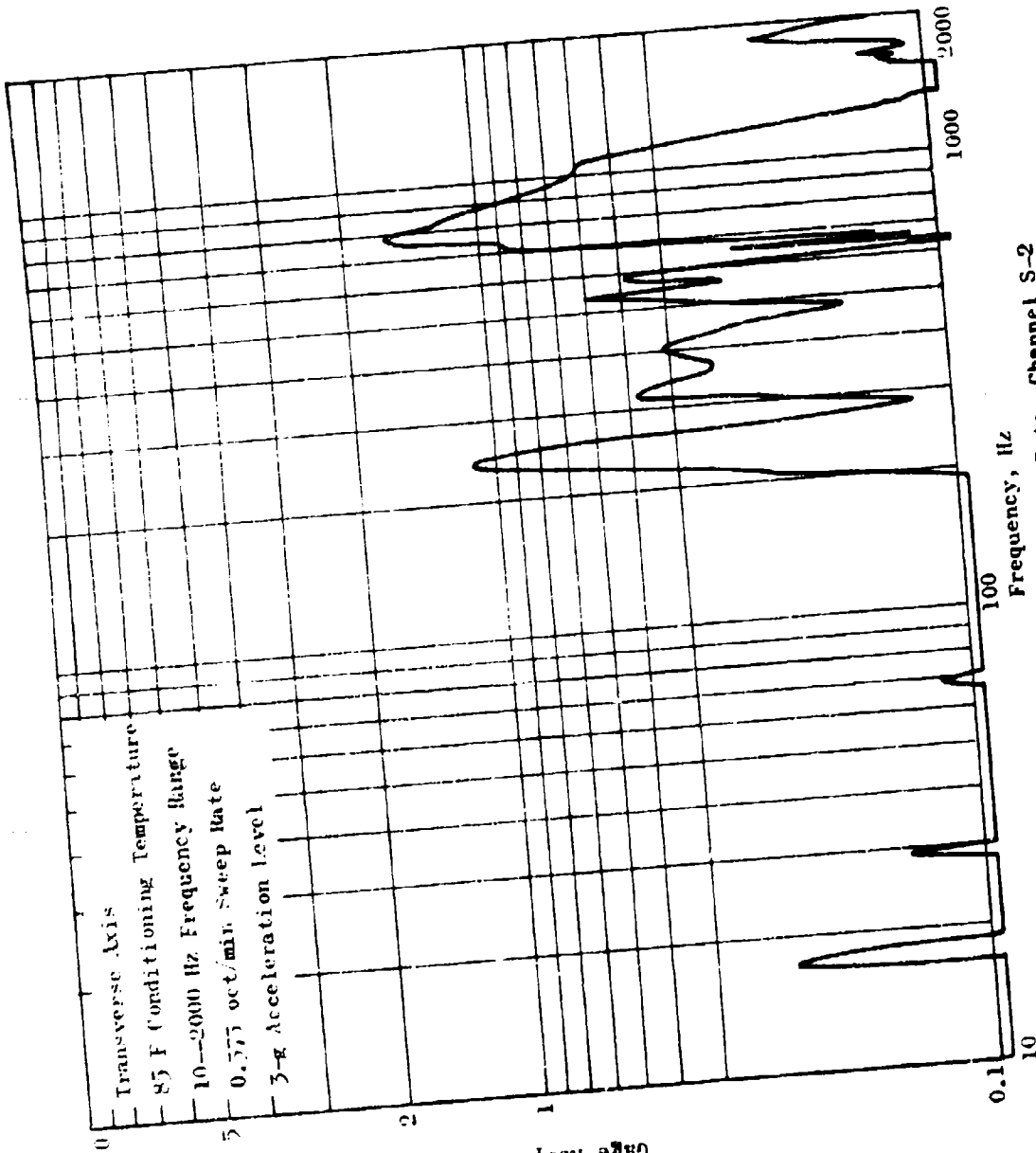

Figure 112. Ambient Sine Sweep Data, Channel S-2

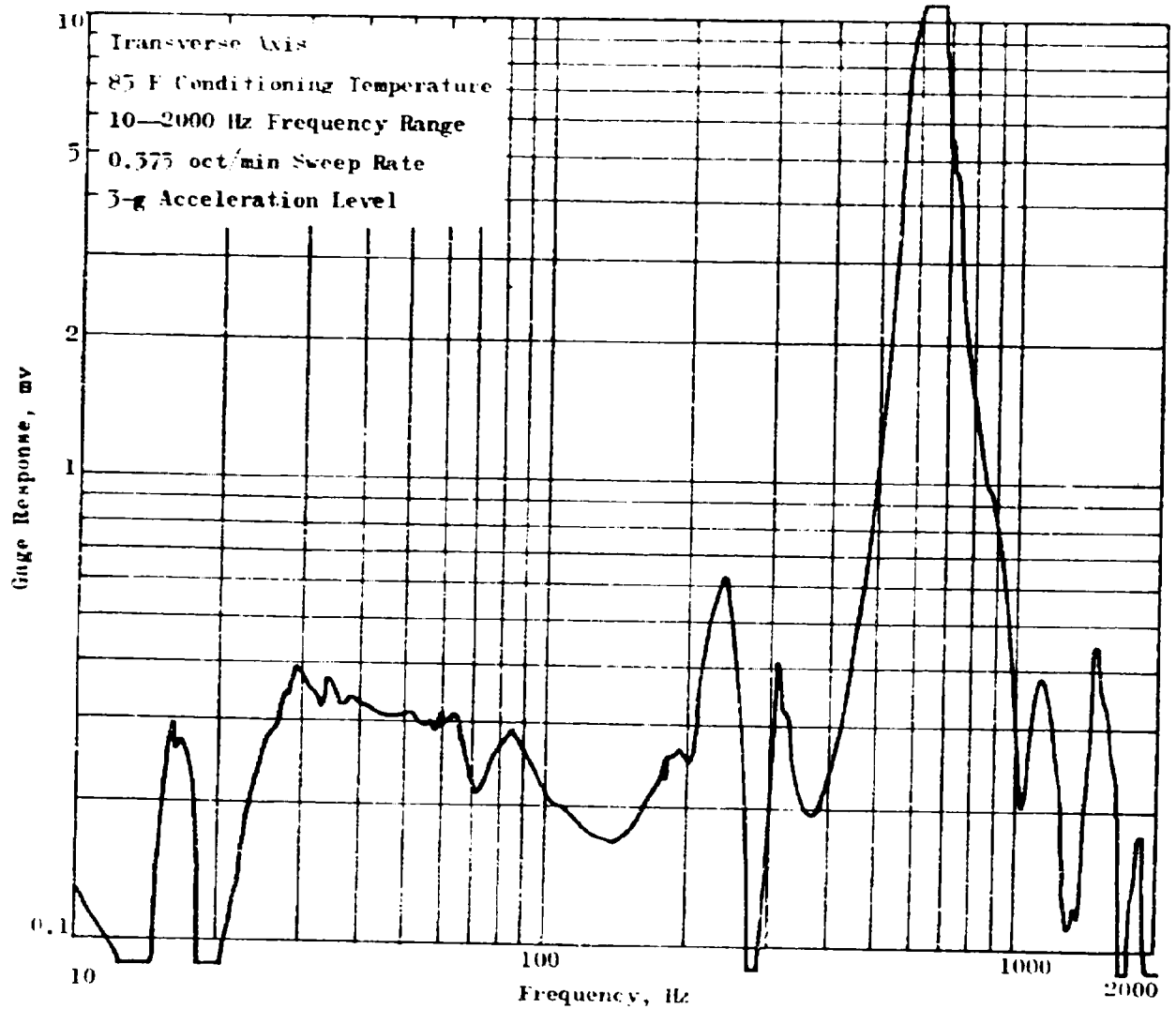

Figure 115. Ambient Sine Sweep Data, Channel C-4

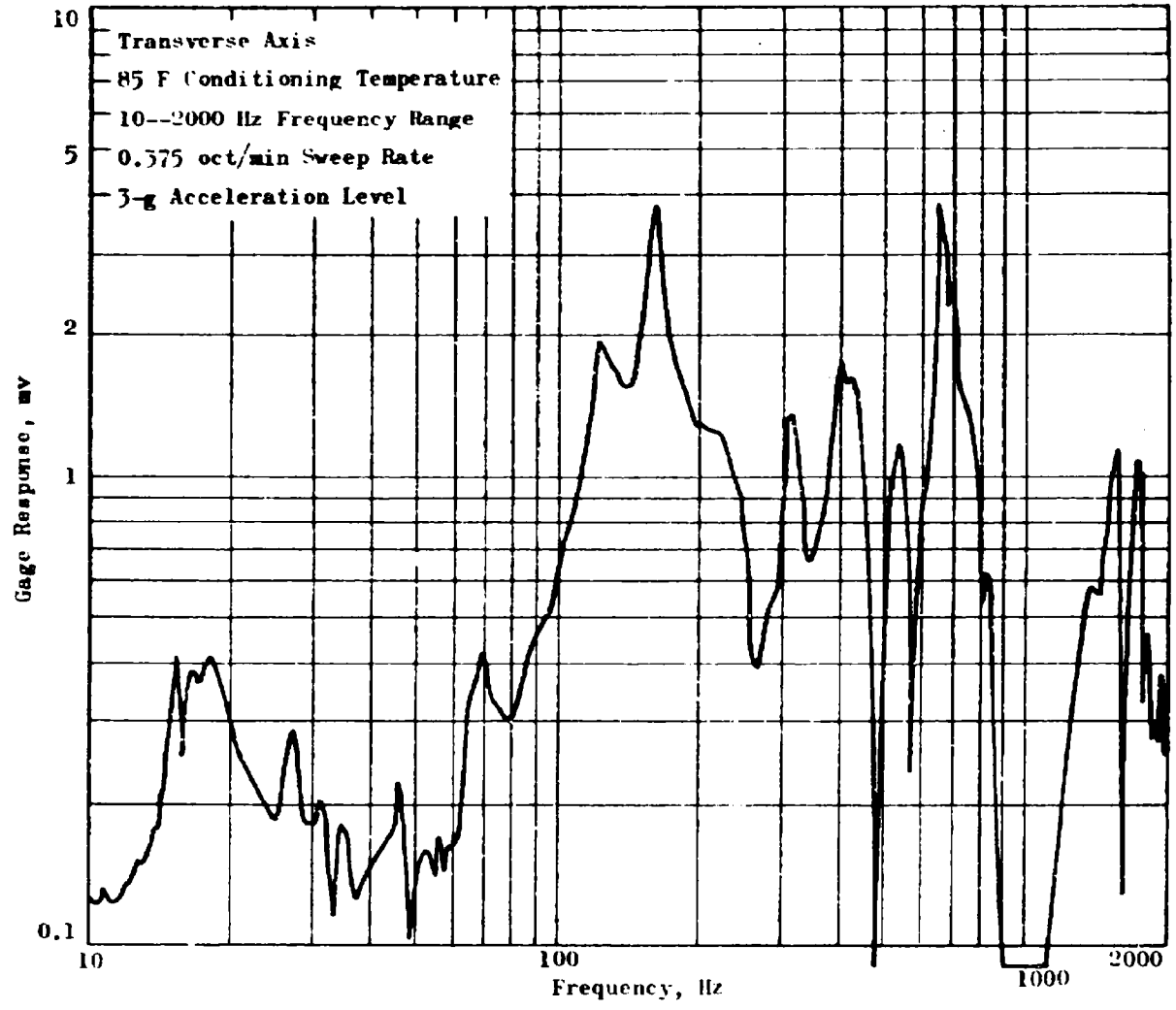

Figure 114. Ambient Sine Sweep Data, Channel C-5

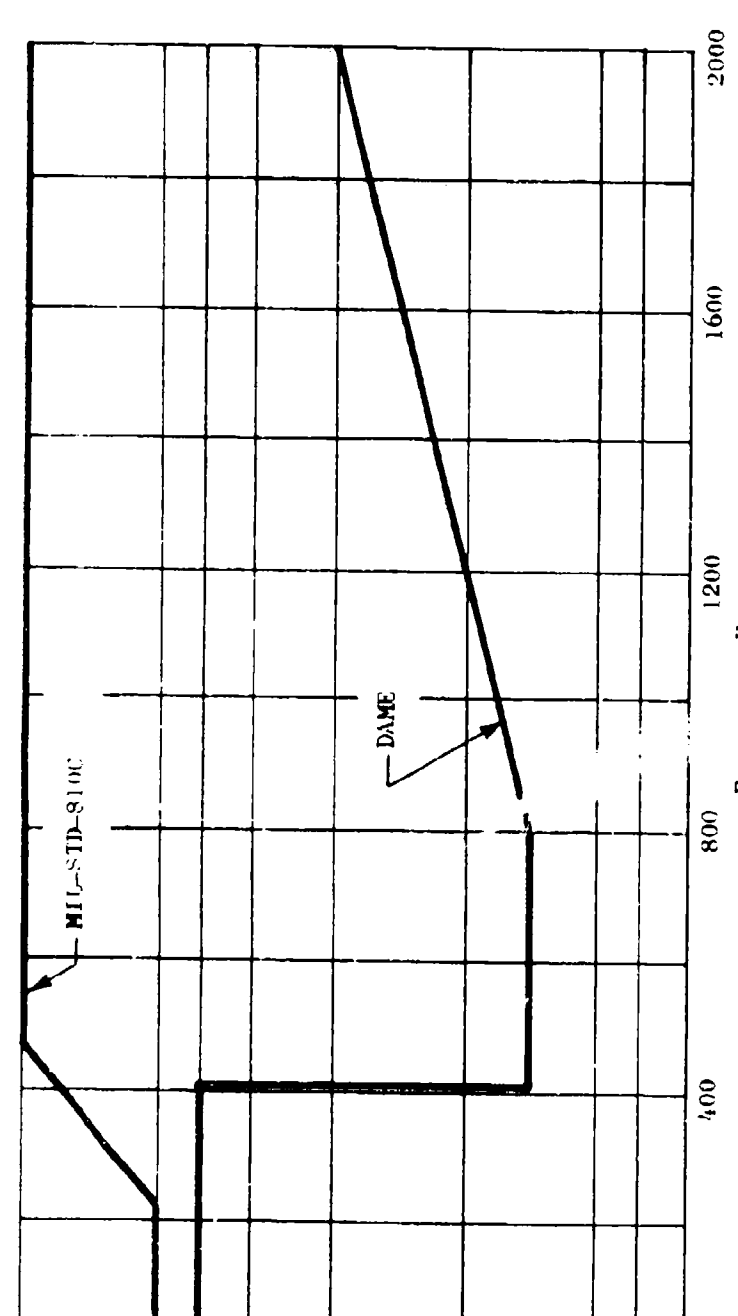

Figure 115. Nominal Vibration Control at Mk 38 Center of Gravity

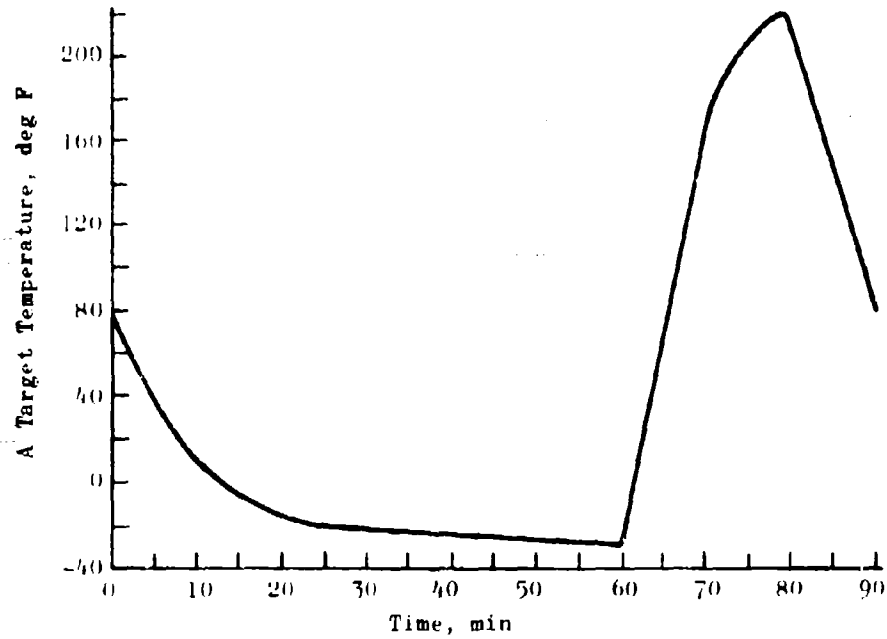

Figure 116. A Target Control Temperature

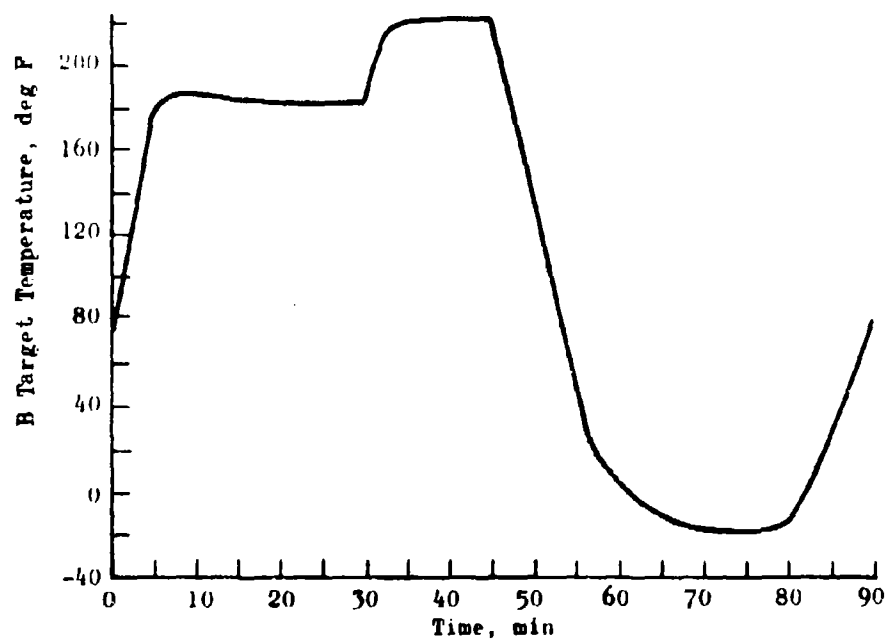

Figure 117. B Target Control Temperature

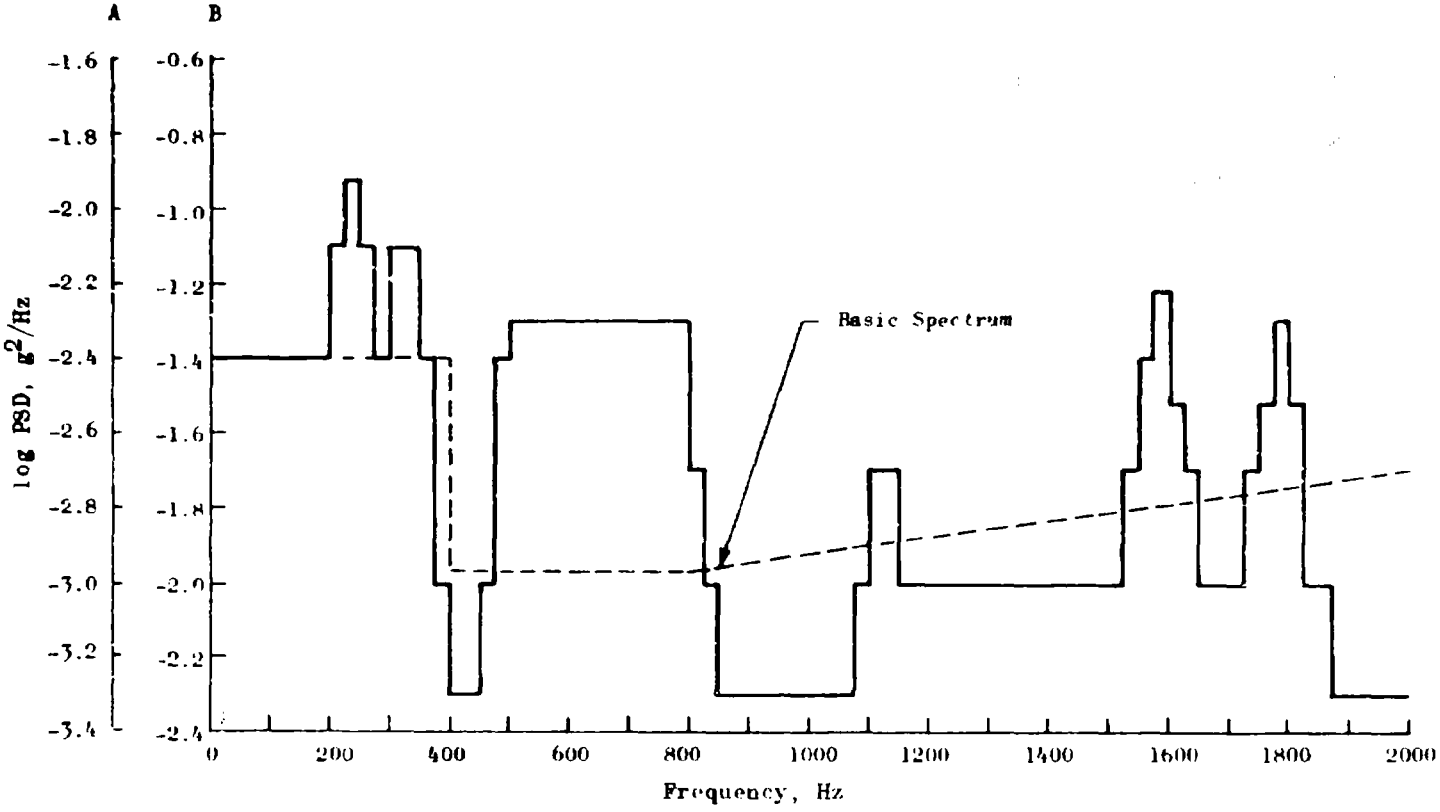

Figure 118. SPARROW Inert Motor High-Performance Severe Flight Dynamic Spectrum Enhanced by Motor Response Data, Data Input Control, Motor Ends

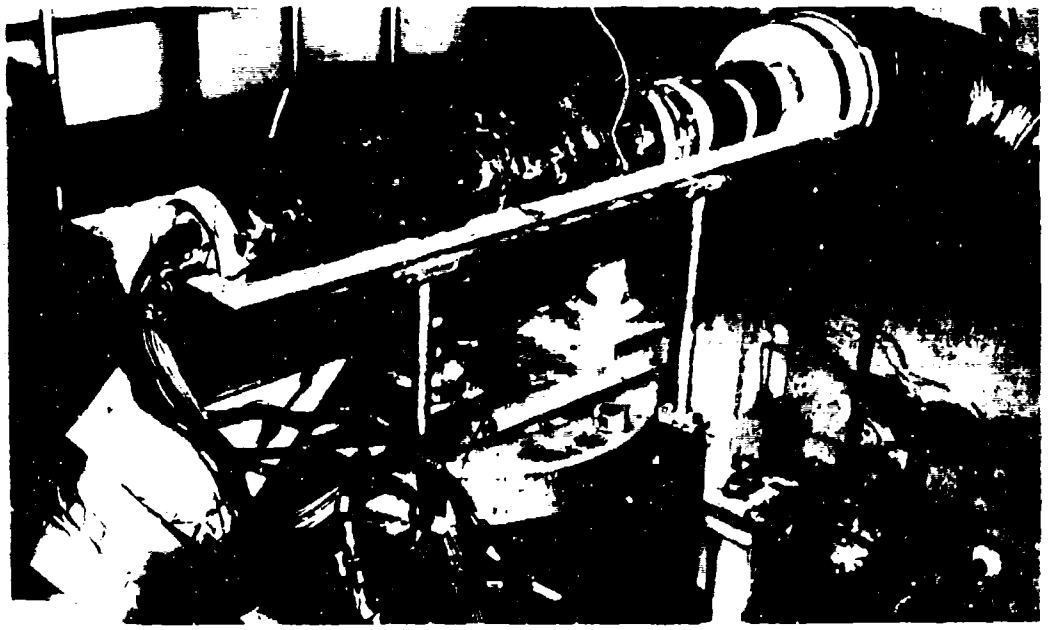

76-302

Figure 119. Captive-Flight Test Set Up with Shroud Open

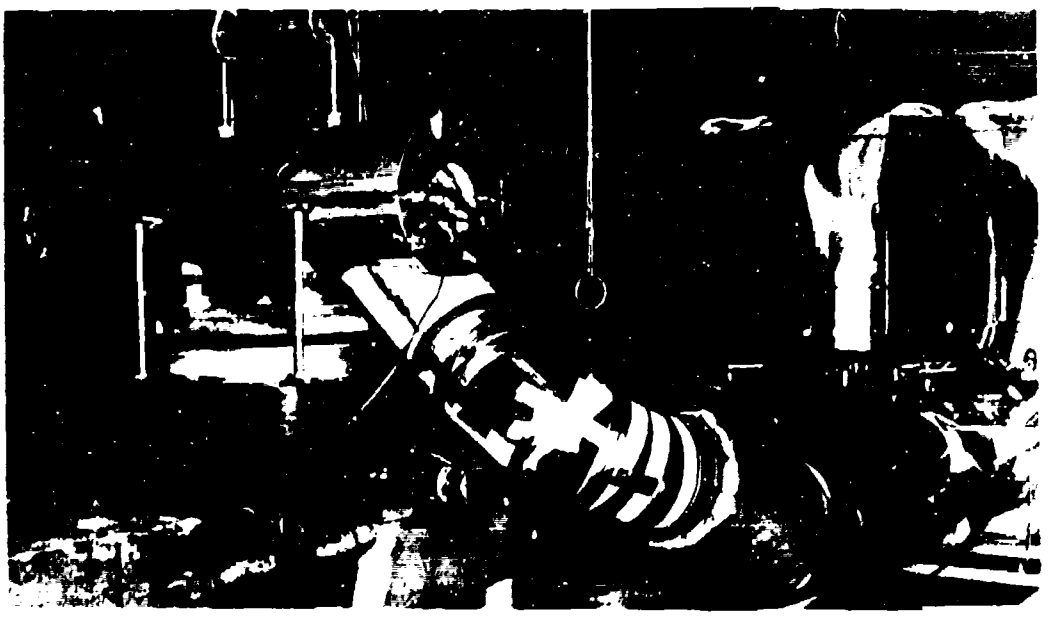

76-303

Figure 120. Captive-Flight Test Set Up with Shroud Closed

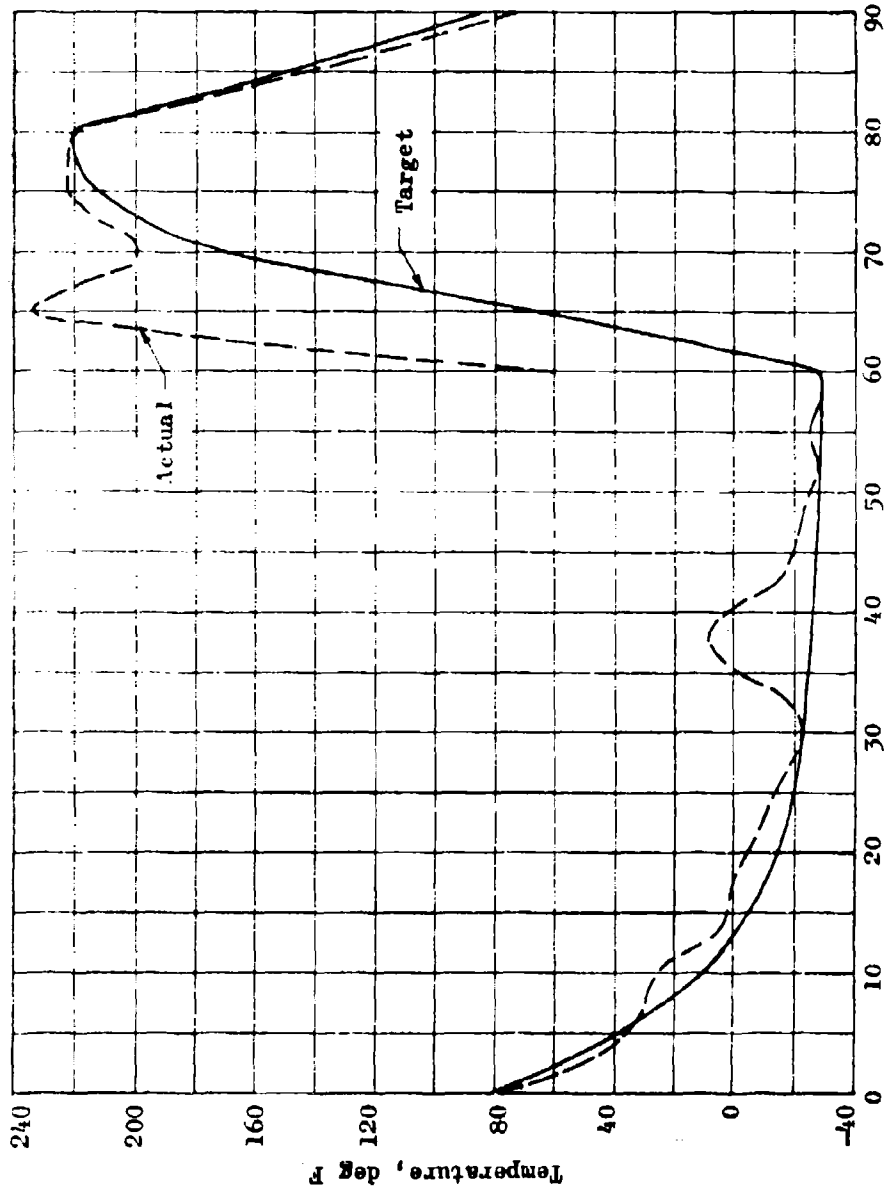

Figure 121. First Aerobrat Test

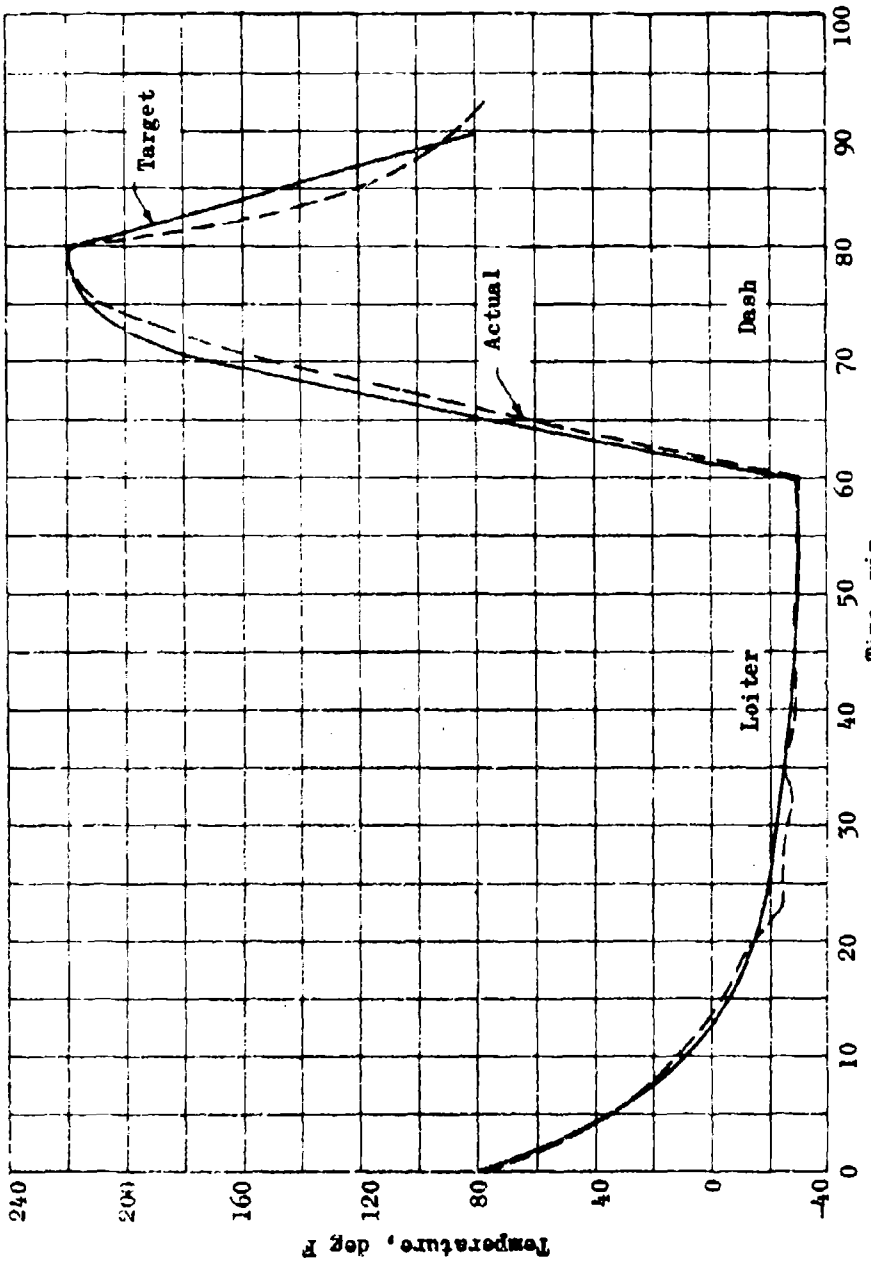

Fighre 122. Second Aeroheat Test

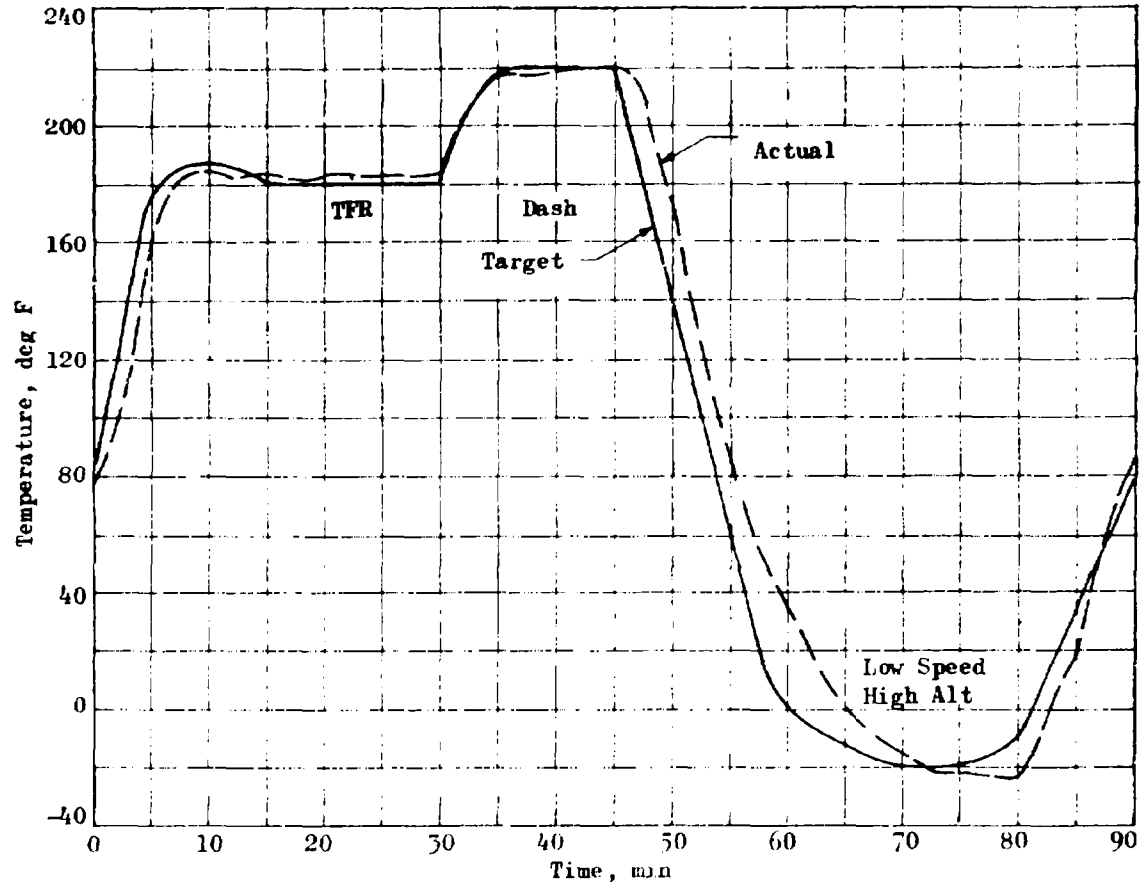

Figure 123. Third Aeroheat Test

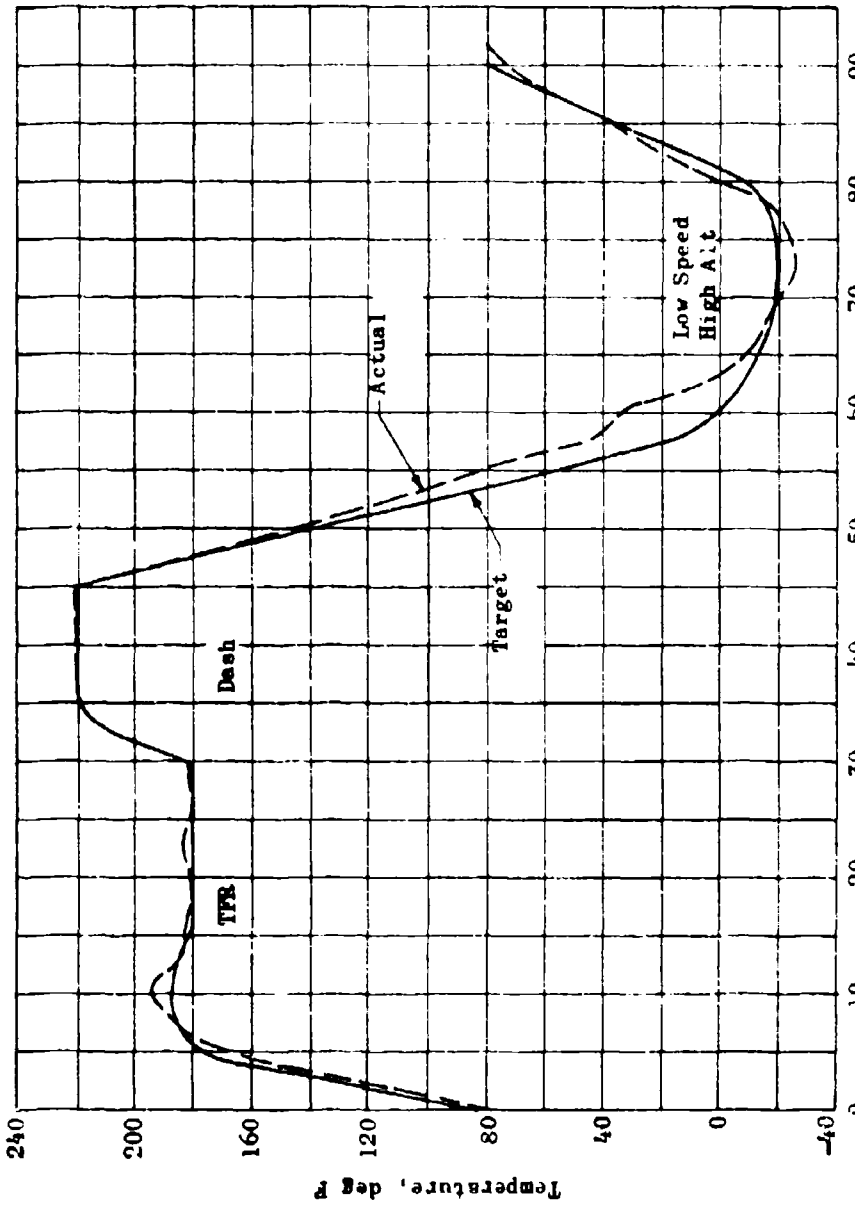

Figure 124. Fourth Aeroheat Test

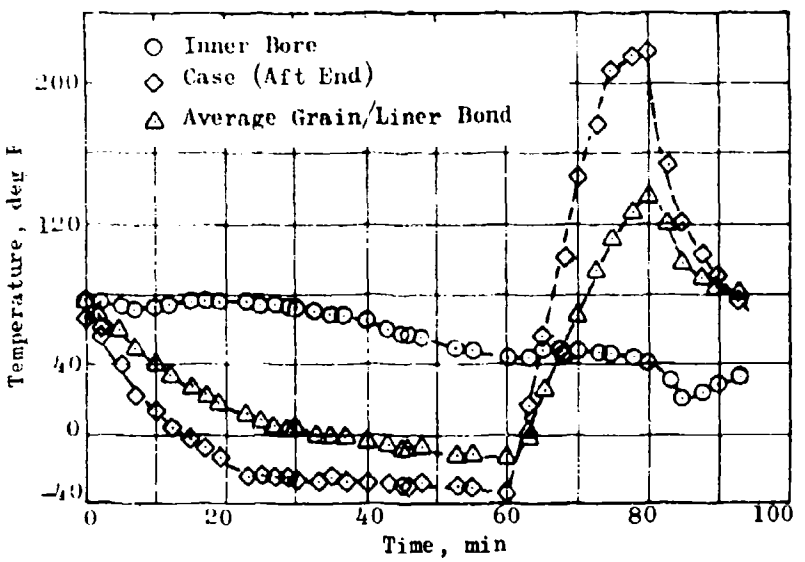

Figure 125. Aeroheat Test 2 Thermal Response

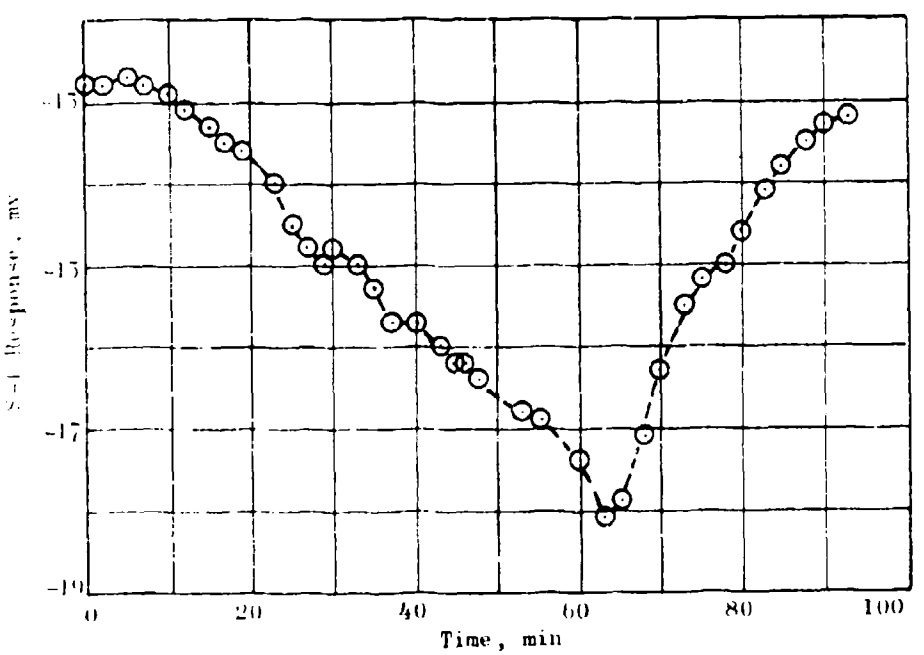

Figure 126. Aeroheat Test 2, S-1 Thermal Response

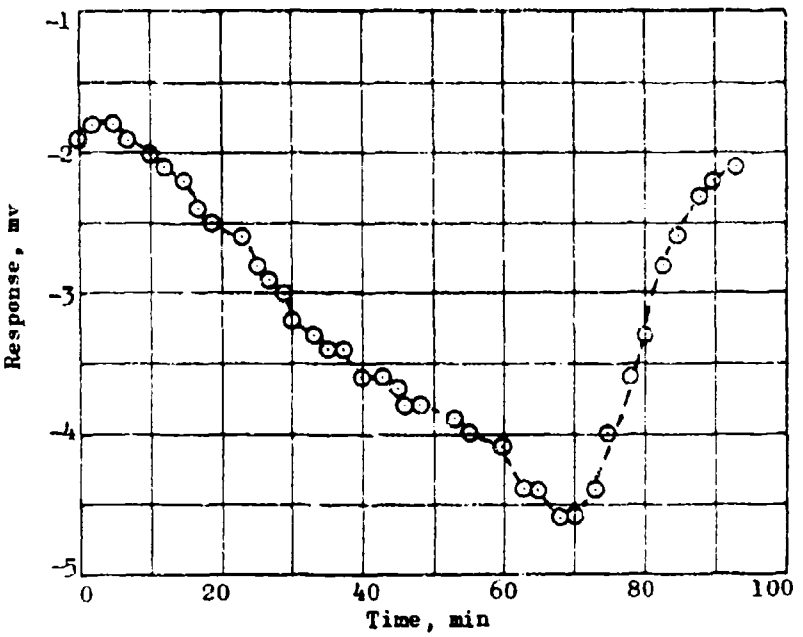

Figure 127. Aeroheat Test 2, S-2 Thermal Response

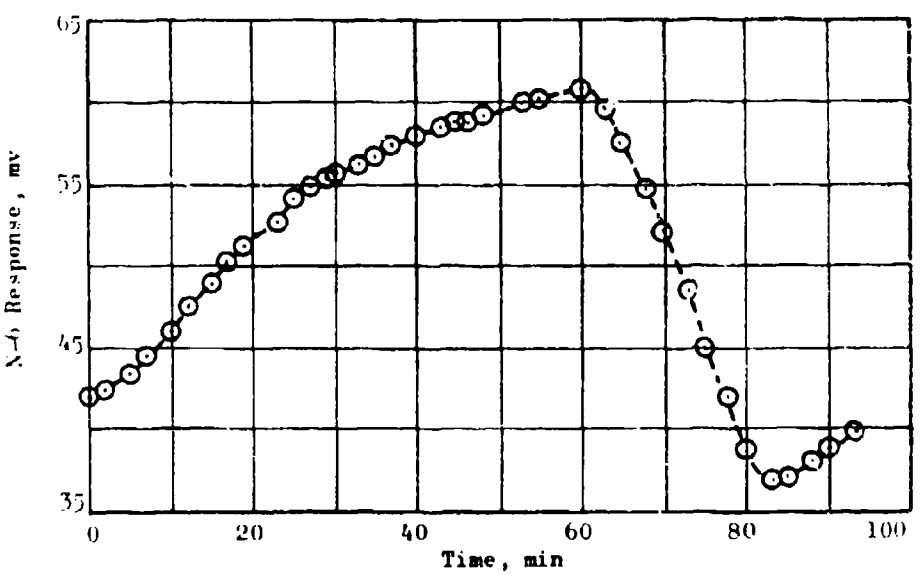

Figure 128. Aeroheat Test 2, N-6 Thermal Response

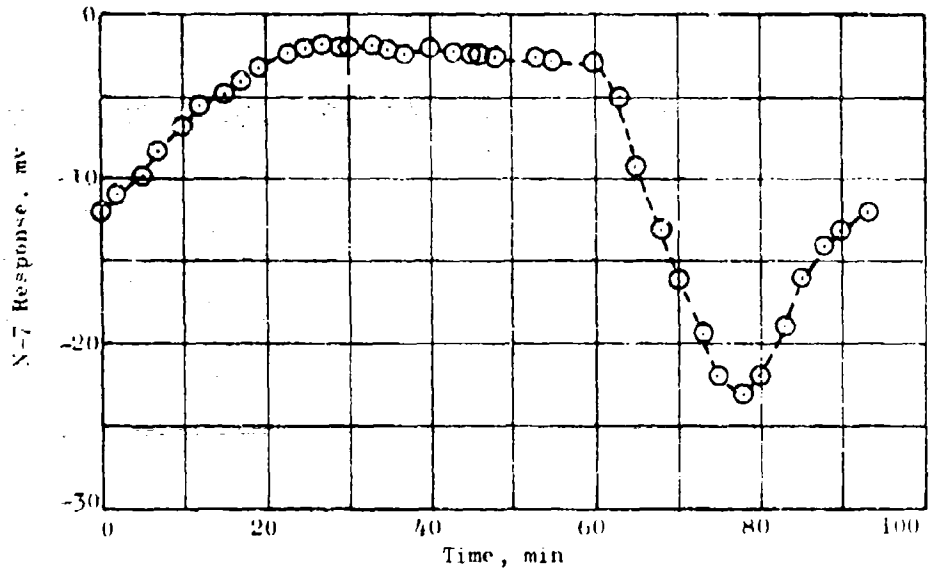

Figure 129. Aeroheat Test 2, N-7 Thermal Response

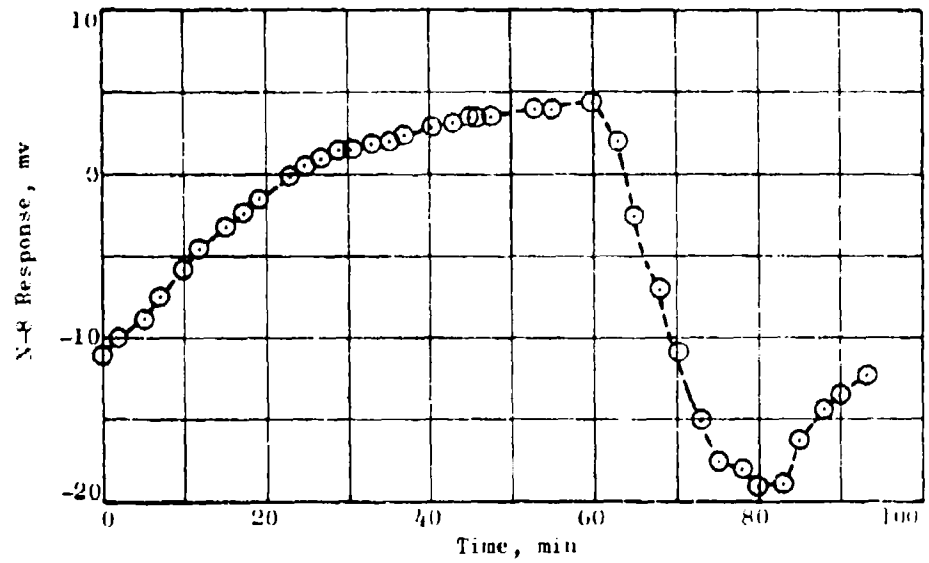

Figure 130. Aeroheat Test 2, N-8 Thermal Response

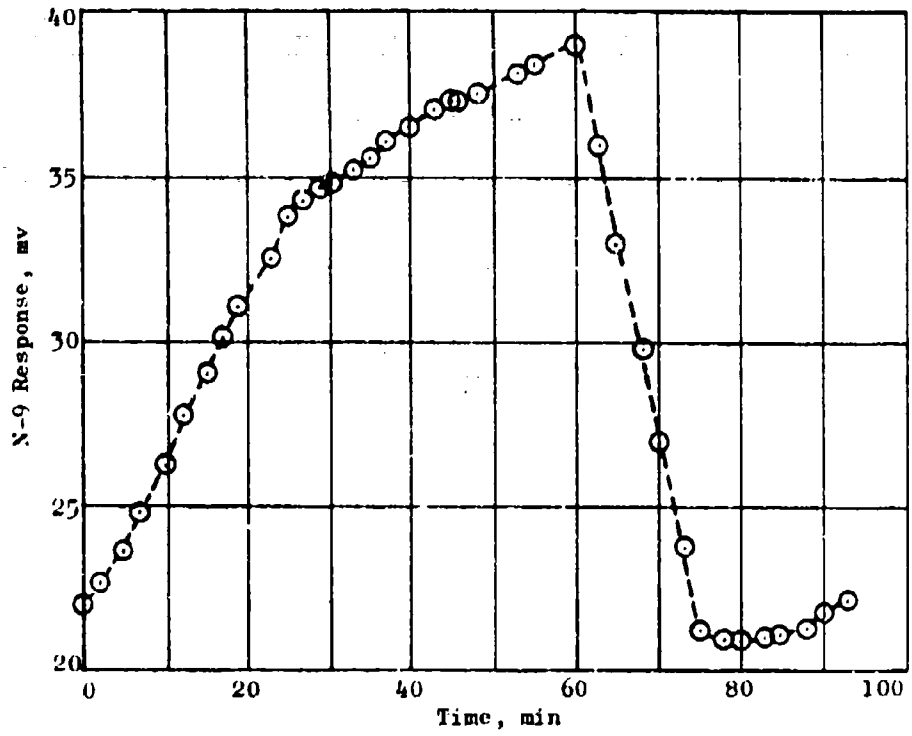

Figure 131. Aeroheat Test 2, N-9 Thermal Response

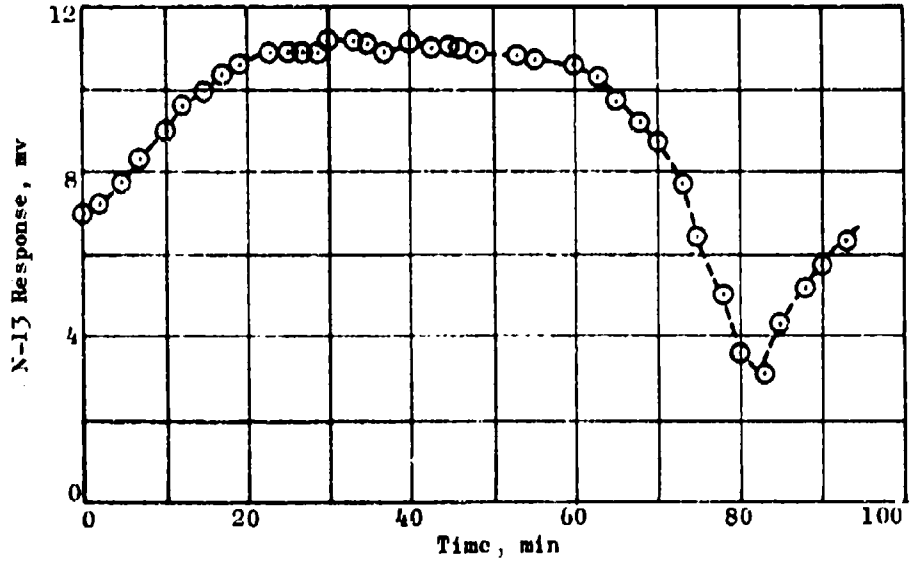

Figure 132. Aeroheat Test 2, N-13 Thermal Response

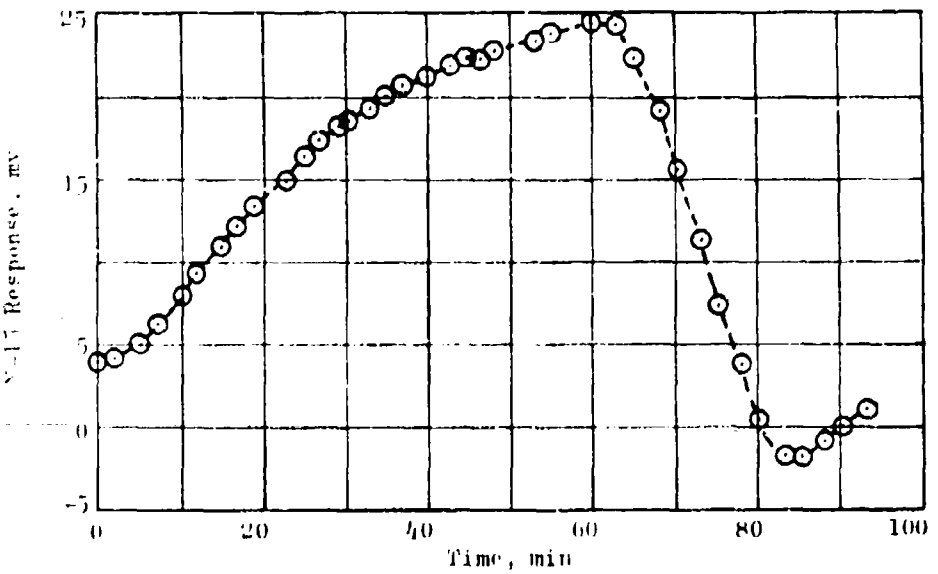

Figure 133. Aeroheat Test 2, N-15 Thermal Response

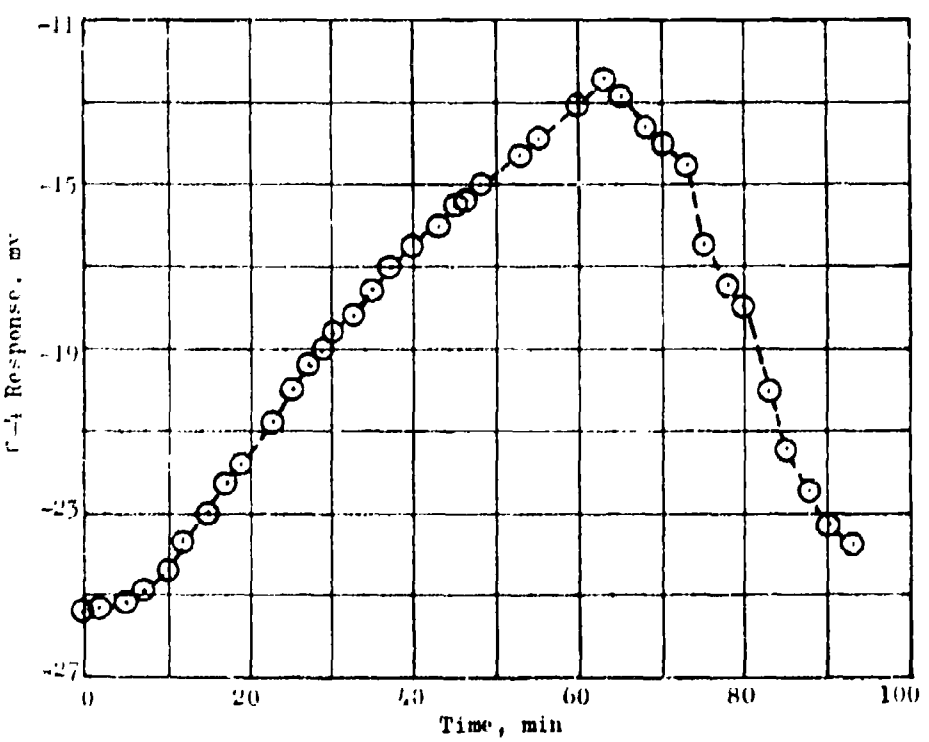

Figure 134. Aeroheat Test 2, C-4 Thermal Response

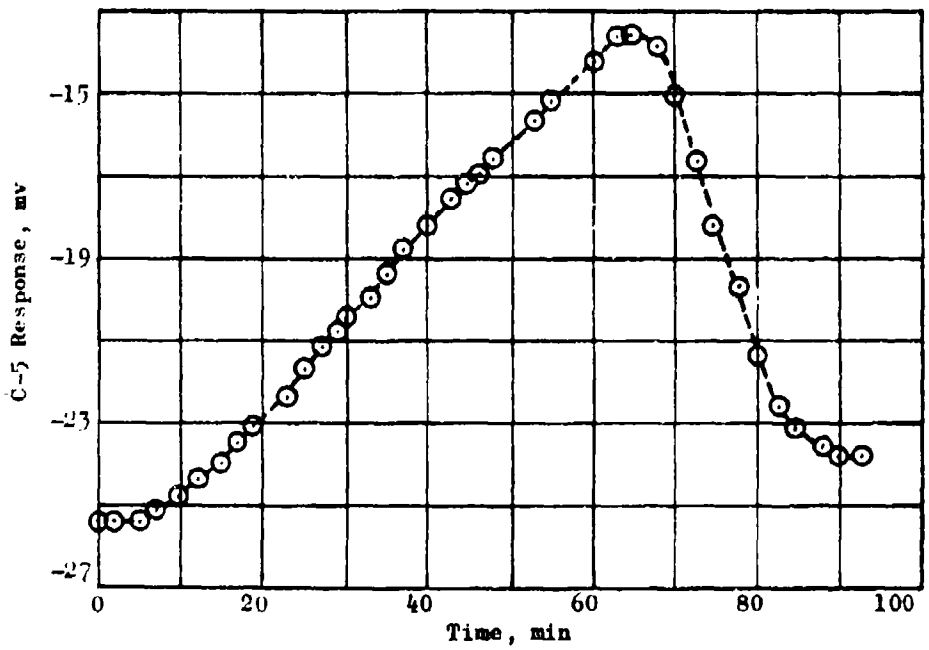

Figure 135. Aeroheat Test 2, C-5 Thermal Response

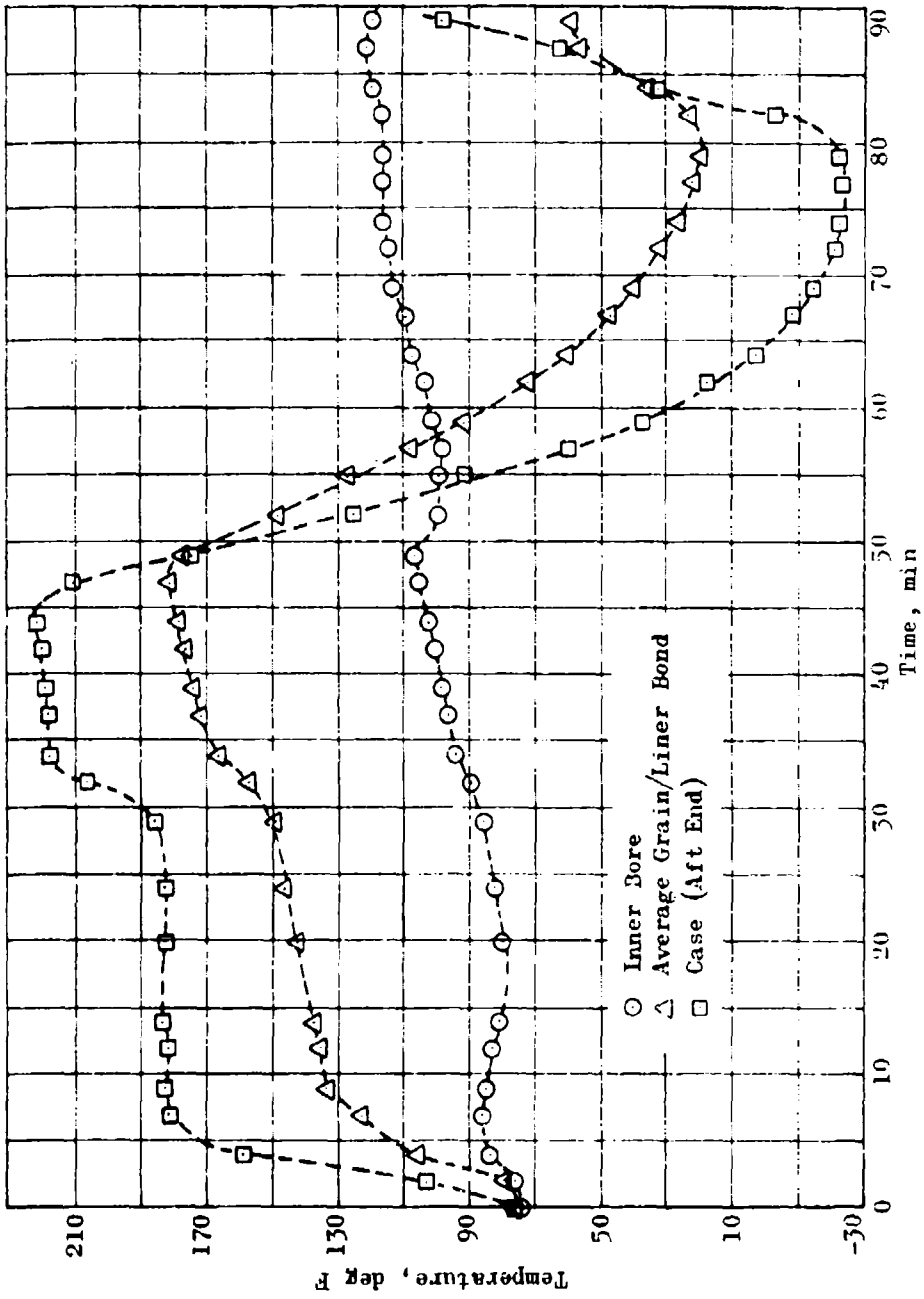

Figure 136. Aeroheat Test 3, Thermal Response

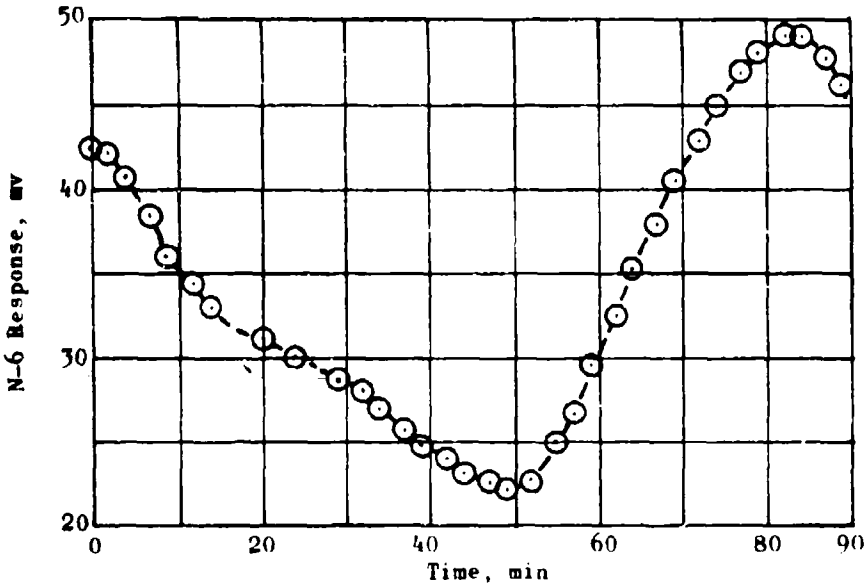

Figure 137. Aeroheat Test 3, N-6 Thermal Response

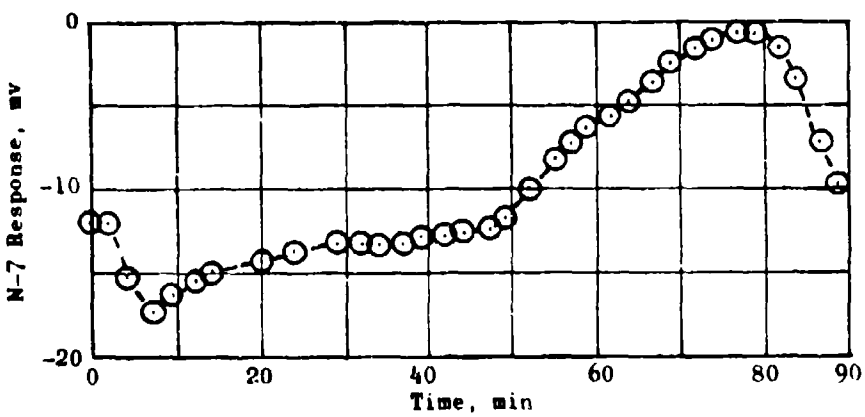

Figure 138. Aeroheat Test 3, N-7 Thermal Response

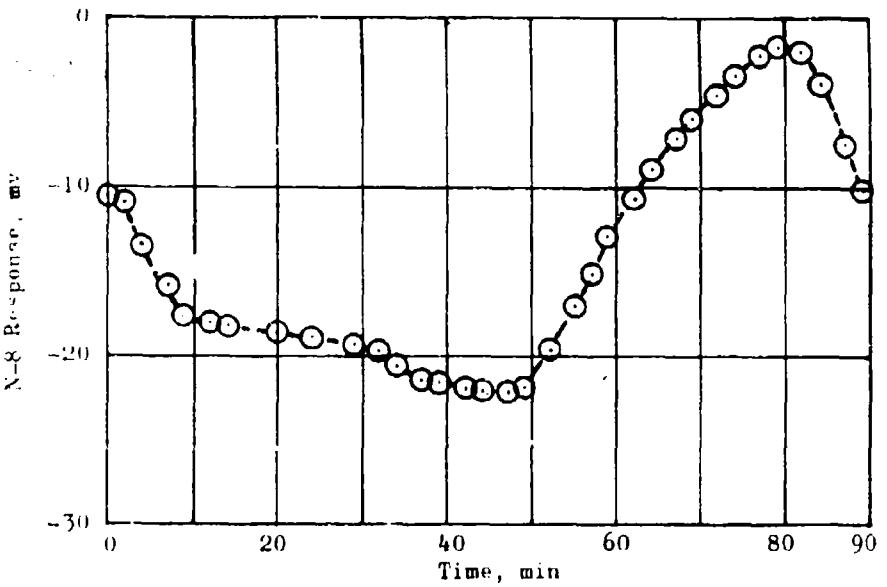

Figure 139. Aeroheat Test 3, N-8 Thermal Response

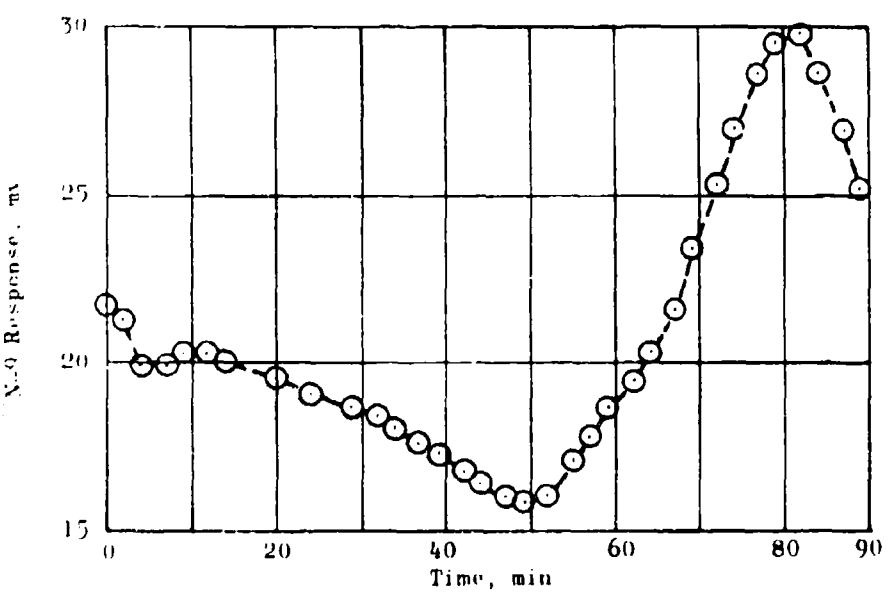

Figure 140. Aeroheat Test 3, N-9 Thermal Response

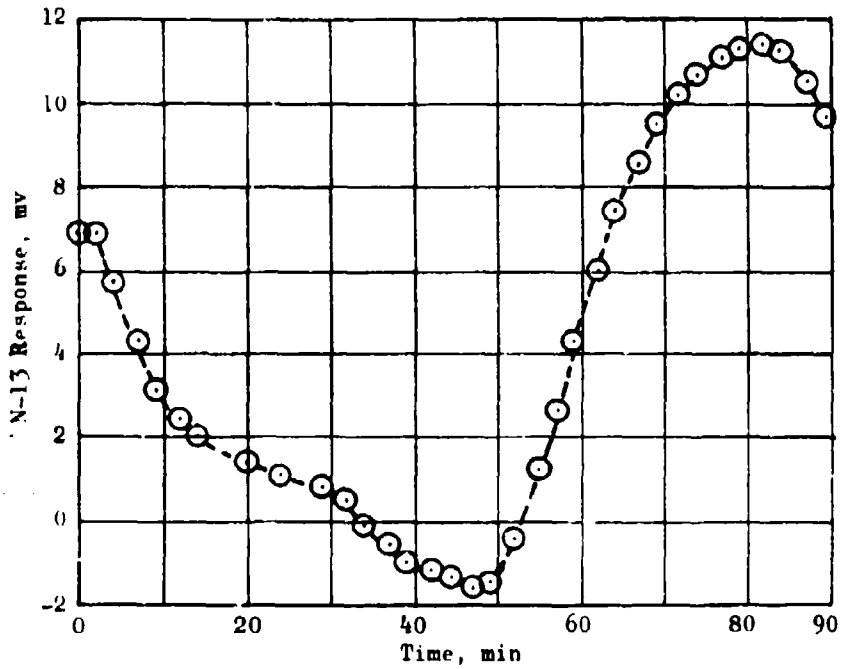

Figure 141. Aeroheat Test 3, N-13 Thermal Response

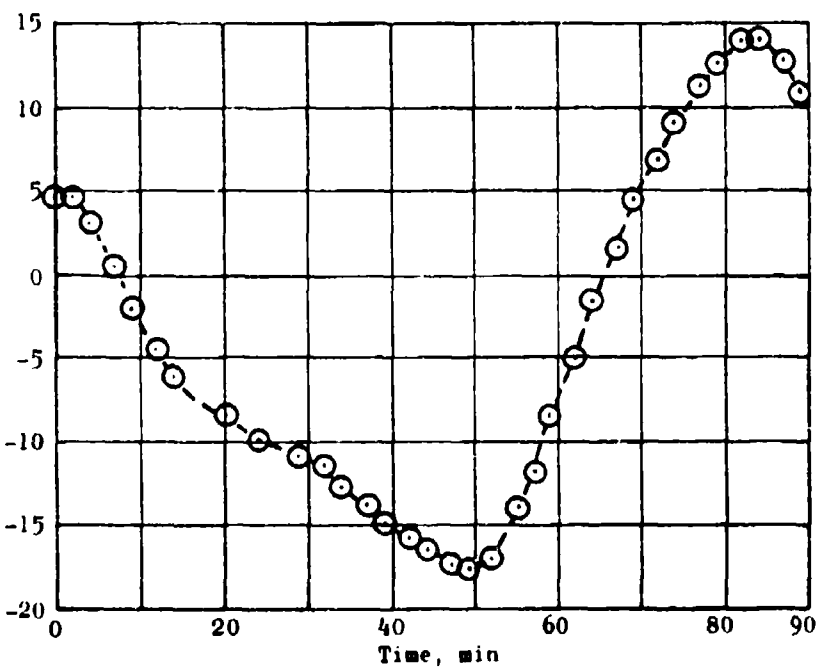

Figure 142. Aeroheat Test 3, N-15 Thermal Response

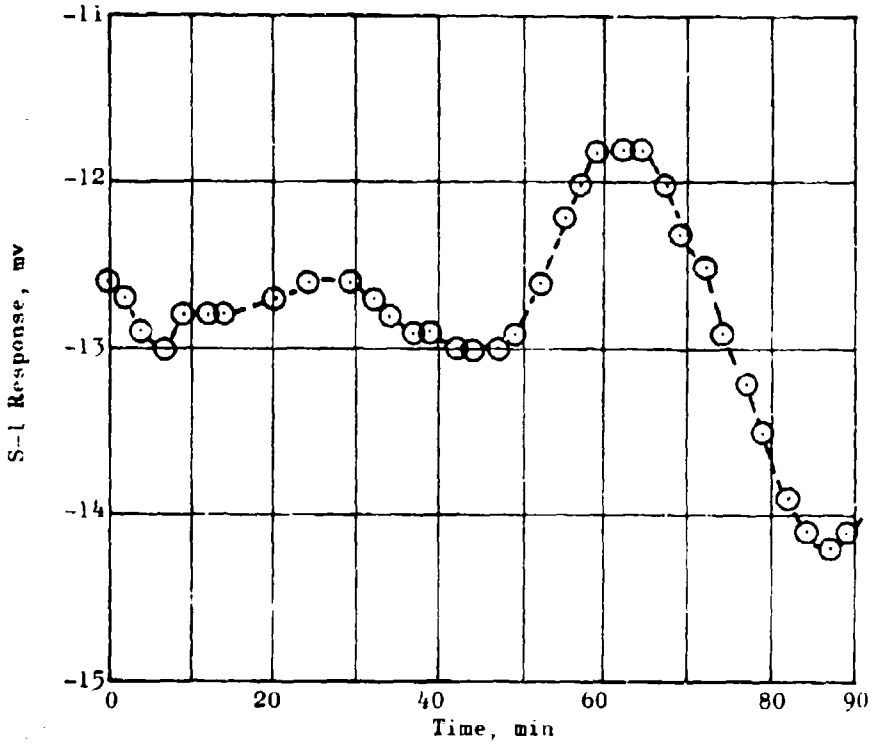

Figure 143. Aeroheat Test 3, S-1 Thermal Response

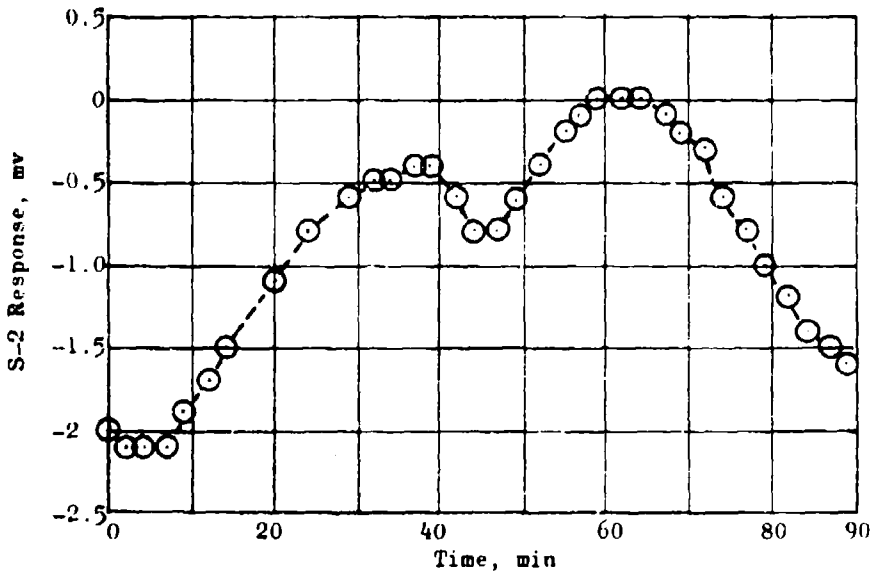

Figure 144. Aeroheat Test 3, S-2 Thermal Response

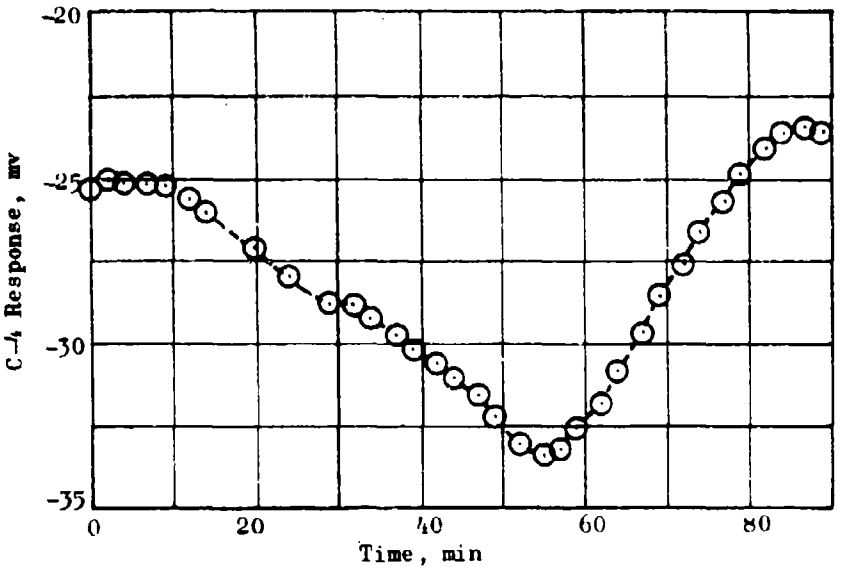

Figure 145. Aeroheat Test 3, C-4 Thermal Response

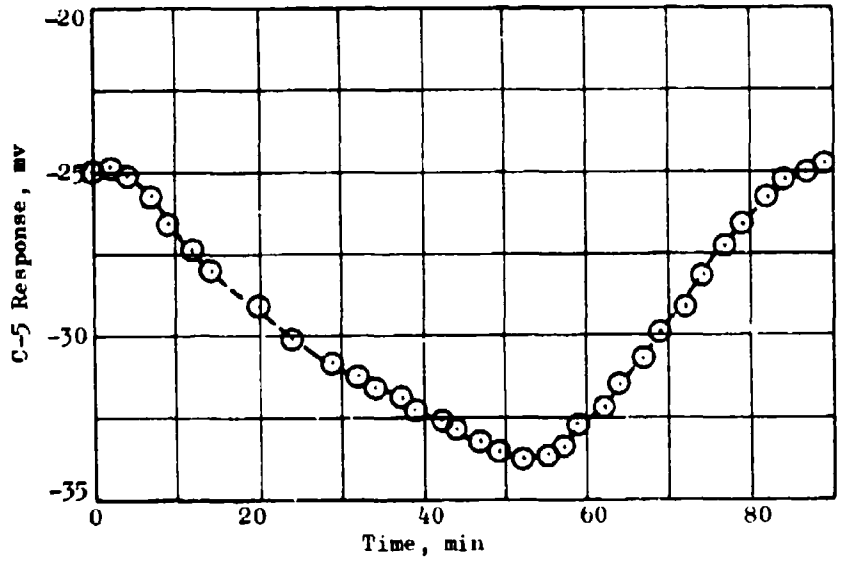

Figure 146. Aeroheat Test 3, C-5 Thermal Response

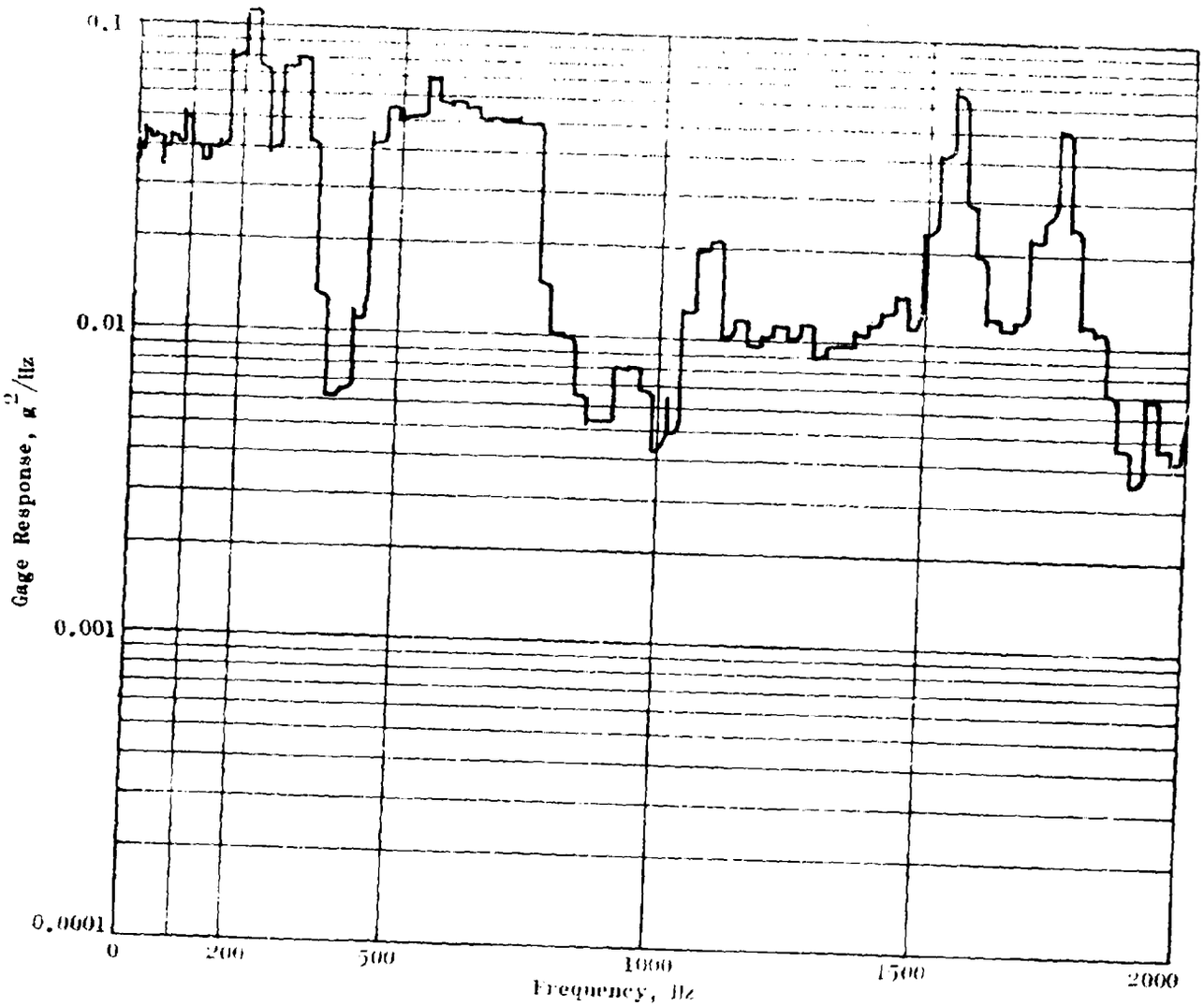

Figure 147. Random Vibration, Averager Channel

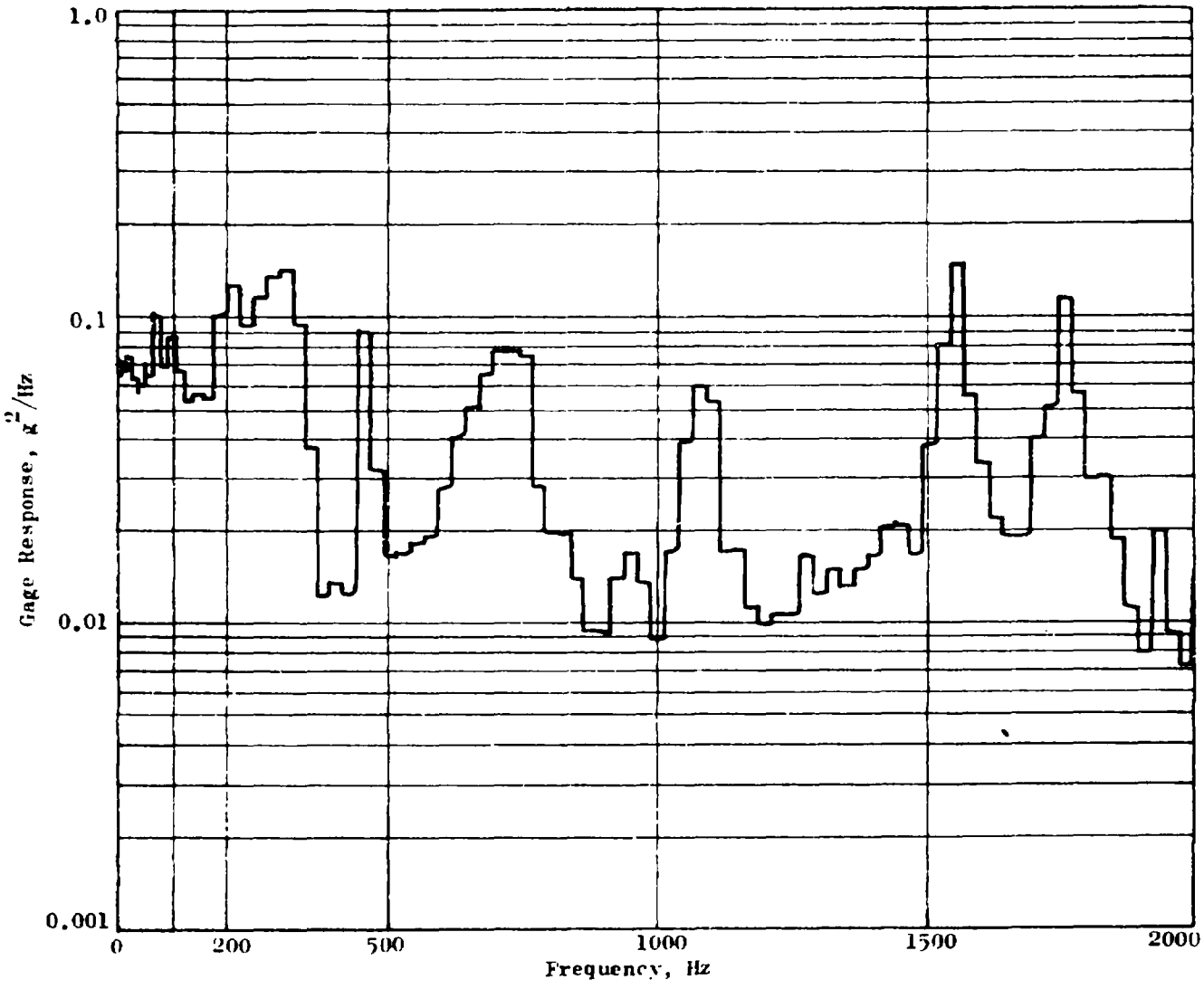

Figure 148. Random Vibration, Channel A-3

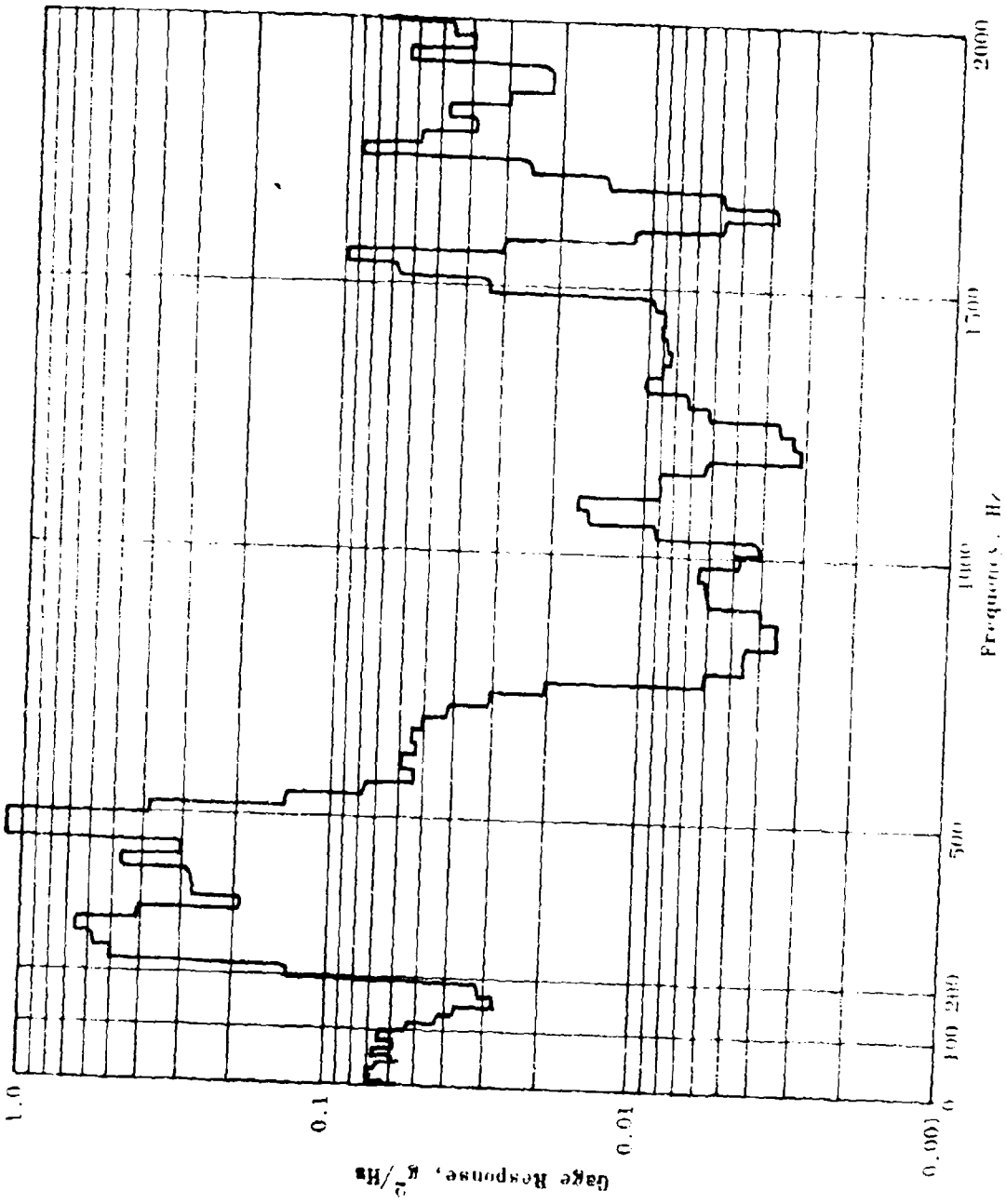

Figure 149. Random Vibration, Channel 1-4

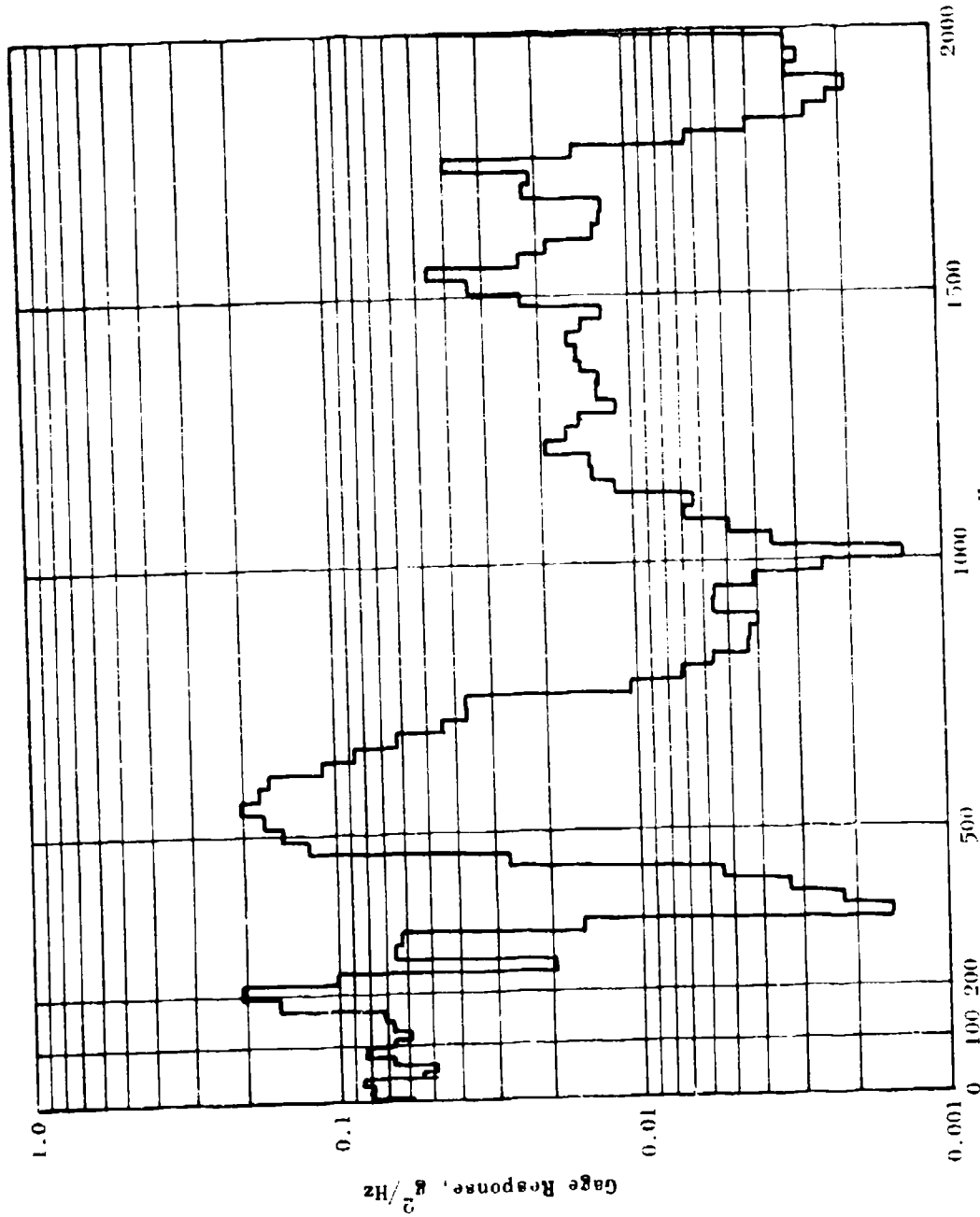

Figure 150. Random Vibration Aeroheat, Channel A-5

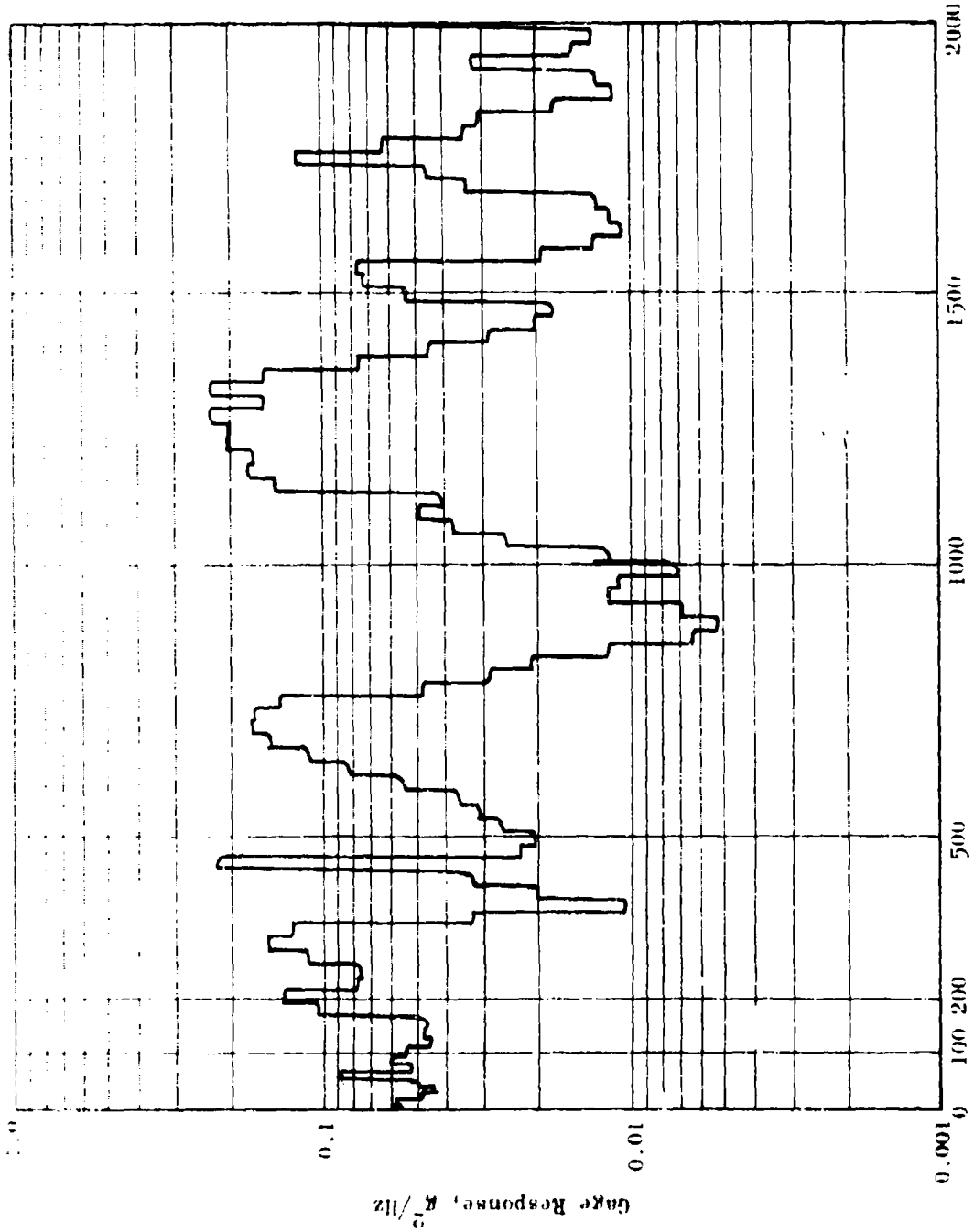

Figure 151. Random Vibration/Aeroheat, Channel A-7

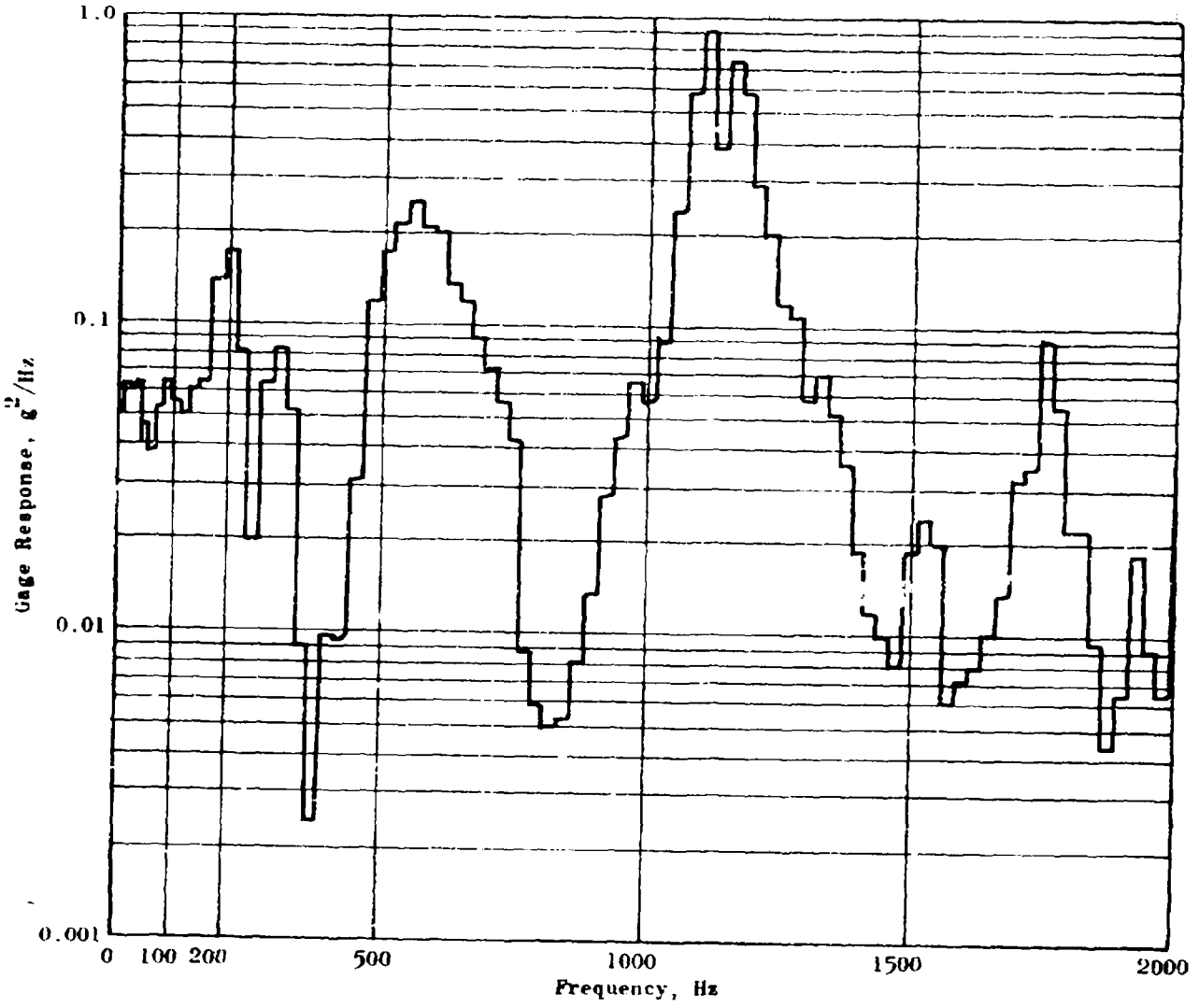

Figure 152. Random Vibration/Aeroheat, Channel A-8

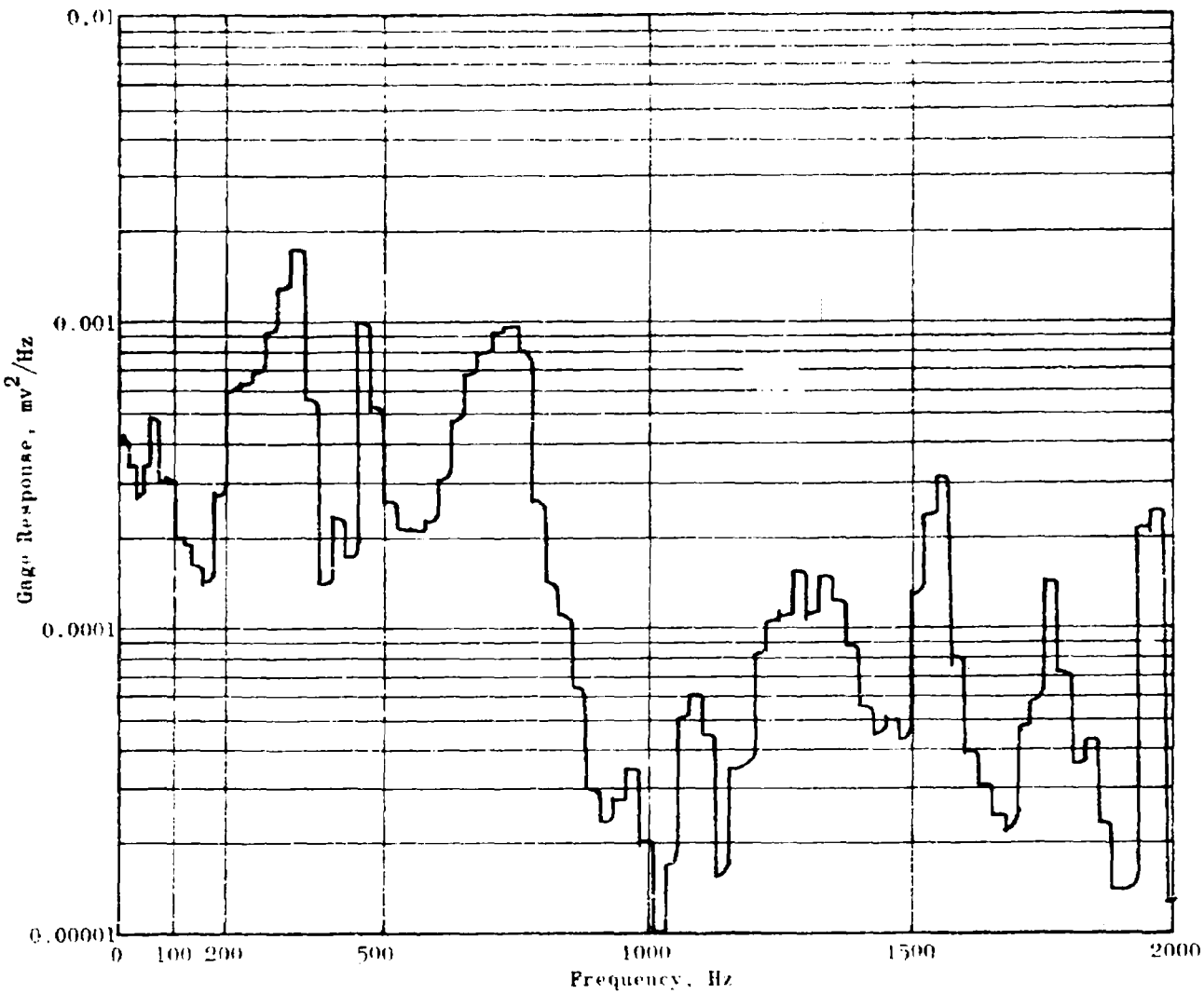

Figure 153. Random Vibration Aeroheat, Channel N-6

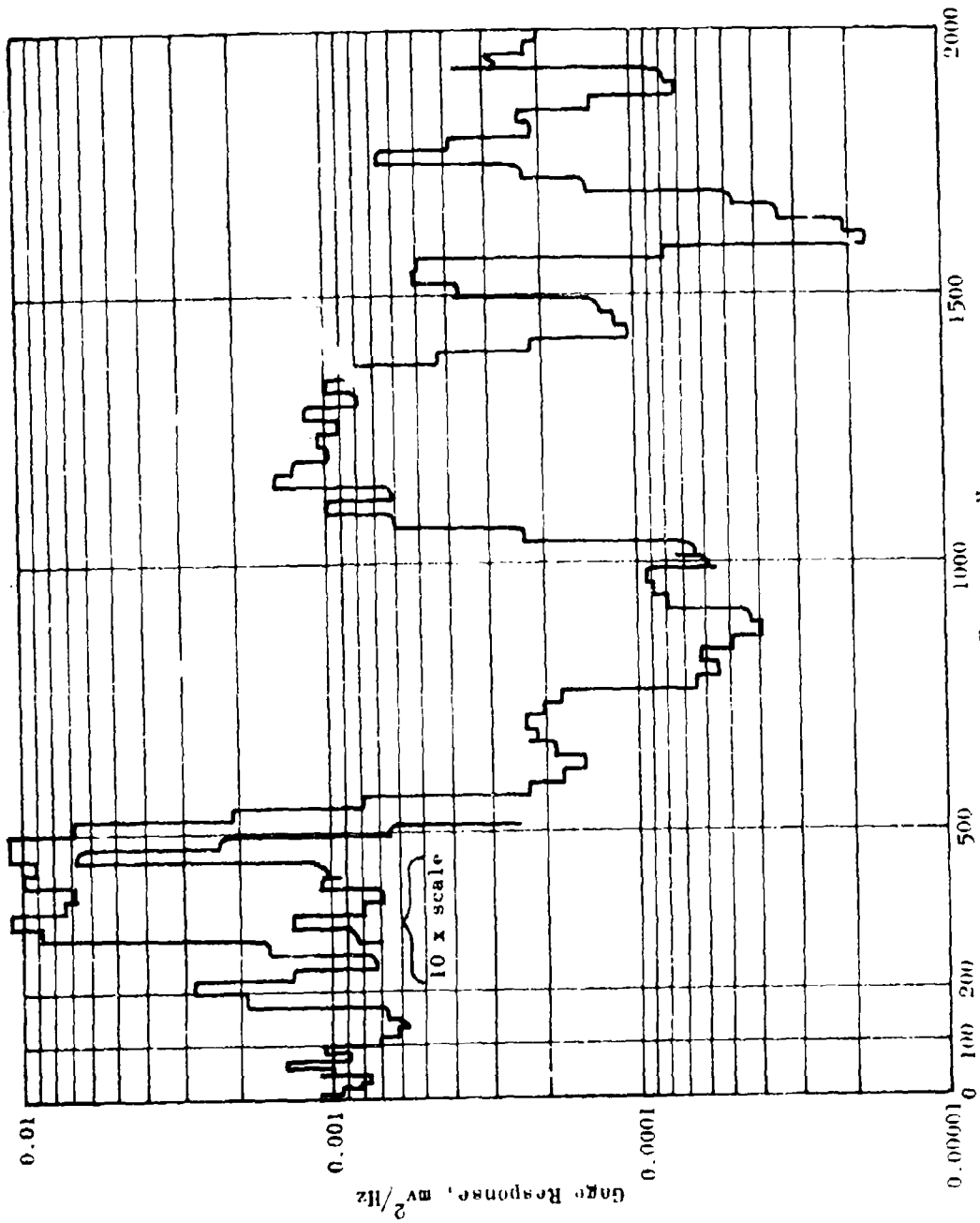

Figure 154. Random Vibration Aeroheat, Channel N-7

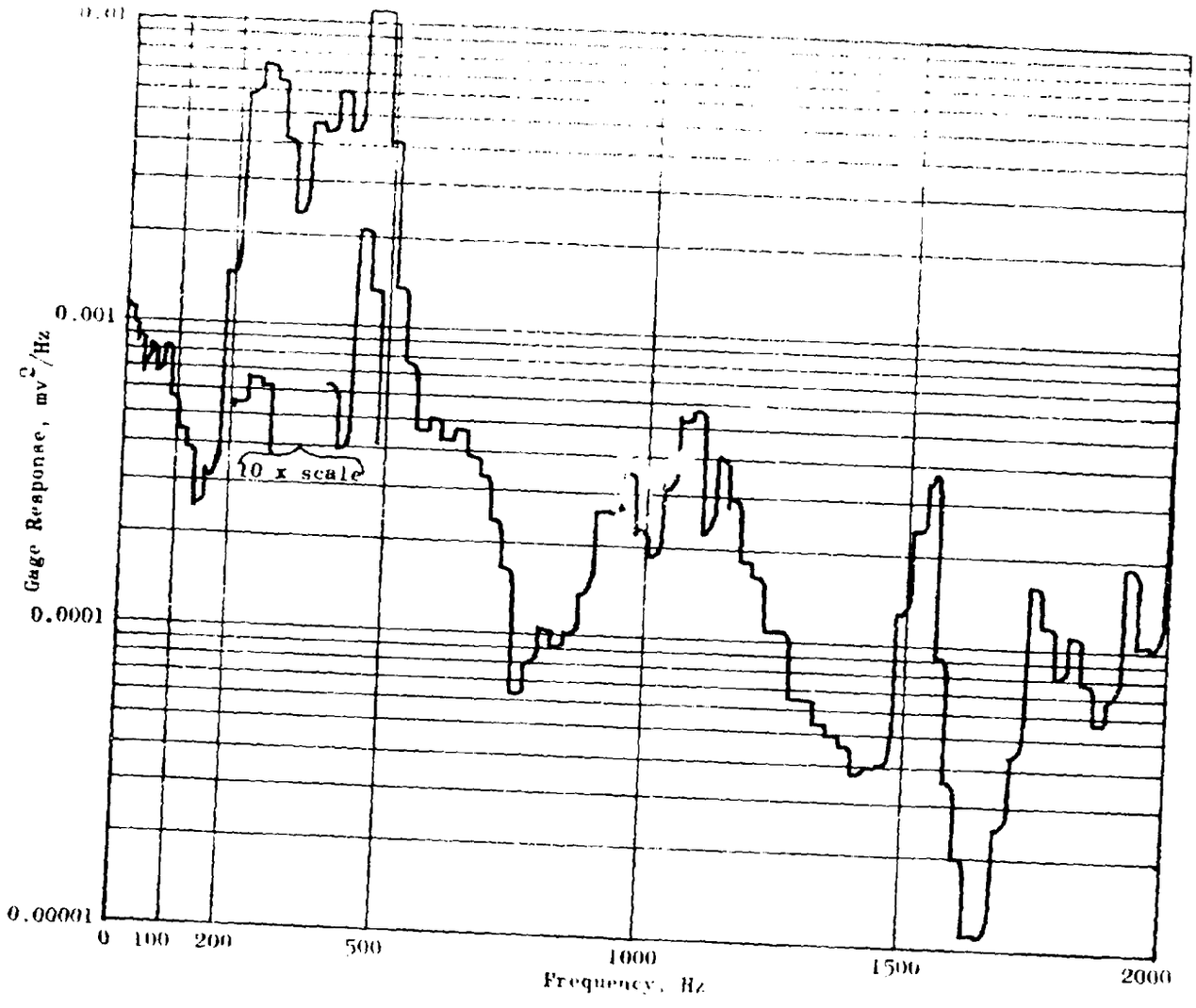

Figure 155. Random Vibration/Aeroheat, Channel X-9

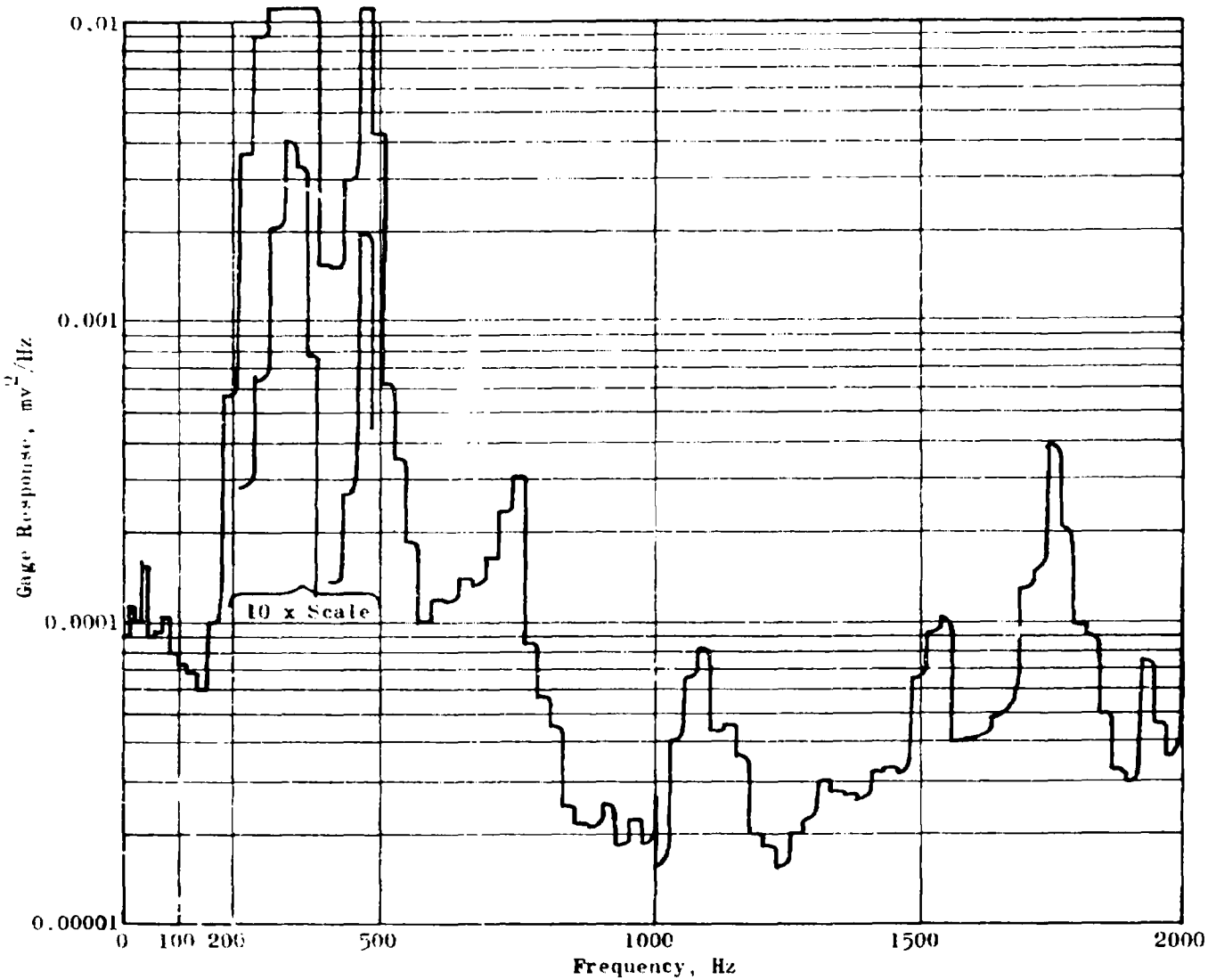

Figure 156. Random Vibration/Aeroheat, Channel N-13

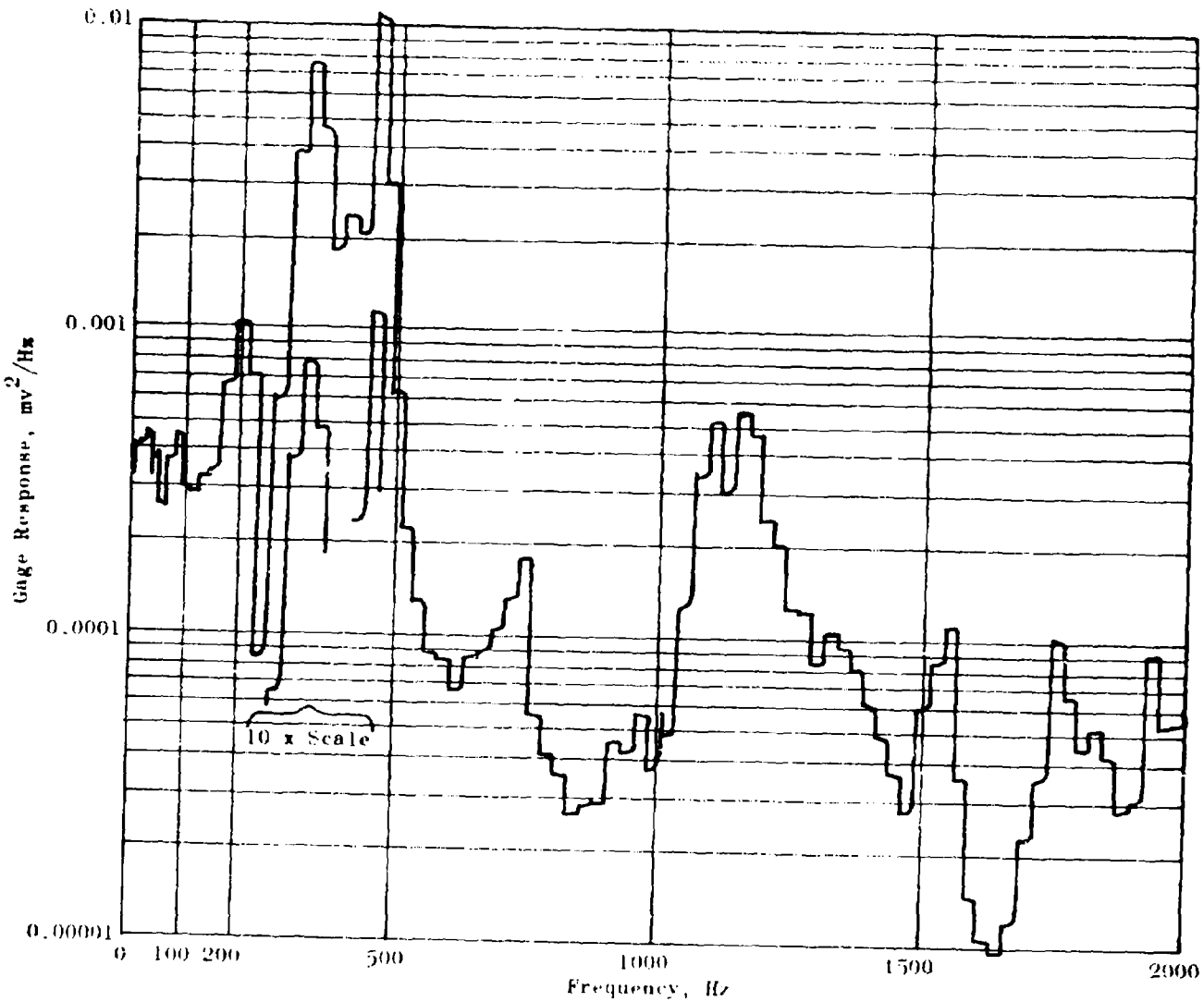

Figure 157. Random Vibration Aeroheat, Channel N-15

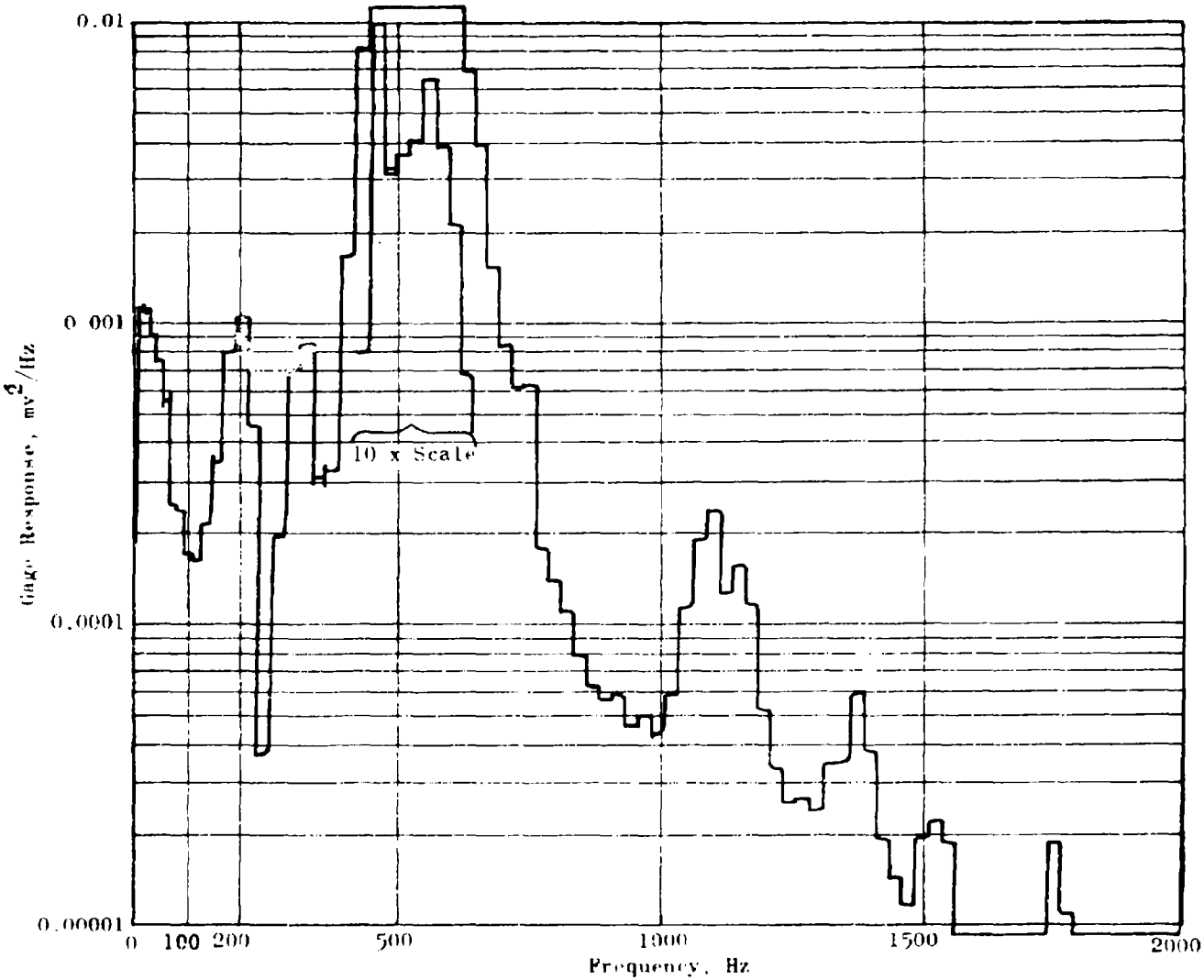

Figure 158. Random Vibration Aeroheat, Channel C-5

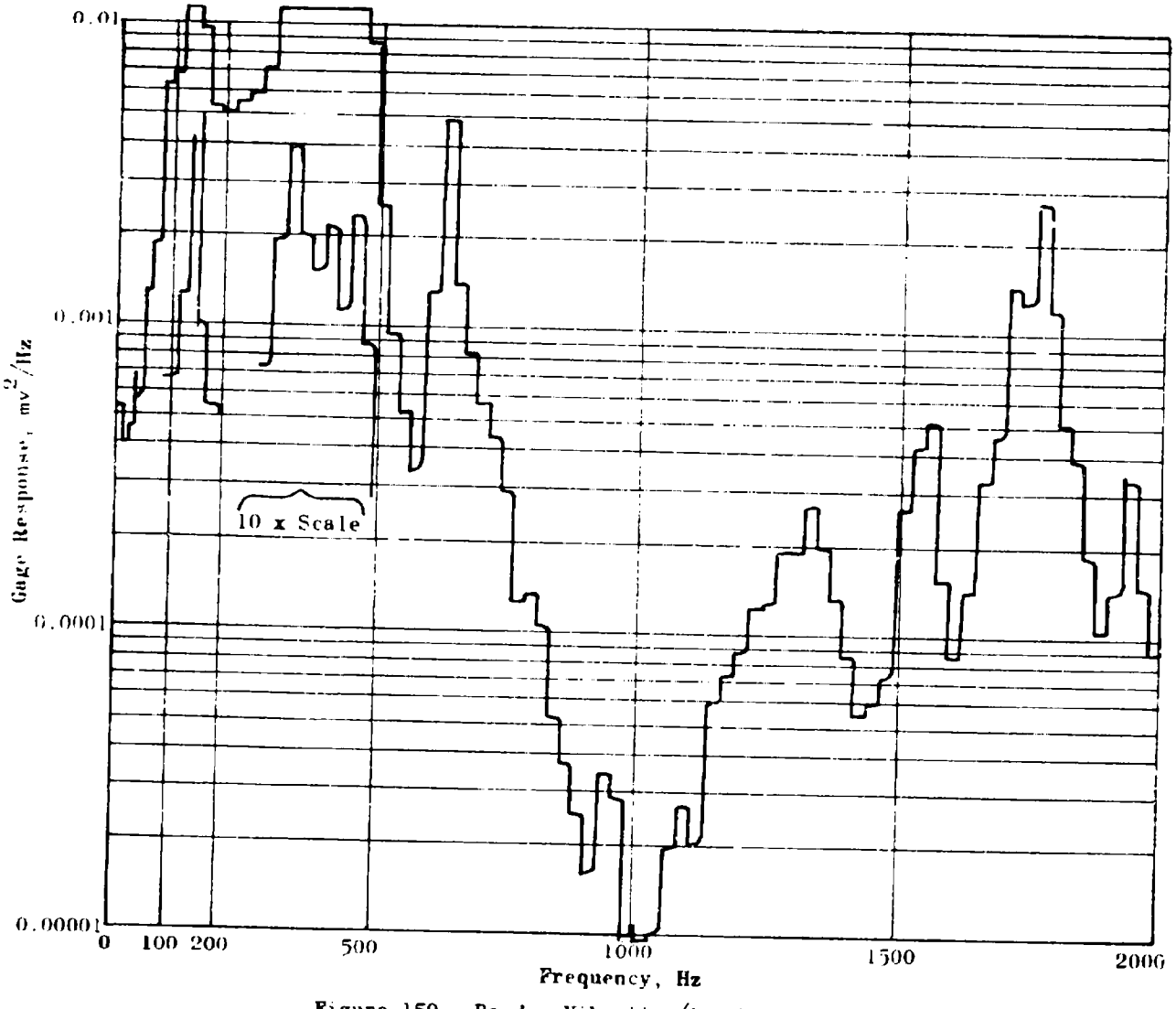

Figure 159. Random Vibration/Aeroheat, Channel C-4